Photocatalysis for Reductive Transformation of Nitrate and Chromate in Drinking Water

by

Heather O'Neal Tugaoen

A Dissertation Presented in Partial Fulfillment
of the Requirements for the Degree
Doctor of Philosophy

Approved May 2017 by the
Graduate Supervisory Committee:

Paul Westerhoff, Co-Chair
Kiril Hristovski, Co-Chair
Candace Chan

ARIZONA STATE UNIVERSITY
August 2017

ABSTRACT

Contamination of drinking water supplies from oxo-anion pollutants necessitates treatment prior to potable use. This dissertation aims to inform and improve light delivery (emission spectra, radiant intensity, reactor configuration) in order to enhance the photocatalytic reduction of hexavalent chromium (Cr(VI)) and nitrate, two common oxo-anions in drinking water, and photocatalytic oxidation of two model organic pollutants (methylene blue, (MB) and para-chlorobenzoic acid (pCBA)). By varying the photon fluence dose, two metrics (contaminant quantum yield (Φ), and electrical energy per order (E_{EO})) were used to assess photocatalytic reactor performance. A detailed literature review and experimental results demonstrated how different irradiance sources with variable intensity and emission spectra synergistically enhanced contaminant removal by a coupled photolytic/photocatalytic reaction mechanism. Cr(VI) was photocatalytically reduced on TiO_2 and formed $Cr(OH)_{3(s)}$ in a large-scale slurry reactor, but Cr(III) was then photolyzed and reformed Cr(VI). UV light also led to photo-aggregation of TiO_2 which improved its recovery by the ceramic membrane within the reactor. For nitrate reduction, light source emission spectra and fluence dose delineate the preferred pathways as intermediates were reduced via wavelength-dependent mechanisms. HONO was identified as a key nitrate reduction intermediate, which was reduced photocatalytically (UV wavelengths) and/or readily photolyzed at 365nm, to yield nitrogen gases. Photocatalytic nitrate reduction efficiency was higher for discrete wavelength irradiation than polychromatic irradiation. Light delivery through aqueous media to the catalyst surface limits efficiency of slurry-based photocatalysts because absorption and scattering of light

in nanomaterial slurries decreases effective photon transmittance and minimizes photolytic reactions. The use of optical fibers coupled to light emitting diodes (OF-LED) with immobilized catalyst demonstrated higher performance compared to slurry systems. OF-LED increased Φ for MB degradation by increasing direct photon delivery to the photocatalyst. Design of OF-LED reactors using bundled optical fibers demonstrated photocatalytic pCBA removal with high Φ and reduced E_{EO} due to increased surface area and catalytic sites compared to single OF/LED couples. This work advances light delivery as well as the suspension and attachment of nanoparticles in photocatalytic water treatment for selective transformation of oxo-anions and organic compounds to innocuous species.

DEDICATION

I first dedicate this culminating work to the two people who have made the most fundamental impact in my twenty seven years of life. To my mother: who is my best friend, constant supporter and prayer warrior, I thank you infinitely for your support and the love you have selflessly given me throughout my life. To my father: though I cannot thank you in person anymore, I appreciate the character, perseverance, and determination you instilled in me, along with the immense love and support you gave even when it was beyond your capability.

Secondly, I dedicate this work to the love of my life, who I would not have had the fortune to meet if I hadn't persevered through this doctoral program. Mr. Tugaoen, you are absolutely the best person to have walked into my life and turned everything upside down. Your depth of love, protective spirit, and dedication are inspirational and your care for me has allowed me to push forward even when everything goes haywire.

Lastly, I dedicate this dissertation to the people who have loved me through the last five years while I was pursuing my doctorate, and those who came before. Though I am far away, my family and family of friends have provided immense support, love, encouragement, and joy. You have continued to remind me that I can do anything I put my mind to, and helped me to persevere. To my new Arizona family, thank you for the lunches, dinners, the advice, the help and support and the late nights with tough issues. Living life together has brought me to a place of success and overcoming amidst the desert.

ACKNOWLEDGMENTS

I wish to thank all of my committee members who graciously served to advise, troubleshoot, review, and provide their expertise and equipment (Dr. Kiril Hristovski, Dr. Candace Chan). A special thank you goes to Dr. Paul Westerhoff, who has trained me in chemistry, engineering and plumbing within my time at ASU. You have provided countless insights for how to proceed in research. A second special thank you goes to Dr. Kiril Hristovski, who has kindly provided a listening ear, intellectual and personal insights to my research and holistic development, and countless revisions which required untold hours of time.

I am also deeply grateful for the fellow researchers who have contributed to this work significantly as co-authors: Li Ling and Sergi Garcia-Segura. Further, for the moral and material support of my colleagues: Anjali Mulchandani, Xiangyu Bi, Justin Kidd, Natália Fischer, Dr. Kyle Doudrick, Alexandra Bowen, Dr. Michelle Barry, Jared Schoepf, Dr. David Hanigan, Marisa Masles and Dr. Ting Yang. I also would like to thank those that I had the opportunity to mentor, as your advancement promoted growth in me as well: Jasper Robinson, Michael Burnett, Grigoria Athanasaki, Ashley Curiel.

I would like to thank and acknowledge the National Science Foundation (CBET 1132779, EEC-1449500), the United States Environmental Protection Agency (RD835175, EPA STAR 83560301), and the Ira A. Fulton Schools of Engineering Dean's Fellowship and Arizona State University for funding my work.

TABLE OF CONTENTS

Page

LIST OF TABLES xi

LIST OF FIGURES xiii

CHAPTER

1 INTRODUCTION 1

Dissertation Objectives 6

Dissertation Organization 7

2 BACKGROUND 8

Defining the Critical Need 8

Photocatalysis for Reductive Transformation of Oxyanions in Drinking Water 12

Photocatalytic Reduction of Oxyanions 19

Photocatalytic Oxidation of Model Pollutants 27

Light Delivery into Photocatalytic Systems 30

Fiber Optic Technology to Deliver Light into Water 33

Light Emitting Diodes for Engineered Photocatalysis 38

Fiber Optic Reactor Design 39

Deficiencies in the Literature and Novelty of Work Herein 42

3 HEXAVALENT CHROMIUM REMOVAL USING UV-TIO2/CERAMIC MEMBRANE REACTOR 46

Abstract 46

Introduction 47

CHAPTER Page

Methodology 49

Results and Discussion 54

Conclusions 63

Acknowledgements 64

4 CHALLENGES IN PHOTOCATALYTIC REDUCTION OF NITRATE AS A WATER TREATMENT TECHNOLOGY 65

Abstract 65

Section 1: Prevalence and Impact of Nitrogen Oxyanions in Ground Water and Drinking Water 67

Section 2: Direct Photolysis of Inorganic Nitrogen Species 72

Section 3: Photocatalytic Nitrate Reduction 82

Section 4: Hole Scavengers Influence 122

Section 5: Influence of Light Sources and Spectral Outputs on Photocatalytic Reduction of Nitrate 133

Section 6: Competitive Oxidation Reactions of Inorganic Nitrogen Species 140

Section 7: Photocatalytic Reduction of Nitrate in Real Water Matrices 153

Section 8: Summary of Key Insights 159

Acknowledgements 164

CHAPTER Page

5 ULTRAVIOLET WAVELENGTHS INFLUENCE KINETICS AND SELECTIVITY FOR N-GASES DURING TIO2 PHOTOCATALYTIC REDUCTION OF NITRATE 165

Abstract 165

Introduction 167

Methods and Analyses 173

Results and Discussion 177

Conclusions 192

Acknowledgements 193

Supplementary Information 194

6 COUPLING LIGHT EMITTING DIODES WITH PHOTOCATALYST-COATED OPTICAL FIBERS IMPROVES QUANTUM EFFICIENCY OF POLLUTANT OXIDATION 196

Abstract 197

Introduction 198

Experimental Methods and Materials 200

Results and Discussion 203

Engineering Implications 216

Acknowledgements 217

Supplementary Information 218

Supplementary Figures 222

CHAPTER Page

7 COMPACT LIGHT-EMITTING DIODE OPTICAL FIBER IMMOBILIZED TIO2 REACTOR FOR PHOTOCATALYTIC WATER TREATMENT 229

Abstract 229

Introduction 230

Experimental 234

Results and Discussion 240

Engineering Implications 252

Acknowledgements 253

8 SYNTHESIS 254

Introduction 254

A Combined Photolytic/Photocatalytic Approach to Drive Selectivity Outcomes 261

Implementation Constraints for Photocatalytic Reactors 264

Managing Light Delivery to Enhance Photocatalytic Performance in a Fixed Film Reactor 266

9 SUMMARY, CONCLUSIONS AND FUTURE RECOMMENDATIONS 268

Summary 268

Conclusions 273

Recommendations for Future Research 274

REFERENCES 276

APPENDIX Page

A SUPPLEMENTARY BACKGROUND INFORMATION 331

BIOGRAPHICAL SKETCH.....351

LIST OF TABLES

Table Page

1-1. Objectives and Organization of Dissertation Chapters 7

2-1. Best Available Treatment Technologies for Cr(VI) (adapted from (Sharma et al., 2008)) 11

2-2. Best Available Treatment Technologies for NO3- (adapted from (Archna, Sharma, & Sobti, 2012)) 12

2-3. Definitions of Photonic Terminology Utilized in Fiber Optic Design (adapted from (Paschotta, 2016) 36

4-1. Nitrate Conversion and Products Selectivity for Pristine TiO_2 Photocatalysts ... 87

4-2. Nitrate Conversion and Products Selectivity for Doped Photocatalysts 102

4-3. Nitrate Conversion and Products Selectivity for Photocatalyst Composites with 4^{th} Period Metals 109

4-4. Nitrate Conversion and Products Selectivity for Photocatalyst Composites with Platinoids 114

4-5. Nitraet Conversion and Products Selectivity for Photocatalyst Composites with Noble Metals: Silver and Gold 117

4-6. Nitrate Conversion and Products Selectivity for Bimetallic Photocatalyst Composites 121

4-7. Ammonia Conversion and Products Selectivity during Photocatalytic Oxidation 149

4-8. Nitrite Conversion and Products Selectivity for Photocatalytic Oxidation 152

Table Page

4-9. Nitrate Conversion and Products Selectivity during Photocatalytic Reduction Treatment of Actual Matrices 155

5-1. Reduction of Nitrate or Nitrite under Wavelength Filtered (240-400nm or 240-280nm) Xenon Lamp Irradiaton 183

5-2. Summary of Kinetic Data for NO_3^- Reduction Experiments under Varied Irradiance Conditions 186

6-1. Experimental Matrix 203

7-1. Comparison of E_{EO} values for the OF/LED Configurations Tested 251

LIST OF FIGURES

Figure Page

2-1. Critical Juncture of Photocatalysis: Light Source Irradiation Wavelength and Catalyst Properties 15

2-2. Mechanism of Light Propagation, Exit, and Absorption in Coated and Uncoated Fiber Optics (adapted from Wang and Ku 2003b) 35

3-1. Schematic of pilot-scale photocatalytic reactor, Photo-Cat L®, by Purifics 50

3-2. Hexavalent Chromium Removal for Varied TiO_2 Photocatalyst Dose 54

3-3. Removal Efficiencies of Photocatalytic Hexavalent and Total Chromium Removal at Varied TiO_2 Dose..... 55

3-4. Hexavalent Chromium Removal for Varied Water Matrix and TiO_2 Dose 57

3-5. Hexavalent Chromium Removal for Varied pH Conditions 58

3-6. SEM Images of Virgin and Post-Treatment P90 Used in Photocatalytic Reduction of Cr(VI) 59

3-7. Photocatalytic Evolution of Cr(VI) from an Initial Cr(III) Input 60

3-8. Outline of Mechanisms for Cr(VI) Reduction, Cr(III) Re-Oxidation and Need for Catalyst Regeneration 61

3-9. Concentration of TiO_2 Leached into Permeate for Varied Irradiation Schemes ... 63

4-1. Methodologies for Nitrate Management in Drinking Water 70

4-2. Publication Record for Nitrate Removal Technologies and Photocatalysis 71

4-3. Molar Absorptivity of Aqueous Nitrogen Species 73

4-4. Mechanisms of Nitrate Photolysis in Water 77

4-5. Mechanisms of Nitrite Photolysis in Water 81

Figure Page

4-6. Scheme of Photocatalytic Oxidation/Reduction Reactions and Relationship of Band Structure for Semiconductors with NO_3^- Reduction Potential. 83

4-7. Mechanism of Nitrate Photocatalysis in Water 91

4-8. Photocatalytic Reduction Processes for Varied Semiconductor Catalysts..... 103

4-9. Nitrate Conversion and Selectivity to N-gases for Cu/TiO_2 photocatalyst and Varied Formic Acid:Nitrate Ratio. 130

4-10. Comparison of Light Source Irradiance Spectrum with Electromagnetic Spectrum for Varied Light Sources..... 135

4-11. Speciation of NH_4^+/NH_3 as a Function of pH 142

4-12. Speciation of HNO_2/NO_2^- as a Function of pH..... 153

4-13. Double Layer Scheme for Synthetic Model Water and Actual Water Matrix... 159

5-1(S). Conceptual Sequence for Nitrate Reduction to Desirable Nitrogen Gas (N_2) and Undesirable Ammonium Ion. 171

5-1. Diffuse Reflectance Absorption Spectra of TiO_2 and Molar Absorptivity of Relevant Aqueous Nitrogen Species. 178

5-2(S). Conceptual Model for Nitrate Reduction to Nitrogenous Intermediates and By-Products 193

5-2. Ultraviolet Spectral Output of Varied Irradiance Sources. 179

5-3. NO_3^- Photocatalytic Reduction and Product Formation under Medium Pressure Mercury Lamp Irradiation 181

5-4. NO_3^- Photocatalytic Reduction and Product Formation under Simultaneously Operated UV-LED Irradiation. 185

Figure Page

5-5. Pseudo-First Order Nitrate Removal Kinetics with Respect to Time, Photons and Energy under Medium Pressure Mercury Lamp Irradiation. 187

5-6. Half-Life of NO_3^- Reduction with Respect to Time, Photons, and Energy for Varied Light Sources. 188

5-7. Photolytic and Photocatalytic Nitrite (HONO) Reduction at 365nm with Formic Acid. 191

6-1. Photocatalyst-Absorbed Light Intensity of 318nm UV-Led for Varied Optical Fiber Coating Length and Coating Mass..... 205

6-2. Pseudo-First Order Degradation Kinetics for Methylene Blue for Varied TiO_2 Coating Methodologies..... 208

6-3. Quantum Yield of Methylene Blue Bleaching for Photolytic or Photocatalytic Optical-Fiber Reactor under Varied Coating Methodologies..... 210

6-4. Conceptual Scheme of the Two Potential Mechanisms for Photocatalyst Excitation in Optical Fiber/Light Emitting Diode Reactor: Total Internal Reflection and Evanescent Wave 214

6-5. Evanescent Wave Intensity as a Function of Radial Distance from the Optical Fiber Surface and Incident Angle..... 216

7-1. Mechanism of Light Transport through the Optical Fiber and Light Delivery to the Photocatalyst 233

7-2. Scheme of Optical TiO_2/Optical Fiber Coupling with the Light Emitting Diode Light Source 236

Figure Page

7-3. Scheme of Flow-Through Reactor Design for Optical Fiber/Light Emitting Diode System 237

7-4. Scanning Electron Microscopy Images of TiO_2-Coated Optical Fibers 241

7-5. Photon Fluence Differential Estimated between Uncoated and Coated Optical Fibers with Varied Optical Fiber Length and Coating Thickness 243

7-6. Photocatalytic Degradation of 0.1mM para-Chlorobenzoic Acid in the Optical Fiber/Light Emitting Diode Flow-Through Reactor under Varied Photon Fluence 245

7-7. Photocatalytic Degradation of 0.1mM para-Chlorobenzoic Acid in the Optical Fiber/Light Emitting Diode Flow-Through Reactor under Varied Photon Fluence: Surface Area Ratio 248

8-1. Electrical Energy per Order for Photolytic and Photocatalytic Removal of Cr(VI) in the PhotoCat® Reactor 257

8-2. Electrical Energy per Order and NH4+ Selectivity with Varied Irradiance Input for Photolytic and Photocatalytic Reduction of Nitrate and Nitrite 261

8-3. Quantum Yield and Electrical Energy per Order for Optical Fiber/Light Emitting Diode Reactor for Methylene Blue Bleaching or Oxidation of para-Chlorobenzoic Acid 264

CHAPTER 1

INTRODUCTION

Access to high-quality water supplies represents one of the key challenges at the beginning of the 21st century. The geospatial context of global water supplies increases the complexity of approaching a solution in that both groundwaters and surface waters are threatened (Danielopol, Griebler, Gunatilaka, & Notenboom, 2003). Scarcity of freshwater resources has already increased the need for high-energy treatment and delivery systems (Postel, 2000). The demand for innovative systems to overcome these water quality and quantity challenges is of paramount importance, particularly for remediation of widespread drinking water contamination by organics and oxy-anions.

Diminishing freshwater water quantity is linked to climate change, while water quality is predominantly attributable to anthropogenic inputs, such as those from industrial processes, sanitation, and agricultural activities. As such, a variety of potential contaminants challenge scientists and engineers in water treatment such as trace organic compounds, bacteria and viruses, and inorganic compounds such as oxyanions. Common among these constituents is their inherent toxicity to humans and aquatic ecosystems (Gangolli et al., 1994), widespread geospatial distribution (Mandal & Suzuki, 2002), and complexity to achieve satisfactory removal per national standards (Fuerhacker, 2009).

Pesticides, pharmaceuticals, azo-dyes, as well as other endocrine disrupting compounds (plasticizers, fire retardants, etc.) represent the class of chemicals denoted by contaminants of emerging concern. They are notably recalcitrant and persistent in the environment, and cause adverse effects to humans and the environment such as: carcinogenicity, mutagenicity, and hormone disruption (Benotti, Trenholm, et al., 2009). Similar effects have been documented from

exposure to inorganic compounds such as oxyanions and heavy metals (Sedman et al., 2006). This class of compounds includes mercury, arsenic (arsenate), chromium (chromate), halogenated compounds (perchlorate, bromate), and nitrogen (nitrate) and phosphorus (phosphate). National maximum contaminant level standards for both inorganic and organic compounds vary widely based on known or suspected toxicity, ranging in scale of parts per trillion (e.g., polychlorinated biphenyls, PCBs) to parts per million (e.g., NO_3^-) (Electronic Code of Federal Regulations, 2017).

Emerging and persistent contaminants are not mitigated by conventional drinking water treatment processes (Michael R. Burkart & Kolpin, 1993; Kolpin et al., 2002; Stackelberg et al., 2004), yielding increased demand for novel treatment processes. These shortcomings are in part due to the low concentration of these contaminants compared to more abundant aqueous constituents. In conventional treatment processes, high-liquid phase partitioning and low biodegradability are important factors that hinder removal of these contaminants (Radjenovic, Petrovic, & Barceló, 2007). Certain chemicals (1) may pass untreated (Benotti, Trenholm, et al., 2009) or (2) be transformed into more toxic metabolites (Kolkman, Martijn, Vughs, Baken, & Van Wezel, 2015). Accordingly, new technologies should transform contaminants to their least toxic state in addition to physically removing them from the aqueous phase.

Emerging technologies that induce transformative chemical reactions *in situ* for the oxidation or reduction of target compounds have risen to prominence in the past 20 years. These technologies include: catalysis, photocatalysis, and photoelectrocatalysis. Through these processes, an initial compound is chemically transformed into partially- or terminally-reduced/oxidized products. Of these technologies, photocatalysis emerges as a promising alternative to conventional treatment processes due to: its capacity for the mineralization of organic compounds (Nan, Jin, Chow, & Saint, 2010), potency for disinfection (Dalrymple, Stefanakos,

Trotz, & Goswami, 2010), and simultaneous potential for reduction of inorganic oxyanions and heavy metals (Sharma, Petrusevski, & Amy, 2008). Further, photocatalysis is notable for its low chemical consumption (Barakat & Kumar, 2016).

Research on photocatalysis began with the discovery of photocatalytic water splitting by Fujishima and Honda in 1972 (Fujishima & Honda, 1972). Since that time, there has been thorough research regarding photocatalytic materials (Fujishima, Rao, & Tryk, 2000; Linsebigler et al., 1995) and environmental applications of the technology (Akpan & Hameed, 2009; Pirkanniemi & Sillanpää, 2002; Teh & Mohamed, 2011). Little of the published research has focused methodologies of implementation, namely engineered reactor design (Cassano, Martin, J., & Alfano, 1995; Shan, Ghazi, & Rashid, 2010; Wenderich & Mul, 2016). Whereas photocatalysis has been widely studied from a scientific bench scale and materials point of view, the greatest barrier to engineered implementation is the lack of understanding of systemization and light delivery. Whereas photocatalytic systems have been proven highly effective for remediation of a range of contaminants, the applied conditions are typically use of a model water and <1L total aqueous volume (Ibhadon & Fitzpatrick, 2013; Pirkanniemi & Sillanpää, 2002). While this is an excellent approach for determining photocatalytic mechanisms, complications of scale up are remain predominantly unexplored.

Current barriers to the implementation of photocatalytic technologies are the lack of full- or pilot- scale investigations to understand operational difficulties and improve engineered reactor design (Stancl, Hristovski, & Westerhoff, 2015a). As a result, issues such as the reutilization of the catalyst and required technology to achieve regeneration are of yet unknown. Management of competing ions and catalyst fouling due to other aqueous constituents remain hurdles for implementation (T. Yang, Doudrick, & Westerhoff, 2013; F. Zhang et al., 2005). Determination

of a safe and effective separation technology is another barrier to implementation which results from the predominant use of nanoparticle-based slurry systems in the photocatalytic literature (Qu, Alvarez, & Li, 2013). To date, immobilization technologies have not been demonstrated to surpass slurry systems in kinetic performance (Shan et al., 2010; van Grieken, Marugan, Sordo, Martinez, & Pablos, 2009). Achieving higher performance in an immobilized catalyst reactor could significantly diminish operational complexity for photocatalytic systems.

The delivery of light, both with regard to transmittance into the system and to activate the photocatalyst, represents another challenge to photocatalytic system design. This is a critical area because the delivery of light determines (1) the kinetic performance and (2) the by-products of the photocatalytic reaction. These two outcomes are based on the successful transmittance of light to the photocatalyst and excitation of electrons to react or produce radical species, and the photoactivity of certain aqueous constituents to result in photolysis *in situ*. This dissertation aims to provide insights into the barriers to implementation of full scale photocatalysis with a particular focus on light delivery systems and investigation of a novel reactor scheme to enhance light delivery.

Dissertation Objectives

Chapter 2 includes a comprehensive literature review which provided insights into current gaps of scientific and engineering expertise that are addressed in this dissertation. Based on previously published work, light delivery was identified as the critical element to facilitating innocuous products selectivity and high reaction kinetics. The overarching research goal of this dissertation was to:

Provide insight into the influence of light and catalyst delivery (emission spectra, radiant intensity, reactor configuration) to enable and enhance the photocatalytic reduction of two common oxo-anions (Cr(VI) and NO_3^-) in drinking water.

In an effort to address the overall goal above, the following specific research objectives guided the dissertation study:

1. *Quantify reduction and removal of hexavalent chromium via pilot-scale photocatalytic reactor under UV-C irradiation in real water matrix and identify engineering deficiencies to improve reactor use and design;*
2. *Review literature on the photocatalytic and photolytic reduction of nitrate and outline mechanistic pathways for the selective reduction to nitrogen gases;*
3. *Compare irradiation wavelengths and light sources for the photocatalytic reduction of nitrate and nitrite to nitrogen gases and determine specific wavelengths of interest for N-gas pathway selectivity;*
4. *Develop an immobilized catalyst, in-situ light delivery system for photocatalytic oxidation of methylene blue and demonstrate efficacy compared to slurry photocatalysis;*
5. *Demonstrate efficacy and determine efficiency of optical fiber/light-emitting diode flow through reactor for aqueous contaminant treatment.*

Dissertation Organization

The research completed to accomplish each objective is presented in the following chapters of this dissertation. Table 1.1 provides an outline for each objective and its corresponding chapter along with relevant citation information. At present, Chapters 3 and 4 has been published in a peer-reviewed journal, and Chapters 5-7 are in preparation for submission. Chapter 8 provides a synthesis of all completed objectives in addition to synthesizing the conclusions from each chapter into a holistic summary. Chapter 9 provides brief conclusions and recommendations for future research work based on the discoveries of this dissertation.

Table 1-1. Objectives and Organization of Dissertation Chapters

Objective 1 *Quantify reduction and removal of hexavalent chromium via pilot-scale photocatalytic reactor under UV-C irradiation in real water matrix and identify engineering deficiencies to improve reactor use and design* Dissertation Chapter 3 Published: Stancl, H.O., Hristovski, K., Westerhoff, P., 2015. Hexavalent Chromium Removal Using UV-TiO_2/Ceramic Membrane Reactor. *Environmental Engineering Science* 32(8): 676-683. doi:10.1089/ees.2014.0507.
Objective 2 *Review literature on the photocatalytic and photolytic reduction of nitrate and outline mechanistic pathways for the selective reduction to nitrogen gases* Dissertation Chapter 4 Published: Tugaoen, H.O., Garcia-Segura, S. Hristovski, K., Westerhoff, P., 2017. Challenges in photocatalytic reduction of nitrate as a water treatment technology. *Science of the Total Environment* 599-600: 1524-1551. doi: 10.1016/j.scitotenv.2017.04.238
Objective 3 *Compare irradiation sources for the photocatalytic of nitrate and nitrite to nitrogen gases and determine specific wavelengths of interest for N-gas pathway selectivity* Dissertation Chapter 5 In preparation: Tugaoen, H.O., Herckes, P., Hristovski, K., Westerhoff, P., 2017. Ultraviolet wavelengths influence kinetics and selectivity for N-gases during TiO_2 photocatalytic reduction of nitrate.
Objective 4 *Develop an immobilized catalyst, in-situ light delivery system for photocatalytic oxidation of methylene blue and demonstrate efficacy compared to slurry photocatalysis* Dissertation Chapter 6 In preparation: Ling, L.,* Tugaoen, H.O.,* Brame, J., Sinha, S., Li, C., Schoepf, J., Hristovski, K., Kim, J., Shang, C., Westerhoff, P. Coupling light emitting diodes with photocatalyst-coated optical fibers improves quantum efficiency of pollutant oxidation.
Objective 5 *Demonstrate efficacy and determine efficiency of optical fiber/light-emitting diode flow through reactor for aqueous contaminant treatment* Dissertation Chapter 7 In preparation: Tugaoen, H.O., Garcia-Segura, S., Hristovski, K., Westerhoff, P., 2017. Photocatalytic oxidation of pCBA in optical fiber/light emitting diode flow-through reactor: optimization of reactor conditions

CHAPTER 2

BACKGROUND

Defining the Critical Need

Prevalence and Impact of Oxyanions in Drinking Water

Nitrate (NO_3^-) and hexavalent chromium (CrO_4^{2-}) are two of the most ubiquitous and concerning oxyanions found in groundwater supplies. Both contaminants occur naturally, but also are produced at large scale commercially for agricultural and industrial purposes, respectively. NO_3^- and CrO_4^{2-} are very stable oxidized species, but may be reduced to innocuous products: N_2 and $Cr(OH)_3$. Predominant partitioning of these constituents into groundwater purports a direct risk to human consumption. Over 14.6 billion gallons of groundwater are utilized for public-supply purposes for drinking/household waters and another 3.7 billion gallons are withdrawn for domestic supply (individual households off-municipal grids) (Perlman, 2014). Further, redox conditions in groundwater can increase constituent transport and toxicity by transforming contaminants (e.g., Cr reduction or oxidation or denitrification) (Blowes, Ptacek, & Jambor, 1997; Puckett, Tesoriero, & Dubrovsky, 2011). Nutrient transport (Tesoriero, Liebscher, & Cox, 2000) and migration of volatile organic compounds and trace metals have all been linked to redox conditions in groundwater (Tesoriero, Terziotti, & Abrams, 2015), which vary at national scale (McMahon et al., 2008; McMahon & Chapelle, 2008). Adequate treatment technologies are available at larger municipal scale, but small systems are particularly impacted by these contaminants and often are limited in treatment options due to operational intensity, cost, and accessibility.

Chromium in drinking water has been regulated most stringently by the state of California, which in 2014 passed a ruling to limit Cr(VI) in water to 10μg/L (California EPA, 2014) and

recommended a public health goal of 0.02μg/L. The United States Environmental Protection Agency (USEPA) maximum contaminant ruling focuses on total chromium (Cr(VI)+Cr(III)), and currently is under review but presently remains at 100μg/L (California EPA, 2014). A 2010 study from the US Environmental Working Group found Cr(VI) concentrations in drinking waters frequently exceed 1μg/L, with less frequent occurrence of >10μg/L (Sutton, 2010). USEPA monitoring found one public water system in excess of the national 100μg/L standard in 2013-2014 (United States Environmental Protection Agency, 2014). At sufficient concentrations, both trivalent and hexavalent chromium are linked to adverse health effects, particularly increased: cancer risk, gastrointestinal disruption, accumulation and toxicity to vital organs, damage to DNA, gene mutation (Beaumont et al., 2008; Costa, 1997; Dayan & Paine, 2001; Sedman et al., 2006).

Nitrate in drinking water is regulated nationally by the USEPA to an MCL of 10mg/L. A 2010 study of nitrate in groundwater in the United States indicated 24 million people utilize a supply above the 10mg-N/L MCL (Burow, Nolan, Rupert, & Dubrovsky, 2010). The predominant reason for regulation is methanoglobonemia, or blue baby syndrome, which can cause suffocation and death in infants and fetuses. Nitrogen is relatively stable in other aqueous forms, namely nitrite and ammonium. Nitrite is regulated at 1mg/L due to its high conversion to carcinogenic nitrosamines in the body (United States Environmental Protection Agency, 1996). Ammonium remains unregulated in drinking water supply, but causes disruption by promoting biological growth and exerting an oxygen demand and is thus an undesirable endpoint. Nitrogen gases are stable reductive endpoints of nitrate, and may be sparged due to their low solubility in the aqueous phase. Nitrogen gases remain the priority product of nitrate reduction as they are innocuous and reduce total fixed nitrogen.

Anthropogenic loadings of nitrogen into the environment are currently 150Tg-N/year, with 15Tg-N/year percolating into groundwater (Schlesinger, 2009). Figures of nitrate input into groundwater for North America are estimated at 3Tg-N/year, indicating that North America contributes 20% of the global N-percolation (Schlesinger, 2009). Groundwater nitrates are highest in regions of intensive agriculture (Foley et al., 2005; Gruber & Galloway, 2008), leaving less urbanized systems with the highest burden of pollutant removal. Negative consequences arise from increased nitrogen levels in aquatic systems: algal blooms, anoxic conditions (e.g., Dead Zone in Gulf), and increased nitrate concentrations (Bianchi et al., 2010; Howarth et al., 2012). The National Academy of Engineering has cited management of the nitrogen cycle as a Grand Challenge for the 21st century, requiring immediate attention and engineering innovation. In 2011, Compton et al. estimated the loss of ecosystem services in the US attributable to increasing nitrogen loadings without renumeration: clean air, biodiversity, recreation and clean water to cost approximately $50 per kg of N (Compton et al., 2011).

Current Treatment Technologies

Remediation of oxyanion contaminants has largely been approached via traditional physical-chemical treatment processes, with the exception of biological treatment for denitrification. Best available treatment technologies (BAT) are promoted by USEPA, and largely represent scalable, high-removal processes for oxyanions. Table 2-1 and Table 2-2 articulate the recommended BATs for Cr(VI) and NO_3^-, respectively.

Though high removal capacity is a key reason for the use of these best available treatment technologies, the disadvantages make some of these processes prohibitive for use in small systems. All of the above listed physical-chemical treatment processes are non-destructive in nature and nominally transfer the contaminant from the aqueous phase to the solid or gaseous phase.

Adsorptive processes, though highly efficient, may also be non-regenerable in certain cases due to strong sorption affinity with the contaminant. If regenerable, a highly concentrated, toxic brine is produced during regeneration, which must be remediated on site or removed for off-site disposal or treatment. Hence, investment in renewable/regenerable transformative technologies for nitrate and Cr(VI) reduction and removal from the aqueous phase is a priority. Particular interest is in technologies with complete reduction to innocuous products, i.e., $Cr(OH)_3$ or N_2. Current technologies that are able to achieve reductive decontamination of oxyanions include: biological denitrification, electrolysis, hydrogen-driven bimetallic catalysis, and photocatalysis. A number of key metrics indicate photocatalysis is the best option for reductive decontamination in drinking water: catalyst safety and economic/environmental cost, energy input, and residuals post-treatment.

Table 2-1. Best Available Treatment Technologies for Cr(VI) (adapted from (Sharma et al., 2008))

Treatment Technology	Example	Advantages	Disadvantages
Coagulation-Precipitation-Filtration	Reductive Fe(II) Sulfate Alum and Fe(III) Coag.	High capacity, solid partitioning	Multiple stage process High volume of sludge
Adsorption to Different Media	Activated carbon Iron-oxide coated adsorbents	High capacity, solid partitioning	pH adjustment required Limited capacity
Ion Exchange	Strong basic anion (Cr(VI)) Cation (Cr(III))	High capacity, solid partitioning	Disposal, regeneration and fouling issues Impacted by competing ions
Membrane Technology	Reverse Osmosis	Physical removal via size exclusion	High initial investment Disposal and fouling

Table 2-2. Best Available Treatment Technologies for NO_3^- (adapted from (Archna, Sharma, & Sobti, 2012))

Treatment Technology	Example	Advantages	Disadvantages
Chemical Denitrification	Iron hydroxide and copper catalyst at basic pH	Produced ammonia may be sparged via air stripping	Multiple stage process; high cost High volume of sludge
Reverse Osmosis	Membrane size exclusion from 300-1500psi	High removal of NO_3^-	Fouling, deterioration, brine production High life cycle cost
Ion Exchange	Strong basic anion	High capacity, solid partitioning, significantly lower cost than RO (purchase/use)	Disposal, regeneration and fouling issues Impacted by competing ions (SO_4^{2-})
Electrodialysis	Direct current induces ion transfer across membrane	Membrane can be designed for NO_3^- selectivity	Liquid-liquid partitioning, ongoing flux reversal

Photocatalysis for Reductive Transformation of Oxyanions in Drinking Water

Fundamentals of Photocatalysis

Surface Photochemistry

Photocatalysis is a light driven process that provides photons to a semiconductor to promote reactions on the surface. The semiconductor photocatalyst is most often a metal oxide, e.g., TiO_2, and has a particular bandgap energy, which is equal to the energy required to excite an electron from the valence band to the conduction band. The majority of TiO_2-based catalysts have a bandgap greater than 3.2 eV, indicating that excitation by ultraviolet light is required. Adding noble metals or other semiconductors to create a composite may lower the bandgap energy which allows for a wider absorbance spectrum. For example, when silver is coated onto TiO_2

nanoparticles, a Schottky barrier is formed at the Ag-TiO_2 interface, which diminishes the potential energy barrier for electron transport. Additionally, silver can serve as an electron trap to prolong electron-hole recombination, one of the predominant sources of inefficiency in photocatalysis.

Successful photocatalytic systems should consider the nature of the contaminant and how it will interact with the light source and catalyst. Cr(VI), for example, is easily reduced photocatalytically to Cr(III), but adsorbs as a precipitate to the catalyst, causing fouling that must be regenerated for ongoing use. Alternatively, nitrate is more challenging to reduce photocatalytically, but is a non-fouling contaminant in that by-products are either highly soluble (aqueous ammonium) or sparingly soluble which evolve as gases. Thus, the approach to designing systems is to some extent contaminant specific, and requires attention to contaminant absorbance spectra and quantum yields for photolytic activity as well as catalyst bandgap for photocatalysis. Surface charge, which is discussed in detail to follow, is a critical factor in the attraction of the contaminant to the metal oxide surface. Whereas at low pH a TiO_2 catalyst will have a positive charge and attract anionic contaminants, in alkaline conditions a neutral/negative surface charge will cause less efficient removal of contaminants. Adding acid is often undesirable, but can dramatically increase reactivity and adsorption of anions to the catalyst surface.

Delivery of light and choice of catalyst are critical to successful implementation of photocatalysis (Figure 2-1). Choice of irradiation source impacts photolysis, behavior of hole scavenger, and ultimately impacts by-product selectivity. For example, nitrate and nitrite undergo photolysis reactions under UV irradiation. In the case of nitrate, the quantum yield is 20-40x lower than that of other nitrogenous intermediates (Mack & Bolton, 1999b). Therefore, the primary reaction of nitrate to nitrate is predominantly driven by photocatalysis. Alternatively, further reduction reactions may be significantly enhanced by introduction of particular discrete

wavelengths to illicit a photolytic response. Further, the sacrificial electron donor (hole scavenger) may also undergo photolysis, which is undesirable in many systems due to the loss of catalyst hole-scavenger recombination management. However, for nitrate reduction, the $CO_2^{\bullet-}$ produced by the photolytic and photocatalytic oxidation of HCOOH is essential for catalyzing reduction to nitrite. Thus, carefully selecting a light source to accommodate for these alternative outcomes is critical to engineer specific reaction pathways. Ultimately, this allows for design of selectivity outcomes, with highest priority to innocuous products, e.g., N_2, in NO_3^- reduction.

A final category of focus for photocatalysis is on the life cycle properties of the catalyst: safety, regenerability, potential for capture or immobilization. Desired sustainability outcomes for the catalyst include creating safe-by-design systems for use and disposal. Again, Cr(VI) via a reductive/sorption process, may be reduced to less-toxic Cr(III), but remains on the catalyst surface, which requires regeneration to recycle the catalyst. Thus, understanding the complexation of foulants to the catalyst can guide optimal regeneration options. Different scenarios for capture/immobilization have been explored, including fixed film processes and use of ceramic membranes to separate catalysts. Further discussion of these topics will be explored herein.

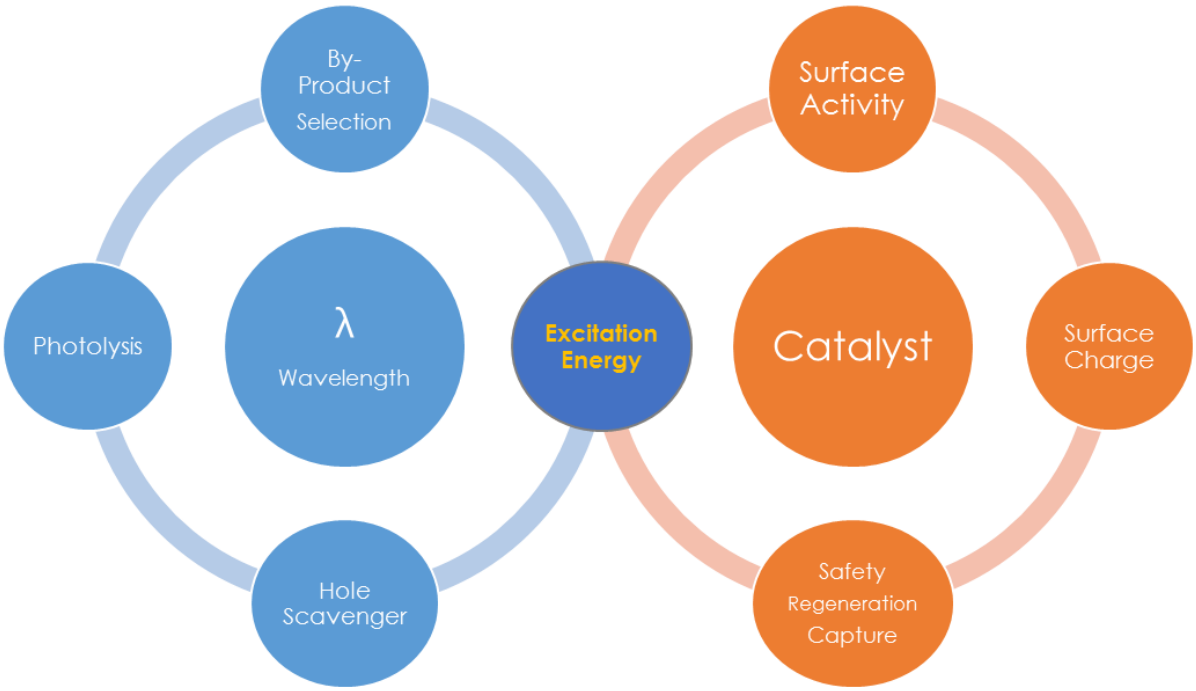

Figure 2-1. Critical juncture of photocatalysis: light source irradiation wavelength and catalyst properties.

Bandgap Influence on Photon Absorption

Absorption of photons with greater energy than the bandgap of a photocatalyst generates conduction band electrons and subsequently, valence band holes. This 'bandgap energy' is the threshold of energy needed for the semiconductor to undergo redox upon absorption of a photon. Influent photons must meet this minimum threshold of energy in order to activate the photocatalyst, whereas other photonic wavelengths may be absorbed but with insufficient energy to promote electron-hole separation. An example of successful activation for a titanium dioxide catalyst is as follows:

$$TiO_2 + h\nu \rightarrow TiO_2(e_{cb}^- + h_{vb}^+) \qquad \text{Equation 1}$$

where e^-_{cb} represents the electron promoted to the conduction band and h^+_{vb} represents the hole that theoretically remains in the valence band. Holes may also be mobile depending on the influent energy, structure of the lattice, and defect occurrence.

In an ideal semiconductor, there are no energy states within the band gap. A 'fundamental absorption' occurs if the light absorption is due only to the transfer of e^- from the valence band to the conduction band (Seeger, 2002) and not resultant in lattice vibrations. Because electrons can only have discrete energy values, transitions between energy levels can either be spontaneous or instigated by photons (Schiavello, 1997). For TiO_2, the band gap is well studied, and consensus values are 3.03 eV for rutile and 3.20 eV for anatase (Scanlon et al., 2013). Thus, for a titanium dioxide nanoparticle, a maximum photonic wavelength (minimum energy) is required for excitation:

$$E = \frac{hc}{\lambda} \qquad \text{Equation 2}$$

$$\lambda_{BG-TiO_2} = 3.88x10^{-7}m = 388nm \qquad \text{Equation 3}$$

where h (Planck's constant) = $6.62606957 \times 10^{-34}$ m^2 kg / s, 1 eV = 1.6×10^{-19} joules, c (speed of light) = $2.998x10^8$ m/s, and a joule is equal to 1 kgm^2/s^2. From this relationship of bandgap, or the energy that must be overcome to excite an electron into the conduction band of TiO_2, and wavelength, it is shown that a maximum wavelength of 388nm can activate TiO_2 electrons. Due to the inverse relationship of energy and wavelength, lower wavelength light must be utilized to have sufficient energy to excite TiO_2 electrons photocatalytically.

However, impurities within the crystal lattice may introduce allowable levels for electrons that are within the band gap. Influent photons below the bandgap threshold energy cause perturbations within the vibrational modes of the crystal lattice or absorption within impurities in the lattice (Elliot & Gibson, 1974). This is also impacted electronically in the Fermi energy. The

Fermi energy, E_F, is the energy of the highest occupied electronic state at zero kelvin. At 0K, the hypothetical Fermi energy represents the boundary of filled and unfilled electron energy states, where all states below E_F are full, and all electronic states above E_F are empty. Upon excitation, electrons move to higher energy states thus creating a new and ephemeral excited electron configuration. In the bulk of a perfect semiconductor, no electrons exist at the Fermi energy level because there are no electronic states available, i.e., the density of states is zero at the Fermi level. However, in a non-ideal semiconductor, structural defects allow for states to exist in the bandgap above zero kelvin.

Resultant excitation depends on energy of the light, inclusive of frequency, wavenumber or wavelength of the photon. If the final and initial energy state do not fulfill the resonance condition, photon absorption will not occur. The absorption properties depend not only on the chemical identity of the substance and light wavelength, but also on the light's angle of incidence and polarization. Semiconductors require visible (for narrow bandgap) or ultraviolet irradiation in order to absorb photons due to the band gap energy requirement. Infrared light cannot be absorbed because the energy is below the bandgap energy. If the photon energy is sufficient to excite electrons from filled valence states to the vacant conduction states, electronic excitation occurs as a result of light absorption. The minimum energy for these transitions to produce free electrons is a quality intrinsic to materials and varies; the bandgap energy of TiO_2 is 3.2eV. Bound electron-hole pairs, called excitons, exist below the threshold of the conduction band and also participate in recombination reactions.

The existence of a bandgap in a semiconductor has a number of important implications. Outright electrical conductivity is low due to the energy barrier of the bandgap to drive electrons in the conduction band. Additionally, electron-hole pair formation is limited by the input energy

required to overcome the gap between the valence and conduction bands. These properties of semiconductors necessitate an addition of energy in order to be meaningfully employed for contaminant reduction.

Photocatalytic Implications

Predicting the viability of photocatalytic processes can, at least preliminarily, be assessed utilizing knowledge of the physics and chemistry of: lamps, semiconductors, and chemical contaminants of concern. The proper pairing of output wavelength and semiconductor bandgap is essential to photocatalytic functionality, for if excitation does not occur, the only component of change would likely be adsorption due based on the pH, ionic strength, and surface chemistry of the semiconductor (see Appendix A). However, if the bandgap energy can be met by irradiation, both electrons and holes become available for reaction with adsorbed contaminants. The proximity of contaminants relates to the zeta potential of the surface, either creating a repulsive or attractive force for the chemical of concern. Additionally, with changing pH, the surface charge changes, inducing different preferences for surface speciation. Without sufficient surface reactivity and electron-hole pair evolution, recombination will dominate, resulting in loss of transformation productivity on the semiconductor surface. However, if electrons (and holes) can be trapped at surface sites, the potential for reaction increases and oxidation-reduction reactions will occur. Thus, the solid-liquid interface plays a significant role in the success of photocatalytic processes. These theoretical predictions can be verified through experimental results to better understand the mechanisms, pathways, and activities of contaminants with semiconductors in an aqueous environment.

Photocatalytic Reduction of Oxyanions

Photocatalysis of Hexavalent Chromium, CrO_4^{2-}

Hexavalent chromium is an oxyanion that adsorbs poorly to most metal oxides at neutral pH ranges (pH=7 ±1) because of the repelling forces generated by the negatively charged surface of the metal oxide and the anionic chromate/dichromate forms. Ion-exchange technologies have been able to overcome these obstacles and adsorb Cr(VI) (Sharma et al., 2008), yet they generate brines containing high concentrations of hexavalent chromium which require secondary remediation. Other technologies remain uneconomical or cannot remove sufficient hexavalent chromium to achieve anticipated regulatory limits. In contrast, water treatment technologies based on photocatalytic reduction processes are able to overcome these challenges by reducing hexavalent chromium to a trivalent form, reversing the charge on the chromium species, and inducing favorable sorption to metal oxide surfaces.

A number of studies have demonstrated that uniquely synthesized and modified semiconductor ultraviolet and visible (UV/VIS) light active photocatalysts are capable of reducing and removing hexavalent chromium from water to concentrations anticipated in the upcoming regulations (J. Li, Wang, & Du, 2012; Vignesh, Priyanka, Rajarajan, & Suganthi, 2013). However, much of the documented work focuses on laboratory scale conditions and commercially unavailable photocatalysts, and as such it is not readily translatable to full scale commercial applications (W. Liu, Ni, & Yin, 2014). The existing literature suggests that titanium dioxide (TiO_2) may be among the few inexpensive and commercially available photocatalysts capable of addressing the majority of these deficiencies (Kyle Doudrick, Monzón, Mangonon, Hristovski, & Westerhoff, 2012; Ghorab, Djellabi, & Messadi, 2013). Although titanium dioxide is

conventionally viewed as a photocatalyst suitable for full scale advanced photo-oxidation processes because of its hydroxyl radical generation (i.e., oxidation), properly designed experimental conditions also allow for successful utilization of its photo-induced reduction capabilities. This has been demonstrated in a limited number of a laboratory scale studies (D. Chen & K. Ray, 2001; Gimenez, Aguado, & Cervera-March, 1996; Ku & Jung, 2001; Xiaoling Wang, Pehkonen, & Ray, 2004; JK Yang, Lee, & Farrokhi, 2012), but the photocatalytic reduction properties of TiO_2 for removing hexavalent chromium in a full-scale commercially available reactor have not been explored. Further review of the literature on hexavalent chromium is presented in Chapter 3.

Photocatalysis of Nitrate, NO_3^-

Reduction of nitrate via photocatalysis presents an opportunity to reductively transform nitrate to nitrogen gases. Hereby, zero aqueous nitrogen residual (e.g., NH_4^+) may be achieved via selective reduction processes. A thorough review of the current state of the art for photocatalytic nitrate reduction and intermediate/by-product selectivity pathways may be found in Chapter 4.

To date, many photocatalysts have been employed to investigate the reduction of nitrate to innocuous gases. Exotic catalysts, with noble/precious metals or rare-earth elements have been explored for visible light photocatalysis or highly N-gas selective reduction of nitrate (Hamanoi & Kudo, 2002; J. Hirayama, Abe, & Kamiya, 2014; Mohamed & Baeissa, 2014; Pelaez et al., 2012; Soares, Pereira, Orfao, Faria, & Silva, 2014; Suriyaraj, Benasir Begam, Deepika, Biji, & Selvakumar, 2014; R. Wang, Yue, Cong, Gao, & Yang, 2015; Juan Yang, Dai, & Li, 2013), but present challenges in synthesis and future possibility of scale-up. Additional visible light catalysts

have been synthesized by doping low weight elements such as carbon, fluorine, nitrogen, and sulfur into TiO_2 (Soares, Pereira, Orfao, et al., 2014), but problems with replicability of synthesis protocols limit implementation. Critical to the success of photocatalysis is the environmental and economic benefit to competition with prominent nitrate removal technologies, which must be carefully managed but has yet to be fully realized.

Photocatalytic reduction of nitrate has been thoroughly explored utilizing titanium based catalysts (Bems, Jentoft, & Schlögl, 1999; Kobwittaya & Sirivithayapakorn, 2014; Shand & Anderson, 2013a), most commonly employing P25 or P90 and/or a combination of TiO_2/Ag. Most recently published studies utilize Ag/TiO_2 (K Doudrick, Yang, Hristovski, & Westerhoff, 2013; Gekko, Hashimoto, & Kominami, 2012; Kominami, Nakaseko, Shimada, Furusho, Inoue, et al., 2005; Ren, Jia, Zou, Wu, & Han, 2015; Sowmya & Meenakshi, 2015; D. Sun et al., 2016), which has been shown to remove up to 95% NO_3^- (100mg-N/L) with 90% selectivity to N-gases (D. Sun et al., 2016). Higher activity is shown with Ag-coating or doping compared to neat-TiO_2 due to the electron capture and hindered electron-hole recombination resultant from adding the silver to form a Schottky Barrier (F. Gao, Yang, & Wang, 2015; Grabowska et al., 2013; Kedziora, Strek, Kepinski, Bugla-Ploskonska, & Doroszkiewicz, 2012; Ko, 2014; Liga, Bryant, Colvin, & Li, 2011; Meng, Lu, Sun, & Lü, 2010; Mogal et al., 2014; Pipelzadeh et al., 2009; Seery, George, Floris, & Pillai, 2007; Sobana, Muruganadham, & Swaminathan, 2006; Suwanchawalit, Wongnawa, Sriprang, & Meanha, 2012; Vamathevan, Amal, Beydoun, Low, & McEvoy, 2002; Vereb et al., 2012; F. Zhang et al., 2007). Fairly consistent in the literature since 2005 is the use of formic acid as the sacrificial electron donor, at concentrations ranging from 40mM to 200mM (K Doudrick et al., 2013; Kyle Doudrick et al., 2012; Ren et al., 2015; Sá, Agüera, Gross, & Anderson, 2009; D. Sun et al., 2016; F. Zhang et al., 2005). Another point of consensus is the 100mg-N/L starting

nitrate concentration (K Doudrick et al., 2013; Kyle Doudrick et al., 2012; Wenliang Gao et al., 2004; R. Jin et al., 2004; Kato & Kudo, 2002; Ren et al., 2015; Sá et al., 2009; Sowmya & Meenakshi, 2015; D. Sun et al., 2016; F. Zhang et al., 2005), which is justified by authors to get an effective determination of reduction kinetics, particularly important for experiments using high-wattage irradiation sources.

In contrast, there is little consistency in the published literature with regard to facilitating selectivity outcomes via irradiation source. The irradiation sources utilized include: xenon lamp, medium pressure lamp(s), and high pressure mercury lamp; these lamps are of widely different input power, and thus highly vary in intensity and light delivery. With minimal information provided by many authors as to the photon flux of the lamp or dose required for the published nitrate removal, comparison between published research is incredibly challenging. The highest removal (>98%) and selectivity (100%) for nitrate reduction to nitrogen gases was achieved by Zhang et al.(F. Zhang et al., 2005), utilizing a P25/Ag catalyst, 0.04M HCOOH, 125W high-pressure mercury lamp. The spectrum for a high pressure mercury lamp primarily emits at 365nm, but yields high emission at lower UV wavelengths (302.3nm, 313.2nm) and the visible spectrum (435.8nm, 545.1nm) (Heraeus, 2016). Both xenon and mercury lamp sources in combination with P25/Ag have achieved >90% removal and >90% conversion to N-gases (Sowmya & Meenakshi, 2015; D. Sun et al., 2016). Though medium pressure Hg lamp yields high kinetics, the conversion of nitrate to nitrogen gases is <90% (K Doudrick et al., 2013). Herein, wavelength may play a factor in the determination of nitrate reduction kinetics and selectivity to nitrogen gases, as under identical conditions, varying results were obtained (discussed more in-depth in Chapter 5).

Choice of Hole Scavenger (Electron Donor)

As is required for biological treatment (Fowdar, Hatt, Breen, Cook, & Deletic, 2015), photocatalytic reduction of nitrate is significantly enhanced by the addition of an aqueous sacrificial electron donor, commonly an acid or acid salt that can simultaneously lower the pH (K Doudrick et al., 2013). This compound is oxidized at the metal oxide catalyst surface, to deliver electrons to propagate valence-conduction band transitions for photocatalytic reduction at the surface. In order to have satisfactory reduction, the complementary oxidative process must be well managed to provide electrons on appropriate timescales such that recombination is minimal.

Formic acid has been identified as the most effective hole scavenger for nitrate reduction (F. Zhang et al., 2005), and is commonly investigated for its degradation properties and radical production (Aristova, Leitner, & Piskarev, 2002; Bianchini, Forte, Musumarra, Pinzino, & Sergi, 1997; Cao, Berski, Latajka, Räsänen, & Khriachtchev, 2014; D. H. Kim & Anderson, 1996; Mariani, Brandi, Cassano, & Zalazar, 2013). Products of TiO_2 photocatalytic reaction with formic acid include H_2, CO, CO_2, and CH_4 depending on other aqueous conditions (pH, fluence dose, concentration) (Dey, Nair, & Pushpa, 2009). Proximity and adsorption of the hole scavenger to the catalyst are the prevailing limitations to effective reduction of nitrate via hindrance of electron-hole recombination (Q. Chen, Chang, Li, & Yuan, 2008). The Langmuir-Hinshelwood model effectively describes the kinetic reduction of formic acid, whereas the Langmuir model describes the adsorption to the catalyst (Q. Chen et al., 2008; Turki et al., 2014).

Intermediates and Facilitating N-Reduction Selectivity

Proposed reactions and intermediates in the reduction of nitrate to aqueous and gaseous products are thoroughly discussed in Chapter 4. The primary reaction in nitrate reduction is

transformation of nitrate to nitrite, which has been well documented as the first reduction intermediate (Lu, Gao, Deng, & Li, 2009; Mack & Bolton, 1999b; Villars, 1927). The photocatalytic pathway is discussed as the dominant mechanism for this work; however, photolysis of aqueous nitrate does occur at UV-C (λ<290) wavelengths (Mark, Korth, Schuchmann, & Von Sonntag, 1996), yielding HONO and $NO_{2\,(g)}$ in acidic solutions (Barat, Gilles, Hickel, & Sutton, 1970b; Scharko, Berke, & Ra, 2014). Nitrate has a strong UV absorption peak at 200nm (ε=9900$cm^{-1}M^{-1}$, π-π* transition) and weaker absorption peak at 300nm (ε=7.4$cm^{-1}M^{-1}$ n-π* transition) (Daniels, 1968; Petriconi & Papee, 1968; Wagner, Strehlow, & Busse, 1980). Quantum yields for nitrate photolysis have been thoroughly investigated at ultraviolet wavelengths, but are minimal ($<10^{-3}$) in all cases (Warneck & Wurzinger, 1988). Vacuum ultraviolet irradiation (λ=195nm) was demonstrated to produce an unknown intermediate that led to the evolution of oxygen from nitrate reduction in the aqueous phase (L. Chu & Anastasio, 2003; Gankanda & Grassian, 2014a; Lesko et al., 2015; Marcotte et al., 2015; Schuttlefield, Rubasinghege, El-Maazawi, Bone, & Grassian, 2008; Svoboda & Slavíček, 2014). Alternatively, some work has involved the photolysis of nitrate in atmospheric processes under natural irradiation conditions (L. Chu & Anastasio, 2003; Gankanda & Grassian, 2014a; Lesko et al., 2015; Marcotte et al., 2015; Schuttlefield et al., 2008; Svoboda & Slavíček, 2014) with particular emphasis on the evolution of nitrogen dioxide and nitric oxide. Atmospheric studies also attribute HONO as a significant intermediate in nitric acid and nitrate photolysis in natural processes (Gankanda & Grassian, 2014a; Ye, Gao, Zhang, & Zhou, 2016). Nitrate radical species production are generated in photolysis and photocatalysis of nitrate and its intermediates. The nitrate radical was first reviewed by Wayne et al. (Wayne et al., 1991), as a concern for tropospheric chemistry in that it may form nitric acid or other toxic nitrogen compounds such as NOx (Malecki & Malecka, 2006).

Nitrite, NO_2^-, responds photolytically and photocatalytically in the aqueous environment. In acidic conditions, nitrite will be present as nitrous acid (pKa = 3.39), which is less stable (Van Cleemput & Baert, 1984) and may be transformed via photolytic and photocatalytic processes in ultraviolet light (Zuo & Deng, 1998). With a +3 oxidation state, nitrite can undergo oxidation (Shifu & Gengyu, 2002) or reduction in natural (Jacobi et al., 2014) or artificial conditions to form dissolved or gas-phase N-species (De Laurentiis et al., 2015; Michael Fischer & Warneck, 1996). Quantum yields for nitrite (O C Zafiriou & Bonneau, 1987) and HONO have been determined in photolysis experiments with phenol: (NO_2^-) Φ_{OH} = 0.069±0.008 at 280nm decreasing to 0.022±0.004 at 390nm and pH=6; (HNO_2) Φ_{OH} =0.35± 0.02 between 280-390nm at pH 2 (Michael Fischer & Warneck, 1996). Alternatively HONO has been studied with predominant photocatalytic products (TiO_2) of NO and NO_2 (El Zein, Bedjanian, & Romanias, 2013) under black light irradiation.

Ephemeral aqueous, evolving gaseous, or adsorbed-gaseous species play an important role in aqueous nitrogen reduction including NO_2, N_2O, NO, NH_3, and the per-nitrates such as peroxynitrite, pernitrite, and peroxonitrite. Nitric oxide participates in gaseous reaction with NO_2 to produce N_2O_3, whereas adsorbed NO^+ reacts with water to produce HNO_2 (Yeom, Henao, Li, Sachtler, & Weitz, 2005). In gaseous interactions, optimal yield of nitrogen gas (N_2) occurs with an equivalent concentration mixture of NO and NO_2 (Yeom et al., 2005). In a comparative study of NO and NO_2 photocatalysis with titania nanotubes, NO reaction proceeded much faster than NO_2, and NO_2 conversion to NO_3^- was the rate limiting step (Nguyen & Bai, 2014). TiO_2-adsorbed NO was found to primarily produce N_2O gas, which can be photo transformed to NO or remain adsorbed on the TiO_2 surface (Rusu & Yates, 2000). In the presence of carbon monoxide (CO), NO reduction on TiO_2 yields N_2 and N_2O (Lisachenko et al., 2007). Alternatively, the presence of

surface hydroxyls on the TiO_2 can yield NO reaction to NH_3 (D.-H. Kim, Lee, Ryu, Kim, & Choi, 2014), whereas hydroxyl radicals can oxidize NO stepwise to HNO_3 (Devahasdin, Fan, Li, & Chen, 2003). Nitrous oxide (N_2O) forms readily from numerous nitrogen radical species unstable in the aqueous phase and nitrogen containing compounds, e.g., hyponitrous acid (HON-NOH) (Trogler, 1999). Products of N_2O are predominantly nitrogen gas in photocatalysis over TiO_2 (M. A. Henderson, Szanyi, & Peden, 2003; Rusu & Yates Jr., 2001).

A thorough review of photocatalytic products of nitrogen oxides (NOx) has been conducted by Lasek et al. (Lasek, Yu, & Wu, 2013) due to many existing applications of photo-asssisted NOx removal technology. NOx forms aqueous phase nitrates in oxidative photocatalytic reactions over TiO_2 (Dalton et al., 2002). Nitrogen dioxide can also be oxidized to nitrous acid under natural sunlight in the environment (Gustafsson, Orlov, Griffiths, Cox, & Lambert, 2006; Han, Yang, Wu, Yang, & Xue, 2016). Gaseous products of the reaction of NO_2 include primarily NO and <1% N_2O when reacted over heterogeneous metal oxides (Underwood, Miller, & Grassian, 1999). Relative humidity (RH) and availability to partition to the aqueous phase can affect the products of NO_2 reactivity over TiO_2, wherein higher RH conditions yielded predominantly HONO, whereas low RH predominantly produced NO (Bedjanian & El Zein, 2012). Alternative nitrogenous gas species are not desired products of NOx reactivity on TiO_2 due to their greenhouse gas potential compared to innocuous N_2 (Rosseler et al., 2013).

Removal of ammonia/ammonium from the aqueous phase has also been successful via TiO_2 photocatalysis (UV-A) with primary products (>99%) N_2, NO_2^-, and NO_3^- (Altomare, Chiarello, Costa, Guarino, & Selli, 2012). Initial studies, such as Mozzanega et al., found N_2 and N_2O were primary products of TiO_2 photocatalysis, and yield was directly proportional to incident light intensity (Mozzanega, Herrmann, & Pichat, 1979). More recently, pH of photocatalytic

oxidation of aqueous NH_3/NH_4^+ was found to proceed more effectively at higher pH due to the higher NH_3/NH_4^+ ratio; NH_3 oxidation yields NO_2^- and NO_3^- more readily than NH_4^+ (Zhu, Castleberry, Nanny, & Butler, 2005). Under standard atmospheric conditions, air pollution studies have found photo-oxidation of NH_3 over TiO_2 yields HONO prior to N_2 evolution (M. A. Kebede, Scharko, Appelt, & Raff, 2013) in addition to NO and NO_2 (M. a Kebede, Varner, Scharko, Gerber, & Raff, 2013). Reactions of ammonia oxidation are primarily catalyzed via OH* generation (Huang, Li, Dong, Liu, & Hou, 2008), which occurs readily on the surface of TiO_2 in favorable pH conditions.

Other proposed intermediates in nitrate reduction to nitrogen gases or aqueous ammonium are highly ephemeral peroxynitrite, pernitrites, and peroxonitrite and their radicals (Mack & Bolton, 1999b). These species have been primarily investigated for their photolytic interactions with ultraviolet light, via lamp irradiation (Thøgersen et al., 2015), flash photolysis (Barat et al., 1970b; Kissner, Nauser, Bugnon, Lye, & Koppenol, 1997), or pulse radiolysis (Goldstein, Saha, Lymar, & Czapski, 1998; Logager & Sehested, 1993). Details of the reactions of these species may be found in the review of Goldstein et al. (Goldstein et al., 1998). The instability of these pernitrite species and fast reaction kinetics render them as hindrances to efficiency evidenced by a yellow tinge (Plumb & Edwards, 1992), but not overwhelmingly competitive in the primary reduction of aqueous nitrate to nitrogen gases or ammonium (M N Hughes & Nicklin, 1968).

Photocatalytic Oxidation of Model Pollutants

Methylene Blue as a Probe Chemical for Photoactivity

Initial photocatalytic study of methylene blue oxidation was utilized for the destructive removal of organic constituents from the aqueous phase, focusing on mineralization or

transformation via TiO_2 slurry or thin film (Kapinus, Viktorova, & Problems, 2010; Kuo & Ho, 2001; Matthews, 1989; Reeves et al., 1992). From the mid-1990s, TiO_2-mediated photocatalysis of methylene blue was more thoroughly investigated, yielding replicable quantum yields and adsorption characteristics (Lakshmi, Renganathan, & Fujita, 1995). Natural solar (Kuo & Ho, 2001; Reeves et al., 1992), artificial solar (Reeves et al., 1992), high pressure mercury lamp (Lachheb et al., 2002) and blacklight irradiation (Dariani, Esmaeili, Mortezaali, & Dehghanpour, 2016; Lakshmi et al., 1995; Matthews, 1989) were utilized to photobleach methylene blue. P25 (Degussa, now Evonik) was utilized in slurry studies (Akpan & Hameed, 2009; Lachheb et al., 2002), whereas sol-gel (Kwon, Shin, Kim, Choi, & Yoon, 2004) or dip coating (Kuo & Ho, 2001) methods were utilized for fixed film studies.

Methylene blue is a heteropolyaromatic cationic dye, distinguishable from other dye structures: anthraquionic, or azoic of which methylene blue had the fastest kinetics a study comparing varied structure dyes (Lachheb et al., 2002). High pH is favorable for adsorption onto TiO_2 due to the cationic structure and attractive negative surface charge above pH 6.2. Thus, in neutral waters, a MB-TiO_2 adsorption is promising, providing proximity for reaction on the TiO_2 surface upon illumination. Mineralization of methylene blue may be described by the following equation (Lachheb et al., 2002):

$$C_{16}H_{18}N_3S + 25.5O_2 \rightarrow 16CO_2 + 3NO_3^- + SO_4^{2-} + 6H^+ + 6H_2O \quad \text{Equation 4}$$

Alternatively, other bleaching mechanisms have been proposed, including a clear unstable reduction intermediate *leuco*-methylene blue which can be reoxidized to methylene blue by oxygen (S.-K. Lee & Mills, 2003). This system has been described in the literature as ambiguous due to the oxidation/reduction capacity of methylene blue (Mills & Wang, 1999), but remains a widely used surrogate organic pollutant (Shan et al., 2010). More recently, methylene blue has

been utilized in the investigation of illuminated optical fiber reactivity, both in photolysis and photocatalysis (Barton, Matejec, & Matousek, 2016; J. Chu & Zhong, 2012).

Para-Chlorobenzoic Acid (pCBA) as a Model Organic Compound and Hydroxyl Radical Probe

Para-chlorobenzoic acid (ClC_6H_4COOH, pCBA) has been widely used as a probe compound to determine hydroxyl radical production in advanced oxidation processes: catalytic ozonation (J. S. Park, Choi, & Cho, 2004), disinfection (Jeong, Kim, & Yoon, 2009; J. Jin, El-Din, & Bolton, 2011; D. Park et al., 2016), and heterogeneous photocatalysis (He, Grieser, & Ashokkumar, 2011). It demonstrates high oxidation kinetics resultant from contact with hydroxyl radicals, with a $k_{OH/pCBA}$ of $5.2x10^9\ M^{-1}s^{-1}$ (Elovitz & von Gunten, 1999). This proceeds according to the following steady state concentration of •OH (Elovitz & von Gunten, 1999; Zhao, Shang, Zhang, Ding, & Yang, 2011):

$$d[pCBA]/dt = -k_{OH/pCBA}[\bullet OH]_{ss}[pCBA] \qquad \text{Equation 5}$$

Degradation of pCBA can be quantified using liquid chromatography coupled with mass spectrometry (LC-MS) (Vanderford, Rosario-Ortiz, & Snyder, 2007) or more commonly high pressure liquid chromatography (HPLC) with photodiode array (Radeka et al., 2014). Using these methods, specific degradation products may be observed as a result of reaction with hydroxyl radical (Zona, Solar, Getoff, Sehested, & Holcman, 2010). Reactions of pCBA are influenced by co-occuring aqueous constituents that contribute to ionic strength as well as in the presence of hydrogen peroxide (Dionysiou, Suidan, Bekou, Baudin, & Laîné, 2000).

To promote attraction of pCBA to the photocatalyst surface, acidic pH was utilized in most works (J. S. Park et al., 2004). A fundamental pulse radiolysis study found efficient dehalogenation

pCBA and a 1:1 ratio of •OH production and pCBA degradation in the presence of oxygen (Zona et al., 2010). This indicates that pCBA is directly oxidized by •OH to products. Therefore, its use as a probe in photocatalytic reactor testing is quite appropriate to assess the production of •OH on the photocatalyst surface.

Light Delivery into Photocatalytic Systems

Irradiance Sources

Irradiance sources utilized vary widely throughout the literature. These differences are in the chemical nature of how photons are produced as well as other parameters such as the wattage, geometry, and produced wavelength spectrum (Appendix A). The chemical nature of photon production influences the produced wavelength spectrum, whereas the wattage and geometry are more correlated to the intensity of light emitted. Photon fluence is the representative metric for comparison of kinetic data across irradiation sources (J. R. Bolton, Mayor-smith, & Linden, 2015). This is because photon fluence is normalized to the number of photons produced on an energy per wavelength basis. Hence, all numerical values of photon fluence correspond to not only the irradiance (radiant intensity), but also to the wavelength spectrum produced. Therefore, determining the photon fluence or photon fluence dose (time-integrated) is critical to experimental analysis (J. R. Bolton et al., 2015) and begins with the ability to measure the emitted light.

Measurement of Light

Chemical actinometry has been a validation tool for determining photon flux into a reactor configuration and more recently, for photocatalytic activity. Actinometry may be utilized for single-source or multi-source irradiation and at broad or discrete wavelengths (J. R. Bolton, Stefan,

Shaw, & Lykke, 2011; Y, SO, & MB, 2004). Potassium ferrioxalate, first suggested by Hatchard and Parker in 1956 (Hatchard & Parker, 1956), has been widely used for accurate estimation of ultraviolet photonic flux into solutions. A more thorough explanation of the chemistry and mathematics required to compile chemical actinometry data is provided in Appendix A.

In lieu of chemical actinometry, a calibrated radiometer may be utilized to directly measure photon flux (J. R. Bolton et al., 2011). Limitations to radiometry are the challenges in determining flux into the water at all points due to reactor geometry (J. R. Bolton et al., 2011). However, an accurate estimate of the produced light intensity and wavelength spectra are readily obtained with the radiometer and can be normalized over the surface area of the light/water interface. Radiometer measurements are recorded in $\mu W/cm^2$, units of radiant intensity, or irradiance. Irradiance has been defined as the total radiant power incident onto an infinitesimal portion of a surface of designated area (J. R. Bolton, Bircher, Tumas, & Tolman, 2001; JR Bolton & Stefan, 2002). Fluence rate is equivalent to irradiance for the cases in this investigation. Preferred units for irradiance are mJ/cm^2-s for the scale of work in this prospectus, which are equivalent to mW/cm^2. Through a series of mathematical permutations of irradiance, described in Appendix A, calculation of photon fluence and photon fluence dose may be achieved. These two metrics represent a normalized flux of photons (energy/light) across a surface area, with the latter being time-integrated. Hereby an overall photon dose can be utilized to compare varied irradiance sources.

Applications of Light Delivery

Influence of Light in Photolysis and Photocatalysis

Photolysis and photocatalysis are both critically influenced by the delivery of light into the reactor system. As such, research into improved configurations for light delivery into photolytic

and photocatalytic systems is necessary. For photolysis, the aqueous constituents of concern are directly transformed via the incident irradiation. Alternatively, in photocatalysis, the irradiation source promotes electron excitation which then induces redox conditions in the aqueous phase near to/on the photocatalyst surface. Thereby, reaction by photolysis is directly dependent on irradiation, whereas photocatalytic reactions are catalyst mediated and thereby indirectly dependent on the incident wavelengths.

Photons delivered to aqueous systems may undergo a series of reactions depending on (i) incident wavelength, (ii) transmittance, and (iii) photoactivity of aqueous constituents. According to the irradiation spectrum, incident photons of different energies are delivered into the system. Particularly for polychromatic irradiation sources, wavelengths ranging from ultraviolet light ($10nm<\lambda<400nm$), visible light ($400nm<\lambda<700nm$), and infrared light ($700nm<\lambda<1mm$) may be incident to the solution. Alternatively, discrete wavelength irradiation sources such as light emitting diodes typically emit photons ±10nm around a specific wavelength, e.g., 365nm. Comparing the photon flux between polychromatic and discrete wavelength irradiation sources demonstrates significant differences both in incident wavelengths delivered as well as the overall energy flux into the aqueous system. Thereby the temporal rate of reaction may be influenced by the type of irradiance source utilized.

Transmittance of light into the system will vary significantly based on the presence/absence of a photocatalyst. For photolytic reactions in the absence of a photocatalyst, other aqueous components may preferentially absorb photons in lieu of the target compound, which detracts from kinetic performance. Therefore, the transmittance of the solution is a key variable for the photolytic degradation of compounds, as has been widely noted in disinfection literature (Sommer, Cabaj, Pribil, & Haider, 1997). For photocatalysis, photocatalysts are most commonly introduced

into reactors as a slurry due to the maximized surface area and contact with targeted contaminants. This creates a significant hindrance to transmittance of incident irradiation due to the high absorption and scattering present in a semiconductor slurry (Carneiro, Berger, Moulijn, & Mul, 2009). Alternatives of slurry photocatalysis are immobilization in a fixed-bed or fixed-film system, where light transmittance based solely on the quality of the influent water. However, the limited surface area and rapid fouling of these photocatalytic systems have limited their practical use at scale (Katz, McDonagh, Tijing, & Shon, 2015).

Photoactivity of aqueous constituents is most readily apparent in photolytic systems. Quantum yields for photolysis vary widely across wavelengths for a given contaminant. Hence, the intersection of incident wavelength and photoactive spectrum is critical to achieve successful photolytic reaction. Alternatively, in photocatalytic systems, the predominant spectrum of concern is that of the catalyst due to the aforementioned transmittance limitation. Again, light of sufficient energy (short enough wavelength) is required to excite conduction band electrons. This band-gap energy is widely varied based on the chemistry of the semiconductor, lattice substitutions or defects, and possible composite materials. Therefore, designing a workable photocatalytic system requires accounting for the catalyst, contaminant, and source of irradiation.

Fiber Optic Technology to Deliver Light into Water

Due to the aforementioned considerations and limitations that are inherent to conventional photocatalytic systems, a novel approach is required to achieve high performance and efficiency. An ideal system would provide (1) sufficient photon fluence to excite the photocatalyst and catalyze any photolytic reactions; (2) efficient conversion of photons via the photocatalyst into conduction band electrons and reactive radical species; (3) the achievement of (1) and (2) in an

immobilized catalyst format for enhanced safety and recovery of adsorbed contaminants and regeneration of the catalyst. Therefore, to meet these benchmarks, a fiber optic reactor configuration is assessed.

Fiber optics have been used in numerous industrial applications for their excellent propagation of photons via total internal reflection (Scheme 1, Table 3). The capability for the fiber to propagate light with minimal losses is due to the optical properties and indices of refraction, both of the fiber and of the surrounding materials. To achieve total internal reflection, the index of refraction of the coated material must be lower than the index of refraction of the quartz fiber optic, thus reflecting the light back into the fiber for ongoing propagation. However, if the coated material is replaced with a material that has a higher index of refraction than quartz, light will begin to transmit via the interface into the coating. Thereby, coating a catalyst on the surface of the quartz fiber will induce light scattering from the fiber to promote photon-electron conversions within a TiO_2 catalyst ($\lambda < hc/E_{bandgap}$).

Marinangeli and Ollis initially proposed the concept of heterogeneous catalysis on optical fibers in the 1970s-1980s (Marinangeli & Ollis, 1977, 1980, 1982). This principle was first utilized for environmental applications in the early 1990s by the Hoffmann group to remove organic contaminants via artificial (xenon) and solar irradiation (N J Peill & Hoffmann, 1997b; Nicola J. Peill, Bourne, & Hoffmann, 1997; Nicola J Peill & Hoffmann, 1995, 1996, 1998). Both single-fiber (Danion, Bordes, et al., 2004; Danion, Disdier, Guillard, Abdelmalek, & Jaffrezic-Renault, 2004; Danion, Disdier, Guillard, Paisse, & Jaffrezic-Renault, 2006) and bundled fiber (J. Chu & Zhong, 2012; Nicola J. Peill & Hoffmann, 1998) approaches have been attempted in a batch mode, with highest performance noted in the multi-fiber configurations, though still less effective on a per-photon basis than comparable slurry systems (Nicola J. Peill & Hoffmann, 1998).

Development of side-glowing optical fibers has been an area of research to promote photon dispersion into solution, including silicon cladding (L. Lin, Wang, Luo, & Xu, 2015; J. Xu et al., 2008), nanomaterials (Barton et al., 2016; Tandon, Li, Bookbinder, Logunov, & Fewkes, 2013), and phosphors at the commercial scale (Inc., 2016).

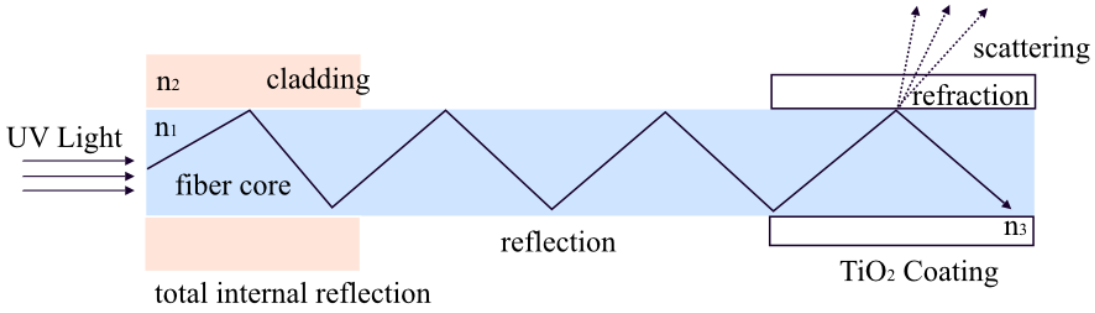

Figure 2-2. Mechanism of light propagation, exit and absorption in coated and uncoated fiber optics; adapted from (W. Wang & Ku, 2003b).

TABLE 2-3. DEFINITIONS OF PHOTONIC TERMINOLOGY UTILIZED IN FIBER OPTIC DESIGN ADAPTED FROM (Paschotta, 2016)

Photonic Terminology	Definition
Total internal reflection	propagation of light continues to fully reflect at the interface between two transparent media so long as the angle of incidence is larger than the critical angle
Index of refraction	for optically transparent media, the fraction of the speed of light travelling in vacuum to the speed of light in the media $n = \frac{c\,(3x10^8) m/s}{v_{media}\, m/s}$
Critical Angle	angle at which incident light enters a media to propagate via total internal reflection, defined via the relation between refractive indices: $\alpha_{critical} = \arcsin\frac{n_2}{n_1}$
Numerical aperture	sine of the acceptance angle of a fiber optic or waveguide; sine of the maximum angle (with respect to the axis of the fiber optic) of an incident ray that can be transmitted in the quartz core; relates to refractive index: $NA = \frac{1}{n_o}\sqrt{n_{core}^2 - n_{cladding}^2}$
Reflection	occurs at an interface between two media in which a propagating wave returns into the medium in which it originated instead of continuing into the second medium
Refraction	occurs at an interface between two media in which a propagating wave continues into the second medium, but at an altered angle based on the index of refraction of the two media according to Snell's law
Absorption	light may be absorbed by the catalyst coating due to the propagation of photons via refraction into the media of higher refractive index ($nTiO_2$>>nquartz)
Scattering	propagation losses in optical fibers are predominantly due to Raleigh scattering (atom/molecule) within the optical fiber or Mie scattering (larger aggregates) for catalyst coated optical fibers due to irregularity at the core/coating interface; both are particularly prominent for fibers propagating ultraviolet irradiation and scattering photons are radially emitted
Evanescent waves	in cases of total internal reflection, all photons are reflected at the interface between the two media, however, the optical field energy will penetrate the second media via evanescent waves

Mechanisms of Light Delivery in Fiber Optic Reactors

Coating photocatalysts onto optical fibers for immobilization and light delivery has been approached via dip-coating premade catalysts with (Nicola J. Peill et al., 1997; Nicola J Peill & Hoffmann, 1996) or without calcination (W. Wang & Ku, 2003b) and sol-gel methods (Barton et al., 2016; Danion, Bordes, et al., 2004; Danion, Disdier, et al., 2004; Danion et al., 2006; L. Lin et al., 2015; Miller & Anderson, 1998; J. Xu et al., 2008). Study into the optimal coating length and thickness (Nicola J. Peill & Hoffmann, 1998; Nicola J Peill & Hoffmann, 1996; W. Wang & Ku, 2003b) for light delivery have been addressed in the literature, but are inherently light-source dependent, and thus must be investigated in each modification of the reactor configuration. Focused work on light delivery modeling has been attempted both to address the light emanating from the tip of the fiber optic (Kozodoy, Lundahl, Bell, & Harrington, 1994), and that into the catalyst via adsorption/scattering (Pulz, Gerbsch, & Buchholz, 1995; Tandon et al., 2013; W. Wang & Ku, 2003b) or evanescent waves (MacCraith, 1993; Matejec, Chomat, Pospisilova, Hayer, & Kasik, 1995; Y. Xu, Cottenden, & Jones, 2006). Additionally, incident light efficiency has been assessed for direct (fiber-irradiation) coupling or via lenses (Zaboub, Guessoum, Demagh, & Guermat, 2016). Losses are inherent to each additive step (e.g., light source-lens-fiber versus light source-fiber), though enhancements to light delivery have been noted utilizing lenses due to the numerical aperture of the fiber optic utilized and angle of light delivery, particularly with collimated irradiance sources (Barton et al., 2016).

Deficiencies in the literature include definitive correlation and proactive utilization of the benefit of combined light delivery to deliver targeted wavelength light to excite a catalyst and induce aqueous reactions. Further, there remains an unclear relationship between coated thickness, incident light flux, and quantum efficiency of aqueous constituent removal which

limits the implementation of fiber optic photocatalysis designs. Reactor design and demonstration in a flow-through regime has not yet been well described.

Light Emitting Diodes for Engineered Photocatalysis

The use of light emitting diodes in photocatalytic systems has emerged in the past decade, particularly due to environmental concerns of mercury-based lamps and their limited operational lifetime (Jenny, Simmons, Shatalov, & Ducoste, 2014). LEDs are recognized for their high-efficiency conversion of electrical input to photon output and increased flexibility for reactor design as well as wavelength input. Further, light emitting diodes are a promising solution not only for disinfection (Chatterley & Linden, 2010; Close, Ip, & Lam, 2006; Würtele et al., 2011), but photocatalysis in the UV- and visible-wavelength range (Autin et al., 2013; L H Levine et al., 2011). Predominant focus of UV-LED photocatalysis has been on the remediation of toxic organic compounds, such as PCE (D. H. Chen, Ye, & Li, 2005), dyes (K. Natarajan, Natarajan, Bajaj, & Tayade, 2011; T. S. Natarajan, Thomas, Natarajan, Bajaj, & Tayade, 2011; Tokode, Prabhu, Lawton, & Robertson, 2014; W. Y. Wang & Ku, 2006), phenol (Jamali, Vanraes, Hanselaer, & Van Gerven, 2013), 4-chlorophenol (Ghosh, Sui, Langford, Achari, & Berlinguette, 2009), benzylamine (Matsushita et al., 2007), bisphenol A (Subagio, Srinivasan, Lim, & Lim, 2010; Xiaoping Wang & Lim, 2010). With the production of relatively efficient UV-C LEDs around 2010, investigation of germicidal efficiency became a focus, either in purely photolytic disinfection (C. Bowker, Sain, Shatalov, & Ducoste, 2011; Chatterley & Linden, 2010; Oguma, Kita, Sakai, Murakami, & Takizawa, 2013) or photocatalysis.

Light delivery into photocatalytic systems is a critical design challenge (B. a. Wols et al., 2010; B. A. Wols & Hofman-Caris, 2012), for which LEDs offer a more flexible solution due to their compact size and focused emission angle (Jenny et al., 2014; Yeh, Yeh, Shih,

Byadgi, & Cheng, 2014). LED sources have been demonstrated to be effective in slurry or fixed film processes (Eskandarloo, Badiei, Behnajady, & Ziarani, 2015; Rasoulifard, Fazli, & Eskandarian, 2014). Water quality parameters can impact transmittance into the solution, hindering UV-LED effectiveness in slurry systems, incentivizing immobilization of the catalyst for irradiation (Leblebici, Rongé, Martens, Stefanidis, & Van Gerven, 2015). A lamp-type cylindrical irradiance immersion reactor has been successfully employed for the photocatalytic oxidation of volatile organic compounds using near-UV LEDs; however, authors noted the performance (time-based) was lower than conventional lamp sources, but had higher energetic efficiency (Jo & Kang, 2012). A unique LED slurry was implemented for methylene blue bleaching, wherein wirelessly powered LEDs were fluidized into the reactor for in-situ light delivery to a P25 slurry (Kuipers, Bruning, Yntema, & Rijnaarts, 2015). Another of the key parameters of effective UV-LED implementation is effective thermal management as LEDs, like all irradiance sources, produce excess heat subsequently reducing efficiency with increasing temperature (Ploch et al., 2013). This is managed quite effectively via the use of external heat-sink devices and fans in LED arrays.

Fiber Optic Reactor Design

Pairing light emitting diodes and fiber optics provides a direct coupling of light delivery source (Matthias Fischer, Wahl, & Friedrichs, 2012) and fixed-film substrate for the photocatalyst. However, this has yet to be implemented as a solution for photocatalysis in water treatment. The following review will focus on alternative methods implemented for fiber optic reactors, both for air pollution remediation and water treatment as well as important studies and limitations for the scale-up of photocatalytic reactors. Design criteria for photocatalytic systems necessarily addresses: light distribution within the reactor, catalyst immobilization or capture, resilient design to combat reactively-competitive aqueous

constituents or catalyst foulants, maintaining useful surface area to volume ratio of nanoparticle photocatalysts within the reactor to provide sufficient active sites (Mukherjee & Ray, 1999). Most studies have focused on light delivery optimization to a slurry catalyst in either batch or flow through configurations (Coenen et al., 2013; Elyasi & Taghipour, 2006; Imoberdorf, Taghipour, & Mohseni, 2008; Mukherjee & Ray, 1999; Raupp, Alexiadis, Hossain, & Changrani, 2001; Shen & Wang, 2002; Q. Yang, Ling Ang, Ray, & Pehkonen, 2005), with negligible work on foulants and optimal surface area to volume distribution for increased active sites.

Modeling efforts conducted on photocatalytic systems have demonstrated the complex interplay between light delivery and limits of reaction rate due to mass transport limitations and diffusion of constituents of interest as described by the Damköhler number (Gorges, Meyer, & Kreisel, 2004; Raupp et al., 2001; B. a. Wols et al., 2010). An attenuation of performance with increased light delivery (Shen & Wang, 2002) confirms that mass transport inherently limits photocatalytic processes as light saturation will occur prior to catalyst-contaminant saturation. Additionally, scattering and absorption coefficients of the catalyst as well as catalyst concentration has been demonstrated to change optical properties of the solution, thereby affecting optimal removal performance (Q. Yang et al., 2005). Optimization of reactor design is best approached via experimentally-validated computational modeling (Elyasi & Taghipour, 2006; Imoberdorf et al., 2008), which contributes insight into irradiation distribution, mass transport of the contaminant and expected removal rate via quantum yield at batch scale. A 1999 review of photocatalytic reactors determined the most promising reactor configurations based on the previously listed criteria to be (1)distributive type of photocatalytic reactor design wherein hollow class tubes serve as a catalyst substrate; (2) narrow tube diameter lamp immersion type reactor (Mukherjee & Ray, 1999). Multi-lamp reactors have dominated more recently in modeled flow through scenarios due to their increased radiant intensity

(Alexiadis & Mazzarino, 2005; Coenen et al., 2013; Imoberdorf et al., 2008). Insights from previous work in fixed bed catalysis (Alexiadis, Baldi, & Mazzarino, 2001; Kamble, Sawant, & Pangarkar, 2003; K. Natarajan et al., 2011; Raupp et al., 2001) include relative efficiencies of catalyst light absorption through the immobilization substrate or water and quantification of catalyst attrition to the solution.

Delivery of light to photocatalyst-coated fiber optics has been attempted a variety of configurations since proposed by Mariangeli and Ollis in the 1970s (Marinangeli & Ollis, 1977, 1980, 1982) and Hoffmann et al., in the 1990s (N J Peill & Hoffmann, 1997b; Nicola J. Peill et al., 1997; Nicola J. Peill & Hoffmann, 1998; Nicola J Peill & Hoffmann, 1995, 1996). In line configurations, where optical fibers are parallel to fluid flow, have been utilized for both water decontamination (Hofstadler, Bauer, Novalic, & Heisler, 1994) and remediation of air pollutants (Denny, Scott, Pareek, Peng, & Amal, 2010; Denny, Scott, Peng, & Amal, 2010; Hou & Ku, 2013; Wu, Wu, Chu, Huang, & Tsai, 2008). Monolith reactors have been implemented for remediation of wastewater pollutants (H. Lin & Valsaraj, 2006; "Removal of indoor alpha-pinene with a fiber optic illuminated honeycomb monolith photocatalytic reactor.pdf," n.d.). Configurations include singular or multiple fibers connected to a light source collimated via a column or lenses (Denny, Scott, Pareek, et al., 2010; Denny, Scott, Peng, et al., 2010; Hofstadler et al., 1994; Hou & Ku, 2013; N J Peill & Hoffmann, 1997b; Nicola J. Peill et al., 1997; Nicola J. Peill & Hoffmann, 1998; Nicola J Peill & Hoffmann, 1996, 1998; Nicola J Peill, Hoffmann, & Laboratories, 2002; Wu et al., 2008). These systems, though rich with scientific novelty, have not resulted in further progress of achieving an optical fiber reactor for the treatment of aqueous contaminants.

Deficiencies in the Literature and Novelty of Work Herein

From a comprehensive review of the literature, deficiencies in current state of knowledge emerged, particularly with regard to (i) catalyst selection, (ii) light delivery and (iii) reactor design of photocatalytic systems. The interplay of the contaminant of focus and the resultant needs of a treatment system are highly relevant. Factors of cost, environmental impact and safety, in addition to overall performance of the reactor are a priority in system design, but access to this information is limited for photocatalytic systems. Thus, parameterizing the effectiveness of the system based on electrical energy per order (EE/O) remains one of the best solutions for rapid and comprehensive assessment. Further availability and assessment of more life-cycle parameters to implement in decision-making would be of imminent use, but without extensive data on both photocatalysis and the primary competitive processes, this is beyond the present scope.

Literature on hexavalent chromium has to date focused on pH of reaction, other aqueous constituents, and kinetics in batch reactors at bench scale. In order to implement photocatalysis for hexavalent chromium removal, larger scale investigation and assessment of critical obstacles was a key priority. Furthermore, a feasibility assessment (economic, presented as EE/O), had not been completed to determine the efficacy of hexavalent chromium removal in a photocatalytic reactor. As a contaminant, hexavalent chromium is perhaps the most significant foulant to the slurry catalyst, due to its reduction to Cr(III) and precipitation onto the TiO_2 surface. Thus, determination of the rate of fouling and recycling options was critical for larger scale implementation. Though the reactor utilized in the study (Chapter 3) was not optimized for hexavalent chromium removal, the experimental work was able to prove that hexavalent chromium is economically viable in higher-concentration conditions (e.g., 100ppb+), whereas in the reactor investigated, the energy requirement was not viable for minimal reduction needs (i.e., 10ppb). A flow-through scenario presented challenges of

contaminant reduction due to lack of sufficient catalyst-light interaction within the narrow window of irradiation contact time.

One of the principle realizations throughout a survey of the literature is the minimal focus of the irradiance source in the study of photocatalysis (Chapter 4). Experimental work focuses frequently on the absorption of the catalyst, either visible-light or ultraviolet based on the band-gap, but rarely assesses the potential to select an irradiance source to more effectively manage the system efficiency. More emphasis on light delivery has been evidenced in the disinfection community, where wavelengths in the UV-C range have been thoroughly explored and only irradiance sources emitting UV-C irradiation are utilized. In contrast, photocatalysis work tends to select light sources on a fairly arbitrary basis, and with little attention to correct delivery of pertinent parameters upon publication: lamp spectrum, photon flux or irradiance data, and even at times lacks in describing the type of lamp or wavelength(s) of emission. Photocatalytic processes are inextricably tied to the source of light, and great efficiency gains are possible when pairing appropriate catalysts and light sources to targeted contaminants. Whereas the catalyst is the interface for aqueous photochemistry to occur, focus on targeted light delivery to the catalyst or secondarily the decision to opt for photolytic reactions if more favorable is solely dependent on irradiation source.

Thus, in this investigation, a light delivery focus is emphasized for the photocatalytic reduction of nitrate (Chapter 5) and the effective photon dose clearly articulated. Instead of purely focusing on kinetic parameters with regard to time (1/s for first order), I approach the problem from a photon and energetic input perspective to determine a normalized effectiveness across light sources of widely different wavelength output and intensity. Additionally, an assessment of discrete wavelength impacts on nitrate reduction is contrasted to multi-wavelength output to determine highest selectivity for nitrate to innocuous nitrogen gases and priority pathways for implementation of the technology. Further, the literature has noted varied

quantum yields for reduction of nitrate, nitrite and subsequent aqueous and gaseous intermediates (Chapter 4), but a discrete wavelength light delivery system had, prior to this work, not been utilized for the assessment of selectivity outcomes and reaction kinetics in engineered photocatalysis (Chapter 5).

Further research in effective light delivery was inspired by the identification that multi-lamp high-surface area reactors are optimal, but no work has of yet been completed to implement such a scenario. The deficiencies of modern lamp irradiance sources were noted to include: mercury content, broad emission spectrum with <50% effective photons (to excite band-gap), and rigid design that complicates implementation with immobilized-catalyst fixed-films. Accordingly, a novel approach was explored based on some seemingly abandoned work by the Hoffmann group in the area of nanoparticle coated fiber optics. Due to the immense technological advancements that have occurred since this previous work, it is presently more feasible to implement catalyst coated fiber optics than when the work was previously endeavored in the 1990s. Additionally, whereas previous investigations into light delivery to fiber optics focused on solar or artificial lamp sources, which require significant efforts in wavelength filtering (infrared) or collimation, we chose to continue developing the work with discrete wavelength LEDs as explored in Chapter 5 to produce a fiber optic/light emitting diode reactor for the treatment of aqueous contaminants (Chapter 6, 7). Though catalyst-coated optical fibers have been implemented and effective catalyst coatings investigated, these parameters were found to change with incident light source, enabling immense flexibility in design, but also necessitating further investigation and consideration at each phase of development. Thus, providing a more holistic assessment of the system via photon fluence and its relation to photocatalytic or photolytic conversion was completed including computation of kinetic rates and quantum efficiencies, Φ. Thereby, a direct comparison was made and modeling work completed to validate the effectiveness of the system and determine an optimal

configuration for escalation from methylene blue bleaching (Chapter 6) to pCBA (Chapter 7) and ultimately nitrate and nitrate reduction (Chapter 9).

A significant outcome of this dissertation is a viable photocatalytic flow through reactor implementing the optical fiber/light emitting diode configuration. This pairing allows for direct light delivery *in situ*, a novel outcome without the necessity of quartz sleeves. Further, with nanoparticles (TiO_2) immobilized on the surface of the quartz fiber optics for direct photon transfer, viability increases as nanomaterial exposure decreases while providing significant surface area to make contact with aqueous contaminants.

CHAPTER 3

HEXAVALENT CHROMIUM REMOVAL USING UV-TiO_2/CERAMIC MEMBRANE REACTOR

This chapter has been published as:

Stancl Heather O'Neal, Hristovski Kiril, and Westerhoff Paul. *Environmental Engineering Science*. August 2015, 32(8): 676-683. doi:10.1089/ees.2014.0507.

Abstract

Photocatalytic reduction of hexavalent chromium (Cr(VI)) was investigated to evaluate effectiveness for removing all chromium species from drinking and industrial waters. Deionized and tap water experiments were performed using a system that recirculates TiO_2 through an integrated process consisting of UV lamps and a ceramic membrane. Hexavalent and total chromium concentrations were simultaneously reduced during treatment. Cr(VI) removal gradually increased with higher energy input and TiO_2 dosage, achieving greater than 90% removal for a 1g/L dose of TiO_2. Cr(VI) was photochemically reduced to Cr(III) on the surface of TiO_2, where the Cr persisted as a precipitate. Upon further irradiation, Cr(III) could be reoxidized to Cr(VI). High volume flow-through experiments indicated significantly diminished chromium removal due to catalyst fouling during continuous catalyst use. To greater extents in tap water than in DI water, photoaggregation of the TiO_2 catalyst was evidenced by increased particle size. This photoaggregation effect was further supported by decreased breakthrough of TiO_2 with increased irradiation intensity.

Keywords: hexavalent chromium, photocatalysis, titanium dioxide, reduction, ultraviolet

Introduction

Stemming from natural and industrial sources, chromium is a drinking water contaminant that poses significant risks to human health (Lurie and Wolfe, 2002). While a 2010 study conducted by the U.S. Environmental Working Group revealed that hexavalent chromium (Cr(VI)) concentrations in drinking waters across the U.S. frequently exceeded 1 μg/L, with cases sometimes exceeding 10 μg/L (Sutton, 2010), EPA monitoring showed concentrations in excess of the MCL for at least one public water system in 2013-2014 with concentration in excess of 100 μg/L (EPA, 2014). Both hexavalent and trivalent chromium (Cr(III)) forms have been linked to adverse health effects, including, but not limited to: increasing risk for cancers (respiratory, prostate, lymphoma, leukemia, bone, and stomach); gastro-intestinal system disruption; uptake, accumulation, and toxicity in vital organs; damage to DNA; and gene mutation (Costa 1997; Dayan and Paine 2001; Sedman et al., 2006; Beaumont et al., 2008). These findings have raised a concern among the general public and spurred a campaign to regulate Cr(VI) and decrease its level in drinking water. With California leading the way and setting an enforceable maximum contaminant level for hexavalent chromium at 10 μg/L, and in expectation of a major effort led by the EPA to promulgate a similar national hexavalent chromium standard, many utilities are exploring treatment options to address these upcoming regulatory requirements (Barrera-Diaz et al., 2012; California EPA, 2011; Gore, 2014).

Treatment options for Cr(VI) have traditionally fallen into six categories (Sharma et al., 2008): (1) coagulation-precipitation-filtration, (2) adsorption to different media, (3) ion exchange, (4) membrane technology, (5) electrodialysis, and (6) biological removal. Challenges with these technologies include cost, scalability, and reliability to achieve low Cr(VI) concentrations. (McNeill et al., 2012; Owlad et al., 2009). Hexavalent chromium is an oxyanion that adsorbs poorly to most metal oxides at neutral pH ranges (pH=7 ±1) because of

the repelling forces generated by the negatively charged surface of the metal oxide and the anionic chromate/dichromate forms. Ion-exchange technologies generate brines containing high concentrations of hexavalent chromium, while the other technologies are either uneconomical or cannot remove sufficient hexavalent chromium to achieve anticipated regulatory limits. In contrast, water treatment technologies based on photocatalytic reduction processes are able to overcome these challenges by reducing hexavalent chromium to a trivalent form, reversing the charge on the chromium species, and inducing favorable sorption to metal oxide surfaces, which simultaneously may serve as photocatalysts.

A number of studies have demonstrated that uniquely synthesized and modified semiconductor ultraviolet and visible (UV/VIS) light active photocatalysts are capable of reducing and removing hexavalent chromium from water to concentrations anticipated in the upcoming regulations (Vignesh et al., 2013; Chakrabarti et al., 2009; Li et al., 2012). However, much of the documented work focuses on laboratory scale conditions and commercially unavailable photocatalysts, and as such it is not readily translatable to full scale commercial applications (Liu, Ni, & Yin, 2014). The existing literature suggests that titanium dioxide (TiO_2) may be among the few inexpensive and commercially available photocatalysts capable of addressing the majority of these deficiencies (Doudrick et al., 2012; Ghorab et al., 2013). Although titanium dioxide is conventionally viewed as a photocatalyst suitable for full scale advanced photo-oxidation processes because of its hydroxyl radical generation capacity (i.e., oxidation), properly designed experimental conditions also allow for successful utilization of its photo-induced reduction capabilities. These capabilities have been demonstrated in a limited number of a laboratory scale studies(Wang et al. 2008; Chen and Ray, 2001; Ku and Jung, 2001; Yang et al., 2012; Gimenez et al., 1996), but the photocatalytic reduction properties of TiO_2 for removing hexavalent chromium in a full-scale commercially available reactor have not been explored.

The overarching goal of this study was to examine the feasibility of using a commercially available integrated UV reactor system with commercial grade titanium dioxide to reduce and remove hexavalent chromium from water. To achieve the goal, five objectives were assessed: (1) the efficacy of the commercially available photocatalytic system for reduction of hexavalent and total chromium was verified in ultrapure water to exclude potentially interfering species; (2) the influence of water matrix effects on contaminant removal was examined in tap water and buffered deionized water to assess system performance under realistic conditions and to evaluate potential for scale-up; (3) oxidation of trivalent chromium adsorbed on titanium dioxide surfaces to hexavalent chromium and subsequent suspension upon further irradiation was investigated to quantify potential for back-reaction within the photocatalytic system; (4) surface analysis of the titanium dioxide catalyst for the presence of chromium on the titanium dioxide surface and photo-induced aggregation of the catalyst was conducted to validate removal mechanisms and investigate potential limitations of continuous catalyst use without regeneration; and (5) the potential for catalyst leaching was investigated via analysis of membrane permeate to determine a realistic catalyst loss scenario.

Methodology

Determining the photocatalytic efficacy of a commercially available system for reduction of hexavalent and total chromium

Based on previously published work, which demonstrated that commercially available photocatalytic systems can successfully oxidize organic compounds (Westerhoff et al., 2009; Benotti et al., 2009) and disinfect water (Gerrity et al., 2008), the Photo-Cat® Serial 0700 system (Purifics ES Inc., Ontario, Canada) was selected to investigate the photocatalytic reduction capabilities of such systems for treatment of hexavalent chromium. The Photo-Cat® Serial 0700 system is an integrated UV/ceramic membrane reactor containing four 220W low

pressure mercury UV lamps controlled by an automated process control system (Figure 3-1). These low pressure lamps emit UV light with $\lambda = 253.7$ nm, which is sufficient to activate the TiO_2 bandgap 3.2 eV (Doudrick et al., 2012) and create hole/electron pairs. Unmodified Evonik P90 TiO_2, which has with same crystallinity as P25 but smaller crystal particle size and higher surface area, was used as a TiO_2 photocatalyst to minimize the electron/hole recombination effect (Doudrick et al., 2012; Doudrick et al., 2013). The Photo-Cat® system allows for complete recovery and reutilization of the TiO_2 photocatalyst by recirculating it through the ceramic ultrafiltration membrane. In addition to operating in a recirculation mode only (i.e., no active lamps), the Photo-Cat® system allows for variable power output control by operating one or multiple lamps simultaneously.

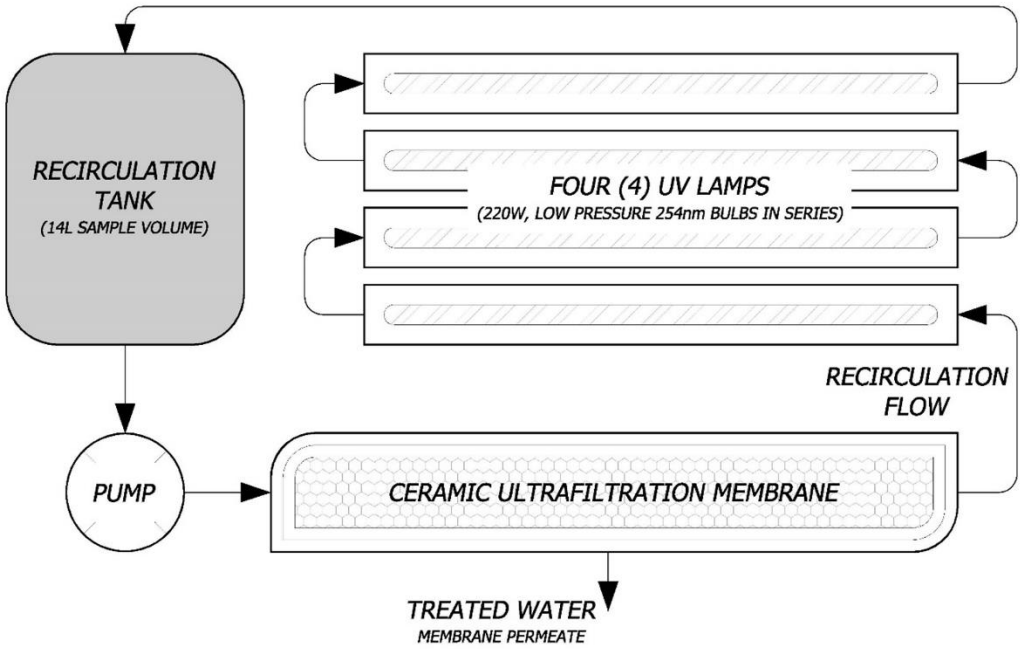

Figure 3-1. Schematic of pilot-scale photocatalytic reactor, Photo-Cat L®, by Purifics.

The initial photocatalysis experiments were conducted in ultrapure water (< 1.5 µS/cm, >18.3MΩ*cm) to verify the system's ability to remove chromium and exclude the potential interference of species that could impair the photocatalytic reduction process. The experimental matrix examined the hexavalent chromium reduction performance of the system at different

contaminant/catalyst ratios, which included two initial hexavalent chromium concentrations (100 μg/L and 500 μg/L) and three TiO_2 doses (0.01g/L, 0.1g/L, and 1.0g/L P90). Although these hexavalent chromium concentrations generally exceed values found in natural systems (Seidel and Corwin, 2013), high concentrations were used to ensure observable concentration changes throughout experiments. Potassium dichromate ($K_2Cr_2O_7$, Sigma Aldrich, >99%) was used as the source of the hexavalent chromium.

The experiments were conducted using the Photo-Cat® system's recirculation mode at a programmed flowrate of 20 L/min and at UV lamp energies ranging from 0 to 8 kWh/m^3 with total treatment volume of 14 L. Temperature of the system was maintained at 27.5 ± 2.5 °C by running cooling water across the lamps. Control experiments with no TiO_2 were also conducted to assess the reduction capability of the system without presence of TiO_2 via photolysis. External organic hole scavengers and pH control were not used during experiments. During the experiments, the pH ranged between 6.5 and 7.1. The system was purged with minimum of 250 L of deionized water between experiments to eliminate potential for crossover contamination. As part of the quality control process, lamp performance was assessed periodically by conducting methylene-blue photo-degradation tests. These tests ensured comparable performance for all lamps. Electrical energy per order (EE/O) was calculated for photocatalytic batch experiments following the method described by Bolton and Stefan (2002). Separate experiments were performed in flow through operation using a feed of dechlorinated tap water (pH ~7.5) spiked with either 10 or 100 μg/L Cr(VI). The steady state flow rate through the system was 2.1 L/min. Lamps were operated at full power in the presence of 1 g/L TiO_2, which was captured by the ceramic membrane, recirculated, and mixed with feed water.

Sample aliquots (40 mL) were taken at regular time intervals from the system's effluent port located after the ceramic membrane. The aliquots were additionally filtered through 0.45 μm filters to ensure absence of any aggregated TiO_2 nanoparticles. Samples were acidified (1)

with ultrapure nitric acid for analysis via inductively coupled plasma mass spectrometry (ICP-MS) or (2) with ammonium hydroxide buffer solution for ion chromatography. Modified EPA Method 218.6 was used to determine hexavalent chromium concentrations by ion-chromatography (Dionex ICS, 2000) following a manufacturer recommended post-column derivatization method with 1,5-diphenylcarbazide and ammonium sulfate eluent. Total chromium concentrations were measured using a quadrapole inductively coupled plasma mass spectroscopy (ICP-MS; Thermo Fisher Scientific XSeries 2).

Experiments in buffered deionized, pH-adjusted deionized, and tap water

To examine the influence of water matrix on contaminant removal and assess the system's performance, water matrices with increasing complexity were used: (1) 5 mM $NaHCO_3$ buffered ultrapure water, (2) deionized water with added potassium hydroxide to adjust pH without adding carbonate alkalinity, (3) and a more complex tap water matrix (dechlorinated tap water from the City of Tempe, Arizona, distribution system with hardness = 220 mg/L as $CaCO_3$, TDS = 615 mg/L and conductivity 1.0 ± 0.1 mS/cm). The pH of the 5 mM $NaHCO_3$ buffered ultrapure water was 8.6 ± 0.1, and the pH of the tap water was 7.8 ± 0.1. The pH of the KOH-adjusted solution was varied from 6.5 ± 0.1 to 9.0 ± 0.1. Water samples were prepared by spiking 500μg Cr/L hexavalent chromium (potassium dichromate, $K_2Cr_2O_7$, Sigma Aldrich, >99%) into the various water matrices. Input lamp energies ranged from 0 to 31kWh/m^3. Experimental protocol was identical to that followed for the ultrapure experiments above.

Quantifying potential for oxidizing photocatalytically reduced Cr(III) to Cr(VI)

As titanium dioxide photocatalysis is inherently an oxidation-reduction system, the potential for oxidation of photocatalytically reduced trivalent chromium sorbed onto the titanium dioxide surface was quantified to determine potential for re-suspension of hexavalent chromium upon excess irradiation. Chromium (III) chloride hexahydrate ($CrCl_3 \cdot 6H_2O$, Sigma-

Aldrich, >98%) was used as the source of trivalent chromium and was spiked into the system to achieve dosages of 100 and 500 μg-Cr/L. Identical protocols were followed to previous photocatalytic experiments at catalyst dosages of 0.1g/L and 1.0g/L P90.

Characterization of spent TiO_2 photocatalyst

Spent TiO_2 photocatalyst samples from all three water matrices were examined to determine any photocatalyst poisoning or sorption of chromium onto the P90. The samples were dried at 100 °C on an aluminum stub and left to equilibrate at room temperature (22 °C) before electron microscopy analysis. Scanning electron microscopy equipped with an energy dispersive X-ray microanalysis system (SEM/EDX) (Philips XL30-EDAX) was used to determine presence of chromium on the surface of the titanium dioxide photocatalyst.

Occurrence of TiO_2 photocatalyst nanoparticles in treated effluent

Samples for aqueous titanium analysis were collected from the ceramic membrane permeate sample port (Figure 3-1) to determine potential for nanoparticle leaching from the reactor. Single particle ICP-MS (spICP-MS), an emerging nanoparticle quantification and size characterization technique (Degueldre et al., 2005; Mitrano et al., 2012), was used to evaluate the particulate TiO_2 equivalents in the photocatalytic reactor effluent. Effluent samples were introduced directly into the ICP-MS, and the instrument signal in counts per second (cps) was documented over time. Dwell time, the unit time interval in which one reading was integrated, was set as 10 ms, and the sample flow rate was set as 0.69 ml/min. Nebulizer transport efficiency to be used in Ti quantification was determined as 1.58% based on previous research (Pace et al., 2011). Total Ti concentration was evaluated by considering the elevated baseline relative to the blank and counting the pulses that stand for the detectable particle signals.

Results and Discussion

Cr(VI) Removal from Ultrapure Water

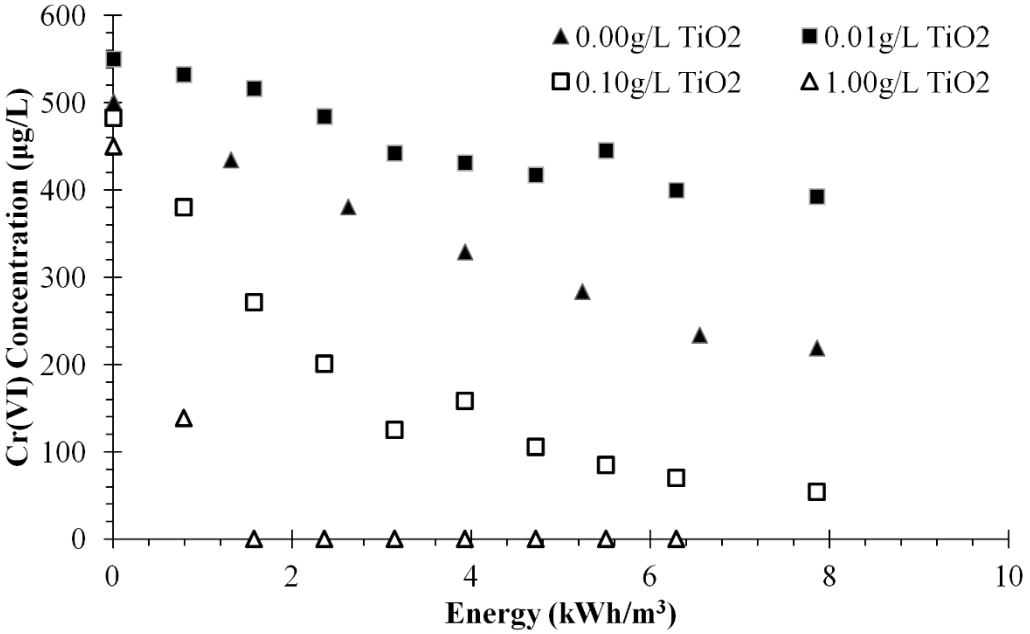

Figure 3-2. Hexavalent chromium removal as a function of energy using four TiO_2 catalyst dosages in model water matrix (18.3MΩ nanopure deionized water) with one of four operational lamps running in recirculation mode. pH ranged from 6.5 to 7.1 (initial to final), and temperature was maintained between 25 and 30°C.

Cr(VI) concentrations slowly decreased by direct UV photolysis in an ultrapure water, without TiO_2 (Figure 3-2). Initial concentrations appear to vary but reflect different amounts of dark adsorption for the varied catalyst doses. A 1g/L TiO_2 dosage had the highest rate and most complete removal of Cr(VI), achieving non-detect levels. An unexpected finding was that photolysis (no added TiO_2) was marginally more effective than adding a very low dosage of 0.01g/L. It is likely that the low TiO_2 dosages reduced UV transmittance, thus limiting direct photolysis of Cr(VI) while providing minimal surface on the TiO_2 for electron transfer to Cr(VI). The highest titanium dioxide dose (1.0g/L TiO_2) had an EE/O value of 0.36 kWh/m^3, which is within the cost effective range (Crittenden, 2012). The EE/O for 0.1g/L TiO_2 was found to be an order of magnitude higher (8.3 kWh/m^3). Based on these findings, two TiO_2

dosages (0.1 g/L and 1.0 g/L) were tested for four water matrices and under different irradiance conditions.

Cr(VI) Removal from Complex Water Matrices

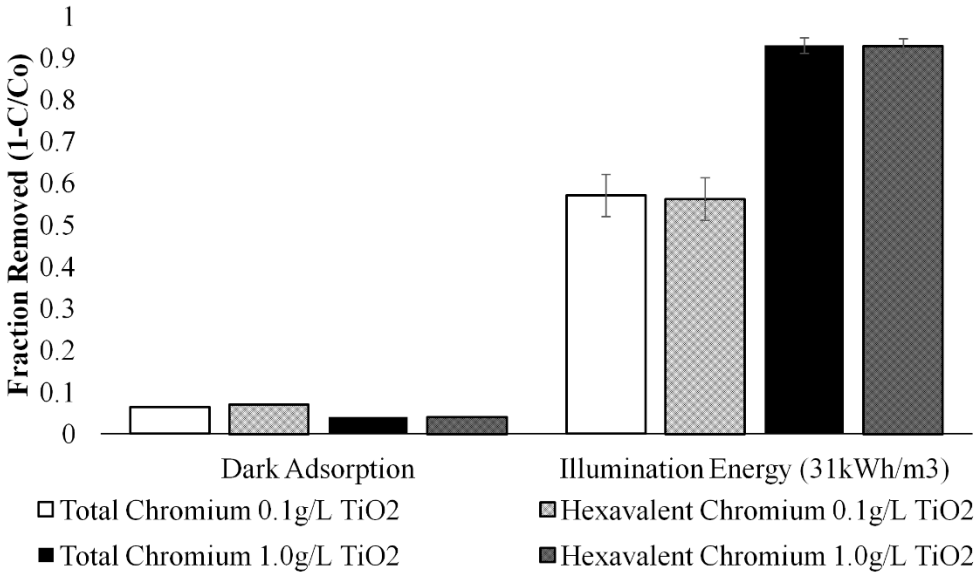

Figure 3-3. Removal efficiencies for hexavalent and total chromium in dechlorinated tap water with initial Cr(VI) concentration of 500 µg/L. The y-axis represents calculated removal of either hexavalent (striped) or total chromium (solid), while the x-axis represents the energy input. Dark adsorption was measured after a runtime of one hour without illumination. Illumination data sets show removal normalized to an equivalent energy input (31kWh/m^3) with error bars (n=1/2).

In recirculation experiments, hexavalent and total chromium concentrations decreased simultaneously for a dechlorinated tap water matrix spiked with different initial Cr(VI) concentrations. This indicates both hexavalent and total chromium were removed from the aqueous solution (Figure 3-3). Using 1g/L TiO_2, chromium removal varied between 89% and 98% for initial concentrations of 500 µg/L Cr(VI). Only 4% of Cr(VI) adsorbed onto TiO_2 in the dark. Therefore, Cr(VI) removal greater than 4% is attributable to photocatalytic processes. With only 0.1g/L TiO_2 and 100 µg/L Cr(VI), removal varied from 45% to 70% with approximately 6.5% dark adsorption. The change in Cr(VI) concentration equaled the removal of total chromium in the system, indicating sorption of chromium species onto titanium

(discussed below). EE/O for dechlorinated tap water was substantially (~10x) higher than ultrapure water resultant from catalyst fouling and diminished availability of sites for adsorption and reduction.

The impact of water matrix was assessed using four water sources: 18.3MΩ*cm nanopure water, buffered deionized water (5 mM $NaHCO_{3,}$), pH-mediated deionized water with KOH, and dechlorinated tap water. In ultrapure water with only Cr(VI), >99% Cr(VI) reduction occurred with 2 kWh/m^3 of energy input (Figures 3-1 and 3-4). In 5 mM $NaHCO_3$ buffered deionized water, TiO_2 dosages below 1 gTiO_2/L achieved less than 20% Cr(VI) removal, regardless of energy input, and a 1 g/L dose of TiO_2 achieved 50% reduction of 500 µg/L Cr(VI) at 10 kWh/m^3.

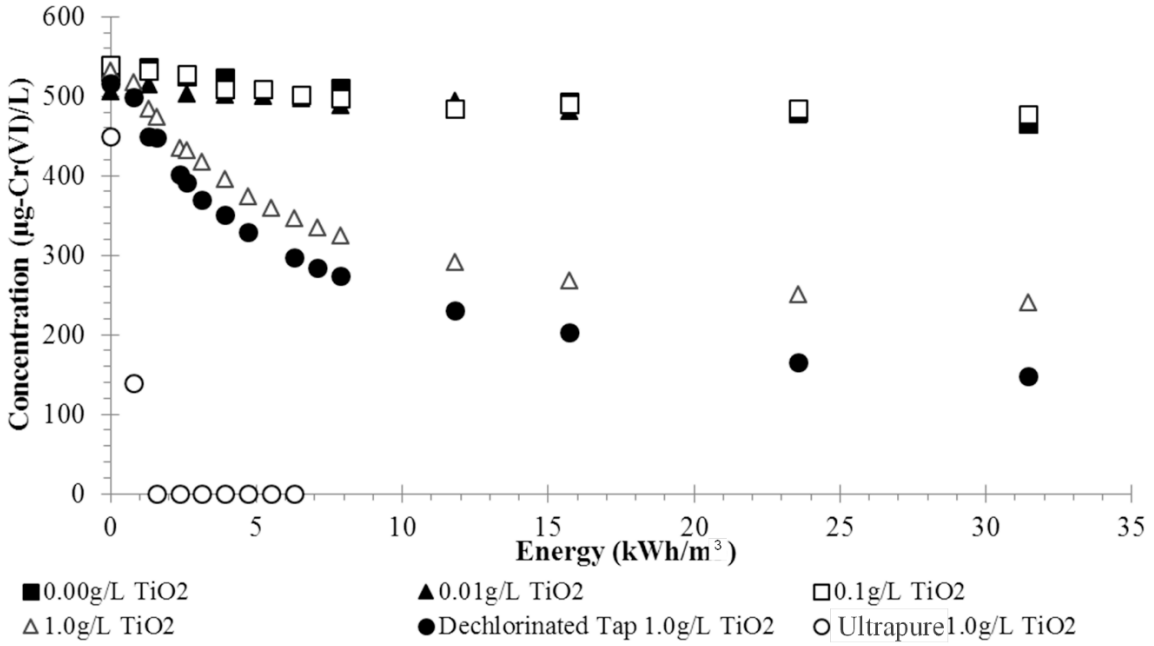

Figure 3-4. Effluent chromium concentrations based on initial input P90 dosage. Initial Cr(VI) concentration was 500 ug/L, and P90 titanium dioxide was 0.0 g/L, 0.01 g/L, 0.1 g/L, or 1.0 g/L. Experiments were conducted using buffered deionized water (5mM $NaHCO_3$, pH 8.5 to 8.7) unless otherwise noted in the legend. pH for dechlorinated tap matrix ranged from 7.7 to 7.9 from C_{in} (at t=0) to C_f (final sampling); pH for ultrapure ranged from 6.5-7.1. Temperature was controlled to remain between 25ºC and 30ºC for all experiments.

Dechlorinated tap water exhibited slightly more effective Cr(VI) reduction than 5 mM $NaHCO_3$ buffered deionized water, with removal highest at 62% with a 1g/L TiO_2 dose. Because 5 mM $NaHCO_3$ increases pH by one unit, which creates less favorable thermodynamic conditions for Cr(VI) reduction, further experiments were completed using deionized water without a buffer (Figure 3-5). A significant dark adsorption of chromium (CrO_4^{2-}, pK_a= 0.6 and 5.9 from Brito et al., 1997) occurred when the solution pH was within ±1.5pH units of pH_{zpc} for TiO_2 (pH_{zpc}=6.2). Desorption occurred upon initial irradiation followed by reduction to Cr(III) upon further irradiation, sorption, and thus removal from the aqueous phase. When the pH of the solution was greater than 7.8 ($pH>1.5+pH_{zpc}$), less dark adsorption of chromium species was observed. With multivalent cations (i.e., Cr(III)), small changes in pH can lead to relatively large changes in sorption capacity (Kinniburgh & Jackson, 1981), as evidenced in Figure 3-5.

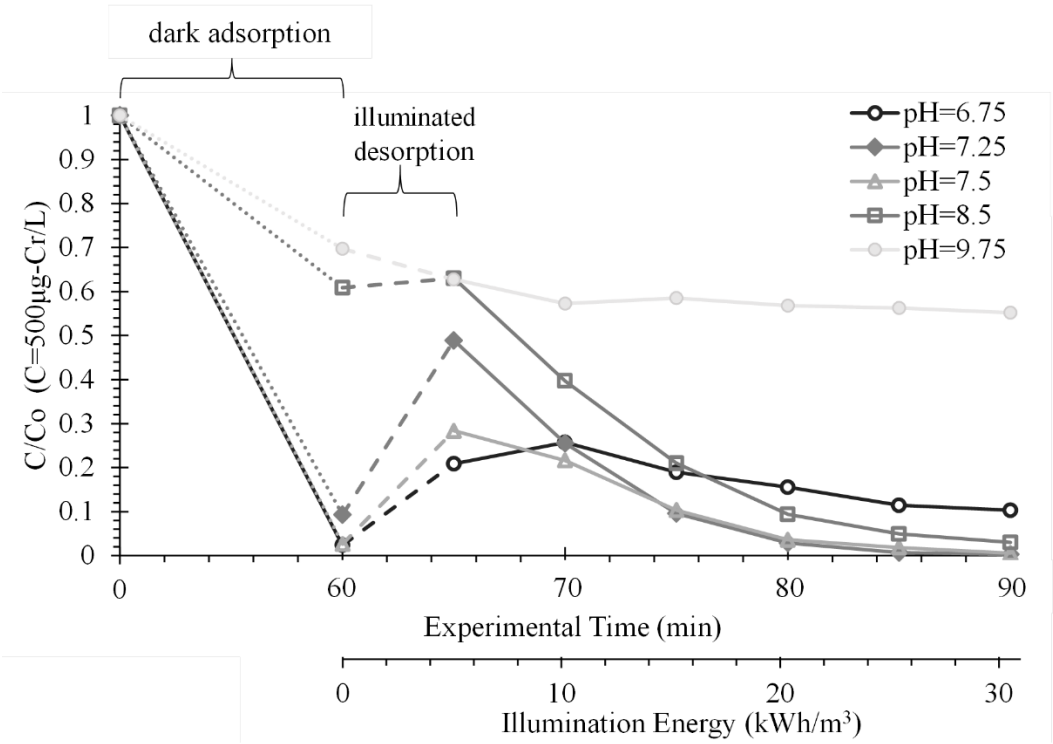

Figure 3-5. Comparison of chromium removal at varied pH for a deionized matrix. Initial Cr(VI) concentration (C_0) was 500 µg Cr(VI)/L. pH was varied using aliquots of KOH solution

and equilibrated for 60 minutes before irradiation. Secondary x-axis corresponds to the illumination energy upon irradiation (beginning at t=60min).

Spent TiO_2 Surface Analysis

Analyses conducted on slurry effluent samples taken after dechlorinated tap experiments showed accumulation of Cr on the TiO_2 solid surface. While virgin P90 TiO_2 is a pure white, the dried titanium samples from experiments were green, an indicator of chromium species on the surface of the titanium dioxide. SEM was conducted on both virgin P90 and a Photo-Cat® slurry effluent from a dechlorinated tap water experiment series of 1 g/L P90 and 500 µg/L Cr(VI) to determine presence and quantity of chromium on the surface (Figure 3-6). For the case of virgin P90, SEM-EDX showed only Ti and O present at the surface, with a carbon response from the stub on which the P90 was mounted. SEM-EDX analysis on spent TiO_2 indicated chromium in addition to a number of common tap water constituents (based on EDX: Na > Cl > Mg > Cr > S > Ca > K) on the TiO_2. SEM of TiO_2 after flow through experiments revealed a doubling in size of TiO_2 particles compared to batch mode but with comparable distribution of elements on the catalyst surface. Though chromium represented a relatively low atomic weight percentage of surface coverage, detection shows that it was present and attached to the surface in some manner.

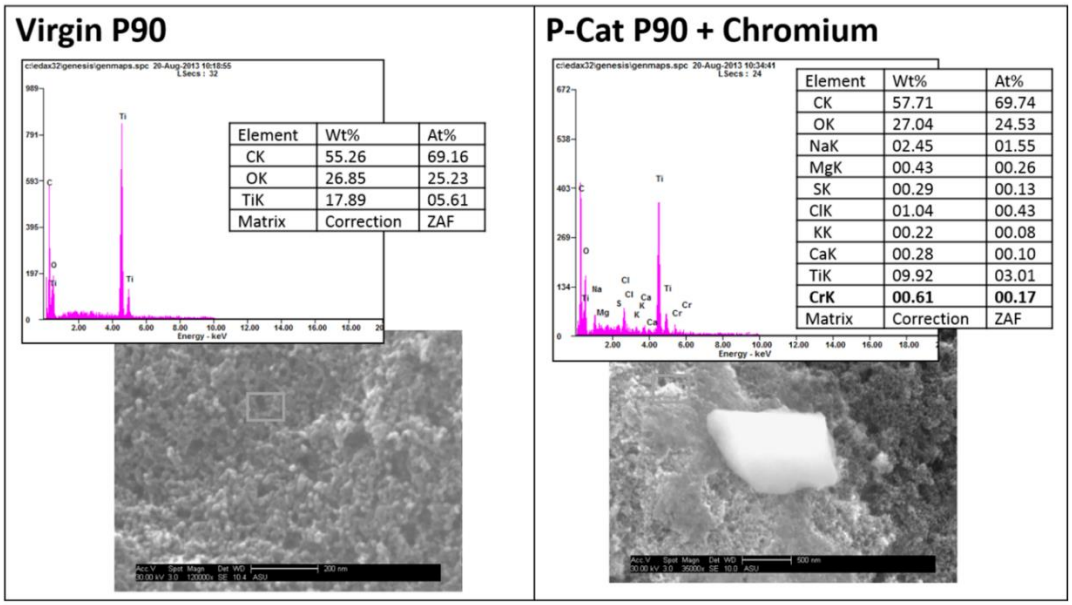

Figure 3-6. SEM images of virgin P90 versus P90 run in Photocat® with 500 µg-Cr/L and 1g-P90/L.

Cr(VI) Re-formation for Tap Water Spiked with Cr(III)

Figure 3-3 shows that in recirculation operation mode, a steady state concentration of Cr(VI) and an equal concentration of soluble Cr_{total} (total chromium) occurs in solution. After Cr(VI) concentrations in the ceramic membrane permeate water decreased to below detection levels, continued and prolonged UV irradiation and photocatalysis may re-form Cr(VI). This likely occurred as Cr(III) bound to the surface of the TiO_2 was oxidized to Cr(VI). Cr(VI) re-formation potential was investigated using an initial input of 100 µg/L Cr(III) with 0.1g/L P90 and 500 µg/L Cr(III) with 1.0g/L P90. Figure 3-7 shows that in both cases, Cr(VI) evolved from the Cr(III) initial solution. Less than 10% of the Cr(III) became soluble Cr(VI) at 0.1g TiO_2/L and 100µg-Cr/L, and even less (<2%) formed at the higher TiO_2 and Cr(III) doses. This may be due to both the high sorption of Cr(III) to TiO_2 and precipitation of $Cr(OH)_{3(s)}$ at neutral pH. The conceptual model presented in Figure 8 articulates the sorption-desorption-reduction cycle with recommendation of a mid-process recycle for the spent TiO_2.

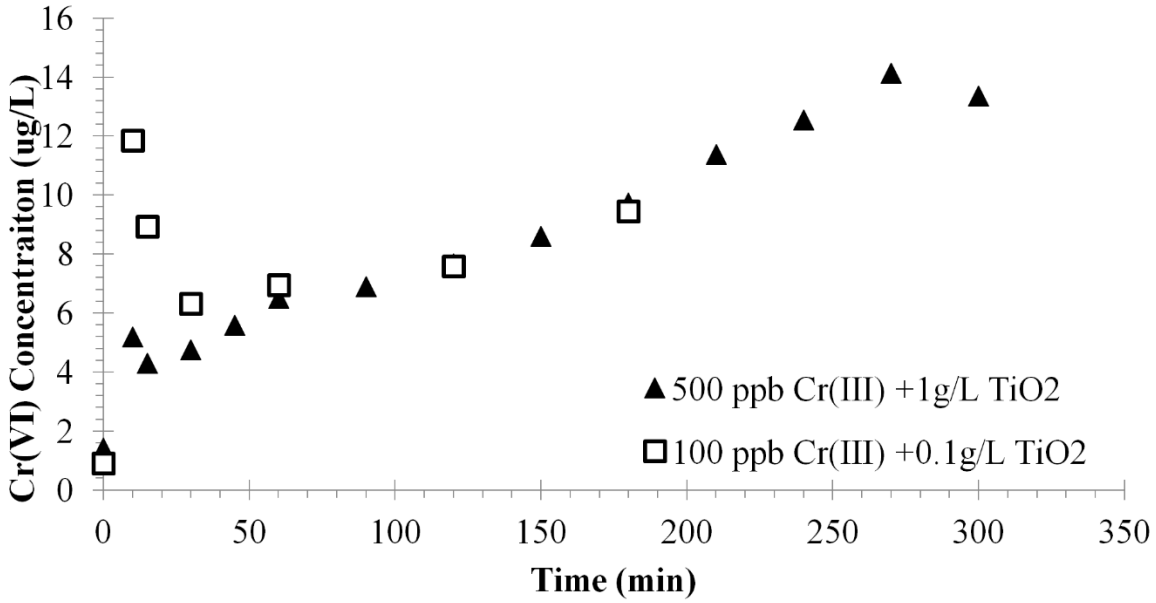

Figure 3-7. Evolution of Cr(VI) from starting concentration of only Cr(III) in dechlorinated tap water. pH increased over the course of the experiment (7.5 to 7.75 and 7.85 to 7.95 for 1.0 g/L TiO_2 and 0.1g/L TiO_2, respectively).

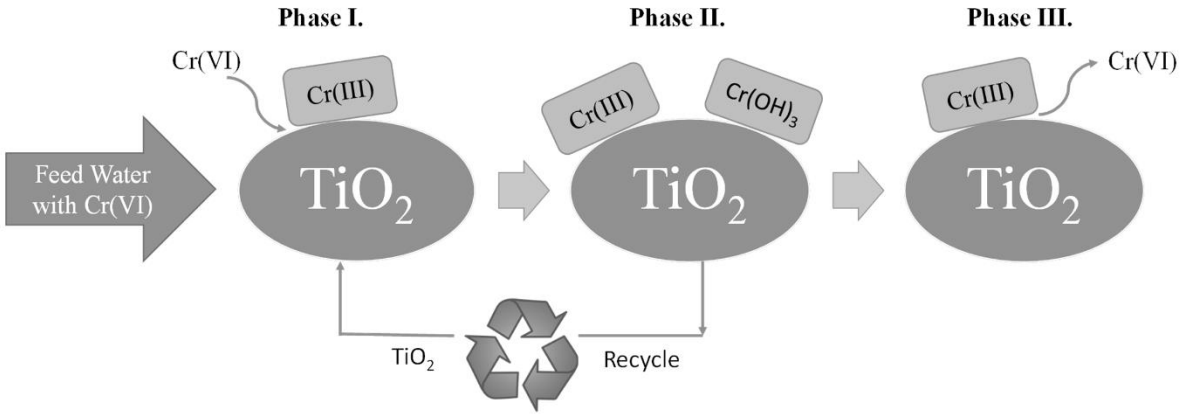

Figure 3-8. Conceptualization of mechanisms involved in the reduction of hexavalent chromium and removal from aqueous solution of total chromium species via reduction and sorption processes. Boxed items represent sorbed species. The phases indicated represent: I. Cr(VI) reduction to Cr(III) and sorption to TiO_2 surface; II. Cr(III) stability on the surface and opportunity to recycle titanium and remove chromium species using acid rinse; III. Cr(III) oxidation and desorption upon additional irradiation.

For 10 and 100 μg/L influent Cr(VI) flow-through experiments, effluent measurements of Cr(VI) and Cr_{total} were indifferent and averaged 9.4 ± 0.7 μg-Cr/L and 79.8 ± 1.8 μg-Cr/L after 30 minutes, respectively. These experiments suggest either poor photocatalytic reduction of Cr(VI) in the tap water or steady state removal and re-formation. Poor photocatalytic reduction is suspected because evaluation of spent TiO_2 indicated significant aggregation of the media, which would reduce light exposure on the surfaces and potentially reduce ability for Cr(VI) to directly contact the TiO_2. Figure 6 shows SEM images of virgin TiO_2 and spent media from continuous flow tap water experiments. EDX analysis of the latter media indicated the presence of Na, Cl, Mg, Cr, S, Ca, and K. In contrast to a limited concentration of natural water foulants in batch experiments with tap water, continuous loading of foulants from tap water appears to have caused aggregation of TiO_2 and reduction in chromium removal

efficiency. Prior research has suggested that fouling of TiO_2 reduces effectiveness of the Photo-Cat® system during long term operation oxidizing trace organics in reclaimed wastewater (Gerrity et al., 2008).

Recovery and Release of TiO_2 Across the Ceramic Membrane

Potential passage of TiO_2 across the ceramic membrane into the treated water was investigated. Figure 9 shows the concentration of TiO_2 in the ceramic membrane permeate for 0.1g/L TiO_2 in 5 mM $NaHCO_3$ deionized water as well as in dechlorinated tap water; all samples were taken at a run-time of 15 minutes and analyzed by spICP-MS. The permeate concentrations depended on water matrix and illumination (3-4 lamps operating). Without illumination, TiO_2 was poorly recovered by the ceramic membrane. Increasing irradiation significantly improved TiO_2 recovery, indicating photoaggregation of the TiO_2. There are only a few reports indicating illumination of catalysts results in aggregation (W. Liu et al., 2014; J. Sun, Guo, Zhang, & Zhao, 2014), what we term here as photoaggregation, but results indicate TiO_2 surface hydroxyl groups enhance aggregation which results in changes to photocatalytic properties and longevity of the catalyst. Without illumination of tap water, 24% of the TiO_2 passed the ceramic membrane. With any level of illumination in tap water, less than 5% of the TiO_2 passed the membrane. Tap water contains roughly 5 μg/L of Ti, but the spICP-MS mode clearly indicated TiO_2 particles in the membrane permeate that were not present in the initial tap water, i.e., above the background concentration. Primary particle size of well-dispersed P90 TiO_2 is 12 – 18 nm. Because pores in ultrafiltration membranes range from 0.001 to 0.1 μm (1 to 100 nm), some pores may be larger than the individual TiO_2 particles, leading to particle breakthrough. Reasons for observed variations in leaching may be TiO_2 aggregation patterns upon illumination, pH and ionic strength differences of the water matrix (Tong et al., 2013; Domingos et al., 2009), or decreased ability to pass the ultrafiltration membrane upon higher chromium surface loading onto TiO_2 and thus increased size of TiO_2 particles.

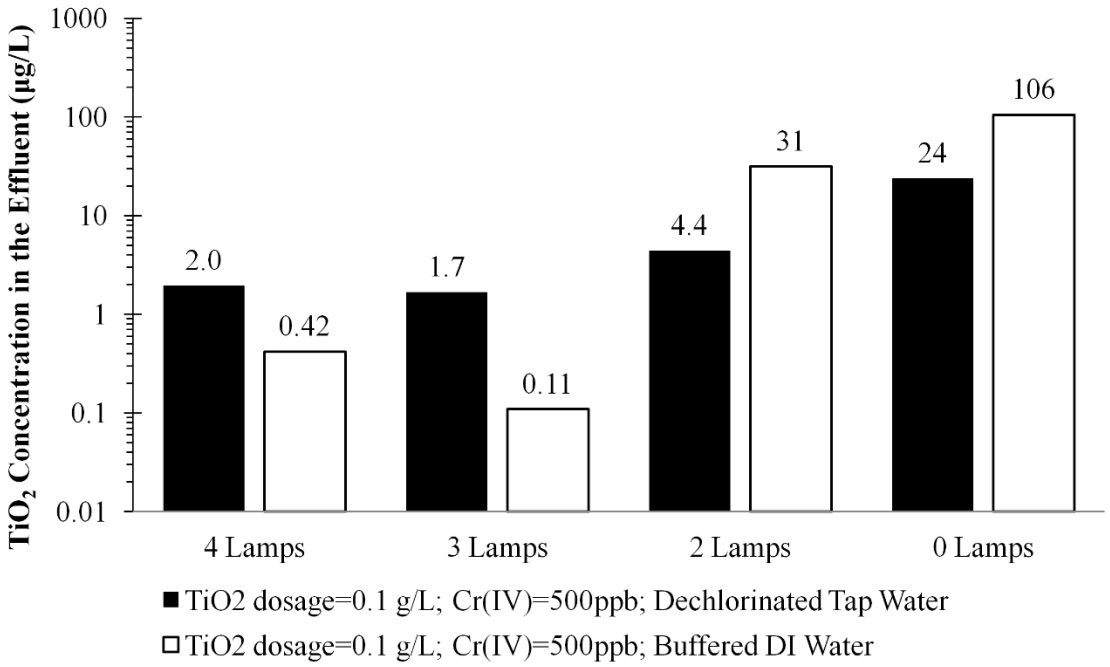

Figure 3-9. Titanium dioxide concentration in membrane permeate samples taken at t=15min as a function of lamps and water matrix. pH for 5mM $NaHCO_3$ buffered DI matrix increased from 8.5 to 8.7 from C_{in} to C_f; pH for dechlorinated tap increased from 7.7 to 7.9 from C_{in} to C_f.

Conclusions

The removal of hexavalent chromium was investigated for several water matrices, titanium dioxide dosages, and energy inputs using an engineering-scale photocatalytic reactor system. The integrated UV-TiO_2-ceramic membrane system reduces Cr(VI) and removes all aqueous chromium species. Catalyst dosage was the most impactful parameter investigated, with the most successful dosage being 1 g TiO_2/L. Higher alkalinity, pH, or presence of divalent salts decreased the effectiveness of Cr(VI) adsorption and subsequent reduction, which required higher EE/O . The presence of divalent cations in the tap water likely aggregated the TiO_2. P90 has primary particle sizes of 12 – 18 nm, which are on the same size or smaller than some ultrafiltration membrane pores. Agglomeration of the initial media or aggregation of TiO_2 during use increases its size, making passage through the membrane less favorable. This phenomenon may occur as the catalyst produces electrons and holes on the TiO_2 surface during

illumination, thus changing the local surface charges and allowing aggregation to occur. Additional research is needed to understand this photoaggregation process alone as well as on the role of divalent salts and the role of TiO_2 photoaggregation on this advanced photo-oxidation process.

Surface analysis confirmed chromium species were present on the surface of the TiO_2 in the effluent slurry and significant aggregation of TiO_2 particles when in flow-through mode. As Cr or inorganic foulants accumulate on TiO_2, catalyst effectiveness is reduced as evidenced in the flow-through experiments. Based on full-scale implementation data, recovery and regeneration of the spent TiO_2 may be completed via acid washing the media to remove Cr(III) species and foulants, allowing for reuse of the TiO_2. While Cr(VI) photocatalytic reduction occurs readily in ultrapure water at low irradiance levels, the presence of salts, alkalinity, and elevated pH increase energy requirements. These factors must be overcome for full-scale implementation, and feasibility studies must determine regeneration rates for the catalyst to maintain optimal running conditions. Overall, photocatalytic reduction of Cr(VI) appears feasible in complex water matrices after managing aggregation and foulants. Combined reduction and removal via photocatalytic processes for drinking water treatment may alleviate chromium exposures and risk of adverse health effects while addressing new regulatory limits.

Acknowledgements

This research was supported by the National Science Foundation (CBET 1132779). Graduate student support was partially provided by a Dean's Fellowship from the Ira A. Fulton Schools of Engineering at Arizona State University. Materials were characterized in the LeRoy Eyring Center for Solid State Science at Arizona State University.

CHAPTER 4

CHALLENGES IN PHOTOCATALYTIC REDUCTION OF NITRATE AS A WATER TREATMENT TECHNOLOGY

This chapter has been accepted for publication as:

Stancl, Heather O'Neal, Garcia-Segura, Sergi, Hristovski, Kiril, and Westerhoff, Paul. *Science of the Total Environment*.

Abstract

Management of ubiquitous nitrate contamination in drinking water sources is a major engineering challenge due to its negative impacts from eutrophication to immediate risk to human health. Several water treatment technologies exist to manage nitrate pollution in water sources. However, the most widely used technologies are phase separation treatments. In this context, nanoscale photocatalysis emerges as a highly promising transformative technology capable of reducing nitrate to innocuous nitrogen with noticeable selectivity. This critical review describes the photocatalytic reduction mechanisms of nitrate toward undesirable products (nitrite, ammonium) and the more desirable product (dinitrogen). The mechanisms are based on the standard reduction potential of each individual species and highlight the contribution of reducing species (e.g. $CO_2^{\bullet-}$) radical formed from different hole scavengers. The strategic use of different pure, doped, and composite nanoscale photocatalysts is discussed on the basis of reduction mechanisms' overall conversion, kinetic rates, and selectivity towards N_2. The influence of light source affects pathways and influence by-product selectivity because direct photolysis of N-intermediates, which has been overlooked in the literature. In addition, the re-oxidation of nitrite and ammonia as drawback process is explained. Finally, an exhaustive analysis presents the photocatalytic reduction applications for treating real water matrices and the competing effect of other species. Overall, this critical review aims to

contribute to the understanding of the potential application/constraints of photocatalysis in inorganic nitrogen management, and guide researchers toward future efforts required for widespread implementation.

Keywords: Water treatment; Titanium dioxide (TiO_2); Nitrogen cycle; Photocatalysis; Nanoparticle; Nanotechnology.

Section 1: Prevalence and impact of nitrogen oxyanions in ground water and drinking water

Managing the nitrogen cycle in water is one of the Grand Challenges for the 21st century society identified by the US National Academy of Engineers (Afzal, 2006; NAE, 2017). The nitrogen cycle is a process by which nitrogen species are exchanged between organisms and the environment. Thereby, the nitrogen species naturally found are interconverted by different chemical and biochemical reactions. Nitrogen is present in soils and waters in three forms: (i) organic nitrogen, (ii) inorganic cation ammonium (NH_4^+), and (iii) nitrogen oxyanions as nitrite (NO_2^-) or nitrate (NO_3^-) (Spalding & Exner, 1993). Anthropogenic nitrogen transforms the global nitrogen cycle with environmental repercussions to this natural balance, such as the increase on nitrate content in water resources (J. N. Galloway et al., 2004; James N Galloway et al., 2008; Gruber & Galloway, 2008). In fact, nitrate is the most frequently occurring anthropogenic ground water pollutant in the United States (Nolan, Hitt, & Ruddy, 2002).

Nitrate occurs naturally in a few geological formations and groundwater. However, nitrate concentration in hydric resources increased dramatically worldwide during the last century due to the use of fertilizers in agriculture (M R Burkart & Stoner, 2007; Michael R. Burkart & Kolpin, 1993). Nitrogen fertilizers play a critical role for agriculture, but they lead to nitrate contamination of surface and ground waters (Rupert, 2008).Anthropogenic nitrogen loadings into the environment are currently ~150 Mg-N/year, with ~15 Mg-N/year percolated into the ground and dissolved in groundwater reserves (Schlesinger, 2009).

Nitrate inputs to groundwater for North America are estimated to be 3 Mg-N/year. Thus, North America represents the 20% of the global N-percolation (Schlesinger, 2009).

Nitrogen in aquatic systems promotes biological growth and algal blooms that result in eutrophication of waters. Eutrophication depletes oxygen in water bodies, killing aquatic animals and irreversibly affecting aquatic ecosystems. Additionally, nitrogen oxyanions severely affect human health. Nitrate is reduced to nitrite in the human gut and causes methemoglobinemia (Kapoor & Viraraghavan, 1997; Sobti, Sharma, & Archina, 2011). In methemoglobinemia, ferrous iron in hemoglobin oxidizes to ferric iron, reducing the oxygen transport, which can produce shortness of breath, fatigue, cyanosis, stupor, cerebral anoxia, and death. Methemoglobinemia in infants and fetuses, which are particularly sensitive to the side-effects of nitrate, is also known as "blue baby syndrome". Nitrate in drinking water is regulated nationally by the United States Environmental Protection Agency (USEPA) to a maximum contaminant level (MCL) of 10 mg/L of NO_3^- as N (USEPA, 2017), while similar values of 50 mg/L as NO_3^- (~11 mg/L as N) is recommended by the World Health Organization (WHO, 2016). According to Burow et al. (2010), ~24 million people in the United States utilize a water supply with nitrate above the USEPA MCL of 10 mg/L of NO_3^- as N (Burow et al., 2010). Even though nitrate is the most stable species in aqueous form, the presence of nitrite and ammonium should also be monitored. Nitrite is strictly regulated at 1 mg/L NO_2^- as N because it causes methemoglobinemia directly and also may contribute to formation of carcinogenic nitrosamines, e.g., NDMA, in the human body (USEPA, 2017).

Nitrate removal from water presents a great challenge to securing drinking water resources of suitable quality. In this context, several water treatment technologies have

been considered to address the environmental and health concerns of nitrate anion. Nitrate removal has been predominantly approached via traditional physical-chemical treatment processes (Bhatnagar & Sillanpää, 2011; Loganathan, Vigneswaran, & Kandasamy, 2013) and biological denitrification (Jensen, Darby, Seidel, & Gorman, 2014; Mohseni-Bandpi, Elliott, & Zazouli, 2013). Fig. 4-1 summarizes the current commercially available technologies, with additional detail and discussion provided in other reviews (Jensen et al., 2014; Sobti et al., 2011). While the conventional technologies provide adequate treatment and are available at municipal scale, they have drawbacks for small communities affected by the contaminants, including high operational labor and energy requirements, cost, and residual waste streams including NO_3^-, NO_2^-, and NH_3 (Health, 2005). Hence, developing decentralized, small footprint treatment technologies is desirable for a new generation of systems to secure drinking water (J. Kim & Benjamin, 2004). As it can be deduced from Fig. 4-2a, nitrogen water treatment technologies are a focal point of researchers, with thousands of studies reported yearly on the critical environmental challenge of nitrogen management. The literature contains a hundred papers related to nitrate management using catalysts in the presence of light (Fig. 4-2b). Even though no photocatalytic technologies are currently commercially available, the increasing trend in research publications indicates the potential application of these alternative transformative technologies in the near future.

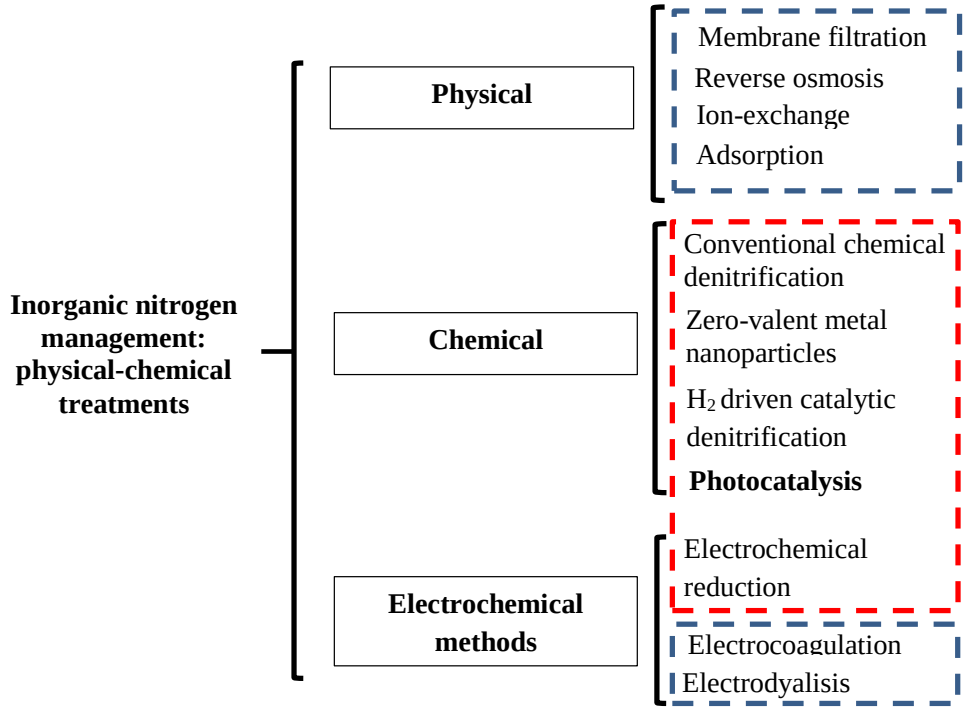

Figure 4-1. Methods applied to manage nitrate in waters. The processes blue framed correspond to phase separation processes while the red framed correspond to transformative technologies.

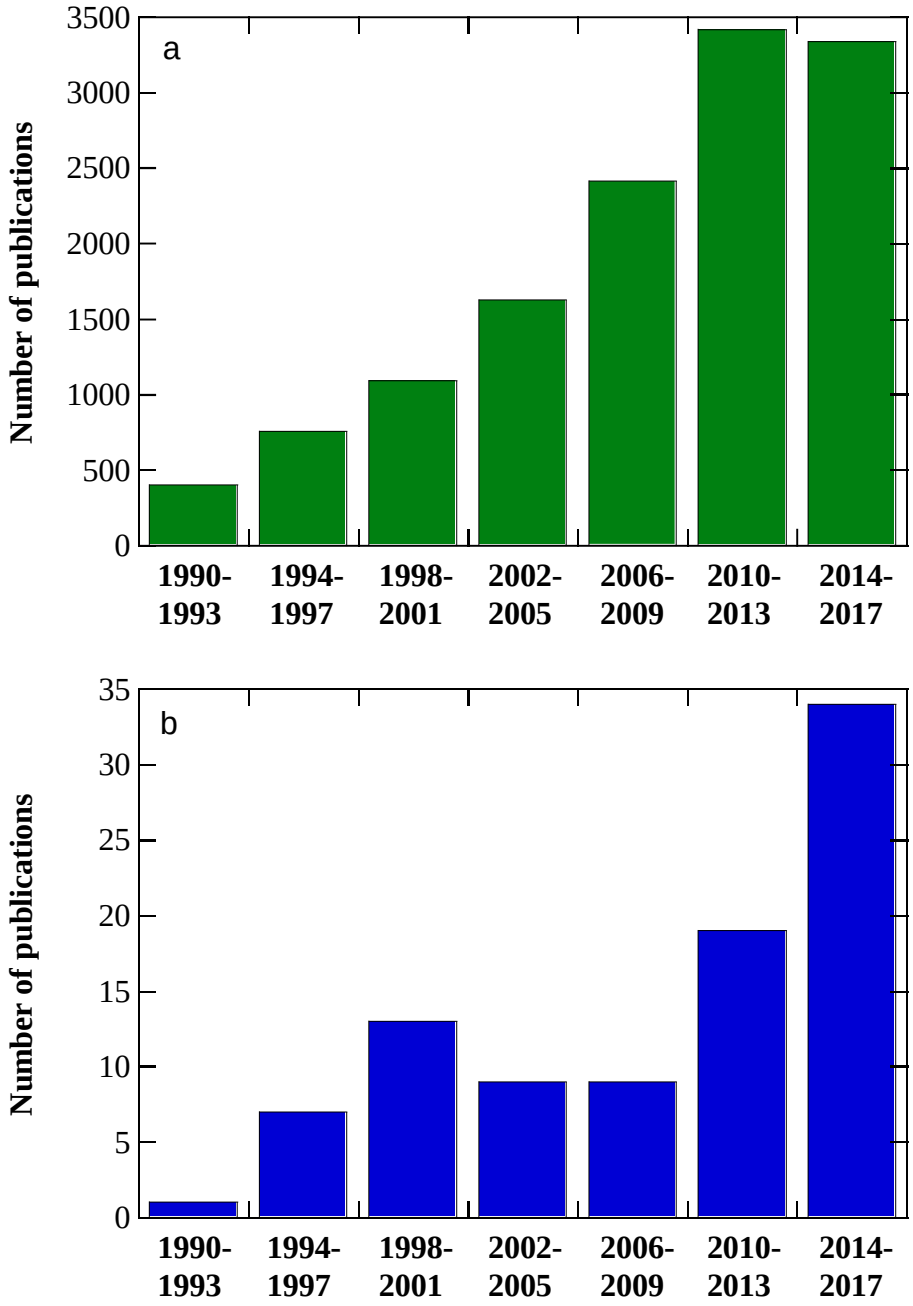

Figure 4-2. Number of publications from 1990 until February 2017 on (a) nitrate removal water treatment technologies and (b) specifically on nitrate photocatalytic reduction.

This review focuses on photocatalytic reduction of nitrate because this nanotechnology-based process can be operated without chemical addition at small scales.

We critically examine the current state of research related to transformative photocatalytic technologies for nitrate remediation that reduce inorganic nitrogen to innocuous nitrogen gas (N_2). Production of nitrite or ammonia in drinking water as product from other technologies is undesirable because nitrite is regulated and ammonia leads to excessive disinfectant demand, increases risk of producing nitrifying biofilms in pipes, and can produce unaesthetic odors in drinking water. The review employs two avenues of examination. First, the direct reactions for photolysis of nitrate and nitrite are examined to substantiate the importance of direct photolysis pathways during nitrate removal in photocatalytic systems. Second, indirect mechanisms for photocatalytic reduction of nitrate using nanoparticles are explored to evaluate the role of different catalyst materials, light sources, and materials on performance of these photocatalytic systems. The review concludes with an outline of opportunities for future research.

Section 2: Direct photolysis of inorganic nitrogen species

Most works concerning photocatalytic reduction of nitrate exclude the consideration of direct photolytic reactions. However, this mechanism could be a very important factor that determines overall system performance (Boule et al., 2005). Specifically, this review focuses on direct photolysis of NO_3^- and NO_2^- because ammonium is a photo-inert cationic species meaning that its direct photolytic activity is negligible in the aqueous phase. However, photolysis of ammonia has been demonstrated under vacuum conditions (Groth & Rommel, 1965; Washida, Inoue, & Suzuki, 1985). Fig. 4-3 shows the molar absorptivity for major aqueous inorganic nitrogen species between wavelengths ($\boldsymbol{\lambda}$) from 200 nm to 450 nm. Photocatalytic processes for these species are typically enabled at

$\lambda < 380$ nm. Due to their photosensitivity, nitrogenous ionic species are susceptible to photolytic transformations when irradiated with ultraviolet (UV) sources (Goldstein & Rabani, 2007; Mack & Bolton, 1999b).

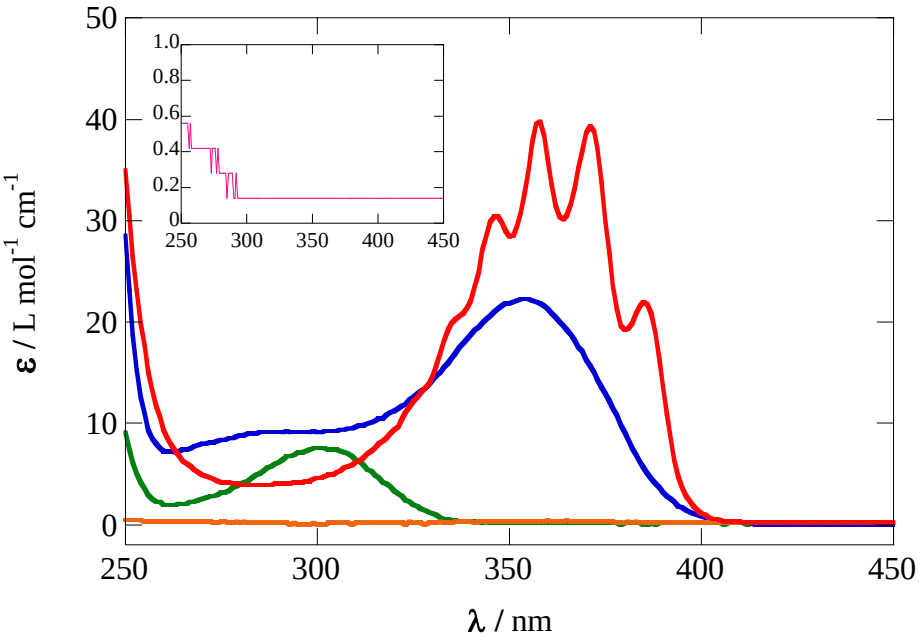

Figure 4-3. Absorptivity of different nitrogen species in solution within the UV-vis spectra range: HNO_2, NO_2^-, NO_3^-, and NH_4^+. The inset panel shows the null absorptivity of H_2NOH.

2.1. Photochemistry of NO_3^-

Nitrate photolysis in water occurs in the range of 270–330 nm with a maximum absorption at 300 nm. The first step in nitrate photolysis is the transition n → π^* (ε = 7.4 M^{-1} cm^{-1}), yielding unstable nitrate species in an excited state according to reaction (1). The unstable species subsequently evolves through two pathways given in reactions (2)

and (3) (Svoboda, Kubelová, & Slavíček, 2013; Svoboda & Slavíček, 2014). However, nitrate presents an additional UV absorption peak at 200 nm due to the $\pi \rightarrow \pi^*$ transition with a strong ε = 9900 M^{-1} cm^{-1} (Daniels, 1968; Petriconi & Papee, 1968; Wagner et al., 1980). The reaction pathway given by equation (2), which produces nitrate and oxygen, is inferior with respect to quantum yield (Φ_λ) ≈ 0.001 at 305 nm (Mack & Bolton, 1999b). As summarized in equation (3), the Φ_{305} in the second pathway is an order of magnitude higher (0.01), releasing two radical species, nitrogen dioxide radical ($NO_2^\bullet$) and deprotonated hydroxyl radical $O^{\bullet-}$ (Barat, Gilles, Hickel, & Sutton, 1970a; Daniels, 1968; Wagner et al., 1980; Warneck & Wurzinger, 1988). The $O^{\bullet-}$ is quickly protonated due to the acid-base equilibria in reaction (4) with a pK_a = 12.0:

$$NO_3^- + h\nu \rightarrow [NO_3^-]^* \quad (1)$$

$$[NO_3^-]^* \rightarrow NO_2^- + \tfrac{1}{2} O_2 \qquad \Phi_{305} = 0.001 \quad (2)$$

$$[NO_3^-]^* \rightarrow NO_2^\bullet + O^{\bullet-} \qquad \Phi_{305} = 0.01 \quad (3)$$

$$O^{\bullet-} + H_2O \leftrightharpoons {}^\bullet OH + OH^- \qquad pK_a = 12.0 \quad (4)$$

The $^\bullet$OH radical can dimerize (reaction (5)). Organic matter, inorganic carbon, and other ions can scavenge $^\bullet$OH (reactions (6)–(8)) (Brillas, Sires, & Oturan, 2009; Buxton, Greenstock, Helman, & Ross, 1988). Nitrogen dioxide radicals preferentially dimerize and release N_2O_4 according to reaction (9) (Bonner & Wang, 1986), which in turn quickly hydrolyzes according to reaction (10) .

$$2\ {}^\bullet OH \rightarrow H_2O_2 \qquad k = 4.2 \times 10^9\ M^{-1}\ s^{-1} \quad (5)$$

$^{\bullet}OH + organics \rightarrow products$	$k = 10^6 - 10^{10}\ M^{-1}\ s^{-1}$	(6)
$^{\bullet}OH + HCO_3^- \rightarrow CO_3^{\bullet-} + H_2O$	$k = 8.5 \times 10^6\ M^{-1}\ s^{-1}$	(7)
$^{\bullet}OH + CO_3^{2-} \rightarrow CO_3^{\bullet-} + OH^-$	$k = 3.9 \times 10^8\ M^{-1}\ s^{-1}$	(8)
$2\ NO_2^{\bullet} \leftrightharpoons N_2O_4$	$k = 2.0 \times 10^6\ M^{-1}\ s^{-1}$	(9)
$N_2O_4 + H_2O \rightarrow NO_3^- + NO_2^- + 2\ H^+$	$k = 1.0 \times 10^3\ s^{-1}$	(10)

Reactions between $^{\bullet}OH$ radical with $NO_2^{\bullet}$ radical can form peroxynitrous acid (reaction (11)) (Goldstein & Rabani, 2007; Logager & Sehested, 1993). At $\lambda < 280$ nm, peroxynitrite can be formed by photo-isomerization of nitrate (reaction (12)) with a Φ_{254} of 0.1, although its occurrence at higher wavelengths is unexpected (Daniels, 1968; Logager & Sehested, 1993; Mark et al., 1996; Wagner et al., 1980). Peroxynitrite can be protonated according to the acid-base equilibria (reaction (13)) with a pK_a =6.5 (Daniels, 1968; Logager & Sehested, 1993; Mark et al., 1996; Wagner et al., 1980). In both cases, peroxynitrous acid is a highly unstable species that disproportionates and yields nitrate from reaction (14) (Michael Fischer & Warneck, 1996; Goldstein & Czapski, 1996; Goldstein et al., 1998; M N Hughes & Nicklin, 1968). Thus, cyclical reductant reformation of nitrate is commonly observed.

$NO_2^{\bullet} + {}^{\bullet}OH \rightarrow HOONO$	$k = 5.0 \times 10^9\ M^{-1}\ s^{-1}$	(11)
$NO_3^- + h\nu \rightarrow ONOO^-$	$\Phi_{254} = 0.1$	(12)
$ONOO^- + H^+ \leftrightharpoons HOONO$	pK_a =6.5	(13)
$HOONO \rightarrow NO_3^- + H^+$	$k = 1.4\ s^{-1}$	(14)

The photolytic pathways are summarized in Fig. 4-4. According to the observed low Φ values, nitrate photochemistry exhibits low conversion efficiency to nitrite (Warneck & Wurzinger, 1988), resulting in nitrate being one of the major final products of the photolytic process in aqueous solution. However, the formation of nitrate radicals by photolysis is of special concern in tropospheric chemistry under natural irradiation conditions (Gankanda & Grassian, 2014b; Wayne et al., 1991) because it may form nitric acid or other unwanted nitrogen compounds such as NO_x (Malecki & Malecka, 2006; Scharko et al., 2014; Schuttlefield et al., 2008).

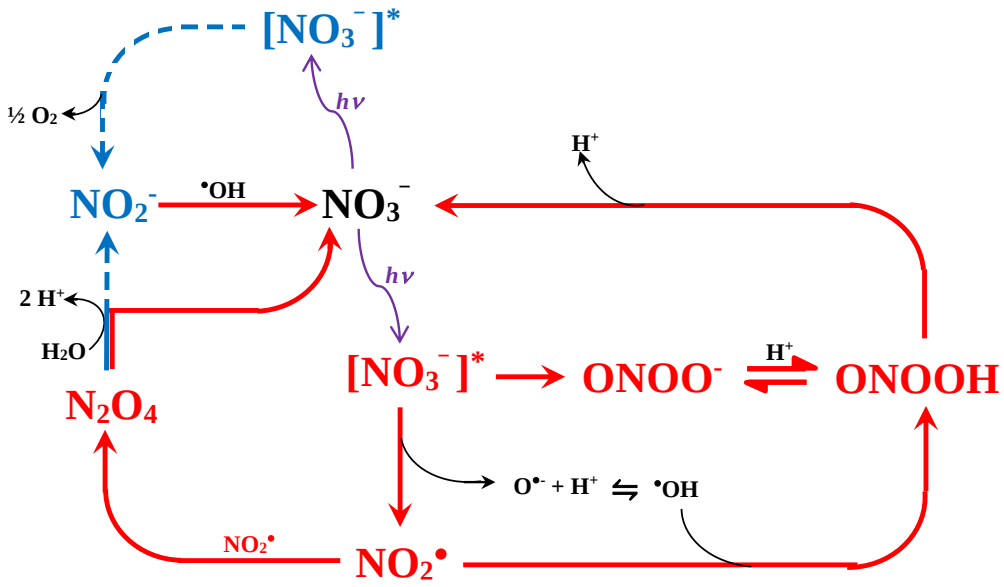

Figure 4-4. Mechanism and main processes of nitrate photolysis in water. **Solid line** highlights the pathway leading to NO_3^- as final product, **dashed line** highlights the pathway yielding NO_2^- as result of the photo-reduction.

2.2. Photochemistry of NO_2^-

Nitrite undergoes photolysis within the λ region between 200 nm and 400 nm (see Fig. 4-3), where the transition n $\rightarrow \pi^*$ is possible (reaction (15)) (ε = 22.5 M^{-1} cm^{-1}) (Michael Fischer & Warneck, 1996; Treinin & Hayon, 1970; O C Zafiriou & Bonneau, 1987). Figure 4-5 depicts the complex mechanism of nitrite photolysis. The main photolytic degradation pathway involves the formation of $NO^\bullet$ and $O^{\bullet-}$ from the excited state following reaction (16), with $\Phi_{355} = 0.025$. Similar to the case of nitrate, $O^{\bullet-}$ is quickly protonated (reaction (4)). At lower pH, the photolysis of nitrous acid, which is in equilibrium with NO_2^- with a pK_a = 3.40 (reaction (17)), undergoes a similar photolytic process but with relatively high quantum yield of $\Phi_{355} \simeq 0.4$ (L. Chu & Anastasio, 2003; Mack & Bolton, 1999b).

$$NO_2^- + h\nu \rightarrow [NO_2^-]^* \qquad (15)$$

$$[NO_2^-]^* \rightarrow NO^\bullet + O^{\bullet-} \qquad \Phi_{355} = 0.025 \qquad (16)$$

$$HNO_2 \leftrightharpoons H^+ + NO_2^- \qquad pK_a = 3.40 \qquad (17)$$

The diffusion-controlled reaction between $^\bullet OH$ radical and $NO^\bullet$ radical yields nitrous acid by means of reaction (18) (Mack & Bolton, 1999b). In parallel, the $^\bullet OH$ radical oxidation of nitrite anion yields $NO_2^\bullet$ radical (reaction (19)) (Mack & Bolton, 1999b; Vione, Maurino, Minero, & Pelizzetti, 2001). Alternatively, $NO_2^\bullet$ can also be produced from the photolysis according to reaction (20) in the presence of electron scavenging species like dissolved oxygen (21), with a Φ_{355} of 0.0019.

$NO^{\bullet} + {}^{\bullet}OH \rightarrow HNO_2$ $k = 1.0 \times 10^{10}\ M^{-1}\ s^{-1}$ (18)

$NO_2^- + {}^{\bullet}OH \rightarrow NO_2^{\bullet} + OH^-$ $k = 6.0 \times 10^{9}\ M^{-1}\ s^{-1}$ (19)

$[NO_2\text{-}]^* \rightarrow NO_2^{\bullet} + e\text{-}$ $\boldsymbol{\Phi}_{355} = 0.0019$ (20)

$O_{2(aq)} + e\text{-} \rightarrow O_2^{\bullet -}$ $k = 2.0 \times 10^{10}\ M^{-1}\ s^{-1}$ (21)

The reaction (22) of both radical nitrogen species ($NO^{\bullet}$ and $NO_2^{\bullet}$) forms dinitrogen trioxide, which is hydrolyzed yielding nitrite by reaction (23) (Mack & Bolton, 1999b). As shown previously in reaction (9), $NO_2^{\bullet}$ can dimerize to N_2O_4, which yields nitrate and nitrite from its hydrolysis (reaction (10)). The dimerization of $NO^{\bullet}$ forms dinitrogen dioxide by reaction (24) and oxidizes to N_2O_4 by dissolved oxygen (reaction (25)), which is hydrolyzed according to reaction (10) (De Laurentiis et al., 2015; Mack & Bolton, 1999b).

$NO^{\bullet} + NO_2^{\bullet} \rightarrow N_2O_3$ $k = 1.1 \times 10^{9}\ M^{-1}\ s^{-1}$ (22)

$N_2O_3 + H_2O \rightarrow 2\ NO_2^- + 2H^+$ $k = 5.3 \times 10^{2}\ s^{-1}$ (23)

$NO^{\bullet} + NO^{\bullet} \rightarrow N_2O_2$ $k = 1.0 \times 10^{9}\ M^{-1}\ s^{-1}$ (24)

$N_2O_2 + O_2 \rightarrow N_2O_4$ k = n.a. (25)

Secondary reactions involving peroxynitrite/peroxynitrous acid, which forms via mechanisms described by reactions (11) or (26), exhibit minor relevance (Goldstein & Rabani, 2007; Martin N Hughes, 1999; Thøgersen et al., 2015). Subsequently, this unstable species disproportionates according to reaction (14) (Anan'ev & Miklin, 2005). Other secondary reactions involve the nitrite release from the reaction of $NO^{\bullet}$ with nitrate or the

reaction of $NO_2^{\bullet}$ with $O_2^{\bullet-}$ by reactions (27) and (28), respectively. However, the yield of these reactions is almost negligible in comparison to the main photolytic mechanism of nitrite (18)-(25).

$$NO^{\bullet} + O_2^{\bullet-} \rightarrow ONOO^- \qquad k = 1.9 \times 10^9\ M^{-1}\ s^{-1} \qquad (26)$$

$$NO^{\bullet} + NO_3^- \rightarrow NO_2^{\bullet} + NO_2^- \qquad k = \text{n.a.} \qquad (27)$$

$$NO_2^{\bullet} + O_2^{\bullet-} \rightarrow NO_2^- + O_2 \qquad k = 1.0 \times 10^8\ M^{-1}\ s^{-1} \qquad (28)$$

Note that the main species yielded after nitrite photolysis is nitrite, which demonstrates a low transformation to other nitrogenous species. Thus, the photolytic process contributes to the formation of radical species that can be involved in the oxidation of organics and other species in solution without severely impacting in the overall nitrite content.

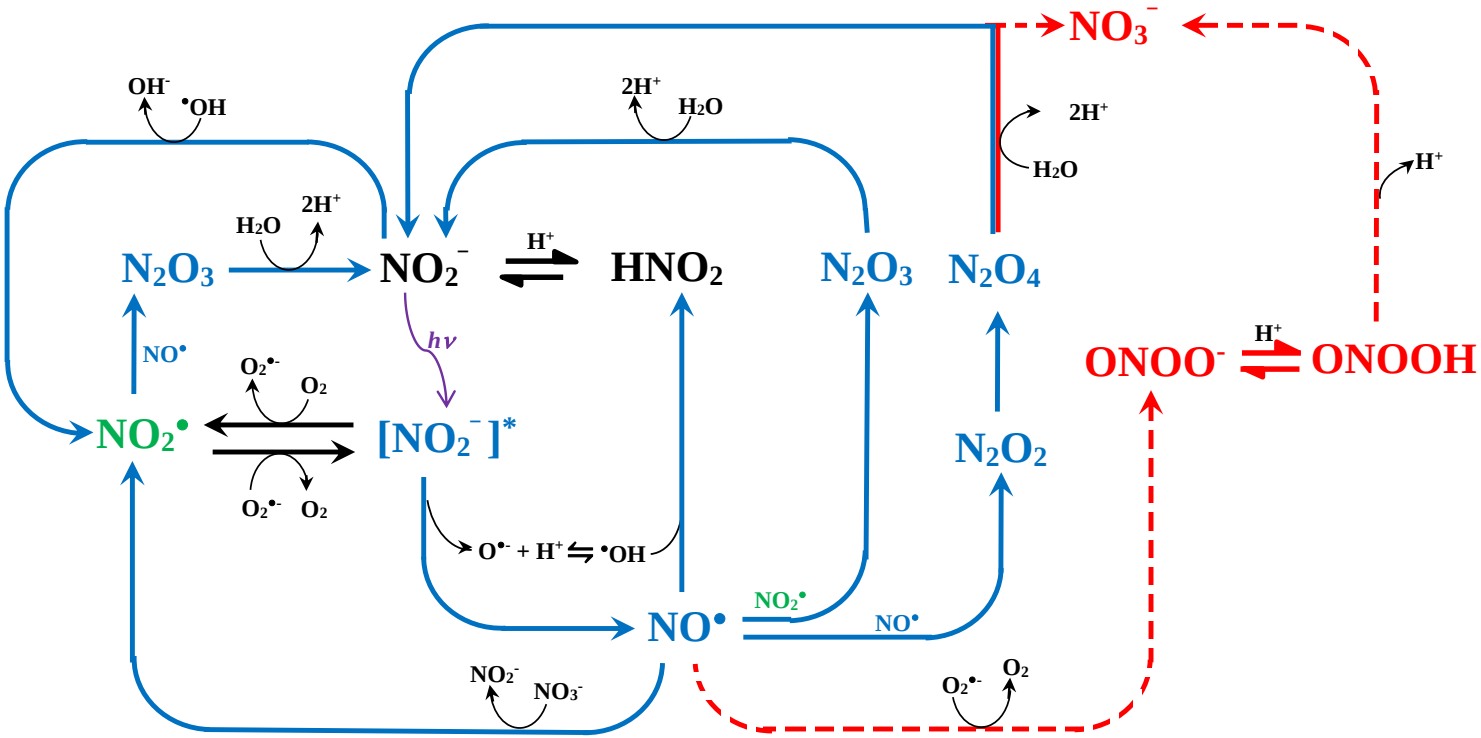

Figure 4-5. Mechanism and main processes of nitrite photolysis in water. **Dashed lines** highlight the pathway leading to NO_3^- as final product, while **solid lines** define the pathways yielding NO_2^- from $NO^\bullet$ and $NO_2^\bullet$.

Section 3: Photocatalytic nitrate reduction

Photocatalysis is a light-driven process that provides photons to a catalyst to promote reactions on its surface. The photocatalytic behavior of semiconductor materials was reported for the first time by Fujishima and Honda in 1972 (Fujishima & Honda, 1972), where they described the photocurrent response of TiO_2 after UV irradiation. Since that initial report, many researchers have studied nuances of photocatalytic water treatment technologies with major efforts devoted to evaluating photo-oxidation processes. In this context, photocatalytic nitrate reduction is one of the emerging transformative technologies capable of yielding innocuous gaseous products.

The absorbance of photons of sufficient energy by a catalyst results in the excitation of an electron (e_{cb}^-) from the valence band (VB) of a semiconductor material to the empty conduction band (CB), generating a positively charged (h_{vb}^+) hole or vacancy as represented in Fig. 4-6. Both aforementioned e_{cb}^-/ h_{vb}^+ species are also referred to as charge carriers. The energy required by the semiconductor to photo-promote an electron from the VB to CB upon absorption of a photon is the "band gap energy" (Fujishima, Zhang, & Tryk, 2008; Hoffmann, Martin, Choi, & Bahnemann, 1995). Incident photons must meet or surpass this minimum energy threshold to activate the photocatalyst, generating the pair e_{cb}^-/ h_{vb}^+ by means of general expression (29). Other photonic wavelengths may be absorbed, but they may not exhibit energy sufficient to promote electron-hole separation.

$$\text{Semiconductor} + h\nu \rightarrow e_{cb}^- + h_{vb}^+ \qquad (29)$$

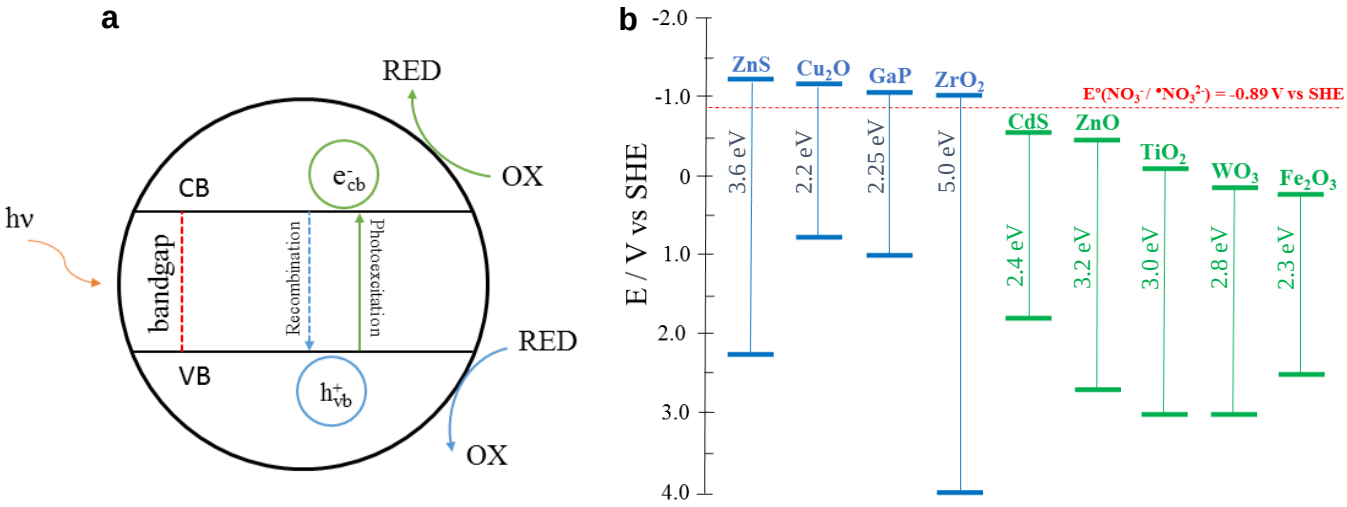

Figure 4-6. (**a**) Scheme of the fundamental photocatalytic excitation that result in the separation of the charge carriers (e^-_{cb}/h^+_{vb}) and the redox processes promoted by each species. (**b**) Relationship between band structure of usual semiconductors, redox potentials vs standard hydrogen electrode, and characteristic band gaps.

Both species, e_{cb}^-/ h_{vb}^+, are generated at the penetration depth of incident irradiation into the photocatalyst, which depends on (i) the material's absorption coefficient, (ii) the irradiation source wavelength, and the (iii) fluence of photons (Fujishima & Zhang, 2006; Hitchman & Tian, 2002; Waldner & Kr, 2005). Charge carriers generated in the bulk of the catalyst must be transported to the surface to be involved in redox reactions (Cai & Feng, 2016). The transit time for e_{cb}^-/ h_{vb}^+ to reach the surface is defined by the radius of the particle or the coating thickness (Dosta et al., 2016; Gratzel & Frank, 1982; Hitchman & Tian, 2002) and the diffusion coefficient of the excited charge carriers in the photocatalyst. For example, the transit time is in the range of picoseconds for TiO_2 nanoparticles 10–20 nm in diameter from the point of origin within the structure to the surface (M. a. Henderson, 2011; Nan et al., 2010). Nevertheless, photo-promoted electrons

are in an unstable excited state and tend to return to the ground state. This occurs in picoseconds during their recombination with the unreacted h^{+}_{vb} following reaction (30), which emits heat (Rossetti & Brus, 1982). Note that this reaction can occur either in the bulk of the semiconductor or at the catalyst surface (M. Bowker, 2007; Schneider et al., 2014a).

$$e_{cb}^{-} + h_{vb}^{+} \rightarrow \text{Semiconductor} + \text{heat} \qquad (30)$$

The e_{cb}^{-}/ h_{vb}^{+} pair recombination is the main drawback of photocatalytic processes and affects their overall efficiency. The e_{cb}^{-}/ h_{vb}^{+} production rate is highly relevant to minimizing the average loss by recombination (30) which may additionally be enhanced by semiconductor doping and the use of co-catalysts. Strategies for improving the charge carrier separation have been already reported and discussed thoroughly in several reviews (Devi & Kavitha, 2013; Kumar & Rao, 2017; Lazar, Varghese, & Nair, 2012; L. Zhang, Mohamed, Dillert, & Bahnemann, 2012).

Considering that the e_{cb}^{-} are highly reductive species, whereas the h_{vb}^{+} are strong oxidizing species, the efficacy of photocatalytic processes is centered around direct charge transfer from photoexcited e_{cb}^{-} or indirect charge transfer by mediating reducing species. For photocatalytic reduction to occur, both species (e_{cb}^{-}/ h_{vb}^{+}) should be engaged in redox processes. However, to have successful oxidation-reduction reactions of constituents at the surface of the photocatalyst, the following two properties must exist: (i) for reduction, the conduction band must have a more negative potential than the reducing species; (ii) for oxidation, the valence band must have a greater positive potential than that of the oxidizing

species. Therefore, the band gap and the nitrogen species to be reduced must be band-paired to be a thermodynamically feasible redox reaction.

The overall surface catalyzed reduction reactions of nitrate to nitrite, ammonium, and nitrogen are described by reactions (31), (32), and (33), respectively. However, this general description does not ease the understanding of the mechanistic steps involved nor how to enhance products selectively towards N_2. Furthermore, charge transfer processes involving more than one electron per step are rare. Therefore, the mechanistic reduction pathways are discussed considering elementary steps involving the short-lived intermediate products. It is important to remark that several mechanistic differences can be attributed to different catalysts that affect the selectivity. Hence the description of the reactions involved are specific to pristine photocatalysts. The differences observed in doped photocatalysts, monometallic composites, and bimetallic composites follow the main mechanism discussed for pristine photocatalysts. The following description refers principally to TiO_2-based catalysts because the majority of works reported use this semiconductor as photocatalyst, although they can be transposable to other metal-oxides and chalcogenides that present similar trends (Lesko et al., 2015).

$$NO_3^- + 2\ H^+ + 2\ e_{cb}^- \rightarrow NO_2^- + H_2O \quad (31)$$

$$NO_3^- + 10\ H^+ + 8\ e_{cb}^- \rightarrow NH_4^+ + 3\ H_2O \quad (32)$$

$$2\ NO_3^- + 12\ H^+ + 10\ e_{cb}^- \rightarrow N_2 + 6\ H_2O \quad (33)$$

3.1. Reduction of nitrate on pristine photocatalyst

Initial studies reported null conversion of nitrate using pure TiO_2 photocatalysts (Ranjit, Varadarajan, & Viswanathan, 1995; Ranjit & Viswanathan, 1997a) in absence of h_{vb}^+ scavengers. The recombination of charge carriers considerably reduces efficiency of the reduction process. Bems et al. (Bems et al., 1999) suggested that if some reduction occurred under the photocatalytic treatment without h_{vb}^+ scavengers, the faster re-oxidation of the by-products leads to a steady concentration of nitrate in solution.

The use of organic h_{vb}^+ scavengers such as oxalic acid, formic acid, or methanol increases the conversion of nitrate by photocatalytic reduction, as presented in the studies summarized in Table 4-1. Selecting the appropriate h_{vb}^+ scavenger is important because it affects both the overall efficiency and product selectivity. For formic acid, for example, direct h_{vb}^+ oxidation (reaction (34)) yields carboxyl radical ($CO_2^{\bullet-}$) (G. Liu, You, Huang, & Ren, 2016b; Mora-Sero et al., 2005; Rengaraj & Li, 2007).

$$HCOO^- + h_{vb}^+ \rightarrow H^+ + CO_2^{\bullet-} \qquad k = 1.6 \times 10^8\ M^{-1}\ s^{-1} \qquad (34)$$

Table 4-1. Nitrate conversion and products selectivity for pristine TiO_2 photocatalysts.

Cata-lyst	Lamp	Loading / g	$[NO_3^-]_0$ / mM	Volume / mL	Sacrificial agent	pH	Time / min	Conversion / %	Selectivity / %			Ref.
									NO_2^-	NH_4^+	N_2	
TiO_2	medium-pressure Hg lamp 150 W	0.2	1.0	80	Oxalic acid 5.2 mM	2.37	120	15	0	100	0	1
TiO_2	medium-pressure Hg lamp 400 W	n.r.	7.14	1800	Formic acid 40 mM	2.6	n.r.	64	0.77	0.60	98.6	2
TiO_2	high-pressure Hg lamp 100 W	0.5	0.2	500	Methanol 2000 mM	4	240	100	0	80.0	20.0	3
TiO_2	high-pressure Hg lamp 110 W	0.25	7.1	600	Formic acid 40 mM	3	180	100	0	42.0	58.0	4
TiO_2	high-pressure Hg lamp 110 W	0.25	0.8	600	Formic acid 1 mM	6.8	120	52.5	34.3	8.9	56.8	5
TiO_2	high-pressure Hg lamp 250 W	0.5	0.97	500	Benzene 0.12 mM	4.2-6.0	240	8	0	56.8	43.2	6
TiO_2	high-pressure Hg lamp 400 W	0.05	10	5	Oxalic acid 40 mM	3	180	9.8	0.61	42.8	56.5	7
TiO_2	n.r.	n.r.	0.08	n.r.	Formic acid 0.1 mM	2.8	60	74	0	40.5	19.0[a] 40.5[b]	8

[a]Refers to the percentage of N_2 experimentally quantified [b]Refers to the percentage of NO experimentally quantified

1 (Y. Li & Wasgestian, 1998) 2 (Kyle Doudrick et al., 2012) 3 (Tawkaew, Yin, & Sato, 2001) 4 (Sá et al., 2009) 5 (G. Liu, You, Huang, & Ren, 2016a) 6 (L. Li et al., 2010) 7 (Kominami, Furusho, Murakami, & Inoue, 2001) 8 (Montesinos, Quici, Destaillats, Litter, et al., 2015)

Initially it was believed that the hole scavengers played only an indirect role on the photocatalytic reduction of NO_3^-, acting similarly to h_{vb}^+ scavengers to minimize (i) recombination drawback reaction (30) and (ii) re-oxidation of by-products to NO_3^- by the h_{vb}^+ or indirect by-product oxidation by hydroxyl radical ($^\bullet OH$) formed by water oxidation as in reaction (35). However, recent studies demonstrate that $CO_2^{\bullet-}$ plays a role of a reducing mediator (Kyle Doudrick et al., 2012; Lozovskii, Stolyarova, Prikhod, & Goncharuk, 2009; Sá et al., 2009; F. Zhang et al., 2005).

$$H_2O + h_{vb}^+ \rightarrow H^+ + {}^\bullet OH \qquad (35)$$

3.1.1. Reduction of nitrate to nitrite

Elementary reactions involve charge transfer processes of one electron per step. The reduction of NO_3^- to NO_2^- (reaction (31)) as the main intermediate during the complete reduction to NH_4^+ or N_2 is a complex three-step mechanism where two steps involve charge transfer (Fig. 4-7). The initial reduction of nitrate and one electron produces nitrate dianion radical (NO_3^{2-}) (reaction (36)). This short-lived (~20 μs) dianion radical is hydrolyzed to yield a nitrogen dioxide radical ($NO_2^\bullet$) following reaction (37) (Cook et al., 2001). Subsequently, $NO_2^\bullet$ undergoes the second charge transfer reaction to yield NO_2^- as the product (38).

$$NO_3^- + e^- \rightarrow NO_3^{2-\bullet} \qquad k = 9.7 \times 10^9\ M^{-1}\ s^{-1} \qquad (36)$$

$$NO_3^{2-} + H_2O \rightarrow NO_2^\bullet + 2\ OH^- \qquad k = 5.5 \times 10^4\ s^{-1} \qquad (37)$$

$$NO_2^\bullet + e^- \rightarrow NO_2^- \qquad k = 4.6 \times 10^9\ M^{-1}\ s^{-1} \qquad (38)$$

The e^- is the general reducing species represented in equations (36) and (38). However, the initial reduction to $^{\bullet}NO_2^-$ hardly occurs by the photogenerated e_{cb}^-. The elementary step in reaction (36) has a standard reduction potential of $E^o(NO_3^- / {}^{\bullet}NO_3^{2-}) = -0.89$ V vs Standard Hydrogen Electrode (SHE) (Cook et al., 2001; Fessenden, Meisel, & Camaioni, 2000). The e_{cb}^- photogenerated on TiO_2 has a standard potential within the range of -0.01 V down to -0.14 V vs SHE depending on the crystalline phases (Dung, Ramsden, & Gratzel, 1982; Ward, White, & Bard, 1983). Therefore, the direct reduction by e_{cb}^- photogenerated on TiO_2 is not thermodynamically possible, and it should be disregarded. However, the $CO_2^{\bullet-}$ radical, which has a high reducing potential of $E^o(CO_2/ CO_2^{\bullet-}) = -1.81$ V vs SHE, acts as an intermediary agent that leads to indirect reduction of NO_3^- (Montesinos, Quici, Destaillats, & Litter, 2015; Sá et al., 2009).

Another important feature that corroborates a mediated reduction is the low adsorption of NO_3^- on TiO_2, which is negligible (Wehbe et al., 2009). Usually, photocatalytic processes involve adsorption of a target pollutant on the catalyst surface and the likelihood of adsorption of formic acid. The redox processes involving the e_{cb}^-/ h_{vb}^+ pair mainly occur within the Helmholtz plane at the solid/liquid interface of the double layer by direct charge transfer between the semiconductor photocatalyst surface and the pollutant adsorbed. However, indirect processes by redox mediators, such as reaction with $CO_2^{\bullet-}$ radical, can occur in the solution bulk. In the first charge reaction where NO_3^- reduces to NO_2^- according to reaction (31), it is the adsorption of the h_{vb}^+ scavenger (e.g., formic acid) that affects the reduction kinetics and not the NO_3^- adsorption, because NO_3^-

reduction occurs predominantly in the bulk (Marcotte et al., 2015; Sá et al., 2009; Wehbe et al., 2009).

The second charge transfer reaction (38) that yields NO_2^- has a $E^o(NO_2^\bullet / NO_2^-)$ = 1.04 V vs SHE, meaning both e_{cb}^- and $CO_2^{\bullet-}$ radical are capable of reducing $NO_2^\bullet$. Considering the overall reaction (31) involves only $CO_2^{\bullet-}$ radical formed by reaction (34), the reduction of 1 mol of NO_3^- would require 2 mol of $CO_2^{\bullet-}$ (or formic acid). However, according to Doudrick et al. (2013), only 1.4 moles of formic acid are required experimentally per mol of NO_3^- (K Doudrick et al., 2013). This result demonstrates that 1 mol is required for reaction (36), while reaction (38) involves both direct and indirect charge transfer processes. Furthermore, the consumption of only 0.4 moles of formic acid during the second elementary reaction (38) suggests that direct charge transfer contributes to ~60% of the reduction.

The possible contribution of direct photolysis on the initial reduction to NO_2^- in reaction (31) could also depend on the irradiation source. The absorption of photons by NO_3^- (Fig. 3) induces NO_3^- photolysis and releases $NO_2^\bullet$ with a $\boldsymbol{\Phi}_{305}$ of 0.01 by reaction (4), which can circumvent the requirement of $CO_2^{\bullet-}$ as reducing species. The divergent results reported in the literature could be partially explained by the use of different irradiation sources that exclude or promote differently the NO_3^- photolysis.

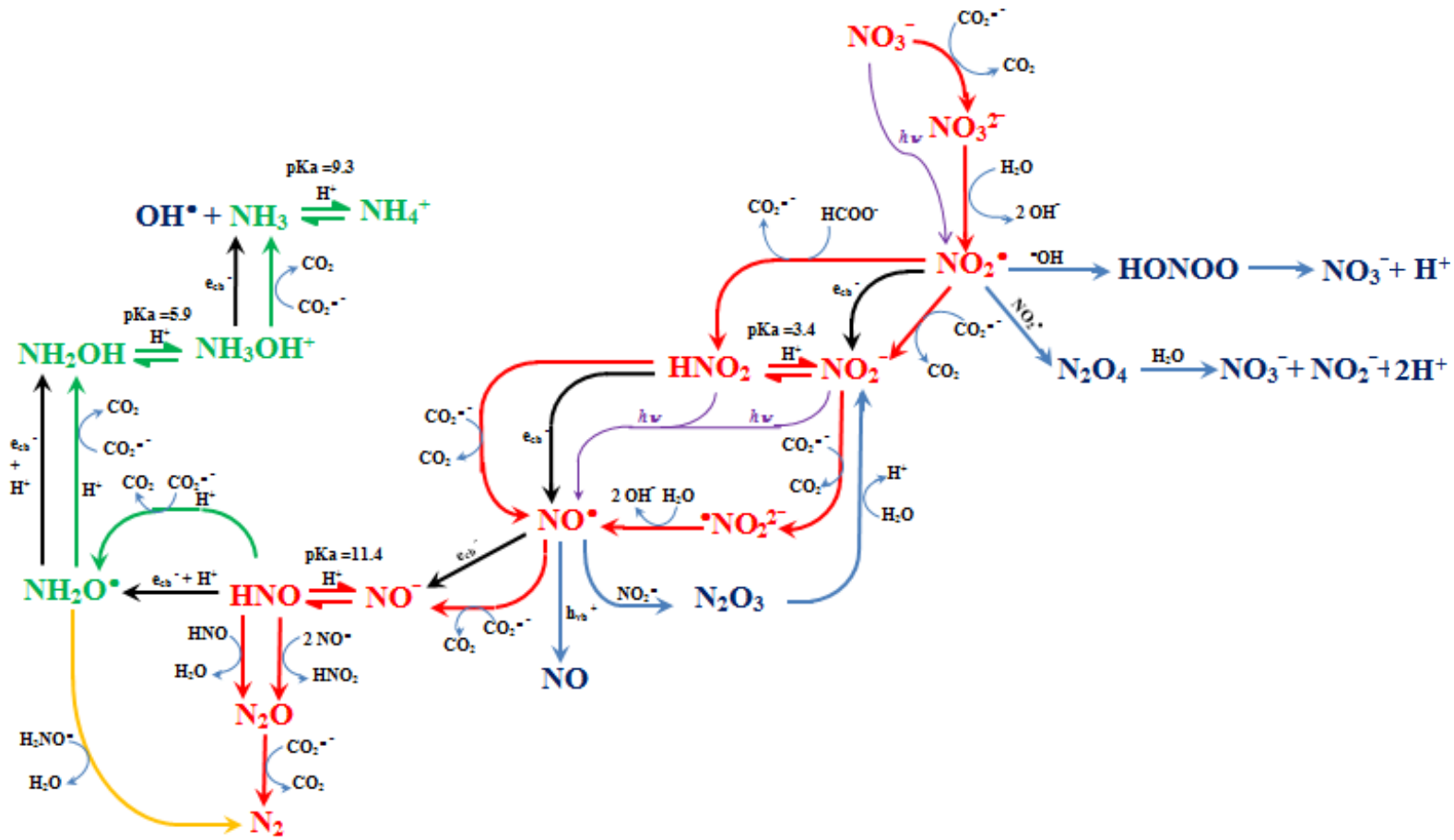

Figure 4-7. Mechanism and main processes of photocatalytic reduction of nitrate in water. The pathways leading selectively to N_2 as the final product are highlighted in **red**, pathways yielding NH_4^+ are shown in **green**, and other colors show minor reactions leading to other products.

3.1.2. Reduction of nitrite to nitrogen and ammonia

It is widely accepted that NO_2^- is the first stable intermediate product obtained from nitrate reduction, and it can remain in solution as NO_2^- or undergo further reduction to N_2 or NH_4^+. Some authors have been unable to detect quantifiable amounts of NO_2^- at the end of the photocatalytic reduction of NO_3^- because it can be easily reduced after its formation (de Bem Luiz, Andersen, Berger, Jose, & Moreira, 2012; Kyle Doudrick et al., 2012; Kominami et al., 2001; L. Li et al., 2010; Y. Li & Wasgestian, 1998). Because of its faster reduction, several works study the direct reduction of NO_2^-. Reduction of this intermediate species is relevant to enhancing the mechanistic understanding of photocatalytic reduction processes, because the reduction of nitrite is the divergent point that defines the selectivity towards innocuous N_2 release or undesired NH_4^+. The overall reduction from NO_2^- to NH_4^+ and N_2 occur according to reactions (39) and (40), respectively.

$$NO_2^- + 8\ H+ + 6\ e^- \rightarrow NH_4^+ + 2\ H_2O \quad (39)$$

$$2\ NO_2^- + 8\ H+ + 6\ e^- \rightarrow N_2 + 4\ H_2O \quad (40)$$

The catalytic sites will severely affect the selectivity towards NH_4^+ or N_2 because both processes involve the same number of electrons in the reduction process. Nonetheless, the release of ammonium results from direct nitrite reduction on the photocatalyst surface. Producing one molecule of N_2 requires a pairing of two nitrogen-containing surface species. Hence, Zhang et al. (2007) suggested that the selectivity of nitrite reduction could be discussed as a function of the ratio of surface coverage of N-species to reductant species

(F. Zhang et al., 2007) . This hypothesis suggests that the adsorption of NO_2^- and the intermediate species on the photocatalyst surface is critical, making pH one of the main factors controlling photocatalytic performances. Solution pH modifies the electrostatic surface charge of the solid surface of metal oxides by acid-base reaction. The photocatalyst surface can have neutral, positive, or negative charge, as it is represented by the point of zero charge (pH_{pzc}). This parameter is also referred to as the isoelectric point; TiO_2 photocatalyst has a pH_{pzc} = 6.2. When solution pH > pH_{pzc}, the surface is highly deprotonated according to reaction (41) for TiO_2 and consequently negatively charged (Kormann, Bahnemann, & Hoffmann, 1991). When pH < pH_{pzc}, the surface is highly protonated and is positively charged according to reaction (42) for TiO_2 (Wenliang Gao et al., 2004). Electrostatic repulsion results between the surface and the ionic species when similarly charged. Neutral molecules can be also adsorbed on the semiconductor surface, although the charged species exhibit stronger interactions. In the case of NO_2^- in acid-base equilibria (17) (pK_a = 3.4), significant NO_2^- adsorption would be observed within pH ranges between 3.4 and 6.2. Therefore, the reduction of NO_3^- and NO_2^- is best carried out below the pH_{pzc}. One can question if the pH influence on selectivity goes further than a simple surface charge effect on adsorption, but the requirement of H^+ in several reactions indicates that acidic pH is required to ensure the complete reduction of nitrate.

$$TiOH \leftrightharpoons TiO^- + H^+ \qquad pH > 6.25 \qquad (41)$$

$$TiOH + H^+ \leftrightharpoons TiOH_2^+ \qquad pH < 6.25 \qquad (42)$$

The elementary steps that lead to formation of either N_2 or NH_4^+ identify the formation of nitroxyl or azanone (HNO) as the true milestone that marks the divergent pathway, as depicted by the overall mechanistic pathway in Fig. 4-7. The reduction pathway of NO_2^- to this highly reactive intermediate involves two elementary charge transfer reactions. The charge transfer reactions are pH-dependent because the reduction standard potentials depend on the speciation of HNO_2/NO_2^-, which depends on acid-base equilibria (reaction (17)). When the predominant species is NO_2^-, the first elementary reaction leads to formation of NO_2^{2-} dianion radical following reaction (43). With an $E^o(NO_2^- / NO_2^{2-}) = -0.47$ V vs SHE (Goldstein, Behar, Rajh, & Rabani, 2016), the reduction process should be mediated solely by $CO_2^{\bullet-}$ radical because a non-direct reduction by e_{cb}^- is not thermodynamically feasible. Then, NO_2^{2-}, similarly to NO_3^{2-}, hydrolyzes quickly by reaction (44), yielding $NO^\bullet$. Subsequently, $NO^\bullet$ reduces further to nitroxyl anion according to reaction (45), which is quickly protonated according to acid-base equilibria reaction (46) with a $pK_a = 11.4$, leaving HNO the predominant species in aqueous solution.

$$NO_2^- + e^- \rightarrow NO_2^{2-} \qquad k = 2.0 \times 10^6\ M^{-1}\ s^{-1} \qquad (43)$$

$$NO_2^{2-} + H_2O \rightarrow NO^\bullet + 2\ OH^- \qquad k = 1.0 \times 10^5\ s^{-1} \qquad (44)$$

$$NO^\bullet + e^- \rightarrow NO^- \qquad k = 800\ M^{-1}\ s^{-1} \qquad (45)$$

$$NO^- + H^+ \leftrightharpoons HNO \qquad pK_a = 11.4 \qquad (46)$$

When HNO_2 is the predominant species in solution, $NO^\bullet$ is released according to reaction (47). $NO^\bullet$ can be produced directly by charge transfer reduction with e_{cb}^- and/or indirectly by $CO_2^{\bullet-}$, according to the potential $E^o(NO_2^- / NO_2^{2-}) = 0.88$ V vs SHE (Hérissan,

Meichtry, Remita, Colbeau-justin, & Litter, 2017). Consequently, HNO_2 converges with the pathway previously referred for NO_2^- involving reactions (45) and (46).

$$HNO_2 + e^- \rightarrow NO^\bullet + OH^- \qquad k = \text{n.a.} \qquad (47)$$

As stated previously, the reaction of HNO shifts photocatalytic selectivity toward either N_2 or NH_4^+. Therefore, the first reaction pathway leads to the innocuous desired product N_2 as a result of the efficient photocatalytic management of NO_3^-. The high number of available nitrogen species adsorbed on the photocatalyst surface leads to preferential removal of aqueous nitrogen to gas species. The dimerization of HNO by reaction (48) and/or the reaction between HNO and $NO^\bullet$ by reaction (49) yield N_2O as intermediate species of N_2 gas evolution. The release of N_2 is tailored to the further reduction reaction of N_2O with an $E^o(N_2O / N_2)$ = -0.96 V vs SHE by $CO_2^{\bullet-}$ according to reaction (50).

$$2\ HNO \rightarrow N_2O + H_2O \qquad k = 8.0 \times 10^6\ M^{-1}\ s^{-1} \qquad (48)$$

$$HNO + NO^\bullet \rightarrow N_2O + HNO_2 \qquad k = 5.0 \times 10^9\ M^{-1}\ s^{-1} \qquad (49)$$

$$N_2O + CO_2^{\bullet-} + H^+ \rightarrow N_2 + {}^\bullet OH + CO_2 \qquad k = \sim 10^9\ M^{-1}\ s^{-1} \qquad (50)$$

Reaction (50) is highly controversial and unclear in the literature. In most published reports, loss of total nitrogen dissolved in solution is directly ascribed to the formation of N_2, and few studies quantify direct yield of N_2. Instead, most papers attribute N_2 evolution as the difference between initial and final concentrations of aqueous inorganic N-species

corresponding to the result of equation (51) where *n* corresponds to the number of moles of each species.

$$n_{N_2} = n_{NO_3^- initial} - n_{NO_3^-} - n_{NO_2^-} - n_{NH_4^+} \quad (51)$$

The lack of reports identifying the gaseous species released during the photocatalytic reduction treatment of inorganic nitrogen anions does not allow to directly discriminate releases of noxious N_xO_y gases as suggested by Wehbe et al. (Wehbe et al., 2009). The quantification of N_2 by gas chromatography was reported by Kominami et al. (Kominami, Nakaseko, Shimada, Furusho, Inoue, et al., 2005) and by Zhang et al.(F. Zhang et al., 2005). Where they found complete mass balance, only 75% of nitrogen species were identified, suggesting the possible release of other nitrogen species using a Pt-Cu/TiO_2 photocatalyst. However, experimental work by Zhang et al. (F. Zhang et al., 2005) concluded that N_2 was the only gas product released using an Ag/TiO_2 photocatalyst. A separate study of Kominami et al. (Kominami, Gekko, & Hashimoto, 2010) analyzed the feasible formation not only of N_2 but also NO and N_2O. NO was not identified as a by-product evolved from NO_2^- reduction; however, N_2O was identified as a by-product in different ratio to N_2 depending on the catalyst used. A recent report by Litter's group (Montesinos, Quici, Destaillats, & Litter, 2015) quantified the release of NO and N_2 during the photocatalytic reduction of NO_3^- by bare TiO_2 corresponding to 68% and 32% of the gas composition, respectively. An important feature to consider is the solubility of the gas species involved. Taking into account that for the vast majority of works (see Tables 1-6) the concentrations of initial NO_3^- are ~1.6 mM, complete conversions would lead a

maximum amount of 1.6 mM of NO or 0.8 mM of N_2/N_2O in aqueous phase. The solubility of NO at 20 ºC is 1.94 mmol L^{-1} atm^{-1} (Zacharia & Deen, 2005), which is far superior to the concentrations that can be generated in experimental conditions with a 100% of conversion to NO. Similar outcomes occur with N_2O with a high solubility of 34.0 mmol L^{-1} atm^{-1} at 15 ºC (Weiss & Price, 1980). The low solubility of N_2 of 6.24 x 10^{-4} mmol L^{-1} atm^{-1} (Hamme & Emerson, 2004) suggests its direct evolution after formation, displacing the reactions towards its formation as observed by Zhang et al (2005). Nevertheless, other gases formed during water splitting such O_2 and H_2 can displace N_2O and NO from the aqueous phase, justifying their identification in the gas phase. Furthermore, the observed differences could be attributed to using different photocatalysts that: (i) modify the extent of some reactions, (ii) incur different enthalpies of adsorption of gaseous intermediates, or (iii) allow alternative pathways. However, N_2O has been identified as an intermediate released in other reductive treatments such as hydrogenation (Nakamura, Yoshida, Mikami, & Okuhara, 2006; Prüsse, Hähnlein, Daum, & Vorlop, 2000; Prusse & Vorlop, 2001). Future studies on photocatalytic reduction of NO_3^- and NO_2^- should quantify the gas species released in order to clarify which gaseous species are released during photocatalytic treatment. Even though N_2 is an inert species, other nitrogen-containing gas species such as N_2O, NO, and other N_xO_y are hazardous species with high environmental implications in atmospheric chemistry (Compton et al., 2011; Garcia-Segura, Mostafa, & Baltruschat, 2017).

The last major product obtained during NO_3^- and NO_2^- reduction is ammonium cation, which is released from an alternative pathway than the one of the HNO intermediate. When a high number of reductant species are available in comparison to the

coverage of N-species, the reduction of HNO is preferred to the dimerization reaction (48) or to reaction (49). The reduction of HNO to aminoxyl radical ($NH_2O^{\bullet}$) with an E^o(HNO / $H_2NO^{\bullet}$) = 0.52 V vs SHE can be conducted by e_{cb}^- and $CO_2^{\bullet -}$ radical following reaction (52). An additional quick charge transfer leads to hydroxylamine (NH_2OH) from this short-term lived by-product according to reaction (53). Even though NH_2OH has not been detected, it has been speculated as intermediate formed in very low quantities (i.e., below detection limit) by several authors (Montesinos, Quici, Destaillats, & Litter, 2015; Ranjit, Varadarajan, et al., 1995). In acidic conditions typically used for NO_3^- reduction experiments, hydroxylamine is protonated according to its acid-base equilibria (54) with a pK_a = 5.93. Then, the reduction of hydroxylamine yields ammonia (NH_3) by reaction (55), which is in equilibria with NH_4^+ with pK_a = 9.25 (reaction (56)).

$$HNO + H^+ + e^- \rightarrow NH_2O^{\bullet} \qquad k = \text{n.a.} \qquad (52)$$

$$NH_2O^{\bullet} + H^+ + e^- \rightarrow NH_2OH \qquad k = 1.0 \times 10^8\ M^{-1}\ s^{-1} \qquad (53)$$

$$H_2NOH + H^+ \leftrightharpoons H_3NOH^+ \qquad pK_a = 5.93 \qquad (54)$$

$$H_3NOH^+ + e^- \rightarrow NH_3 + {}^{\bullet}OH \qquad k = 1.0 \times 10^5\ M^{-1}\ s^{-1} \qquad (55)$$

$$NH_3 + H^+ \leftrightharpoons NH_4^+ \qquad pK_a = 9.25 \qquad (56)$$

The intermediate $H_2NO^{\bullet}$ can dimerize as N_2 by reaction (57); however, this is a minor pathway, which is negligible.

$$2\ H_2NO^{\bullet} \rightarrow N_2 + 2\ H_2O \qquad k = 1.4 \times 10^8\ M^{-1}\ s^{-1} \qquad (57)$$

In summary, the selectivity of nitrate depends on the ratio of surface coverage of N-species to reductant species. A low coverage or high concentration of reducing mediators could deteriorate the selectivity for formation of NH_4^+. An appreciable pseudo-concentration of adsorbed nitrogen intermediates, mainly HNO and $NO^{\bullet}$, would favor the pathway leading to N-gas species. Many reactions are highly pH-dependent; therefore, acidic pH is necessary to assure sufficient H^+ to allow fast kinetic rates. Accordingly, the pH dependence is not only related to the surface charge that modulates the adsorption of species on the photocatalyst surface but also as H^+ source to ensure the complete reduction.

3.2. Doped semiconductor photocatalysts

Several strategies have been considered to modify and improve the photocatalytic properties of pure semiconductors and decrease their band gaps. Depending on the atomic size of the dopant element, it can be introduced into the lattice by (i) substitutional doping or (ii) interstitial doping. In TiO_2 based photocatalysts, metal doping occurs usually via substitutional doping where titanium atoms are replaced by the introduced metallic dopant. Alternatively, non-metal dopants can either replace oxygen atoms or can be inserted in the interstices of the existing semiconductor lattice, depending on the atomic size of the dopant species (Palanivelu, Im, & Lee, 2007; Selase, Low, Qin, Wageh, & Al, 2015).

Even though the band gap energy for the electron photoexcitation is almost identical, introducing intraband levels permits the transition in two steps and requires less irradiation energy to form the charge carriers as illustrated in Fig. 4-8b. In brief, the photoexcitation can be conducted by absorption of visible light instead of UV (Ansari, Khan, Ansari, & Cho, 2016). Using these photocatalyst materials does not affect the

general mechanism of NO_3^- reduction described in the previous subsection. However, using visible light to conduct photoexcitation makes the process more environmentally friendly and more economical because the energy required for photoexcitation can be provided by longer wavelengths or even direct solar irradiation (Dozzi & Selli, 2013; Kamble et al., 2003; Kuo & Ho, 2001; Shinde, Bhosale, & Rajpure, 2011). Furthermore, the narrowing of the band gap is not the only effect reported. Table 2 summarizes the experimental results reported using doped semiconductors and shows doped semiconductors provide higher N_2 selective conversion rates for nitrate than the semiconductors presented in Table 1. Copper-doped TiO_2 photocatalysts produced 100% nitrite as a product, whereas doping with chromium and zinc produced > 95% nitrogen gases (de Bem Luiz et al., 2012). A mixed tungsten-nitrogen co-doped TiO_2 reduced 94% of aqueous nitrate to 96% nitrogen gases (Mishra, Mahato, Aman, Patel, & Sahu, 2011) with formic acid as a hole scavenger. This catalyst was highlighted for both its high surface area and substantial absorption in the visible spectrum, allowing for use of the solar spectrum and natural sunlight as the irradiation source. Thus, doping can provide higher conversion of nitrate and selectivity to nitrogen gases than neat TiO_2, but results are comparable to composite catalysts, raising the question of whether interstitital/substitutional doping is necessary compared to photodeposition methodologies (Kumar & Rao, 2015).

Table 4-2. Nitrate conversion and products selectivity for doped photocatalysts.

Catalyst	Lamp	Loading / g	$[NO_3^-]_0$ / mM	Volume / mL	Sacrificial agent	pH	Time / min	Conversion / %	Selectivity / %			Ref.
									NO_2^-	NH_4^+	N_2	
Cu-doped TiO_2	low-pressure Hg lamp 17 W	2.7	0.6	2700	Formic acid 9.8 mM	2.5	120	93.7	0	100	0	1
Cr-doped TiO_2	low-pressure Hg lamp 17 W	2.7	0.6	2700	Formic acid 9.8 mM	2.5	120	56.3	0	1.5	98.5	2
Zn-doped TiO_2	low-pressure Hg lamp 17 W	2.7	0.6	2700	Formic acid 9.8 mM	2.5	120	91.7	0	4.5	95.5	3
WN co-doped TiO_2	high-pressure Hg lamp 125 W	0.25	1.3	250	Formic acid 4.3 mM	n.r.	n.r.	94.0	1.0	3.0	96.0	4
$MgTiO_3$-TiO_2	high-pressure Hg lamp 125 W	0.2	7.0	200	Sodium oxalate 5 mM	5	120	1.2	4.2	22.5	73.3	5
$BaLa_4Ti_4O_{15}$	high-pressure Hg lamp 450 W	0.5	10.0	350	none	8.0	1260	97.4	2.05	0.29	97.6	6

1 (Bem Luiz et al., 2012) 2 (Bem Luiz et al., 2012) 3 (Bem Luiz et al., 2012) 4 (Mishra et al., 2011) 5 (R. Jin et al., 2004) 6 (Adachi and Kudo, 2012)

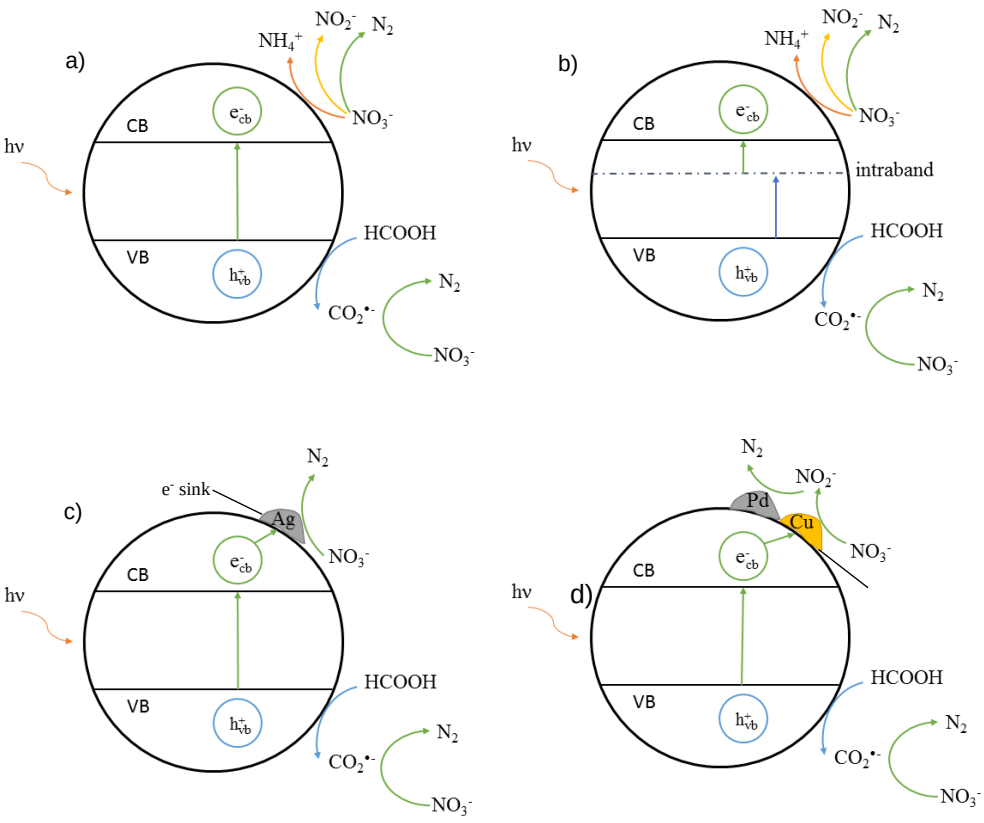

Figure 4-8. Reduction processes on (**a**) bare TiO_2, (**b**) doped TiO_2, (**c**) metallic/TiO_2 composite, and (**d**) bimetallic/TiO_2 composite.

3.3. Metallic/semiconductor composite photocatalysts

A composite photocatalyst is made by combining two or more constituent materials with significantly different chemical properties that, when combined, present different characteristics from the individual components, usually due to synergistic effects (Weiwei Gao et al., 2016; Shah, Park, Zhang, Park, & Yoo, 2012). The individual components of the composite remain separate and distinct within the finished photocatalytic material. For example, a composite metal/semiconductor would present metallic domains with their

characteristic crystalline structure along with the characteristic domains of the semiconductor material such as anatase crystalline phase. Composite photo-catalysts differ from doped semiconductors where the dopant substitutes for other atoms within the semiconductor lattice or in the interstices of the lattice. The composite photocatalyst configuration is represented by both materials separated by a slash representing the interface of both materials and indicates that two separate phases or domains are present. For example, Ag/TiO_2 refers to a composite of silver and titanium dioxide photocatalyst. The use of the term decorated photocatalyst is also prevalent in the literature.

The presence of a metal/semiconductor interface modifies the morphology of the space-charge region and the near surface region of charge density such that it differs from the bulk solution. The lower work function of the noble metal as compared to the electron affinity of TiO_2 is evidence of a high electron affinity by the metal. The metal then behaves as electron sink, forming a Schottky barrier potential as depicted in Fig. 4-8c and d. The charge carrier depletion region at the surface generates an electrical dipole layer that repels the majority of charge carriers from the surface toward the bulk (Tung, 2014). Therefore, the variation in surface states provides a potential for disparity between the electron density at the surface relative to the bulk and allows for diffusive electron transport to lower density regions. The differing electron densities promote the separation between charge carriers and delay the recombination reaction (30), thereby extending the time of life of e^-_{cb} as reducing agents. Apart from the electron trapping mechanism via the decorated metal, the interface can in some cases contribute to achieving a pseudo-lower band gap that allows for lower excitation energies (Kochuveedu, Jang, & Kim, 2013). However, an excessive metal loading in the composite can be detrimental, becoming a recombination center

instead of the desired electron sink (Ranjit & Viswanathan, 1997b). Optimizing metal loads to about 1.0% w/w typically minimize this detrimental effect (H. Park, Park, Kim, & Choi, 2013). Similar effects are observed when two different semiconductors are combined; however, because these composites have been barely reported for nitrate reduction treatment (de Bem Luiz, José, & Peralta, 2014), they are not included in this review.

3.3.1 Monometallic composite photocatalyst

Monometallic composites are the most prevalent types reported in the literature. However, different behaviors and performances are reported in function of the metal used as co-catalyst. The most commonly evaluated metals (Table 3 to 6), which are discussed herein, are the fourth period transition metals—iron, cobalt, nickel, and copper—, platinoids (e.g., platinum, paladium and ruthenium) and noble metals (e.g., gold and silver).

3.3.1.1. Fourth period metals

According to Kominami et al. (2001), using Co and Ni leads to lower N-gas conversions (4.4% and 20%, respectively). Using Co in photocatalyst composites reduces nitrate reduction (Kominami et al., 2001) and does not improve N_2 selectivity whereas using Ni induces nearly 100% NH_4^+ selectivity because it catalyzes reduction of the intermediate HNO species to NH_4^+ as illustrated in Fig. 4-7. Consequently, using Ni and Co composites is not recommended to manage NO_3^- and NO_2^-.

Using iron composites (Fe/TiO_2) considerably improves the NO_3^- selectivity towards N_2 from 58% for bare TiO_2 up to 87% for Fe/TiO_2 under similar experimental conditions (Sá et al., 2009). The mechanisms for improving selectivity are two-pathway reduction by TiO_2 photocatalyst and the decorated nano-zero-valent iron (nZVI). The pathways for reduction of nitrate with Fe^0 exhibit conventional chemical mechanism as

summarized in equations (58), (59) and (60) (Hwang, Kim, & Shin, 2011; Khalil, Eljamal, Amen, Sugihara, & Matsunaga, 2017; Suzuki, Moribe, Oyama, & Niinae, 2012). However, the preferred product obtained during nZVI reduction is NH_4^+, which precludes the use of nZVI for chemical denitrification of drinking water.

$$Fe^0 + NO_3^- + 2\ H_2O \rightarrow NO_2^- + Fe^{2+} + 2\ OH^- \quad (58)$$

$$4\ Fe^0 + NO_3^- + 7\ H_2O \rightarrow NH_4^+ + 4\ Fe^{2+} + 10\ OH^- \quad (59)$$

$$5\ Fe^0 + 2\ NO_3^- + 6\ H_2O \rightarrow N_2 + 5\ Fe^{2+} + 12\ OH^- \quad (60)$$

The combination of photocatalyst and nZVI in a composite promotes increased selectivity towards N-gases in comparison to nZVI reduction alone. Consequently, although the mechanism follows a chemical reduction pathway, the interface with TiO_2 synergistically affects the process by: (i) adsorbing some N-intermediates on the TiO_2 surface, which enhances the ratio of N-species surface coverage to reductant species and favors the evolution of N-gases, and (ii) allowing photogenerated electrons to contribute to the nitrate reduction and also to the recovery of nZVI via reduction of oxidized iron species (Y. Liu et al., 2014; Pan, Huang, Hsieh, & Wu, 2012). Unfortunately, little information is available about the implications of Fe^{2+}/Fe^{3+} leaching from the nZVI. Although nZVI/TiO_2 composites exhibit better performance than nZVI alone, the selectivity towards N-gases, which is 38–60%, is still considerably inferior to the selectivity exhibited by other photocatalysts.

Copper is the most studied metal of the fourth period for use in composites, though contradictory effects have been found, which are more related to the scavenger selected

than to the copper material (R. Jin et al., 2004; Krasae & Wantala, 2016; L. Li et al., 2010; Sá et al., 2009). Kominami et al. (Kominami, Nakaseko, Shimada, Furusho, Inoue, et al., 2005) studied the effect of the pH, demonstrating that highly alkaline media (pH = 11.0) delivers NO_2^- as main product, whereas NH_4^+ is the predominant species in acidic conditions (pH = 3.0). This result could be explained with the overall mechanism described for the pristine TiO_2 photocatalyst, where H^+ is required to attain complete reduction either to N_2 or NH_4^+. Under similar low pH conditions, Sá et al. (Sá et al., 2009) reported a slightly superior selectivity towards N_2 of 63% (5% increase) for TiO_2 (see Tables 1 and 3) when formic acid was used as a scavenger. It could be postulated that Cu facilitates NO_3^- reduction because (i) it easily complexes with nitrogen species and (ii) it could act as a reducing mediator with the complexed nitrogen species with an $E^o(Cu^+/Cu)$ = +0.521 V vs SHE and $E^o(Cu^{2+/}Cu)$ = +0.337 V vs SHE, while being easily regenerated by the e^-_{cb} at the interface metal/semiconductor. However, the stability of Cu composites in acidic media can be compromised by their dissolution as reported by Wehbe et al. (Wehbe et al., 2009) where 45% of initial Cu leached after 2h in a formic acid solution. Even though other authors have not reported Cu leaching studies during and after its use, it is imperative to examine the implications of Cu dissolution in future studies.

Table 4-3. Nitrate conversion and products selectivity for photocatalysts composites with 4th period metal.

Catalyst	Lamp	Loading / g	$[NO_3^-]_0$ /mM	Volume /mL	Sacrificial agent	pH	Time / min	Conversion / %	Selectivity / %			Ref.
									NO_2^-	NH_4^+	N_2	
Co/TiO_2	high-pressure Hg lamp 400 W	0.05	10.0	5	Oxalic acid 40 mM	3	180	4.4	0.9	45.5	53.6	1
Cu/TiO_2	high-pressure Hg lamp 400 W	0.05	10.0	5	Oxalic acid 40 mM	3	180	44 .0	0.2	90.9	8.9	2
Cu/TiO_2	high-pressure Hg lamp 125 W	0.04	7 .0	200	Sodium oxalate 5 mM	5	120	31.4	65.9	16.7	17.4	3
Cu/TiO_2	high-pressure Hg lamp 400 W	0.05	10.0	5	Oxalic acid 40 mM	11	720	28.0	100	0	0	4
Cu/TiO_2	high-pressure Hg lamp 110 W	0.25	7.1	600	Formic acid 40 mM	3	180	100	0	37.0	63.0	5
Cu/TiO_2	high pressure Hg lamp 250 W	0.5	1.0	500	Benzene 0.12 mM	4-6	240	33.0	68.7	4.6	26.7	6
Cu/Cu_2O	high-pressure Hg lamp 80W	Photo-cathode	0.08	250	None (+0.20 V)	7	75	93.0	40.0	10.0	50.0	7

Table 4-3 (continued). Nitrate conversion and products selectivity for photocatalysts composites with 4th period metal.												
Cu/$MgTiO_3$-TiO_2	high-pressure Hg lamp 125 W	0.2	7.0	200	Sodium oxalate 5 mM	5	120	39.2	76.3	18.4	5.3	8
Fe/TiO_2	high-pressure Hg lamp 110W	0.25	7.1	600	Formic acid 40 mM	3	180	100	0	13.0	87.0	9
nzv Fe/TiO_2	cold cathode fluorescent lamp	0.25	0.16	30	none	3	30	95.0	0	62.0	38.0	10
nzv Fe/TiO_2	UV-A lamp 20 W	20	0.8	n.r.	Formic acid 27 mM	3	720	80.0	0	39.1	60.9	11
Ni/TiO_2	high-pressure Hg lamp 400 W	0.05	10	5	Oxalic acid 40 mM	3	360	20.0	0	100	0	12
Ni/ZnS	Xe lamp 300 W	0.5	1000	100	Methanol 1.5 M	n.r.	1200	0.3	91.0	8 .0	1.0	13

1 (Kominami et al., 2001) 2 (Kominami et al., 2001) 3 (R. Jin et al., 2004) 4 (Kominami, Nakaseko, Shimada, Furusho, Inoue, et al., 2005) 5 (Sá et al., 2009) 6 (L. Li et al., 2010) 7 (Paschoal, Nuñez, Lanza, & Zanoni, 2013) 8 (R. Jin et al., 2004) 9 (Sá et al., 2009) 10 (Pan et al., 2012) 11 (W. Liu et al., 2014) 12 (Kominami et al., 2001) 13 (Hamanoi & Kudo, 2002)

3.3.1.2. Platinoids

The use of platinoids in TiO_2 composites drastically alters photocatalyst performance due to associated changes in the reductive mechanisms (Shin, Jung, Bae, Lee, & Kim, 2014). The pioneering work of Ranjit et al. (1994) compared the effects that these metals may have on nitrate conversion. They observed decreasing photocatalytic performance of Rh > Ru > Pt > pristine ZnS > Pd (Ranjit, Krishnamoorthy, & Viswanathan, 1994). These different performances observed for TiO_2 photocatalysts depended on the synthetic method. The performance of impregnated catalysts decreased in the order Ru > Rh > Pd > Pt, while the preparation of the composites by photodeposition was found to be Pd > Rh > Pt > Ru (Ranjit & Viswanathan, 1997b). The different trends related to synthetic method were correlated to differences in the size and morphology of the dispersed metal clusters (Ranjit & Viswanathan, 1997b). However, the metals' performance was also related to the intrinsic capability of each platinoid to stabilize H_{ads} because materials with higher overpotential for H_2 evolution presented predominant yield of NH_4^+. In this context, Li et al. (Y. Li & Wasgestian, 1998) and Kominami et al (Kominami et al., 2001) suggested that, in the case of platinoids, nitrate can be reduced by adsorbed $H^\bullet$ with an $E^o(H^+/ H^\bullet)$ = -2.31 V. The most influential factors affecting efficiency of proton reduction on the metal surface are (i) the hydrogen overpotential during water splitting and (ii) the H_{ads} stabilization (Juan Yang et al., 2013). In support of this hypothesis, Hamanoi et al. (Hamanoi & Kudo, 2002) proved experimentally that a decrease in NO_3^- conversion is observed when hydrogen evolution is increased. Furthermore, bubbling H_2 enhances the reduction of NO_3^- to NH_4^+, demonstrating that the adsorption of H_2 on platinoids surface catalytic sites as H_{ads} contributes to the reduction process (Sá et al., 2009).

The use of metals allows an alternative reductive pathway. The first step is the preferred reduction of H^+ to $H^\bullet$ on the metallic surface (Trasatti, 1972), which remains adsorbed on the Pt surface and creates an electron sink as summarized in reaction (61). The H_{ads} can dimerize and evolve to H_2 (Sehested & Christensen, 1990) following the pathway described in reaction (62) or it can react with NO_2^-, reducing it to N_2 or NH_4^+ (L. Li et al., 2010). For this hydrogenation pathway, the first reduction of NO_3^- to NO_2^- follows the mechanism discussed for pure TiO_2 depicted in Fig. 4-7. The secondary reductive mechanism is still unclear, but a pathway similar to the one reported for nitrate reduction by hydrogenation is suggested (R. Zhang et al., 2013), where the hydrogenation of NO_2^- yields NO by reaction (63). The NO is subsequently easily reduced to NH_4^+ according to reaction (64). The release of N_2 instead requires adsorption of two NO molecules to react with H_{ads} releasing N_2O as intermediate (reaction (65)) that can be reduced by $CO_2^{\bullet-}$ or H_{ads} following pathways in reactions (50) and (66) (Czapski & Peled, 1968; R. Zhang et al., 2013), respectively.

$$H^+ + e^-_{cb} \rightarrow H_{ads} \qquad (61)$$

$$2\ H_{ads} \rightarrow H_2 \qquad k = 5.0 \times 10^9\ M^{-1}\ s^{-1} \qquad (62)$$

$$NO_2^- + H_{ads} \rightarrow NO + OH^- \qquad k = 7.1 \times 10^8\ M^{-1}\ s^{-1} \qquad (63)$$

$$NO + 5\ H_{ads} \rightarrow NH_4^+ + OH^- \qquad k = \text{n.a.} \qquad (64)$$

$$2\ NO + 2\ H_{ads} \rightarrow N_2O + H_2O \qquad k = \text{n.a.} \qquad (65)$$

$$N_2O + 2\ H_{ads} \rightarrow N_2 + H_2O \qquad k = 2.1 \times 10^6\ M^{-1}\ s^{-1} \qquad (66)$$

The experimentally-observed low conversions (2–20%) when using monometallic platinoid photocatalysts could be related to the preferential evolution of H_2 when compared to the alternative pathways for N-based reactions (63) to (66). As seen in Table 4-4, platinoid composites yield NH_4^+ as the main product; although it is still unclear which gas species are released.

Table 4-4. Nitrate conversion and products selectivity for photocatalysts composites with platinoids.

Catalyst	Lamp	Loading / g	$[NO_3^-]_0$ / mM	Volume / mL	Sacrificial agent	pH	Time / min	Conversion / %	Selectivity / %			Ref.
									NO_2^-	NH_4^+	N_2	
Pd/TiO_2	high-pressure Hg lamp 400 W	0.05	10	5	Oxalic acid 40 mM	3	180	2.6	3.1	76.9	20.0	1
Pd/TiO_2	high-pressure Hg lamp 400 W	0.05	10	5	Oxalic acid 40 mM	11	720	6.0	0	0	0	2
Pd/ $NaTaO_3$	n.r. Hg lamp 500 W	0.8	1.6	1000	Oxalic acid 60 mM	3	60	100	n.r.	n.r.	n.r.	3
Pt/TiO_2	high-pressure Hg lamp 400 W	0.05	10	5	Oxalic acid 40 mM	3	180	6.4	1.2	31.3	67.5	4
Pt/TiO_2	high-pressure Hg lamp 400 W	0.05	10	5	Oxalic acid 40 mM	11	720	4.0	0	0	0	5
Pt/TiO_2	high-pressure Hg lamp 250 W	0.5	0.97	500	Benzene 0.12 mM	4.2-6.0	240	25.0	0	63.0	37.0	6
RuO_2/TiO_2	high-pressure Hg lamp 400 W	0.05	10	5	Oxalic acid 40 mM	3	360	17.2	3.5	33.7	62.8	7

1(Kominami et al., 2001) 2 (Kominami, Nakaseko, Shimada, Furusho, Inoue, et al., 2005) 3 (Mohamed & Baeissa, 2014) 4 (Kominami et al., 2001) 5 (Kominami, Nakaseko, Shimada, Furusho, Inoue, et al., 2005) 6 (L. Li et al., 2010) 7 (Kominami et al., 2001)

3.3.1.3. Noble metals: gold and silver

The last group of monometallic composites combine noble metals silver (Ag) and gold (Au) with a semiconductor. Using Au/TiO_2 composites generally demonstrated a low performance for NO_3^- conversion in comparison to Ag/TiO_2 catalysts as summarized in Table 5. The use of oxalic acid as a hole scavenger may be one of the main factors contributing to this reported lower performance for Au/TiO_2 (Anderson, 2011, 2012). Literature reports suggest that formic acid may be a more efficient hole scavenger when compared to oxalic acid (see section 4). However, insufficient data exist to better understand the role of gold on the photocatalytic reduction of nitrate, especially in light of Kominami et al. (Kominami et al., 2001) study, which demonstrates a 6-fold increase when compared to pristine TiO_2 under similar experimental conditions.

In contrast to other monometallic composites, Ag/TiO_2 catalysts exhibit a much higher selectivity towards N_2 evolution in presence of formic acid as hole scavenger (F. Zhang et al., 2005). Major selectivity towards N_2 has been reported by a number of authors (K Doudrick et al., 2013; Kobwittaya & Sirivithayapakorn, 2014; Lozovskii et al., 2009; Parastar et al., 2013; Sá et al., 2009; D. Sun et al., 2016), as summarized in Table 4-5. The different performances could not be attributed only to the Schottky barrier and the recombination rate diminution phenomena because similar results could not be observed for other composites. It could be postulated that silver has the ability to improve the ratio of N-species surface coverage to reductant species. A possible enhancement on the reduction rate kinetics could be attributed to the mediated reduction by e^- on the silver surface by direct charge transfer. However, more data is needed to better elucidate the role of Ag surfaces with respect to improving selectivity.

Table 4-5. Nitrate conversion and products selectivity for photocatalysts composites with noble metals silver and gold.

Catalyst	Lamp	Loading / g	$[NO_3^-]_0$ / mM	Volume / mL	Sacrificial agent	pH	Time / min	Conversion / %	Selectivity / %			Ref.
									NO_2^-	NH_4^+	N_2	
Ag/TiO_2	Xe lamp 300 W	0.125	1.6	250	Formic acid 8 mM	3.0	180	95.0	2.0	8.0	90.0	1
Ag/TiO_2	high-pressure Hg lamp 400 W	0.05	10.0	5	Oxalic acid 40 mM	3.0	180	86.0	0	53.5	46.5	2
Ag/TiO_2	high-pressure Hg lamp 400 W	0.05	10.0	5	Oxalic acid 40 mM	11.0	720	24.0	5.0	0	95.0	3
Ag/TiO_2	high-pressure Hg lamp 125 W	0.25	7.0	250	Formic acid 40 mM	3.0	30	71.7	16.0	0.23	83.7	4
Ag/TiO_2	low-pressure Hg lamp 8 W	0.45	7.1	450	Formic acid 40 mM	3.0	30	96.0	0	0	100	5
Ag/TiO_2	high-pressure Hg lamp 110 W	0.25	7.1	600	Formic acid 40 mM	3.0	180	100	0	4.0	96.0	6

Table 4-5 (continued). Nitrate conversion and products selectivity for photocatalysts composites with noble metals silver and gold.												
Ag/TiO_2	high-pressure Hg lamp 400 W	0.2	7.1	200	Formic acid 40 mM	2.5	n.r.	99.0	0	12.0	88.0	7
Ag/TiO_2	black-light bulb 15 W	Thin film	7.1	4500	Formic acid 59.3 mM	2.8	360	70.0	0.5	0.10	99.4	8
Ag/TiO_2	n.r. UV light 125 W	1.2	1.6	1500	Formic acid 40 mM	5.0	180	82.0	0	0	100	9
Ag_2O/TiO_2	high-pressure Hg lamp 300 W	0.02	7.1	20	Formic acid 8 mM	3.0	240	97.2	2.4	14.4	83.2	10
Au/TiO_2	high-pressure Hg lamp 400 W	0.05	10.0	5	Oxalic acid 40 mM	3.0	360	44.0	0.1	50.0	49.9	11
Au/TiO_2	high-pressure Hg lamp 400 W	0.05	10.0	5	Oxalic acid 40 mM	11.0	720	16.0	75.0	0	0	12
Au/TiO_2	n.r. UV light 400 W	0.25	1.6	1200	Oxalic acid 8 mM	3.0	180	60.0	n.r.	n.r.	n.r.	13
Au/TiO_2	n.r. UV light 400 W	0.25	1.6	1200	Oxalic acid 8 mM	3.0	180	44.0	0	39.0	61.0	14

1 (D. Sun et al., 2016) 2 (Kominami et al., 2001) 3 (Kominami, Nakaseko, Shimada, Furusho, Inoue, et al., 2005) 4 (F. Zhang et al., 2005) 5 (Lozovskii et al., 2009) 6 (Sá et al., 2009) 7 (K Doudrick et al., 2013) 8 (Kobwittaya & Sirivithayapakorn, 2014) 9 (Parastar et al., 2013) 10 (Ren et al., 2015) 11 (Kominami et al., 2001) 12 (Kominami, Nakaseko, Shimada, Furusho, Inoue, et al., 2005) 13 (Anderson, 2011) 14 (Anderson, 2012)

3.3.2. Bimetallic composite photocatalyst

Bimetallic nanoparticles improve kinetics of nitrate reduction by hydrogenation processes due to the synergistic contribution of platinoid metals and fourth period metals (mainly Cu) (Kominami, Nakaseko, Shimada, Furusho, Inoue, et al., 2005; Wehbe et al., 2009). As discussed previously, copper can contribute to faster reduction of NO_3^- to NO_2^-, but it hardly yields a complete reduction to NH_4^+ or N_2. Platinoids, such Pt and Pd, can easily reduce NO_2^- via the hydrogenated mediated mechanism, although low conversion efficiencies are typically observed because NO_3^- reduction is a limiting step. The underlying idea behind these bimetallic composites is enhancement of the overall reduction process by combining both metals with TiO_2 as e^-_{cb} and H_2 source (Sá et al., 2012). In cases like these, the overall performance is considerably enhanced as illustrated in Table 4-6.

Soares et al. (Soares, Pereira, Orfao, et al., 2014) reported evaluating the influence of a Pd-Cu/TiO_2 composite as catalyst for: (i) direct hydrogenation and (ii) direct hydrogenation combined with photocatalysis when bubbling H_2 or H_2/CO_2 mix. The direct bubbling of H_2 in the dark resulted in a 55% of NO_3^- conversion with selectivity of 72% for NO_2^-, 22% for NH_4^+, and 6% for N_2. When light was applied, the conversion increased to 75% with selectivity of 72% for NO_2^-, 18% for NH_4^+, and 10% for N_2. In contrast, when CO_2 and H_2 are simultaneously bubbled, the conversion increases under both dark and light experimental conditions. In dark, 90% NO_3^- conversion was observed with a selectivity of 85% for NH_4^+ and 15% for N_2. This NO_3^- conversion increased to 98% and the selectivity shifted to 48% for NH_4^+ and 52% for N_2 in light conditions. These results emphasize two interesting effects. The first effect is related to pH and stems from the direct use of H_2 vs H_2/CO_2. When H_2 was bubbled, the pH varied from pH ≈ 3 to pH ≈ 8.0. In contrast, pH

was maintained at ~5.0 when H_2/CO_2 was bubbled because CO_2 acted as a buffer for the released OH^- as summarized in reactions (63) and (64). Both experiments confirmed the mechanism of hydrogenation in presence of platinoid metals (mono and bimetallic composites). Considering reactions (63) and (64), the overall process efficiency is markedly influenced by pH changes. The major selectivity towards NO_2^- release in the alkaline condition suggests that the second part of the mechanism, which involves reduction from NO_2^- to NH_4^+ or N_2, is the highly pH-dependent mechanism, as it could be deduced from Fig. 4-7. The alkaline media inhibits additional reduction of NO_2^-, which remains a main product with a selectivity of 72%.

The second effect is related to photon contribution during the photocatalytic reduction. From the shift in N_2 selectivity, which changes from 15% to 52%, it can be concluded that NO_3^- reduction occurs via both mechanisms: (i) reduction via H_2 and (ii) reduction via $CO_2^{\bullet-}$ radical and photogenerated e^-_{cb}. Therefore, when NO_3^- is reduced by H_2, it yields NH_4^+ as main product (also observed in monometallic platinoid photocatalysts in Table 4-5) (Barrabes & Sa, 2011), because release of N_2 via reactions (65) and (66) is negligible. The photocatalytic reduction via $CO_2^{\bullet-}$ and photogenerated e^-_{cb} represents the selective step towards N_2 generation. According to Soares et al. (Soares, Pereira, Orfao, et al., 2014), both the pH and the hole scavenger effects are involved in NO_3^- reduction and could influence product selectivity.

Table 4-6. Nitrate conversion and products selectivity for bimetallic photocatalysts composites.

Catalyst	Lamp	Loading / g	$[NO_3^-]_0$ / mM	Volume / mL	Sacrificial agent	pH	Time / min	Conversion / %	Selectivity / %			Ref.
									NO_2^-	NH_4^+	N_2	
nzv Fe-Cu/TiO_2	3 UV-A lamps, 20 W	n.r.	1.2	100	none	4	360	100	0	15.0	85.0	1
Ni-Cu/TiO_2	high-pressure Hg lamp 125 W	0.2	1.6	200	Oxalic acid 5.0 mM	3.0	300	25.0	16.0	44.0	40.0	2
Pd-Cu/TiO_2	high-pressure Hg lamp 400 W	0.05	10.0	5	Oxalic acid 40 mM	11.0	720	56.0	1.5	0	98.0	3
Pd-Cu/TiO_2	n.r. near-UV to visible light	0.1	1.6	200	Formic acid 40 mM	3.3	240	85.0	0	15.0	85.0	4
Pt-Cu/TiO_2	5 n.r. UV lamps 15 W	1.0	0.8	500	Formic acid 20 mM	2.0	60	39.0	0	0	100	5
Pt-Cu/TiO_2	5 n.r. UV lamps 15 W	1.0	0.8	500	H_2 60 mL/min + Formic acid 20 mM	2.0	60	100	0	13.7	86.3	6
Pt-Cu/TiO_2	high-pressure Hg lamp 250 W	0.5	1.0	500	Benzene 0.12 mM	4.2-6.0	240	66.0	0	0	100	7
Pt-Ni/ZnS	Xe lamp 300 W	0.5	1000	100	Methanol 1.5 M	n.r.	1200	0.03	54.3	42.7	3.0	8

1 (Krasae & Wantala, 2016) 2 (Wenliang Gao et al., 2004) 3 (Kominami et al., 2005) 4 (Soares, Pereira, Orfao, et al., 2014) 5 (Wehbe et al., 2009) 6 (Wehbe et al., 2009) 7 (L. Li et al., 2010) 8 (Hamanoi & Kudo, 2002)

In summary, it could be concluded that the use of bimetallic catalysts and silver monometallic materials represent the most promising avenues for improving both catalytic reduction of nitrate and selectivity towards N_2. Future research efforts directed at elucidating the role of these bimetallic composite photocatalysts and their use in full-scale reactors is necessary to facilitate the development and implementation of photocatalytic technologies for nitrate management. Development of alternative photocatalysts, especially composites, would further aid in solving the challenges related to nitrate reduction efficiency and selectivity.

Section 4: Hole scavengers influence

The importance of hole scavengers, also called sacrificial electron donors, during NO_3^- reduction stems from the need to minimize recombination reactions and also from their role as reduction process mediators (i.e., $CO_2^{\bullet -}$). Based on the existing literature, all hole scavengers employed in nitrate reduction processes are organic compounds. The most common scavengers are methanol, oxalic acid, and formic acid, including their corresponding salts. These three compounds have been connected to slightly different mechanisms that result in diverse scavenging effects and yield different reduction by-products. Formic acid is typically the preferred hole scavenger, although the potential importance of the other organics should not be neglected.

4.1. Methanol as a hole scavenger

Methanol (CH_3OH) was first used as a hole scavenger by Mori et al. (Mori, Suzuki, Fujimoto, Watanabe, & Hasegawa, 1999), who employed xenon light source and a

hollandite photocatalyst ($K_{1.8}Ga_{1.8}Sn_{6.2}O_{16}$) to reduce nitrate. In an attempt to analyze labeled nitrogen compounds via Fourier transform infrared spectroscopy (FTIR) and determine particular gaseous products, Mori et al (Mori et al., 1999) elucidated important mechanistic pathways for reduction of nitrate to N_2. Specifically, they observed the formation of nitroso-compounds with characteristic bands at 1200 cm^{-1} as intermediate by-products, which led them to propose a reaction mechanism for the reduction of NO_3^- to N_2 mediated by methanol as summarized in equations (67) to (69):

$$HNO_3 + CH_3OH \rightarrow [ON\text{-}CH_2OH] + H_2O + \tfrac{1}{2} O_2 \quad (67)$$

$$[ON\text{-}CH_2\text{-}OH] + \tfrac{1}{2} O_2 \rightarrow [ON\text{-}CHO] + H_2O \quad (68)$$

$$[ON\text{-}CHO] \rightarrow (H^+) HCOOH + \tfrac{1}{2} N_2 \quad (69)$$

The formic acid, which is released as a product, can be further oxidized, yielding $CO_2^{\bullet -}$ as described previously in reaction (34). This species could further interact with nitrate via a mechanism illustrated in Fig. 4-7 (see Section 3.1). The studies conducted using methanol as a hole scavenger show low nitrate conversions of ~23–40%, with preferential yield of ammonium and nitrite as main reduction products using CdS based catalysts (Tawkaew, Fujishiro, Yin, & Sato, 2001; Tawkaew, Uchida, Fujishiro, & Sato, 2006; Tawkaew, Yin, et al., 2001). The highest conversion (64.0%) was achieved using methanol and ZnO catalyst, although the authors did not report experimental product yield results and selectivity towards N_2 could not be determined (S. Park et al., 2007). However, Hamanoi et al. (2002) observed preferential generation of NO_2^- along with H_2 produced from water reduction using a Ni-ZnS photocatalyst (Hamanoi & Kudo, 2002), which

further suggests that using methanol may not lead to high N_2 selectivity. Nonetheless, methanol improves the conversion of nitrate compared to a no-scavenger case, but with poor selectivity compared to formic acid (see Tables 4-1 to 4-6). Additionally, methanol is highly toxic to humans, acting as central nervous system depressant and potentially causing permanent blindness, and these health concerns restrict its use in drinking water applications.

4.2. Oxalic acid as a hole scavenger

The second most-used hole scavenger in photocatalytic nitrate reduction is oxalic acid ($C_2H_2O_4$). Experiments with pure TiO_2 using oxalic acid as a hole scavenger at pH < 3.0 yield <15% nitrate reduction (Kominami et al., 2001; Y. Li & Wasgestian, 1998) and high ammonium selectivity. Upon adding silver to the TiO_2, 86% reduction was achieved, but the selectivity was still driven towards ammonium with >50% being ammonium end-product (Kominami et al., 2001). Introducing Ag/TiO_2 as a photocatalyst yielded 95% selectivity to nitrogen gases, but nitrate reduction did not exceed 24% (Kominami, Nakaseko, Shimada, Furusho, Inoue, et al., 2005). Limited nitrate reduction of 28% and 44% was also observed when Cu/TiO_2 and Au/TiO_2, respectively, were used as photocatalysts with oxalic acid as hole scavenger (Kominami, Nakaseko, Shimada, Furusho, Inoue, et al., 2005). The difference in conversion outcomes is attributed to the pH influence on the distribution of oxalic acid and its anionic species in acid-base equilibria with $pK_{a1} = 1.25$ and $pK_{a2} = 4.14$ according to reactions (70) and (71), respectively. This trend is observed in results reported by Kominami et al. (Kominami, Nakaseko, Shimada, Furusho, Inoue, et al., 2005) where the difference in outcomes is attributed to the difference

in pH: faster kinetics and complete reduction at pH 3.0 vs slower kinetics and incomplete reduction at pH 11.0. Therefore, the oxidation of this dicarboxylic acid is highly affected by electrostatic repulsion when the photocatalyst surface is negatively charged.

$$C_2H_2O_4 \leftrightharpoons H^+ + C_2HO_4^- \qquad pK_{a1} = 1.25 \qquad (70)$$

$$C_2HO_4^- \leftrightharpoons H^+ + C_2O_4^{2-} \qquad pK_{a2} = 4.14 \qquad (71)$$

Compared to formic acid, oxalic acid exhibits a different oxidation mechanism during photocatalysis. Formic acid is oxidized directly by h^+_{vb}, whereas oxalic acid is indirectly oxidized by $^\bullet OH$ produced from oxidation of water according to reaction (35) (Kyle Doudrick et al., 2012). The $^\bullet OH$ production step additionally contributes to slower kinetics than alternative scavenging species. Hydroxyl radical, however, has the ability to oxidize NO_2^- and NH_3 to NO_3^-. This competitive re-oxidation mechanism further decreases the nitrate reduction kinetics. The oxidation mechanism of oxalic acid by hydroxyl radical is well known and involves the release of oxalate radical following reaction (72). These radical species can either dimerize releasing CO_2 or disproportionate yielding CO_2 and $CO_2^{\bullet-}$ via reaction pathways (73) and (74), respectively (Ershov, Janata, Alam, & Gordeev, 2008; Garcia-segura & Brillas, 2011; Sá, 2015).

$$^\bullet OH + {}^-OOC\text{-}COOH \rightarrow {}^\bullet OOC\text{-}COOH + OH^- \qquad k = 5.0 \times 10^7\ M^{-1}\ s^{-1} \qquad (72)$$

$$2\ {}^\bullet OOC\text{-}COO^- \rightarrow {}^-OOC\text{-}COO^- + 2\ CO_2 \qquad k = 5.0 \times 10^8\ M^{-1}\ s^{-1} \qquad (73)$$

$$^\bullet OOC\text{-}COO^- \rightarrow CO_2 + CO_2^{\bullet-} \qquad k = 2 \times 10^6\ s^{-1} \qquad (74)$$

Formation of $CO_2^{\bullet-}$ radical as a reducing mediator is considerably slower from oxalic acid than from formic acid. Furthermore, the generated CO_2 from oxidation of oxalic acid, which yields more CO_2 than oxidation of formic acid under similar conditions, increases the CO_2 dissolution by forming carbonic acid as summarized in reaction (75). The dissociation of carbonic acid yields bicarbonate and carbonate anions from reactions (76) and (77), which can compete with $CO_2^{\bullet-}$ and N-species sorption on the catalyst surface and have the ability to poison it. Therefore, the demonstrated low nitrate reduction when oxalic acid is used could also be attributed to these processes.

$$CO_2 + H_2O \rightarrow H_2CO_3 \qquad (75)$$

$$H_2CO_3 \leftrightharpoons H^+ + HCO_3^- \qquad pK_{a1} = 3.63 \qquad (76)$$

$$HCO_3^- \leftrightharpoons H^+ + CO_3^{2-} \qquad pK_{a2} = 10.32 \qquad (77)$$

The existing evidence about the behavior of oxalic acid as a sacrificial electron donor hinders future research aimed at exploiting this hole scavenger in developing photocatalytic nitrate reduction systems and suggests the need for examining more efficient donor species such as formic acid.

4.3. Formic acid as a hole scavenger

The most favorable hole scavenger for nitrate reduction is formic acid because of its simple carboxylic acid structure and single-electron direct transfer mechanism that provides the strong reductant $CO_2^{\bullet-}$ as the only product according to reaction (34). However, using formic acid in photocatalytic nitrate reduction has additional benefits. As

a weak acid with $pK_a = 3.75$, formic acid can release H^+ according to equation (56), which represents one of the key factors to drive the NO_3^- conversion pathways towards N_2. When formic acid is used as hole scavenger, the typical initial pH is reported between 2.5 to 3.0 (de Bem Luiz et al., 2012; Kobwittaya & Sirivithayapakorn, 2014; Lozovskii et al., 2009; Ren et al., 2015; D. Sun et al., 2016) (Tables 4-1 to 4-6). The H^+ consumption during the complete reduction to N_2 increases the pH to quasi-natural conditions of pH > 5.0 (K Doudrick et al., 2013; Sá et al., 2009; D. Sun et al., 2016), demonstrating the requirement of protons to attain complete reduction. To maintain a low pH environment, excess formic acid needs to be provided.

The optimal dose for formic acid as a hole scavenger depends on the catalyst, the available catalytic sites (dosage), and the formic ratio respective to nitrate. For pure TiO_2, metal-composite TiO_2, and carbon-doped TiO_2 (Shaban, El, Kh, & Farawati, 2016b), 40 mM formic acid provides optimal results when 100 mg-N L^{-1} of NO_3^- is treated with varied irradiation conditions (Lozovskii et al., 2009; Sá et al., 2009; F. Zhang et al., 2005). Under optimal conditions, 98.4% conversion of nitrate, with > 99% selectivity for nitrogen gases, has been achieved. Bem Luiz et al. (2012) reported that lower formic acid concentrations led to incomplete conversions and decreased selectivity towards N_2, probably because of insufficient reducing mediators ($CO_2^{\bullet-}$) (de Bem Luiz et al., 2012). Interestingly, excess formic acid also reduced N_2 selectivity by increasing NH_4^+ yields by 20 %. The high formic acid:NO_3^- ratios (over 15:1) in these scenarios contribute to saturation of the photocatalyst's surface area and decrease the ratio of N-species at the surface to reductant species. This is due to the higher occupancy of the active sites by the reducing agent (de Bem Luiz et al., 2012; Sá et al., 2009), as depicted in Fig. 4-9a.

Kinetics also appear associated with the formic acid:NO_3^- ratio. Even though conversion of high formic acid concentrations is similar at extended treatment times (cf. Fig. 4-9a), Doudrick et al. (K Doudrick et al., 2013) found that HCOOH concentration affects the kinetic rate constant. As depicted in Fig. 4-9b, the rate constant increases exponentially when the formic acid:NO_3^- ratio increases to ~4.0–5.0 (which corresponds to the observed optimum concentration of 40 mM to treat 100 mg-N L^{-1}). The rate constant, however, decreases when this ratio increases above 5.0. Furthermore, excess scavenger—apart from being counterproductive in terms of selectivity and kinetics—also affects the required operational times of the photocatalytic reductive treatment because the photocatalytic treatment should be extended until complete removal of the hole scavenger.

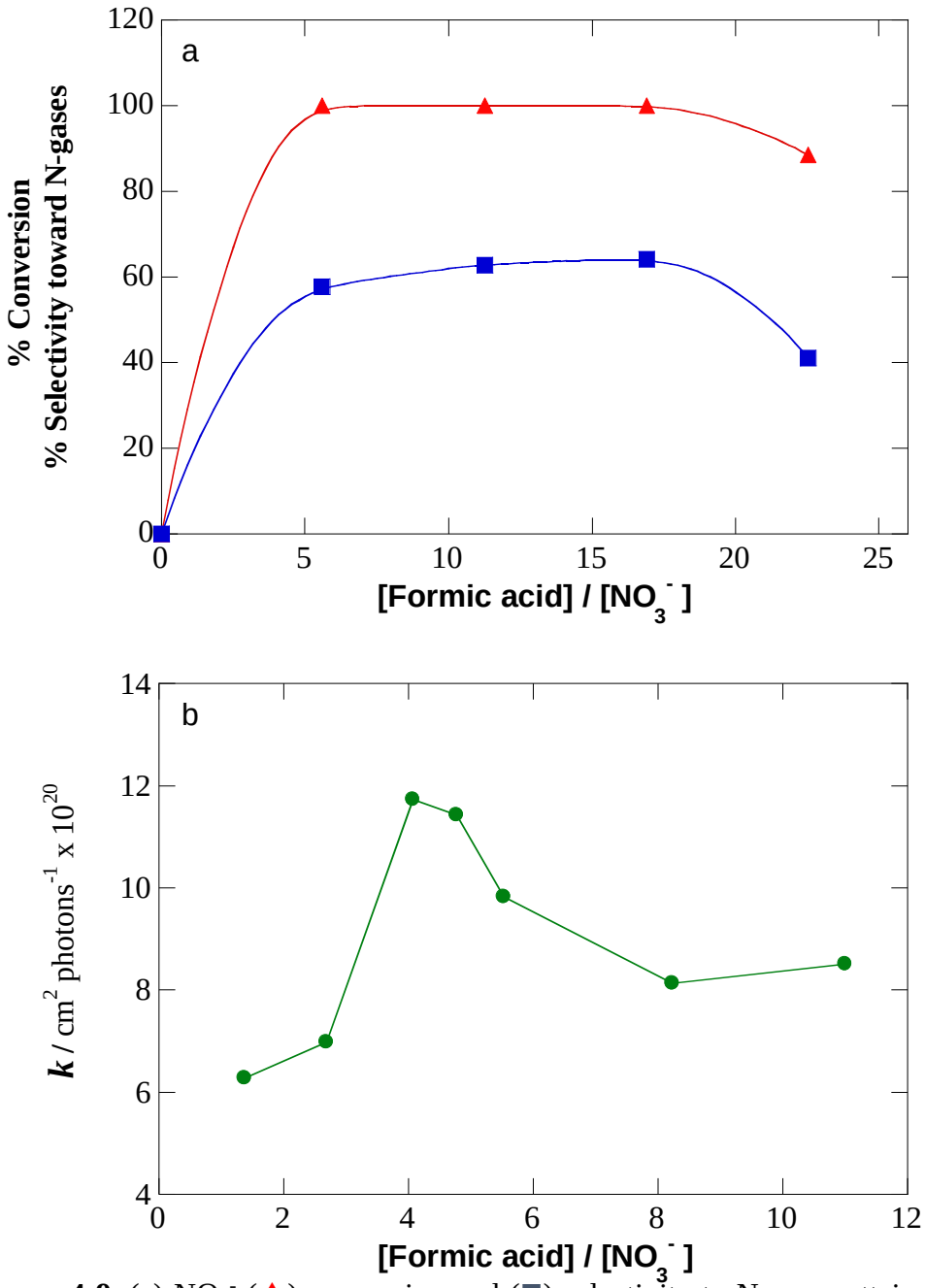

Figure 4-9. (a) NO_3^- (▲) conversion and (■) selectivity to N-gases attained after 3h of treatment of 100 mg-N L^{-1} using a Cu/TiO_2 photocatalyst at different formic acid:nitrate ratios. Readapted from Sá et al. 2009. (b) Variation of the pseudo-first-order rate constant (*k*) for NO_3^- reduction with different formic acid:nitrate ratios during the treatment of 100 mg-N L^{-1} NO_3^- solution using an Ag/TiO_2 photocatalyst. Readapted from Doudrick et al. 2013.

4.4. Other scavengers reported

Methanol, oxalic acid, and formic acid are not the only organic species considered as hole scavengers for nitrate reduction. Alternative hole scavengers also have been explored, although their observed low efficiencies preclude their future uses and investigations.

Ethanol is an attractive alternative to methanol because of its innocuous character. However, Zhang et al. (2005) and Yang et al. (2013) reported lower conversion rates compared to methanol and lower selectivity towards N_2 (Juan Yang et al., 2013; F. Zhang et al., 2005). These results suggest that the increasing the number of carbons in linear alcohols and carboxylic acids is somehow detrimental to the overall reduction process. This undesired effect could be attributed to more complex oxidation mechanism that long carbon chain molecules may have when compared to shorter and simpler molecules such as methanol, which readily release of $CO_2^{\bullet-}$.

Li et al. (L. Li et al., 2010) suggested benzene as hole scavenger. The unusual use of this organic pollutant as a hole-scavenger was considered as a potential scenario for simultaneously treating groundwaters contaminated with multiple common pollutants via photocatalysis: the oxidation of benzene to CO_2 and the reduction of nitrate to N_2. However insufficient nitrate removals of 8.0%, 25.0%, 33.0%, and 66.0% were obtained after 4 h of treatment for TiO_2, Pt/TiO_2, Cu/TiO_2, and $Pt\text{-}Cu/TiO_2$, respectively. Also, the selectivity towards N_2 was low, even though benzene and its by-product phenol were completely degraded within 10 minutes of starting treatment. The formation of phenol as a by-product evidenced that benzene degradation occurs via $^{\bullet}OH$ oxidation mediated pathway (reaction (35)), which could cause potential re-oxidation of NO_2^- and NH_3. Within the same context,

Hirayama et al. (J. Hirayama et al., 2014) conducted similar work using glucose as hole scavenger after considering its availability in waters. However, only 23% NO_3^- reduction was reported using a system combining Pt/TiO_2 and $SnPd/Al_2O_3$ nanoparticles with 75% N_2 selectivity. In contrast, Bems et al. (Bems et al., 1999) considered using humic acids as hole scavenger because their ubiquitous presence in natural water resources, but this achieved only 32% NO_3^- reduction after 76 h of treatment with pristine TiO_2. Nonetheless, their work led to exploring photocatalytic reduction of nitrate in natural waters without the external addition of hole scavengers in exchange for elongating the residence and treatment times.

4.5. Photoelectrocatalytic systems to minimize recombination

An alternative strategy to minimize recombination reaction (30) and enhance the photocatalytic performance is the application of a constant current density (*j*) or defined potential (*E*) through the photocatalyst, which favors the charge carriers' separation by an external electrical circuit (Garcia-Segura & Brillas, 2017). Only a few works have considered this approach of using the catalyst as photo-electrode to enhance photocatalyst performance via electrochemical methods. Wang and Turner (Heli Wang & Turner, 2013) present a short communication demonstrating the enhanced photocatalytic reduction of nitrate using a photocatode of *p*-$GaInP_2$ at E_{cat} = -1.0 V, but they do not identify the released products. A more complete study is reported by Paschoal et al. (Paschoal et al., 2013). The application of E_{cell} = +0.2 V using a Cu/Cu_2O photocathode at pH 7.0 reduces initial NO_3^- by 93% after 75 min with the with a selectivity of 42% NO_2^- and 52% N_2. Therefore, the reduced NO_2^- would likely be further reduced preferentially to N_2 if the treatment duration

is extended. Particularly promising aspects of the photoelectrocatalytic approaches are (i) the good selectivity exhibited at quasi-neutral pH environments and (ii) the great performance exhibited without hole scavenger addition. Note that TiO_2 is not considered a photocathode because the standard potential of e_{cb}^- on TiO_2 surface of -0.14 V vs SHE (Dung et al., 1982; Ward et al., 1983) cannot reduce nitrate as discussed above ($E^o(NO_3^- / {}^\bullet NO_3^{2-}) = -0.89$ V vs SHE). Alternative catalysts such Cu_2O with an e_{cb}^- standard potential of -1.2 V vs SHE can lead to complete nitrate reduction (cf. Fig. 4-6b) (X. Liu, Li, & Yu, 2014; Paschoal et al., 2013). The early results stemming from work with other semiconductor materials encourage further exploration of alternative photoelectrochemical systems.

Section 5: Influence of light sources and spectra outputs on photocatalytic reduction of nitrate

One of the fundamental components of all photocatalytic processes is the irradiation source, which provides the energy required for photoexcitation and generation of charge carriers h^+_{vb}/e^-_{cb} as summarized in reaction (29). The importance of light source selection and optimization has been frequently overlooked in photocatalytic reduction because of the misconception that the light source does not render any influence beyond providing the needed band gap energy for photogeneration of h^+_{vb}/e^-_{cb} in a photocatalyst. However, light source selection may represent the cornerstone element in obtaining effective photocatalytic reduction of nitrate.

As discussed, nitrate undergoes both photocatalytic and photolytic transformations, which could affect by-product selectivity and the overall kinetics. Many irradiance sources

are available for use in photocatalytic systems, and, all of these sources could be parameterized by their light spectra and intensities expressed in terms of photon fluence (photons/cm^2 or Einstein/cm^2) (J. R. Bolton & Stefan, 2002; J Bolton, 2000; M. I. Stefan & Bolton, 2005). These parameters are clearly articulated in the literature (J. R. Bolton & Linden, 2003) and could serve to properly asses light dose and energy efficiency.

The main irradiation sources used in photocatalytic treatments are low-pressure Hg lamps, medium-pressure Hg lamps, and high-pressure Hg lamps. However, the use of Xe lamps or even natural sunlight irradiation has been considered for doped photocatalyst with narrower band gaps. Figure 4-10 depicts the characteristic electromagnetic emission spectra of each irradiation source. Sources emitting within the ranges of 270–330 nm and 200–400 nm where photolysis of NO_3^- and NO_2^- can occur, respectively, are of particular interest in photocatalytic reduction of nitrate (cf. Fig. 4-3).

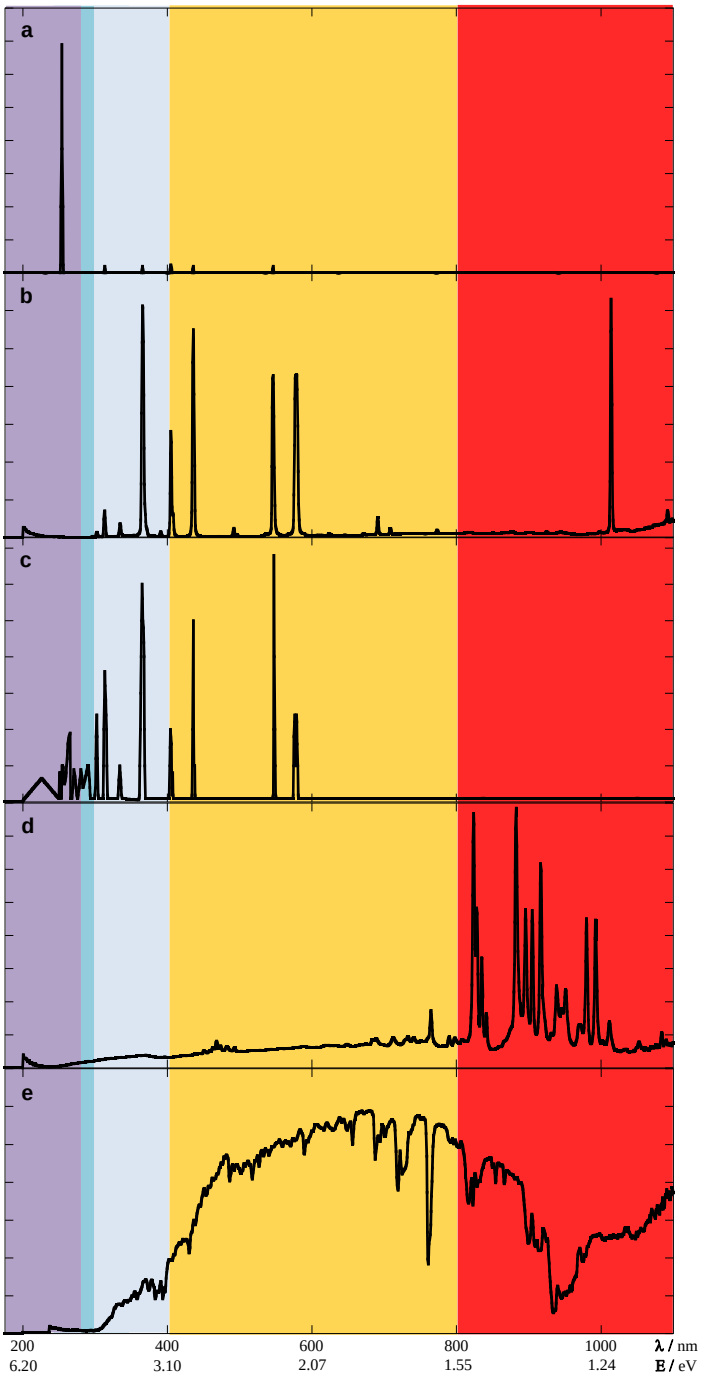

Figure 4-10. Overlay of light source irradiance spectra with electromagnetic spectrum for: (a) low-pressure Hg lamp, (b) medium-pressure Hg lamp, (c) high-pressure Hg lamp, (d) xenon lamp, and (e) natural sunlight. From left to right the colors corresponds to ■ UV-C, ■ UV-B, ■ UV-A, ■ visible light and ■ IR spectrum.

The low-pressure Hg lamp has a distinctive peak at 254 nm (Figure 4-10a) and is most commonly employed for UV disinfection processes. Under this irradiation, nitrate

and nitrite are photolytically active with $\Phi_{254nm} \approx 0.17$ (Mack & Bolton, 1999b) and $\Phi_{254nm} \approx 0.02$ (Sharpless & Linden, 2005), respectively. However, due to the short wavelength output of low-pressure Hg lamps, a high energy input (E= 4.88 eV/photon) is required to produce photons at $\lambda = 254$ nm.

Medium-pressure Hg lamps have become more prominent in the photocatalytic research literature because of their broader polychromatic UV emission compared to low-pressure Hg sources (Figure 10b). However, the visible and infrared wavelengths can reduce photocatalytic efficiency because those photons do not produce photoexcitation even though energy is consumed for their production. Medium-pressure lamps, due to their broader effective UV spectrum range, can target both photocatalytic and photolytic pathways for both nitrate and nitrite reduction. The predominant peak at λ=355 nm has high photolytic quantum yield for nitrite and HNO_2, but it is outside the photolytic window for nitrate photolysis, which is λ<315 nm (Bilski et al., 1992; Mack & Bolton, 1999b) (cf. Fig. 4-3).

High-pressure Hg lamps are the most popular source of irradiance, encompassing about 60% of the reports related to photocatalytic reduction of nitrate. As can be seen in Fig. 4-10c, high-pressure Hg lamps exhibit the highest overall peak density in the UV-spectrum. The majority of photons produced by these lamps are in the UV-A and UV-B spectrum regions, which are sufficient for photocatalytic excitation. A smaller number of photons are emitted in UV-C wavelengths that would promote photolytic reactions of nitrate and nitrite in solution. Key peaks at 302 nm and 313 nm and a broader output between 220–250 nm are beneficial to nitrate reduction, wherein quantum yields are between 0.01 and 0.17 (Mack & Bolton, 1999b). Even though high-pressure lamps are the

most commonly used in photocatalytic processes, their additional photonic benefits have largely been understated in the present literature, leading to inadequate understanding of photolytic synergies beyond photoexcitation of photocatalysts alone.

Xenon irradiance sources and solar light similarly offer disproportionately high fluence of sub-band gap photons (for TiO_2, E_{bg} = 3.25). While these sources have been utilized with some success for nitrate reduction, their photonic efficiency remains quite low because of their significant photon production in the visible and infrared part of the spectrum. Xenon lamps produce broad band irradiation from the UV-C through UV-A wavelength range (Figure 4-10d), which means that photolytic processes may be activated via xenon irradiance sources. Few studies utilize the solar spectrum due to the complexity of engineering light delivery in a scalable reactor design; however, the broad inclusion of UV-A and visible light (Figure 4-10e) allows for employing short band gap photocatalysts for nitrate reduction. The use of natural sunlight has the potential to drastically reduce operational costs and highlights the environmentally-friendly potential of photocatalytic processes from the perspective of using renewable energy sources. Due to the low intensity (<4%) of UV light in the solar spectrum, the likelihood of photolytic activity for nitrogen oxyanions is minimal.

Varying the lamp power changes the radiant flus or irradiance, but it does not change the characteristic emission spectrum. For example, a 100 W high-pressure Hg lamp would be expected to produce intensity about 4-fold lower than a 400 W high-pressure Hg lamp, but both would emit with the characteristic spectrum shown in Figure 4-10c. A minimum fluence rate (photons cm^{-2} s^{-1}) is required to activate the photocatalytic process. Insufficient light hinders radical formation and reductive processes on the photocatalyst

surface, while surplus light diminishes efficiency because photonic saturation reduces the proportion of photons that successfully promote one electron to the empty conductive band (reaction (29)). Therefore, similar conversions can be attained at similar treatment times over certain wattages. However, higher wattage lamps lead to higher energy consumptions.

By accounting for the energy per photon at each wavelength emitted by a light source, widely disparate irradiance sources may be compared directly by assessing the energy emission via the Planck-Einstein relationship (78):

$$E = \frac{hc}{\lambda} \tag{78}$$

where E is the energy per photon of light at the specific wavelength λ in eV; λ is the wavelength; the product of hc corresponds to 1240 eV nm with h being the Planck's constant (6.62×10^{-34} m^2 kg s^{-1}), and c is the speed of light in vacuum (3.00×10^8 m s^{-1}).

Consequently, a combination of spectrum and intensity, well-represented by the photon fluence, could be a meaningful representation of the contribution of light to the photocatalytic reduction of nitrate. Unfortunately, the existing reports do not present a standardized expression of the irradiance results, which makes cross-comparison difficult. For example, studies reporting the use of a composite Ag/TiO_2 photocatalyst and formic acid hole-scavenger have used low-, medium-, and high-pressure Hg lamps as well as black light bulbs and xenon lamps for nitrate reduction (K Doudrick et al., 2013; Kobwittaya & Sirivithayapakorn, 2014; Lozovskii et al., 2009; D. Sun et al., 2016; F. Zhang et al., 2005). Literature reports nitrate removal following the trend: high-pressure Hg > medium-pressure Hg > low-pressure Hg > xenon > black light (UV-A); and these results span from

71% to 100% reduction of nitrate. In contrast, selectivity for nitrogen gases, which can range from 88% to 100%, follows a different trend: low-pressure Hg > black light (UV-A) > high-pressure Hg > xenon > medium-pressure Hg. However, these results are not normalized to fluence because this information is frequently omitted in the reports, which renders the published results incomparable.

The effect of light source in nitrate reduction has largely been ignored, but from the available data analysis, reported variables confound trends. Information gaps and inconsistencies exist related to (i) reported intensity of light source (wattage), (ii) published data on fluence only reported in three articles to-date (K Doudrick et al., 2013; Marks, Yang, Westerhoff, & Doudrick, 2016; T. Yang et al., 2013), and (iii) great diversity of utilized semiconductors and composites (Ketir, Bouguelia, & Trari, 2009; Mohamed & Baeissa, 2014; Oka, Miseki, Saito, & Kudo, 2015; R. Wang et al., 2015; Y. Wang, Yang, Gao, Cong, & Yang, 2014). To illustrate, the radiant intensity of sources reported in the literature varies extensively from one experimental setup to another, and the photonic fluence the lamps is seldomly reported. The lamp powers could vary from 8 W (Lozovskii et al., 2009) for a low-pressure Hg lamp to 500 W for a xenon lamp (Mori, Suzuki, Fujimoto, Watanabe, & Hasegawa, 2000). The wide variation eliminates the possibility of comparing the data. Therefore, normalizing the future reported findings to photon fluence becomes imperative to compare results across diverse experimental conditions, reactor designs, and light sources.

While photocatalytic pathways have the ability to improve nitrate conversion rates, the direct energy absorption by the anionic species (see Fig. 4-3) could lead to direct photolysis, which competes with the absorption of photons by the photocatalysts.

Consequently, the photon absorption by the anionic nitrogen species has the potential to reduce the efficient conversion of photons into charge carriers when light sources that could induce photolysis are used. These factors modify the electrical energy per order (EE/O) and the overall photonic efficiency of a photocatalytic system related to the quantum efficiency for nitrate photocatalytic reduction. Both are relevant parameters scientifically and to engineered applications. To make these systems more competitive from a light-based perspective, careful assessment of light-catalyst-contaminant interactions must be conducted.

Section 6: Competitive oxidation reactions of inorganic nitrogen species

As discussed previously, to propagate the reactions, both photogenerated charge carriers (h^+_{vb} and e^-_{cv}) must undergo redox processes in which h^+_{vb} scavengers play a crucial role. Un-scavenged species, such as h^+_{vb}, or reactive oxygen species, such as $^{\bullet}OH$ or $HO_2^{\bullet}$, could propagate re-oxidation of the main ionic products NO_2^- and NH_4^+ via a series of parallel reactions. Consequently, understanding these parallel reactions is critical to developing an efficient photocatalytic system because they could undermine the overall photo-reduction efficiency.

6.1. Photocatalytic reactions involving NH_4^+

Photocatalytic oxidation could contribute to selective removal of ammonium via innocuous N_2 generation pathway. However, different parallel pathways could lead to NO_2^- and NO_3^- as end-products. The pH plays a key role in directing a photocatalytic ammonium oxidation pathway because it affects ammonium speciation (pKa = 9.25) as illustrated by

its acid-base equilibria described by reaction (56). Adapted from Bonsen et al. (1997), Fig. 4-11 depicts ammonia removal after 6 h of photocatalytically treating 5 x 10^{-4} mol L^{-1} of NH_4Cl at different pH-controlled NH_4^+/NH_3 distributions (Bonsen, Schroeter, Jacobs, & Broekaert, 1997). As reported, no significant degradation is observed at pH< 7.0 (Murgia, Poletti, & Selvaggi, 2005b; H.-H. Ou, Liao, Liou, Hong, & Lo, 2008; Pollema, Milosavljevi, Hendrix, Soluji, & Nelson, 1992b; Zhu et al., 2005), which questions the reactivity of NH_4^+ and its role in the photocatalytic oxidation. In fact, similar conclusions could be deduced from the experimentally determined rate constants for $^{\bullet}OH$ reaction with NH_3 (k = of 10^8 M^{-1} s^{-1}) and NH_4^+ (non-quantifiable k) (Neta, Maruthamuthu, Carton, & Fessenden, 1978; Nilsson, Christensen, Pagsberg, & Nielsen, 1971). Furthermore, Zhu et al. (2005) proved that the adsorption of cationic NH_4^+ on the negatively charged surface of TiO_2 catalyst (pH_{pzc} = 6.2) does not influence the NH_4^+/NH_3 oxidation rate (Zhu et al., 2005). A plot of available NH_3 according to the equilibria reaction (56) demonstrates that the data at different initial pH converge in a single data series fitting with Langmuir-Hinshelwood adsorption model. The increasing rates of NH_4^+/NH_3 photocatalytic oxidation with increasing pH should be explained by the pH-dependent equilibrium (56) and not the pH-dependent electrostatic attraction between NH_4^+ and the negatively-charged TiO_2 surface. In conclusion, these results validate the negligible contribution of NH_4^+ in photocatalytic oxidation. This conclusion is highly relevant because several authors suggest N_2 released during the catalytic reduction of nitrate is produced from ammonia oxidation (de Bem Luiz et al., 2014; Oka et al., 2015; Wehbe et al., 2009), which is incorrect according to the discussed results.

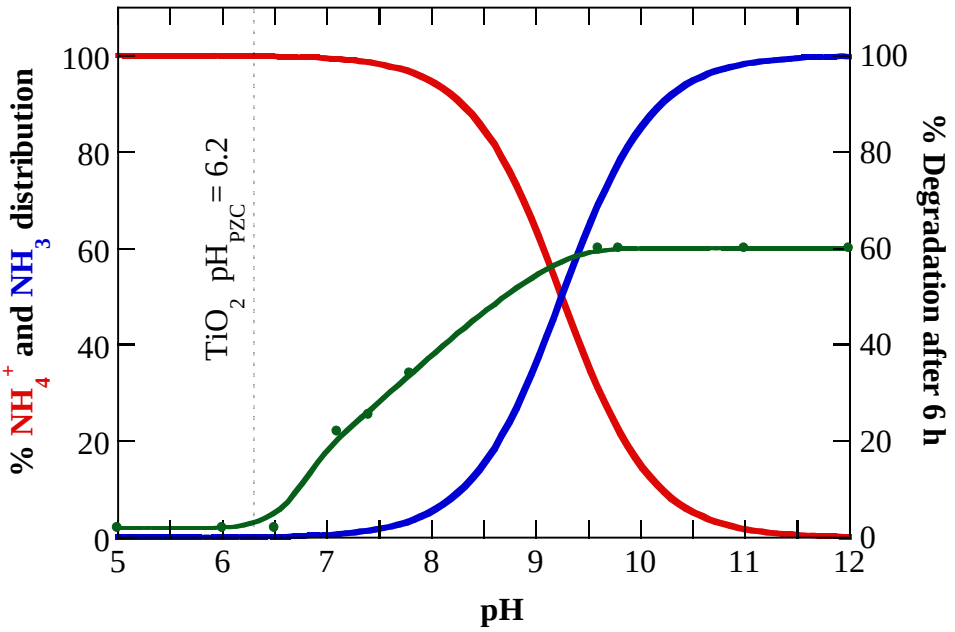

Figure 4-11. Speciation of NH_4^+/NH_3 as a function of the pH, and (●) the percentage of degradation attained after 6 h of treatment of 0.5 mM of NH_4^+ with TiO_2. Readapted from Bonsen et al. 1997.

By using selective hole scavengers, Wang et al. (2014) demonstrated the role of $^{\bullet}OH$ radicals during photocatalytic NH_3 degradation, where NH_3 conversion was reduced 25% by competitors(Hua Wang et al., 2014). Even though h^+_{vb} is primarily engaged in harvesting the sacrificial electrons, both species (h^+_{vb} and $^{\bullet}OH$) play an active role in the ammonia degradation pathways that yield NO_2^-, NO_3^-, and N_2, as main products. As described above, the first step in photocatalytic degradation is adsorption of the target pollutant, NH_3, according to expression (79). The first oxidation reaction of $NH_{3(ad)}$, occurs by h^+_{vb} or $^{\bullet}OH$ and corresponds to the formation of $^{\bullet}NH_2$ radical via reactions (80) and (81), respectively (Hickel & Sehested, 1992; Hua Wang et al., 2014; Yamazoe, Okumura, Hitomi, Shishido, & Tanaka, 2007). The highly reactive $^{\bullet}NH_2$ reacts rapidly with water (reaction (82)) or $^{\bullet}OH$ (reaction (83)) yielding NH_2OH as the main product, which is a

common intermediate found in biological nitrification. The subsequent oxidation of NH_2OH by h^+_{vb} or $^\bullet OH$ yields hydroxylamine radical ($^\bullet NHOH$) following reactions (84) and (85), respectively (Simic & Hayon, 1971).

$$NH_{3aq} \rightarrow NH_{3ad} \quad (79)$$

$$NH_{3ad} + h^+_{VB} \rightarrow {}^\bullet NH_2 + H^+ \qquad k = \text{n.a.} \quad (80)$$

$$NH_{3ad} + {}^\bullet OH \rightarrow {}^\bullet NH_2 + H_2O \qquad k = 9.7 \times 10^7\ M^{-1}\ s^{-1} \quad (81)$$

$$^\bullet NH_2 + H_2O \rightarrow NH_2OH_{(ad)} + H^+ \qquad k = \text{n.a.} \quad (82)$$

$$^\bullet NH_2 + {}^\bullet OH \rightarrow NH_2OH_{(ad)} \qquad k = \text{n.a.} \quad (83)$$

$$NH_2OH + h^+_{VB} \rightarrow {}^\bullet NHOH_{(ad)} + H^+ \qquad k = \text{n.a.} \quad (84)$$

$$NH_2OH + {}^\bullet OH \rightarrow {}^\bullet NHOH_{(ad)} + H^+ \qquad k = 9.5 \times 10^9\ M^{-1}\ s^{-1} \quad (85)$$

Upon formation of $^\bullet NHOH$ radical intermediate, both NO_2^- and NO_3^- species can be yielded. According to Wang et al. (2014), oxidation of $^\bullet NHOH$ by dissolved O_2 occurs via reaction (86), which yields a product that is further reacted with hydroxyl anion in alkaline environment to produce NO_2^- according to reaction (87). NO_2^- then oxidizes to NO_3^- following reaction (88), which stems from reactions started by reaction (19).

$$^\bullet NHOH + O_2(aq) \rightarrow {}^\bullet O_2NHOH \qquad k = \text{n.a.} \quad (86)$$

$$^\bullet O_2NHOH + OH^- \rightarrow NO_2\text{-} + H_2O + {}^\bullet OH \qquad k = \text{n.a.} \quad (87)$$

$$NO_2^- + {}^\bullet OH \rightarrow NO_3^- + H^+ \qquad k = \text{n.a.} \quad (88)$$

An alternative pathway scenario, which is highly plausible without the generation of hydroxylamine, could be also considered (Yamazoe et al., 2007). In this scenario, $^{\bullet}NH_2$ radical reacts with $O_2^{\bullet-}$ (reaction (21)), releasing nitric oxide anion (NO^-) (reaction (89)) that could be easily oxidized by oxygen to NO_2^- and NO_3^- as described by reactions (90) and (91):

$$^{\bullet}NH_2 + O_2^{\bullet-} \rightarrow NO^- + H_2O \qquad k = \text{n.a.} \qquad (89)$$

$$2NO^- + O_2 \rightarrow 2\ NO_2^- \qquad k = \text{n.a.} \qquad (90)$$

$$NO^- + O_2 \rightarrow NO_3^- \qquad k = 5.7 \times 10^7\ M^{-1}\ s^{-1} \qquad (91)$$

Bonsen et al. (1997) corroborated the above pathways (89) to (91) by reporting lower yields for NO_2^- and NO_3^- in absence of O_2 after bubbling N_2 gas. Similar results were observed by Lee et al. (2002), who demonstrated higher NO_2^- and NO_3^- yields in presence of O_2 (Jaesang Lee, Park, & Choi, 2002a). However, these findings also indirectly confirm the existence of an alternative pathway yielding nitrogen oxyanions without the O_2 requirement. This was suggested by Pollema et al. (1992) and is described with reactions (92) and (93) as an alternative to the preferred pathway in presence of oxygen that is described in reaction (94) (Murgia et al., 2005b).

$$NH_3 + 2\ H_2O + 6\ h^+_{VB} \rightarrow NO_2^- + 7H^+ \qquad (92)$$

$$NO_2^- + H_2O + 2\ h^+_{VB} \rightarrow NO_3^- + 2H^+ \qquad (93)$$

$$NH_3 + O_2 + 2\ h^+_{VB} \rightarrow NO_2^- + 7H^+ \qquad (94)$$

In contrast, the evolution of N_2 on pure photocatalysts is considered to be associated with $^{\bullet}NH_2$ radical dimerization (reaction (95)), which releases hydrazine (N_2H_4). Hydrazine is further oxidized by the holes to produce N_2 according to reaction (96) (Yamazoe et al., 2007).

$$2\ {}^{\bullet}NH_2 \rightarrow N_2H_4 \qquad k = \text{n.a.} \qquad (95)$$

$$N_2H_4 + 4\ h^+_{VB} \rightarrow N_2 + 4H^+ \qquad k = \text{n.a.} \qquad (96)$$

Unfortunately, reaction (96) has a low quantum yield with negligible conversion rates when pure semiconductors are used as photocatalysts, as deduced from Table 4-7. Consequently, the reaction selectivity leads to preferential formation of oxyanions as final products of the photocatalytic NH_3 oxidation by pure semiconductors (H.-H. Ou et al., 2008). The N-loss is attributed to N_2 formation, but because the N-loss could be also attributed to NH_3 volatilization, the actual contribution of this pathway to the overall photocatalytic oxidation of NH_3 remains unclear. The N-loss due to NH_3 volatilization could be significant as demonstrated by Luo et al. (2015) who reported 20% NH_3 removal in absence of catalyst after 5 h under stirring (Luo et al., 2015a). Note that NH_3 could evaporate during photocatalytic treatment because of temperature increases due to (i) constant irradiation, (ii) photocatalyst heating from recombination reactions, and (iii) continuous stirring. Furthermore, the NH_3 loss via evaporation becomes more prominent at higher alkaline pH and larger initial NH_3 concentrations, as summarized in Table 4-7. Conducting complete nitrogen mass balance, which include N_2 analysis, becomes an imperative in ascertaining formation of all final product species during photocatalytic

oxidation of NH_3, as demonstrated by Shavisi et al (2014) (Shavisi, Sharifnia, Hosseini, & Khadivi, 2014). Therefore, evolution of N_2 during the photocatalytic treatment of NH_3 rarely occurs if it is not catalyzed by a noble metal co-catalyst.

Enhanced selectivity towards N_2 evolution from NH_4^+ photocatalytic oxidation has been observed in TiO_2 composites with noble metals, such Au/TiO_2 or Pt/TiO_2. Gerischer and Mauerer (1970) proposed that noble metals contribute to stabilization of active intermediate NH_x species (Gerischer & Mauerer, 1970). As described by reaction (97), the $^{\bullet}NH_2$ adsorbed on Pt or Au surface can undergo additional oxidation, forming NH^- anion (NH^-), which could further be oxidized to an adsorbed N atom via reaction (98) reaction. These so-called NH_x species, where *x* and *y* are equal to 0, 1, or 2, are highly reactive and lead to different intermediate species N_2H_x as described by equation (99). N_2H_x species easily decompose to form N_2 as illustrated with equation (100). The final step is desorption and evolution of N_2 (101) (K. Lee, Ku, & Pak, 2016).

$$^{\bullet}NH_{2(ad\text{-}Pt)} + {}^{\bullet}OH\ (h^+_{vb}) \rightarrow NH^-_{(ad\text{-}Pt)} + H_2O\ (H^+) \quad (97)$$

$$NH^-_{(ad\text{-}Pt)} + {}^{\bullet}OH\ (h^+_{vb}) \rightarrow N_{(ad\text{-}Pt)} + H_2O\ (H^+) \quad (98)$$

$$NH_{x(ad\text{-}Pt)} + NH_{y(ad\text{-}Pt)} \rightarrow N_2H_{x+y(ad\text{-}Pt)} \quad (x,y = 0,1,2,) \quad (99)$$

$$N_2H_{x+y(ad\text{-}Pt)} + (x+y)\ h^+_{vb} \rightarrow N_{2(ad\text{-}Pt)} + (x+y)\ H^+ \quad (100)$$

$$N_{2(ad\text{-}Pt)} \rightarrow N_{2(g)}\uparrow \quad (101)$$

Lee et al. (2002) reported an interesting study where the selectivity of pure TiO_2 photocatalyst was compared to Au/TiO_2 and Pt/TiO_2 0.2 wt% nanoparticles containing composites (Jaesang Lee et al., 2002a). As can be seen in Table 4-7, the selectivity towards

N_2 generation increases from 10% for pure TiO_2 to 30% for Au/TiO_2 with similar NH_3 conversion scenarios of ~20%. When Pt/TiO_2 composite is introduced under comparable conditions, selectivity increases to 65%, and photocatalytic conversion is enhanced, attaining a 65% oxidation of initial 0.1 mM of NH_3.

Fundamental studies related to photocatalytic oxidation of NH_3 are mainly conducted in model water matrices and in absence of significant interferences from other co-pollutants, which must be considered if the system is to be employed in realistic conditions. Zhu et al. 2008 and Vohra et al. 2010 conducted their studies in presence of co-pollutants in greywater and simulated wastewater, respectively. Zhu et al. 2008 noted that surfactants and monosaccharides could diminish NH_4^+/NH_3 photocatalytic degradation by 50–90% at pH 10.1. Hydroxyl radical scavenging by organics contributed to 80% performance reduction when compared to pure-water conditions (Zhu, Nanny, & Butler, 2008). However, TiO_2 photocatalysis was able to remediate surfactants, monosaccharides, and ammonia through production of hydroxyl radicals, although at a >50% slower rate than pristine compound kinetics. This research effort demonstrated that applications for photo-catalytically treating greywater remain promising, provided that sufficient irradiation and surface adsorption sites are available for the reactions to occur. Similarly, Vohra et al (2010) demonstrated in realistic conditions that TiO_2 adsorption is less dominant than the pH-dependent speciation for NH_4^+/NH_3 oxidation (Vohra, Selimuzzaman, & Al-Suwaiyan, 2010). In the presence of other co-pollutants, optimal pH in their study shifted from pH 12 (NH_4^+/NH_3 alone) to pH 10 for both binary and ternary systems of NH_4^+/NH_3 with $S_2O_3^{2-}$ and $S_2O_3^{2-}$ /*p*-Cresol, respectively.

Table 4-7. Ammonia conversion and products selectivity during photocatalytic oxidation.

Catalyst	$[NH_3]_0$ / mM	pH	Time / min	Conversion / %	Selectivity / %			References
					NO_2^-	NO_3^-	N loss	
TiO_2	5.8 x 10^{-4}	9.1	120	100	0	54.3	-	(Pollema, Milosavljevi, Hendrix, Soluji, & Nelson, 1992a)
TiO_2	0.1	11.5	3600	100	81.0	19.0	-	(A. Wang, Edwards, & Davies, 1994a)
TiO_2	0.1	10.2	360	98	0	95.0	5.0	(Zhu et al., 2005)
TiO_2	0.5	9.9	360	44.7	12.5	80.7	6.8	(Bonsen et al., 1997)
TiO_2	1.5	10.7	1440	50	41.9	36.4	21.7	(Murgia, Poletti, & Selvaggi, 2005a)
TiO_2 nanotubes	0.6	10	360	40	15.0	42.0	43.0	(H. Ou & Liao, 2008)
TiO_2	0.1	10	120	18	30.0	60.0	10.0	(Jaesang Lee, Park, & Choi, 2002b)
Au/TiO_2	0.1	10	120	18	50.0	10.0	40.0	(Jaesang Lee et al., 2002b)
Pt/TiO_2	0.1	10	120	65	20.0	15.0	65.0	(Jaesang Lee et al., 2002b)
Pt/TiO_2	7	10	360	85	10.0	55.0	35.0	(Altomare et al., 2015)
$La/Fe/TiO_2$	6	10	360	50	5.0	25.0	20.0	(Luo et al., 2015b)

6.2. Photocatalytic reactions involving NO_2^-

Even though the role of different oxidant species (holes, free hydroxyl radicals, or adsorbed hydroxyl radicals) in photocatalysis is still not explained well for all model pollutants, experimental evidence was presented in the early 1990s by demonstrating nitrite is not directly oxidized by photogenerated h^+_{vb} (reaction (29)), but that the pathway is mediated by $^\bullet$OH formed through water oxidation in reaction (35) (Milis & Domenech, 1993; Milis, Peral, & Domenech, 1994a). A mechanistic pathway for nitrite photocatalysis is presented where equations (102) and (103) involve forming several radical intermediate species through elementary steps. Specifically, the oxidation of nitrite by $^\bullet$OH radical leads to $HNO_3^{\bullet-}$ radical formation via reaction (102) (Navio et al., 1998). $HNO_3^{\bullet-}$ radical species are in acid equilibria (103) with their conjugate $(NO_3^\bullet)^{2-}$ bases (Gonzalez & Braun, 1995).

$$NO_2^- + {}^\bullet OH \rightarrow HNO_3^{\bullet-} \qquad k = 2.5 \times 10^9\ M^{-1}\ s^{-1} \qquad (102)$$

$$HNO_3^{\bullet-} \leftrightharpoons H^+ + (NO_3^\bullet)^{2-} \qquad k = 16\ s^{-1} \qquad (103)$$

Following reaction (103), two different pathways are possible. The first pathway involves $(NO_3^\bullet)^{2-}$ radicals reacting with dissolved oxygen to directly yield NO_3^- as illustrated in reaction (104). This reaction reaffirms the improved nitrite oxidation results that are observed when oxygen is bubbled.

$$(NO_3^\bullet)^{2-} + O_2 \rightarrow NO_3^- + O_2^{\bullet-} \qquad k = 1.6 \times 10^8\ M^{-1}\ s^{-1} \qquad (104)$$

The second pathway involves release of $NO_2^{\bullet}$ either from $HNO_3^{\bullet-}$ dissociation by reaction (105) or by $(NO_3^{\bullet})^{2-}$ radical reaction with water by reaction (106). This is coincident with the overall reaction (19) described for nitrite photolysis.

$$HNO_3^{\bullet-} \rightarrow NO_2^{\bullet} + OH^- \qquad k = 2.3 \times 10^5\ M^{-1}\ s^{-1} \qquad (105)$$

$$(NO_3^{\bullet})^{2-} + H_2O \rightarrow NO_2^{\bullet} + 2OH^- \qquad k = 5.5 \times 10^4\ M^{-1}\ s^{-1} \qquad (106)$$

Once $NO_2^{\bullet}$ radicals are produced, they dimerize and form N_2O_4 according to reaction (9), which rapidly decomposes to release NO_2^- and NO_3^- according to reaction (10) (Botta, Navio, Hidalgo, Restrepo, & Litter, 1999; Shifu & Gengyu, 2002). Additionally, $NO_2^{\bullet}$ could further react with $^{\bullet}OH$ to form peroxynitrous acid (reaction (11)) that could quickly isomerize to NO_3^- (reaction (14)).

Table 4-8 summarizes the findings related to photocatalytic oxidation of nitrite. High selectivity of the process forming nitrate can be observed. Although nitrate is less hazardous than NO_2^-, it remains an undesired product. Understanding the factors affecting catalytic oxidation is of high interest because nitrite is a key intermediate species in photocatalytic oxidation of ammonia. For TiO_2, the optimal oxidation to nitrate is achieved at pH values close to the TiO_2 pH_{pzc}, and the pH could dramatically affect the mass transport kinetics and practically inhibit it.

Table 4-8. Nitrite conversion and products selectivity during photocatalytic oxidation.

Catalyst	**$[NO_2^-]_0$ / mM**	**pH**	**time / min**	**Conversion / %**	**Selectivity / %**		**References**
					NO_3^-	**N loss**	
TiO_2	0.1	5.0	120	100	100 (with air) 56.7 (without air)	0	(Shifu & Gengyu, 2002)
Cr-TiO_2 photoanode (1.2 V)	0.2	6.2	180	90	100	0	(Shi, Leng, Zhu, Zhang, & Cao, 2006)
Fe-Doped TiO_2	0.2	6.5	30	100	100	0	(Milis, Peral, & Domenech, 1994b)
WO_3 (1.3 V)	0.1	6.3	180	50	100	0	(Cheng & Leng, 2007)
Zn-WO_3 (1.3 V)	0.1	6.3	180	75	100	0	(Cheng & Leng, 2007)

It has been observed, even during the photocatalytic oxidation of NH_3, that the photocatalytic oxidation of nitrite does not occur at highly alkaline pH (Luo et al., 2015a; A. Wang, Edwards, & Davies, 1994b). Milis et al. (1994) reported a seven-fold decrease in the initial reaction rate when the pH increased from 5.7 to 9.5. Nitrite speciation, which is pH dependent (17) via its acid-base equilibria (pKa = 3.40), plays an important role because photocatalytic oxidation can be achieved only for nitrite that is sorbed on the surface of a photocatalyst.

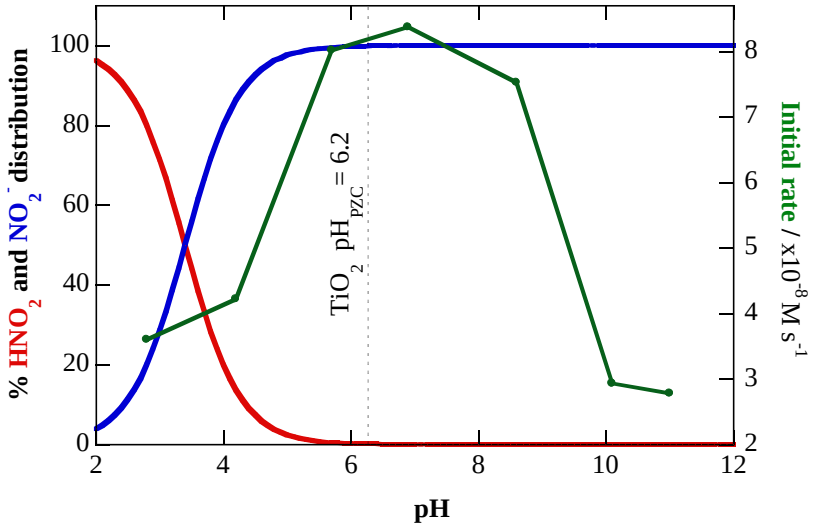

Figure 4-12. Speciation of HNO_2/NO_2^- as a function of pH, and (●) the initial rate determined during the treatment of 0.18 mM of NO_2^- with TiO_2. Readapted from Zhu et al. 2005.

Fig. 4-12 depicts the pH-dependent speciation of HNO_2/NO_2^- and the corresponding rate constants (Zhu et al., 2005). The rate increases below the pH_{pzc} with the increase of NO_2^- due to the favored adsorption of the negatively charged anion on the positively charged surface of TiO_2 in the case discussed. The electrostatic repulsion between the anion and the negatively charged surface of TiO_2 over the pH_{pzc} can explain the dramatic decrease on the oxidation kinetics of nitrite at alkaline pH (Milis et al., 1994a). However, Zhu et al. (2005) noted additional factors contributing to the kinetic decrease. As suggested by Bravo et al. (1993), the competitive adsorption of OH^- could probably inhibit the adsorption of other species under highly alkaline conditions (Bravo, Garcia, Domenech, & Peral, 1993). However, it must not be neglected that the rate of other elementary steps could also be affected by pH (Zhu et al., 2005).

Section 7: Photocatalytic reduction of nitrate in real water matrices

The photocatalytic reduction of nitrate has been predominantly studied in model water matrices without competing species; however, some available studies report nitrate reduction in natural and more complex water matrices including high salinity, other anionic species, and mixed organic constituents collected in Table 409. The presence of species in solution that competitively react with the h_{vb}^{+}, e_{cb}^{-}, or redox mediators could significantly affect performances as well as the competitive adsorption on catalytic sites. Presence of competitive species appears to slow down reaction kinetics by an order of magnitude (Kyle Doudrick et al., 2012; T. Yang et al., 2013). Fortunately, selectivity remains high for nitrogen gases in most cases.

The most significant anionic competitors identified are sulfate (SO_4^{2-}) and carbonate (CO_3^{2-}) species (F. Zhang et al., 2005). These anionic species could competitively adsorb on the photocatalyst surface due to their higher anionic charge when compared to nitrogen oxyanions and conventional hole scavengers (e.g., formic or oxalic acid). Kominami et al. (2005) reported complete suppression of nitrate reduction in the presence of high CO_3^{2-}, which has the ability to poison a photocatalyst (Kominami, Nakaseko, Shimada, Furusho, Inoue, et al., 2005). However, CO_2 stripping could completely recover the catalyst. In addition to photocatalyst inhibition, SO_4^{2-} has been reported to contribute to photo-aggregation of TiO_2 nanoparticles (Y. Shih, Zhuang, Peng, Lin, & Tseng, 2012), which reduces the catalyst's effective surface area and, consequently, its photocatalytic performance.

Table 4-9. Nitrate conversion and products selectivity during photocatalytic reduction treatment of actual matrices.

Reactor Configuration	Matrix Components	Applied Photon Dose	Nitrate Removal	Selectivity toward N_g	Ref.
125W high-pressure Hg, 250mL, Ag/TiO_2 [PD], 30 min, HCOOH	Separate comparison of 100mg/L Na_2SO_4, Na_2CO_3, $NaHCO_3$	-NR-	None: 98% Na_2SO_4: 30% Na_2CO_3: 27% $NaHCO_3$: 85%	None: 100% N_g Na_2SO_4: 83% N_g Na_2CO_3: 82% N_g $NaHCO_3$: 82% N_g	1
17W low pressure Hg, 2.7L, Zn/TiO_2, 9mg/L NO_3^-N, 120 min, HCOOH	Slaughterhouse wastewater, high turbidity, low TOC (5mg/L), high CFU ($>10^5$)	$2.64x10^{-3}$ Einstein/min $2.38x10^{22}$ photons	TiO_2 alone: 87.5% Zn/TiO_2: 91.7%	TiO_2 alone: 70.71% N_g Zn/TiO_2: 95.5% N_g	2
450W medium pressure Hg, 200mL,TiO_2 (P90) 7.1mW/cm^2	IX Brine; Synthetic: 500mg/L NO_3^-, 0-10%wt NaCl	$12x10^{19}$ photons/cm^2	No TiO_2: 30% (0%wt NaCl) 48% (6%wt NaCl) TiO_2: 100%	No TiO_2: >90% NO_2^- TiO_2: 75% N_g, 25% NH_4^+	3
450W medium pressure Hg, 200mL, TiO_2, (P90) 7.1mW/cm^2, HCOOH	IX Brine; Real: 1793mg/L TDN, 23.9mg/L DOC, <50mg/L SO_4^{2-} (precipitated prior), 350mg/L as $CaCO_3$	$26x10^{19}$ photons/cm^2	Sulfate-Removed Brine: 89%	Sulfate-Removed Brine: 83% N_g, 17%NH_4^+	4
15W low pressure Hg, 500mL, C/TiO_2, 65W/m^2, 40 min, HCOOH	Seawater, >600mM Cl^-, >500mM Na^+, 33mM SO_4^{2-}, 61mM Mg^{2+}, <12mM: Ca^{2+}, K^+, Sr^+, HCO_3^-, Br^-	$1.99x10^{19}$ photon/cm^2	C/TiO_2: 100%	C/TiO_2: 100% N_g	5

1 (F. Zhang et al., 2005) 2 (de Bem Luiz et al., 2014) 3 (T. Yang et al., 2013) 4 (T. Yang et al., 2013)
5 (Shaban, El, Kh, & Farawati, 2016a)

Interestingly, high salinity (e.g. seawater or ion exchange brines) produced contrasting effects for predominantly photolytic or photocatalytic reduction processes due to the presence of the chloride anion. For example, Yang et al. (2013) studied a synthetic ion exchange brine and found photolytic reduction of nitrate was 18% higher in the presence of 6%wt NaCl versus no-salt added. However, for photocatalytic reduction (pure-TiO_2, P90), the sodium chloride brine inhibited performance by a factor of 1.5 (T. Yang et al., 2013). This trend can be attributed to nitrite stabilization due to the chloride in the photolytic reduction of nitrate to nitrite (Petriconi & Papee, 1968; T. Yang et al., 2013). The chloride stabilization leads to minimal (<10%) production of gaseous nitrogen via photolysis reaction as nitrite remains the predominant product. For the photocatalytic reaction, the reactivity of the $CO_2^{\bullet-}$ upon oxidation of formic acid is significant to reduce NO_3^- to NO_2^-. Thereby, the photoactivation of chloride ion in the aqueous solution is transformed to a scavenging oxidant, $Cl^\bullet$ ($E^o(Cl^\bullet/Cl^-)$ = 2.43 V vs SHE), and inhibits reduction performance when in competition with formic acid for surface sites.

Similar to the presence of chloride, other anionic species can affect the photocatalytic reduction performance. The kinetic response to additional competitive anionic species varies based on the properties of the added competitor. The inhibition of competing anions has largely been attributed to (i) the lesser availability of catalytic surface sites for nitrate/reductive intermediates adsorption and (ii) reaction due to other constituents with higher adsorption rates. However, as seen in a recent paper employing a C/TiO_2 catalyst in seawater (Shaban et al., 2016b), 100% reduction may still be achieved at a rate similar to previous works in model waters (Table 4-8). Another group utilized Zn/TiO_2 composite catalyst to remove nitrate from slaughterhouse wastewater (de Bem

Luiz et al., 2014) and achieved complete reduction with 95.5% N_2 selectivity under low-pressure Hg irradiation. The complexity of this matrix and photon flux comparable to the high salinity matrices posit feasibility of nitrate photocatalysis in a real water matrix.

Proper hole scavenger dose to treat real water matrices (Shaban et al., 2016b) is important to maintaining performance and selectivity to nitrogen gases. Shaban et al. (2016) observed that an optimum concentration of 40 mM of formic acid was required to treat 1.6 mM of NO_3^- in the presence of 0.64 M of chloride. In other words, a 25:1 ratio of HCOOH:NO_3- was optimum, which is 5-fold higher than the 5:1 ratio typically used in pure waters containing NO_3^-.

Throughout the literature, there is minimal discussion of the catalytic affinity for nitrate and its subsequent effects on promoting N_2 versus NH_4^+ as a reduction product. Particularly in real water matrices, the proximity of nitrate and N-species to the catalyst in lieu of other competing species becomes important for efficient reduction. In all cases, the solid/liquid interface structure should be discussed in terms of the charged semiconductor catalyst surface and the double layer depicted in Fig. 4-13a. As we discussed previously, the direct charge transfer processes occur within the Helmholtz plane; therefore, the approach to the targeted species within this thin layer is crucial. As has been discussed in more recent papers, Figure 4-13b shows how competing species modify the double layer. The influence of the complex water matrix on NO_3^- photocatalytic reduction can significantly slow nitrate photocatalytic performance (de Bem Luiz et al., 2014; Shaban et al., 2016b; T. Yang et al., 2013). According to Korgel et al. (1997), under higher ionic strengths, the effects of the double layer should decrease, and the reduction rates should increase (Korgel & Monbouquette, 1997). However, the experimental results show the

displacement of nitrate and hole scavenger species by other anionic species (such Cl-, CO_3^{2-} or SO_4^{2-}) reduce the efficiency of the desired reactions. Even though the modifications on the double layer also affect the reaction rates, the decrease of nitrate and formic acid concentration close to the photocatalyst surface is the limiting rate step. Further studies using complex water matrices are critical foci to ensure the applicability and scaling-up of photocatalytic technologies.

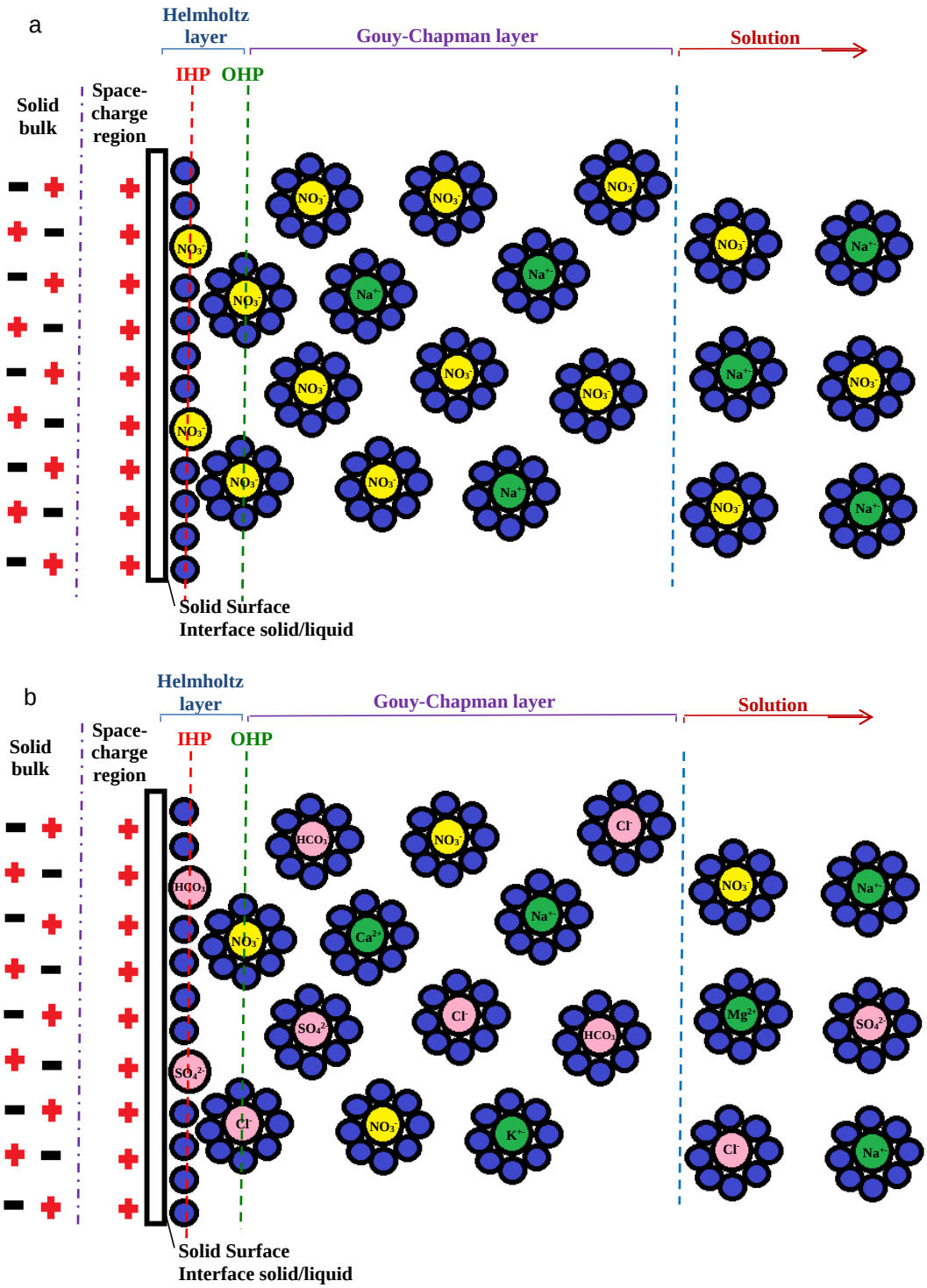

Figure 4-13. Double layer in (**a**) synthetic water matrices containing only nitrate and (**b**) actual water matrices with competing ionic species.

Section 8: Summary of key insights

Nitrogen is essential for all forms of life, yet it suffers from the "goldilocks" paradox where too much or too little nitrogen in the wrong place at the wrong time can be detrimental. Managing the nitrogen cycle, a National Academy of Engineering Grand Challenge, impacts the food-energy-water system because industrial production of ammonia from N_2 fixation (100 Tg N yr^{-1}) from the atmosphere via the Haber-Bosch process consumes 1-2% of the world's annual energy (James N Galloway et al., 2008; Gruber & Galloway, 2008). Nearly 75% of the world's ammonia production goes towards fertilizers. Nitrate contamination of freshwater supplies results from over application of fertilizers (50% are urea-based fertilizers, followed by anhydrous ammonia and ammonium nitrate) and is a major drinking water challenge where nanotechnology holds significant promise to address. Hundreds of papers over the past two decades on photocatalytic reduction of nitrate were critically reviewed to summarize key knowns and to identify important questions that need resolution before the opportunities of this technology can be recognized.

From the discussion of the elementary steps involved in nitrate reduction, a complete mechanism is described in Fig. 4-7. Furthermore, certain differences observed while using modified catalysts and co-catalysts have been discussed. One of the major features is the dual role played by hole scavengers: (i) they minimize the recombination reaction and (ii) they are the source of $CO_2^{\bullet-}$ radical, which functions as the reducing mediator species. Some elementary steps involving charge transfer processes cannot be conducted by the e_{cb}^-, with a standard reduction potential of -0.14 V vs SHE for TiO_2, hence, the presence of $CO_2^{\bullet-}$ radical ($E^o(CO_2/CO_2^{\bullet-})$ = -1.81 V vs SHE) is crucial. In

contrast, the results reported in the literature identify pH as one of the particularly influential variables. The solution pH modifies the superficial charge and adsorption properties of the catalyst, and it also affects the reaction rates because several steps require H^+. Acidic pH conditions of ~3.0 are optimal. Furthermore, the use of different hole scavengers is presented and identifies formic acid as the most efficient because it results in major conversions and selectivity towards N_2. Alternative hole scavengers such methanol, ethanol, oxalic acid, or other organic species have been also reported but with lower conversions due to the lower generation of $CO_2^{\bullet -}$. The pending question that needs addressing is: How can photocatalytic reduction of nitrate be enhanced at near neutral pH without the addition of an external hole scavenger, to reduce chemical usage?

Different photocatalysts have been synthesized and studied, including pure semiconductors, doped semiconductors, metallic composites, and bimetallic composites. Among all the considered options, Ag/TiO_2 photocatalysts presented the best performance with respect to conversion and selectivity. Bimetallic $Pd\text{-}Cu/TiO_2$ and $Pt\text{-}Cu/TiO_2$ also show promising results. Future research should be devoted to the exploration of new materials that improve the products selectivity toward desirable by-products (N-gases) from nitrate.

Light source (i.e., lamp, LED, sunlight spectra output) selection is frequently overlooked in photocatalytic systems, where it is incorrectly thought that light source does not render any influence beyond providing the needed band gap energy. Depending upon reactor design (fixed films versus slurry based reactors) the importance cannot be overlooked for direct photolysis reactions to occur involving nitrate, nitrite or other intermediates. For example, light emitted near the peak absorption wavelengths and

quantum yields for HNO_2/NO_2^- are likely very important for polychromatic light sources with output in the 350-380 nm range. Additionally, the amount of light of different wavelengths that is scattered versus absorbed by nano-scale photocatalysts as a function of nanoparticle slurry or surface concentration is important, yet ill-defined in most experimental reports regarding nitrate removal. A key question that needs to be addressed as this technology advances towards implementation is: What are the correct units (photon flux, energy flux) and optimal wavelength range for photocatalytic reduction of nitrate to desirable N-gas by-products?

Nanotechnology has tremendous opportunity to modulate the lattice structure of photocatalysts and to use bimetallic photocatalysts. While doping metals into photocatalysts influences the spectral bandwidth of absorbed energy and influences the bandgap of the photocatalyst, it does not appear to influence the mechanisms of nitrate reduction. In contrast, production of metallic composites (e.g., silver nanoparticles on the surface of TiO_2) does appear to change the mechanisms of nitrate reduction. An important question to advance this topic that has not been considered in previously published articles is: What is the optimal particle size, aspect ratio, shape or morphology and composition of composite nanoparticle photocatalysts to maximize nitrate reduction rates and improve by-product selectivity?

Aiming toward the application of photocatalytic reduction management as a solution for nitrate pollution, the treatment of real water matrices should be considered. Only a few works articulate the possible competitive ions that may diminish photocatalyst efficiency among other concerns. Photocatalytic treatment may focus on concentrated waste streams from other water treatment processes (e.g., ion exchange brines containing

high salt (5 to 25% NaCl) with nitrate (>1000 mg N L^{-1}) in the presence of sulfate or bicarbonate) or direct treatment of ground and surface waters that must be treated at near neutral pH levels and in the presence of heterogeneous mixtures of anions, cations and natural organic matter that may act as electron or hole scavengers. An insufficient number of studies have evaluated the performance of highly efficient nitrate reducing photocatalysts in complex water matrices. Even fewer studies exist that evaluate the lifetime effectiveness of photocatalysts, because experiments have been performed in batch reactors rather than single-base continuous flow reactors. Key questions that emerge are: What compounds in natural drinking waters serve as "natural" hole scavengers, and do they play a role in nitrate reduction mechanisms and by-product selectivity? What is the role of natural water constituents on fouling or dissolving (composite) photocatalysts during prolonged operation (months) in continuous flow photocatalytic reactors? And how can these issues be minimized through catalyst cleaning or other strategies?

Acknowledgements

This work was partially funded through the Nano-Enabled Water Treatment Technologies Nanosystems Engineering Research Center by the National Science Foundation (EEC-1449500)This research was funded by the United States Environmental Protection Agency (RD 83560301) through the Design of Risk-reducing, Innovative-implementable, Small-system Knowledge (DeRISK) Center. Graduate student support was partially provided by a Dean's Fellowship from the Ira A. Fulton Schools of Engineering at Arizona State University.

CHAPTER 5

ULTRAVIOLET WAVELENGTHS INFLUENCE KINETICS AND SELECTIVITY FOR N-GASES DURING TIO_2 PHOTOCATALYTIC REDUCTION OF NITRATE

Abstract

For drinking water applications, photocatalytic reduction processes beneficially transform aqueous nitrate to innocuous nitrogen gases but can produce nitrite and ammonia as undesirable aqueous by-products. We hypothesize that by-product selectivity is a function of light source and photon fluence dose, such that discrete wavelengths can increase yield of desirable N-gases. Experiments performed under different wavelength irradiation (ultraviolet- [UV] A, B, C) reduced nitrate in water to differing extents based on pH over the range of 1 to 8 or the presence of soluble organic electron donors. At an equivalent photon fluence dose, the most rapid nitrate loss in acidic solutions occurred using a combination of three UV-light emitting diodes (285 nm, 300 nm, 365 nm) closely followed by a polychromatic medium pressure UV lamp. A polychromatic xenon light source was least effective in reducing nitrate. Nitrite is an important intermediate during photocatalytic reduction of nitrate. Nitrite absorbs 330–380 nm light with high quantum efficiency. Thus, polychromatic or monochromatic light sources with strong UV-A emission more rapidly convert nitrite to by-products than UV-C monochromatic light sources. Nitrous acid (HONO) has a higher molar absorptivity (ε) and quantum efficiency than nitrite ion (pK_a = 3.39) around 350-370nm. Selectivity towards nitrogen gases is bifurcated at the nitrite intermediate and is strongly influenced by direct photolysis instead of photocatalytic reduction. Thus, the selectivity of by-products can be controlled by

delivering light in the 350-370nm wavelength range, where it enables photocatalytic processes to rapidly initiate NO_3^- reduction and delivers photons for direct photolysis of HONO.

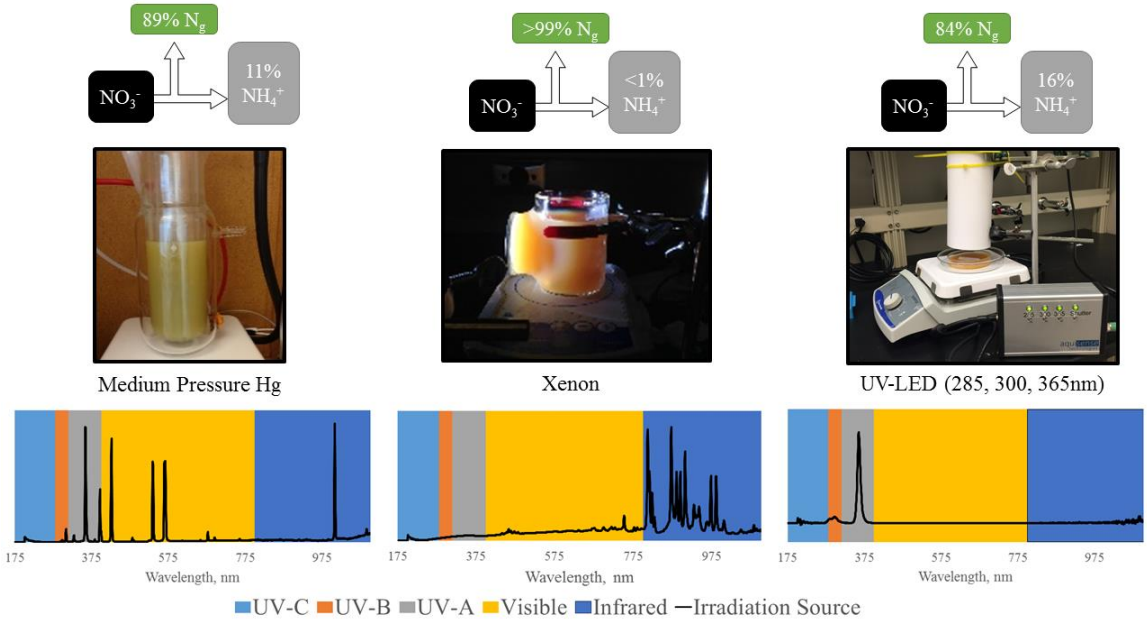

Keywords: drinking water, nitrite, pollution, groundwater, photocatalysis

Introduction

Nitrate contamination in drinking water is globally pervasive, affecting over 24 million people in the United States alone, with concentrations above the 10 mg-N/L maximum contaminant level (MCL) set by the United States Environmental Protection Agency (Burow et al., 2010). The National Academy of Engineering has listed management of the nitrogen cycle and provision of clean water as two of its top twelve grand challenges (National Academy of Engineering, 2017). Dealing with ubiquitous nitrate contamination requires transformation of fixed nitrogen in the aqueous phase to innocuous gaseous products (e.g., N_2). Accepted technologies for nitrate removal from drinking water include ion-exchange and reverse osmosis, but both of those yield product waters (i.e., brines) containing concentrated nitrate instead of transforming nitrate into nitrogen gases. Biological denitrification is excellent for wastewater treatment, but managing organic or hydrogen electron donors, bacteria populations, release of soluble organics, and rapid start up and shut down of systems can be difficult for small drinking water systems (Health, 2005). Physical-chemical treatment processes are more feasible to implement at small system scale because they are less operationally intensive and are more reliable than biological processes for nitrate reduction. Emerging solutions for nitrate reduction are photocatalysis (Sá et al., 2009; Wehbe et al., 2009), catalytic hydrogen reduction (Barrabes & Sa, 2011; Y. X. Chen, Zhang, & Chen, 2003; Lecloux, 1999; Pintar, 2003; Prüsse et al., 2000; R. Zhang et al., 2013), and electrochemical reduction (Mook et al., 2012; Polatides, Dortsiou, & Kyriacou, 2005; Safari, Rezaee, Ayati, & Jonidi-Jafari, 2015), whereby nitrate is terminally reduced to innocuous nitrogen gases (e.g., N_2) and minimal aqueous ammonium. Herein, we focus on photocatalysis for reduction of nitrate

because it uses environmentally benign catalysts, uses efficient photonic light sources, and can completely reduce nitrate to innocuous N-gases (e.g., N_2).

Photocatalytic reduction can treat nitrate in drinking water directly or treat ion exchange brines (T. Yang et al., 2013) to produce both aqueous and gaseous constituents with varying implications and toxicity (Gangolli et al., 1994; Montesinos, Quici, Destaillats, & Litter, 2015; WHO, 2016). A primary challenge for photocatalysis is to avoid ammonium production, which occurs readily at neutral pH (Kominami et al., 2001). Aqueous ammonia production is undesirable in drinking waters because it exerts a chlorine demand upon disinfection in water distribution systems. The preference is a sparingly soluble non-ammonia nitrogen gas by-product (e.g., N_2, NO_x). Selectivity toward non-ammonia nitrogen gases may be further controlled in photocatalytic systems via adjustment of experimental and reactor parameters (Tugaoen, Garcia-Segura, Hristovski, & Westerhoff, 2017).

Previous studies have focused efforts on managing by-product selectivity through manipulation of experimental conditions, including: pH (K Doudrick et al., 2013; F. Zhang et al., 2005), alkalinity (Kominami, Nakaseko, Shimada, Furusho, Inoue, et al., 2005; F. Zhang et al., 2005), sacrificial electron donor (K Doudrick et al., 2013; Sá et al., 2009), salinity (Petriconi & Papee, 1968; Shaban et al., 2016b; T. Yang et al., 2013), and catalyst (Bems et al., 1999; K Doudrick et al., 2013; Kyle Doudrick et al., 2012; Wenliang Gao et al., 2004; Gekko et al., 2012; Hamanoi & Kudo, 2002; R. Jin et al., 2004; Kobwittaya & Sirivithayapakorn, 2014; Kominami, Nakaseko, Shimada, Furusho, Inoue, et al., 2005; L. Li et al., 2010; Y. Li & Wasgestian, 1998; Lu et al., 2009; Penpolcharoen, Amal, & Brungs, 2001; Ranjit, Krishnamoorthy, Varadarajan, & Viswanathan, 1995; Ranjit & Viswanathan,

1997a, 1997b; Ren et al., 2015; Sá et al., 2009; Shand & Anderson, 2013b; Soares, Pereira, Órfão, Faria, & Silva, 2014; Sowmya & Meenakshi, 2015; D. Sun et al., 2016; Juan Yang et al., 2013; T. Yang et al., 2013; F. Zhang et al., 2005, 2007). The literature shows N-gaseous by-product formation ranging from > 80% to < 10%. These differences in selectivity emerge from aforementioned experimental solution conditions (pH (K Doudrick et al., 2013; F. Zhang et al., 2005), presence of external electron donors (K Doudrick et al., 2013; Sá et al., 2009), or catalyst properties (Wenliang Gao et al., 2004; L. Li et al., 2010; Ren et al., 2015; Sowmya & Meenakshi, 2015; D. Sun et al., 2016)). Common experimental conditions (K Doudrick et al., 2013; Kyle Doudrick et al., 2012; Sá et al., 2009; F. Zhang et al., 2005) are 1 g/L of catalyst and 40 mM HCOOH to (1) satisfy low-pH conditions and (2) serve as a sacrificial hole scavenger. Acidic conditions are preferred for nitrate reduction to nitrogen gases, with HCOOH yielding the best kinetics and selectivity at pH ≈ 2.5 (K Doudrick et al., 2013). Recent works have identified $CO_2^{\bullet-}$, a product of HCOOH oxidation (G. Liu et al., 2016b; Mora-Sero et al., 2005; Rengaraj & Li, 2007), as a primary photocatalytic mechanism for reduction of nitrate to nitrite in lieu of the conduction band electron due to its thermodynamic feasibility (Montesinos, Quici, Destaillats, & Litter, 2015; Sá et al., 2009). Near the pKa of 3.39, nitrous acid (HNO_2, HONO; Eqn. 1) forms, which is more photoactive in the mid 300nm range (quantum yield, $\Phi_{280\text{-}385nm}$ = 0.35–0.45 (Michael Fischer & Warneck, 1996; Oliver C Zafiriou & True, 1979; Zellner, Exner, & Herrmann, 1990)) than nitrite ion ($\Phi_{280\text{-}385nm}$ = 0.025–0.15 (Mack & Bolton, 1999a)). However, this photolytic reaction is predominantly circular, yielding NO_2^- (Eqns. 3–5).

$NO_2^- + H^+ \leftrightharpoons HONO$ $pK_a = 3.39$ Equation (1)

$NO_3^- + H^+ \leftrightharpoons HNO_3$ $pK_a < 1$ Equation (2)

$$HONO + h\nu \rightarrow NO^{\bullet} + OH^{\bullet} \quad \text{Equation (3)}$$

$$NO^{\bullet} + NO_2^{\bullet} \rightarrow N_2O_3 \quad \text{Equation (4)}$$

$$N_2O_3 + H_2O \rightarrow 2NO_2^- + 2H^+ \quad \text{Equation (5)}$$

Due to the complex photochemistry, a parallel reaction reforming NO_3^- and NO_2^- is likely co-occurring via Eqns. 6–8 (which may contribute to oxidation of NO_2^- in situ):

$$NO^{\bullet} + NO^{\bullet} \rightarrow N_2O_2 \quad \text{Equation (6)}$$

$$N_2O_2 + O_2 \rightarrow N_2O_4 \quad \text{Equation (7)}$$

$$N_2O_4 + H_2O \rightarrow NO_3^- + NO_2^- + 2H^+ \quad \text{Equation (8)}$$

Titanium dioxide (TiO_2) photocatalysis does not produce e^-_{cb} of sufficient energy to reduce nitrate or its intermediates to nitrogen gases (Tugaoen et al., 2017). Formic acid oxidation occurs directly via h^+_{vb} to yield carboxyl radical ($CO_2^{\bullet-}$) according to Eqns. 9 and 10 (G. Liu et al., 2016b; Mora-Sero et al., 2005; Rengaraj & Li, 2007):

$$\text{Semiconductor} + h\nu \rightarrow h^+_{vb} + e^-_{cb} \quad \text{Equation (9)}$$

$$HCOO^- + h^+_{vb} \rightarrow H^+ + CO_2^{\bullet-} \quad \text{Equation (10)}$$

Combining photocatalysis with photolysis, reactions proceed that yield gaseous products (Eqns. 11–16) (L. Chu & Anastasio, 2003; Mack & Bolton, 1999b):

$$HONO + e^- \rightarrow NO^{\bullet} + OH^- \quad \text{Equation (11)}$$

$$NO^{\bullet} + e^- \rightarrow NO^- \quad \text{Equation (12)}$$

$$NO^- + H^+ \leftrightarrow HNO \quad \text{Equation (13)}$$

$$2HNO \rightarrow N_2O + H_2O \quad \text{Equation (14)}$$

$$HNO + NO^{\bullet} \rightarrow N_2O + HONO \quad \text{Equation (15)}$$

$$N_2O + CO_2^{\bullet-} + H^+ \rightarrow N_2 + {}^{\bullet}OH + CO_2 \quad \text{Equation (16)}$$

Targeting HONO as a key intermediate for evolution of nitrogen gases offers a method to minimize ammonium production via transformative processes yielding nitrogenous gases (Eqns. 11–16). TiO_2 photocatalysis has been postulated in the literature to include nitrate reduction reactions to largely unsubstantiated intermediate constituents as articulated in Scheme 5-1. Photocatalysis reduces nitrate to nitrite (Mack & Bolton, 1999b) via a stepwise two-electron transfer. Both photocatalytic and photolytic pathways are more relevant for nitrite reduction to ammonia or nitrogen gases.

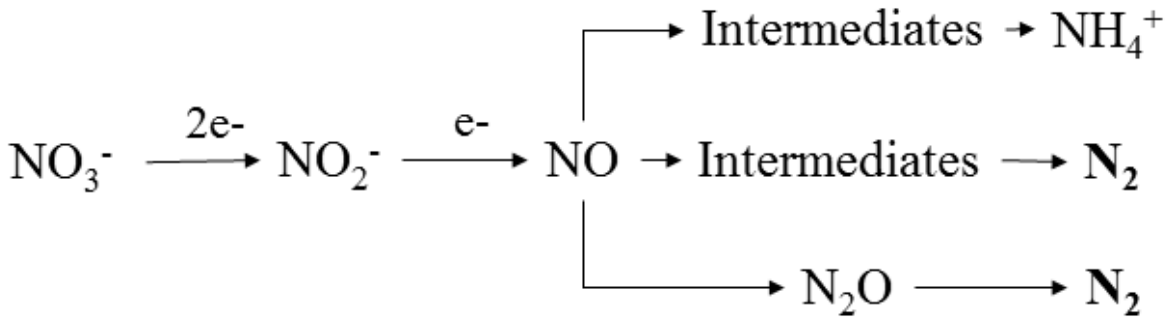

Scheme 5-1. Conceptual sequence for nitrate reduction to desirable nitrogen gas (N_2) and undesirable ammonium ion.

Light sources emit different wavelengths, and the role of light constitutes an excitement of electrons within photocatalysts in parallel to photolysis of aqueous nitrogen species. Each aqueous nitrogen species absorbs photons of different wavelengths corresponding to different photolytic quantum yields. For photocatalysis, the bandgap energy must be exceeded to produce electrons for reduction. Likewise, hole scavengers may undergo photolytic processes under short-wavelength irradiation, yielding oxidation products such as the $CO_2^{\bullet-}$ radical in the case of HCOOH. Thus, incident wavelengths

should play a significant role in reduction kinetics and selectivity, with arbitrary selections leading to energetic/photonic inefficiency and ammonium production. Although many studies report nitrate loss and by-product formation as a function of irradiation duration, they often do not provide the irradiation spectrum or light intensity in the reactor, thereby complicating direct comparisons between studies (Wenliang Gao et al., 2004; R. Jin et al., 2004; Kato & Kudo, 2002; L. Li et al., 2010; Sá et al., 2009; Sowmya & Meenakshi, 2015; F. Zhang et al., 2005).

Photocatalytic nitrate reduction has been explored using a TiO_2 or metal-TiO_2 catalyst under irradiation by xenon lamps or medium pressure or high pressure mercury lamps (Mack & Bolton, 1999b). The highest selectivity toward nitrogen gases under these irradiation conditions utilize TiO_2, TiO_2/Ag, or TiO_2/Cu in acidic solutions containing HCOOH. A detailed literature review on photolysis and photocatalysis of nitrate is provided elsewhere (Tugaoen et al., 2017). From this review, we hypothesize that nitrate photocatalytic degradation and by-product selectivity is a function of light source and photon fluence dose at key wavelengths and that particular discrete wavelengths will predominantly yield N-gases through a combined photocatalytic/photolytic mechanism. To test this hypothesis, multiple light sources with different emission spectra were used to address the following objectives: (1) compare absorbance spectra of aqueous N-species and TiO_2 photocatalyst against emission spectra of polychromatic light sources; (2) demonstrate photocatalytic reduction of nitrate in acidic solutions with an external aqueous electron donor using polychromatic light sources; (3) quantify how wavelength filters coupled with polychromatic light sources change photocatalytic nitrate reduction products; (4) compare the effects of polychromatic light sources and discrete irradiation wavelengths

(using light emitting diode [LED] sources) on photocatalytic reduction of aqueous nitrate and nitrite; and (5) postulate mechanisms for indirect photocatalytic and direct photolytic pathways for reduction of aqueous nitrate to N-gases, identifying nitrite as a critical intermediate and point of bifurcation in selectivity outcomes.

Methods and Analyses

Absorption Spectra Determination

Aqueous absorption spectra were measured using UV/vis spectroscopy (DR5000, HACH) and calculating molar absorptivities according to the Beer-Lambert Law. Quantum efficiencies were compiled from the literature to compare expected photolytic yields of aqueous nitrogen species. Diffuse reflectance spectra of solid photocatalyst samples were measured using a Lambda 18 (Perkin Elmer, USA) with a 150 mm integrating sphere to determine the absorption spectrum of the catalyst.

To quantify the spectral output of the polychromatic light sources, irradiance was measured using a fiber optic spectrometer with cosine corrector (Avantes AvaSpec 2048). Multiple locations were measured in the reactors to provide average irradiance values. Fluence dose (mJ/cm^2) and photon fluence dose ($photon/cm^2$) were calculated (JR Bolton & Stefan, 2002; M. Stefan & Bolton, 2005) to represent (1) the full spectrum of light emitted by the source and (2) partial spectrum based on the assumption that only wavelengths available for P90 (TiO_2) bandgap excitation (ultraviolet, $\lambda \leq 388$ nm) were experimentally relevant.

2.2 Determining Photocatalytic Nitrogen Reduction

Commercially available titanium dioxide (Evonik) was obtained as a powder (P90) and used as received. P90 contains anatase (86%, 12 nm) and rutile (14%, 18 nm) crystal phases and has a surface area of 104 m^2/g (Kyle Doudrick et al., 2012). P90 has a higher nitrate reduction rate compared to P25 (Kyle Doudrick et al., 2012). Sodium nitrate ($NaNO_3$, 99% EMD Millipore) and sodium nitrite ($NaNO_2$, 97% Sigma) were the nitrate and nitrite source, respectively. Formic acid (HCOOH, 98% Fluka) was the sacrificial electron donor (hole scavenger) in experiments where indicated. All experiments were performed in 18.2 MΩ-cm Nanopure® water with no buffering.

Most experimental conditions were consistent with prior work (K Doudrick et al., 2013; F. Zhang et al., 2005). In brief, the pH was 2.5, and the water matrix contained 100 mg-NO_3^--N/L (7.14mM), 40 mM HCOOH, and 1 g/L P90. Parallel experiments were conducted with 100 mg-NO_2^--N/L (7.14 mM) instead of nitrate as noted. In all experiments, 30 min dark adsorption preceded illumination to determine non-photocatalytic removal of nitrogen due to adsorption. In all reactors, magnetic stirring was employed to maintain catalyst suspension.

Samples were collected from the reactors over time and filtered (0.2 μm nylon membrane filters, Pall). Cumulative sample volumes collected from the reactors were <10% of aqueous phase reactor volume. Samples were stored in amber glass vials in dark conditions for analysis within 48 h. Aqueous concentrations of nitrate, nitrite, and ammonium were analyzed (EPA Method 300.0, ASTM Standard Method D6919) using a dual anion/cation ion chromatography instrument (ICS-5000, Dionex). Results are reported

as total nitrogen reduction (TNR), which we define using concentrations [mg-N/L] of initial (0) and final (f) aqueous constituents according to Eqn. 17:

$$\mathrm{TNR} = 100 * \left(1 - \frac{\left[[NO_3^-]+[NO_2^-]+[NH_4^+]\right]_f}{\left[[NO_3^-]+[NO_2^-]+[NH_4^+]\right]_o}\right) \qquad \text{Equation 17}$$

The selectivity to gaseous nitrogen species was based on the difference of initial (0) and final (f) aqueous constituents and was calculated according to Eqn. 18:

$$S(N_{gases}) = \frac{[NO_3^-]_o - [NO_3^-]_f - [NO_2^-]_f - [NH_4^+]_f}{[NO_3^-]_o - [NO_3^-]_f} \qquad \text{Equation 18}$$

To study reactivity of an important intermediate species, experiments were conducted starting with nitrite instead of nitrate. Nitrite or HONO reduction was investigated using either broad-wavelength or discrete wavelength irradiation to elucidate the reaction bifurcation mechanism that produces either aqueous ammonium or nitrogen gases. TNR was used to quantify nitrogen removal from the aqueous phase. Dark adsorption testing at pH 2.5 induced non-photonic HONO oxidation, which likely contributed to the observed nitrate concentrations.

2.3 Photocatalytic Light Sources and Reactors

Experiments using a 450 W medium pressure mercury lamp (UV: 100 mW/cm^2) were conducted in a double-walled quartz immersed-lamp photoreactor (200 mL; Ace Glass power supply, 7830-60; Ace Glass, 78-25-34; Hanovia PC 451.050) with external cooling water to maintain constant temperature (25°C). A borosilicate sleeve surrounded the lamp to filter out wavelengths lower than 280 nm and eliminate direct photolysis of nitrate or formate.

Experiments using a 450 W Xe-arc lamp (300 mW/cm^2, 66924-450XV-R1, Newport) were performed in a 150 mL reactor, which was separated from the lamp by a quartz window (d = 7 cm) and water filter to eliminate infrared irradiation and reactor heating from the irradiation source. For some experiments, an ultraviolet cutoff filter (Newport, 90017074) selectively blocked wavelengths between 280 nm and 450 nm to eliminate UV-A (315 nm to 400 nm) and UV-B (280 nm to 315 nm) irradiation to only transmit 240 nm - 280 nm for isolated UV-C testing. Xenon lamp experiments were performed to compare results of broad-wavelength irradiation to the polychromatic spectrum of the medium pressure mercury lamp.

Experiments at 285, 300, and/or 365 nm were performed in a Petri dish reactor (40 mL) using an LED collimated beam light source (AquiSense PearlBeam custom UV-LEDs) with incorporated heat sink, fan, and quartz viewing lens. Light was collimated (13 cm column, 10 cm diameter) to ensure a uniform LED array across the 10 cm Petri dish diameter. Illumination was delivered using the LEDs individually and in varied combination: 285 nm, 300 nm, or 365 nm alone; 285 nm and 300 nm combined; or 285 nm, 300 nm, and 365 nm combined. LED light source experiments investigated discrete wavelength polychromatic irradiation in comparison to more broadly emitting medium pressure Hg and Xe lamps.

Results and Discussion

Comparison of Light Source Emission Spectra with Absorptivity of N-Species and TiO_2

Among the ionic aqueous nitrogen species, nitrite has the highest molar absorptivity (ε) in the 280 to 400 nm range (Figure 5-1). Between 350 and 370nm, HONO has a maximum ε (~ 40 M^{-1} cm^{-1}) approximately twice that of NO_2^-. Nitrate has a maximum ε at 300 nm and very low ε between 350 and 380nm. Ammonium ion (NH_4^+) and hydroxylamine (H_3NO) have negligible absorbance (ε < 0.5 M^{-1} cm^{-1}) in the UV range. Higher absorptivity does not directly correspond to higher photolytic activity because of the variable quantum yields, as described by Mack and Bolton (Mack & Bolton, 1999b). Thus, depending on the light source used and its particular irradiation emission spectrum, different direct photolysis reactions may occur, both of primary species and aqueous or adsorbed intermediates.

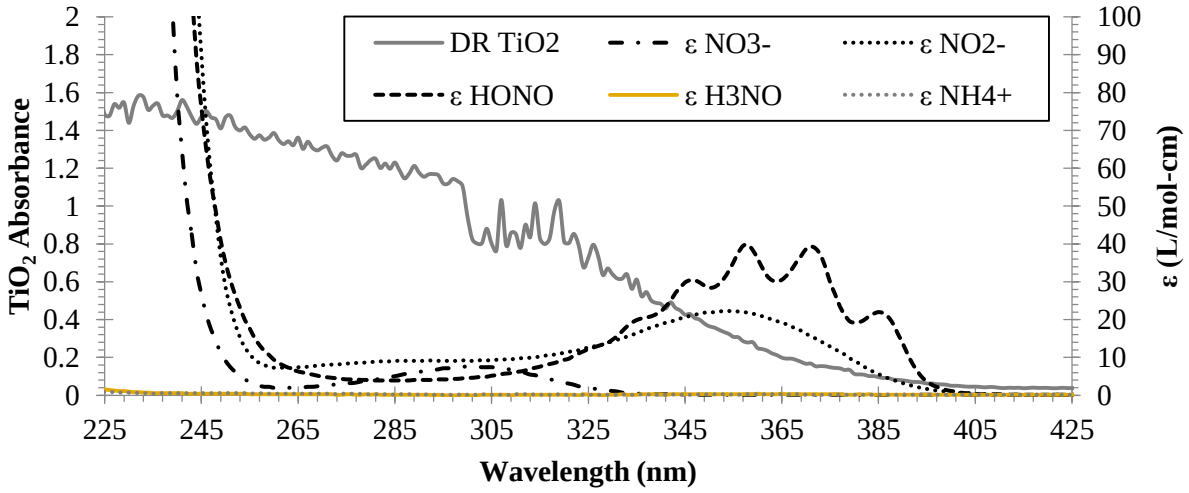

Figure 5-1. Diffuse reflectance (DR) absorption spectra of TiO_2 and wavelength dependent molar absorptivity (ε) for relevant aqueous nitrogen species: NO_3^-, NO_2^-, HONO, H_3NO, NH_4^+ (as mol N).

Figure 5-2 illustrates the ultraviolet spectral output of: (a) the polychromatic medium pressure mercury lamp; (b) xenon lamp filtered to exclude wavelengths between 280 and 450; (c) xenon lamp allowing all wavelengths (i.e., not filtered); and (d) UV-LED irradiation source at 285, 300, and 365 nm. Comparing the absorbance spectra in Figure 5-1 with the emission spectra in Figure 5-2 suggests photons from the 365 nm LED would be absorbed more by HONO than NO_2^-, and little absorbance would occur by NO_3^- or other aqueous N-species. Light with $\lambda \approx 295$ nm that is delivered into the solution would be absorbed by NO_2^-, NO_3^-, and HONO. At 295 nm and throughout the ultraviolet spectrum, these species will undergo direct photolysis to different extents due to their varied quantum yields (Mack & Bolton, 1999b).

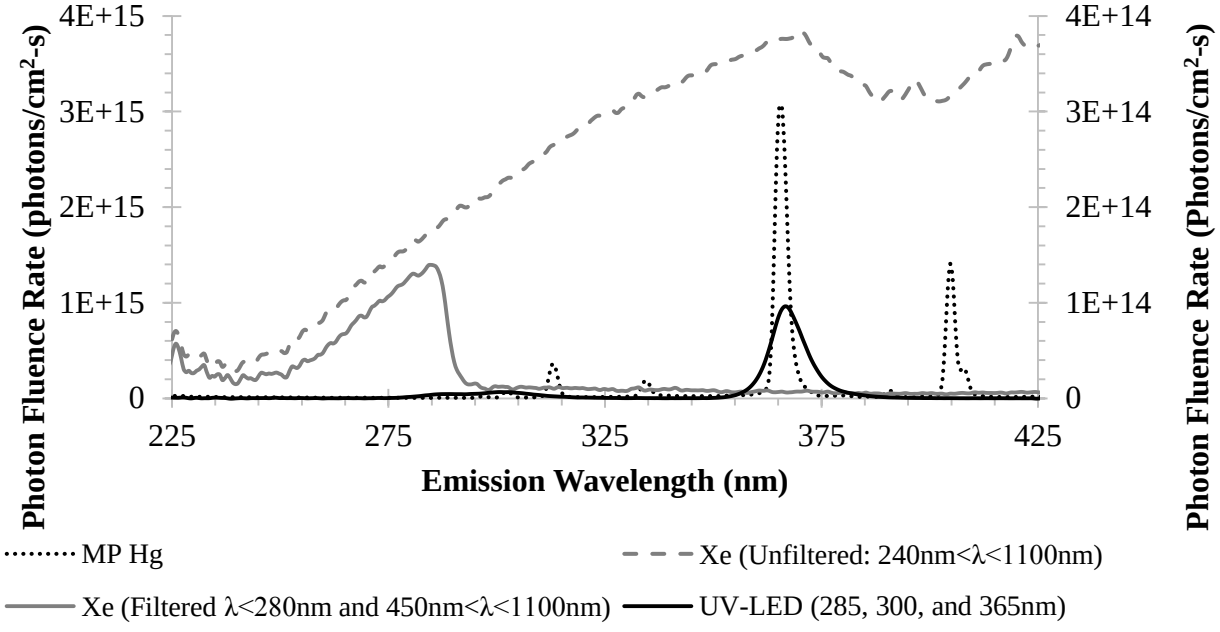

Figure 5-2. Ultraviolet spectral output of: (left axis) polychromatic medium pressure mercury lamp [MP Hg]; (right axis) xenon lamp [Xe; filtered to exclude wavelengths between 280 and 450nm, or allow all wavelengths], UV-LED irradiation of three LEDs (285, 300, and 365nm) operating simultaneously.

Figure 5-1 also illustrates the diffuse reflectance spectra for TiO_2. In suspended slurry, TiO_2 scatters or absorbs light below 400 nm. This scattering reduces photon transmittance into solution and limits direct photolysis of aqueous N-species to the portions of solution that are closest to the light source. As such, the emission spectra of the light source and the interfacial area between the lamp source and water both influence the reactivity due to direct photolysis and the TiO_2 catalyzed areas. Overall, a weaker photolytic and more dominant photocatalytic response would be expected for slurry photocatalysis. P90, with a bandgap of 3.2 eV (Kyle Doudrick et al., 2012), absorbs light below 390 nm as calculated with the Kubelka-Monk Equation. As described by Planck-Einstein relationship, each wavelength corresponds to a different energy. Photons with lower energy ($\lambda > 390$ nm) are thereby not relevant for production of aqueous electrons associated with TiO_2. Further, photons with $\lambda > 390$ nm are also not relevant for direct photolysis reactions with aqueous N-species. Thus, on an energy basis, only photons with $\lambda < 390$ nm are considered effective for nitrate photocatalysis and/or photolysis and are tabulated as such for photon fluence values reported in this work.

3.2 Nitrate Removal during Photocatalysis with Different Polychromatic Light Sources

To assess the variability of nitrate reduction kinetics and by-product selectivity across irradiation sources, three light sources and reactor configurations delivered varied-wavelength photons for photocatalytic reduction of nitrate. Prior experiments using medium pressure mercury lamp photocatalysis with TiO_2 show nitrate reduction (Kyle

Doudrick et al., 2012; Ren et al., 2015; Sá et al., 2009; F. Zhang et al., 2005), but new insights may be gained through assessing the system's photonic efficiency. Figure 5-3 shows nitrate concentrations decreasing over irradiation time with low production of nitrite or ammonia for the medium pressure Hg light source emitting wavelengths longer than 240 nm in the presence of TiO_2 and an external electron donor (HCOOH). Nitrite formed as an intermediate, accounting for a maximum of 20% of the nitrogen after 28 min of irradiation. The net loss of aqueous N-containing species was consistent with evolution of volatile N-gases (Kominami et al., 2010; Montesinos, Quici, Destaillats, & Litter, 2015; F. Zhang et al., 2005). Control experiments in the dark showed no nitrate removal.

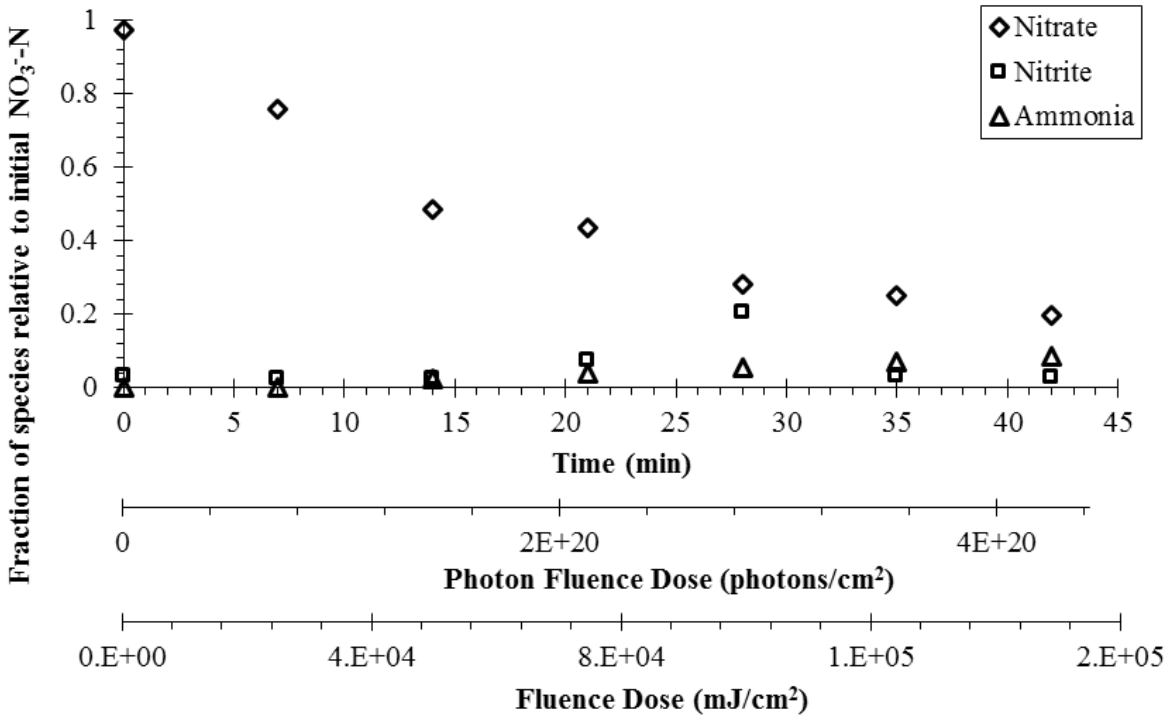

Figure 5-3. NO_3^- photocatalytic reduction and by-product formation (nitrite and ammonia) under medium pressure mercury irradiation with 1 g/L TiO_2 (P90) and 40mM HCOOH (pH=2.51 ± 0.05).

Rather than evaluating concentration changes based on reaction time, reaction kinetics are also plotted as a function of photon fluence dose (photons/cm^2) and fluence dose (mJ/cm^2) to facilitate comparisons between irradiation sources. Energy-based fluence has been used to assess microbial inactivation by UV light (J. R. Bolton & Linden, 2003; Linden & Darby, 1997), demonstrating wavelength-dependent outcomes (Beck et al., 2017) in UV disinfection performance studies. When nitrate reduction is observed experimentally, the irradiation source generates photons at wavelengths that exceed bandgap energy or induce photolytic response from aqueous N-species. Because N-species may undergo direct photolysis at different wavelengths plus indirect reduction on photo-excited TiO_2, photon fluence facilitates comparisons across the various wavelength sources when quantifying N-reduction efficiency.

Table 5-1 summarizes experimental data for the same initial aqueous conditions as illustrated in Figure 5-3 but under irradiation with a xenon lamp. Xenon lamp irradiation can yield both photocatalytic and direct photolytic response for nitrate reduction due to its photon production at $\lambda<290$ nm. For both wavelength-filtered and unfiltered xenon irradiation, negligible ammonium or nitrite formed, indicating complete reduction to nitrogen gases. Irradiation of a nitrate solution with the unfiltered xenon source achieved double the nitrate reduction (46%) after an applied photon fluence dose of 4.8×10^{20} photons/cm^2 with 1 g/L TiO_2 compared against 21% nitrate reduction in the absence of TiO_2 after the same photon fluence dose. This implies that direct photolysis of nitrate

occurs for 240 to 400 nm xenon irradiation, but a higher net removal of nitrogen occurs via combined direct photolysis and photocatalysis in the presence of TiO_2. UV-C only (λ<280nm) irradiation using the xenon source achieved 20% nitrate reduction during direct photolysis (with HCOOH) but less than 14% nitrate reduction during photocatalysis (1 g/L TiO_2) at a photon fluence dose of ~ $5.5x10^{19}$ photons/cm^2, indicating higher efficiency of nitrate photolysis than photocatalysis at wavelengths less than 280 nm. Nitrate undergoes direct photolysis at wavelengths less than 290 nm (Barat et al., 1970a; Gonzalez & Braun, 1995; Scharko et al., 2014), which causes photolytic processes to dominate the mechanisms for its reduction in the UV-C region. In contrast, TiO_2 has broad absorption throughout the UV-A to UV-C range, allowing for photocatalysis to co-occur with photolysis when the xenon lamp is used without the 280–450 nm wavelength filter (transmits 240-280 nm and λ > 450 nm).

Table 5-1. Reduction of Nitrate or Nitrite under Wavelength Filtered or Unfiltered Xenon Lamp Irradiation (UV Wavelengths Emitted: 240-280nm or 240-400nm, respectively).

Initial N-Species	Effective Irradiation Wavelengths (UV-only)	Applied Fluence Dose (mJ/cm^2)	Applied Photon Fluence Dose ($photons/cm^2$)	P90 Dose (g/L)	Initial Formic Acid (mM)	% Reduction of Total Aqueous Nitrogen
NO_3^-	240-400	1.70E+08	4.83E+20	0	0	0.5
NO_3^-	240-400	1.70E+08	4.83E+20	0	40	21.2
NO_3^-	240-400	1.70E+08	4.83E+20	1	40	46.2
NO_2^-	240-400	1.70E+08	4.83E+20	0	0	9.4
NO_2^-	240-400	1.70E+08	4.83E+20	0	40	83.2
NO_2^-	240-400	1.70E+08	4.83E+20	1	40	99.9
NO_3^-	240-280	2.30E+07	5.49E+19	0	0	5.0
NO_3^-	240-280	2.30E+07	5.49E+19	0	40	20.1
NO_3^-	240-280	2.30E+07	5.49E+19	1	40	13.9
NO_2^-	240-280	2.30E+07	5.49E+19	0	0	3.8
NO_2^-	240-280	2.30E+07	5.49E+19	0	40	82.1
NO_2^-	240-280	2.30E+07	5.49E+19	1	40	84.3

Experiments were conducted using 285, 300, and 365 nm LEDs operating simultaneously under identical initial aqueous conditions as those in Figure 3. This LED configuration outperforms the other light sources on a reduction per-photon or per-mJ basis (Figure 5-4), though it requires a longer time to achieve nitrate reduction due to the low photon fluence rate of the LEDs. The maximum achieved photon fluence dose was 2.3×10^{19} photons/cm^2 for the LED, which is 2.4 times lower than the xenon lamp experiment (Table 1) and 18 times lower than the mercury lamp due to the scale of the system employed. At an equivalent 0.23×10^{20} photon/cm^2 photon fluence dose in the mercury lamp experiment, ~9% of nitrate reduction was achieved compared with 15% for polychromatic LEDs. On a time-basis, these two polychromatic photoreactors appear to perform quite differently, but the energetic and photonic efficiency are similar. This result should allow for transitioning from Hg-based irradiation sources to more innocuous and compact LED systems where appropriate (e.g., small systems, point of use facilities) when high output LEDs become available. These experiments show the need to select the appropriate units of fluence to evaluate nitrate photocatalytic reduction; the preferred units consider wavelengths in the photoactive region (200–400 nm) for TiO_2 and aqueous N-species.

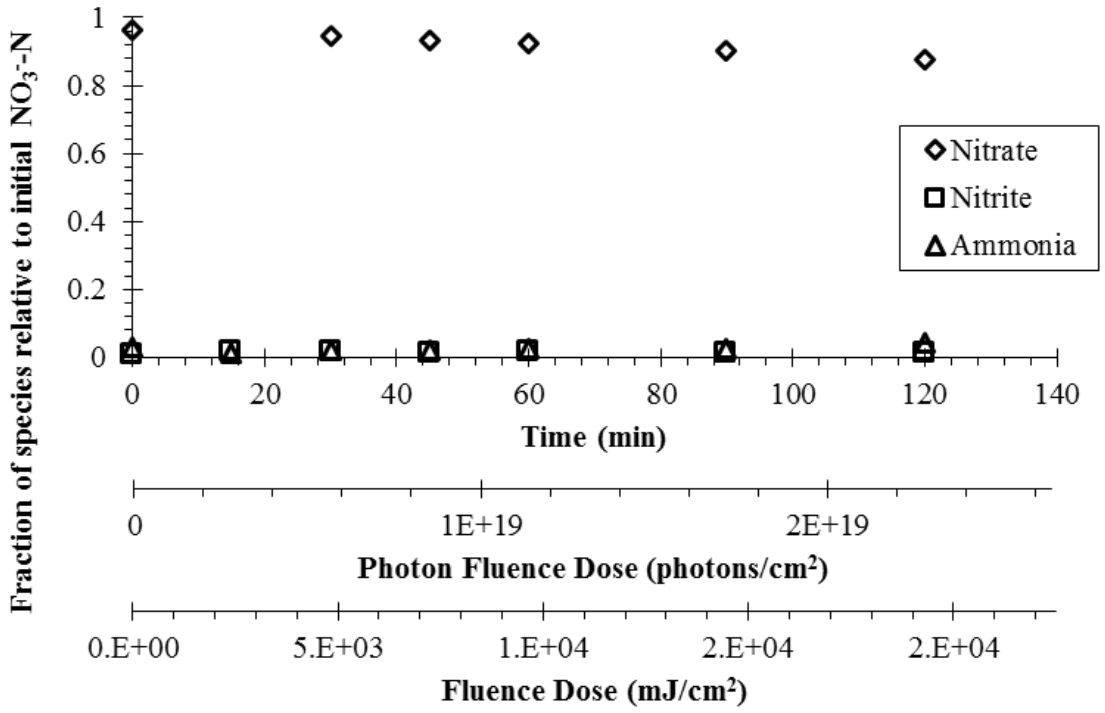

Figure 5-4. NO_3^- photocatalytic reduction and by-product formation (nitrite and ammonia) under 285, 300, 365nm UV-LED irradiation with 1 g/L TiO_2 (P90) and 40mM HCOOH (pH=2.51± 0.05).

3.3 Kinetics and Selectivity of By-Products during Nitrate Photocatalysis

Tables 5-2 and 5S1 show that photocatalytic reduction of nitrate yields the following final conversion of NO_3^- and selectivity to nitrogen gases $S(N_{gases})$ for the medium pressure Hg, Xe (240-280 nm), Xe (240-400 nm), and UV-LEDs (285, 300, 365 nm): 78% with 89% $S(N_{gases})$, 14% with 100% $S(N_{gases})$, 46.2% with 100% $S(N_{gases})$, and 10% with 82% $S(N_{gases})$, respectively. Based on these values alone, comparison would yield significantly different key insights than further examination based on photon fluence and energetic kinetic rates. Changes in nitrate removal throughout an experiment were fitted by pseudo-first order kinetics with respect to time, photon fluence dose, or fluence dose. Figure 5 illustrates an example of photocatalytic nitrate reduction data for the

medium pressure Hg lamp fitted with pseudo-first order kinetics and reporting of rate constants using three corresponding units for kinetics. Table 5-2 and 5S1 show the rate constants (k) expressed in three different forms—time (sec^{-1}), photon fluence dose $(photon/cm^2)^{-1}$, and fluence dose $(mJ/cm^2)^{-1}$—for all irradiance sources. These tables also contain values for aqueous and gaseous selectivity for polychromatic experiments.

Table 5-2. Summary of Kinetic Data for NO_3^- Reduction Experiments under Varied Irradiance Conditions*

Light Source	Final % NO_3^--N Reduction	k_{time} ($10^{-5} s^{-1}$)	k_{light} (10^{-22} cm^2/photon)	k_{energy} ($10^{-6} cm^2$/mJ)	TNR (% N) Removed	Selectivity (%)		
						N_g	NO_2^-	NH_4^+
Medium Pressure Hg	77.96	64.5	38.3	10.9	69.1	89	0	11
Xe (240–280nm)	13.9	2.31	0.18	0.065	13.9	100	0	0
Xe (240–400nm)	46.2	17.3	1.49	0.581	30.6	100	0	0
UV-LED (285, 300, 365nm)	9.76	1.60	63.9	12.3	9.48	82	2	16

*All experiments in Table 2 were conducted with initial NO_3^--N concentration of 100mg-N/L, 40mM HCOOH, and 1 g/L P90 TiO_2 catalyst. Wavelength data include all produced wavelengths (200–1100nm).

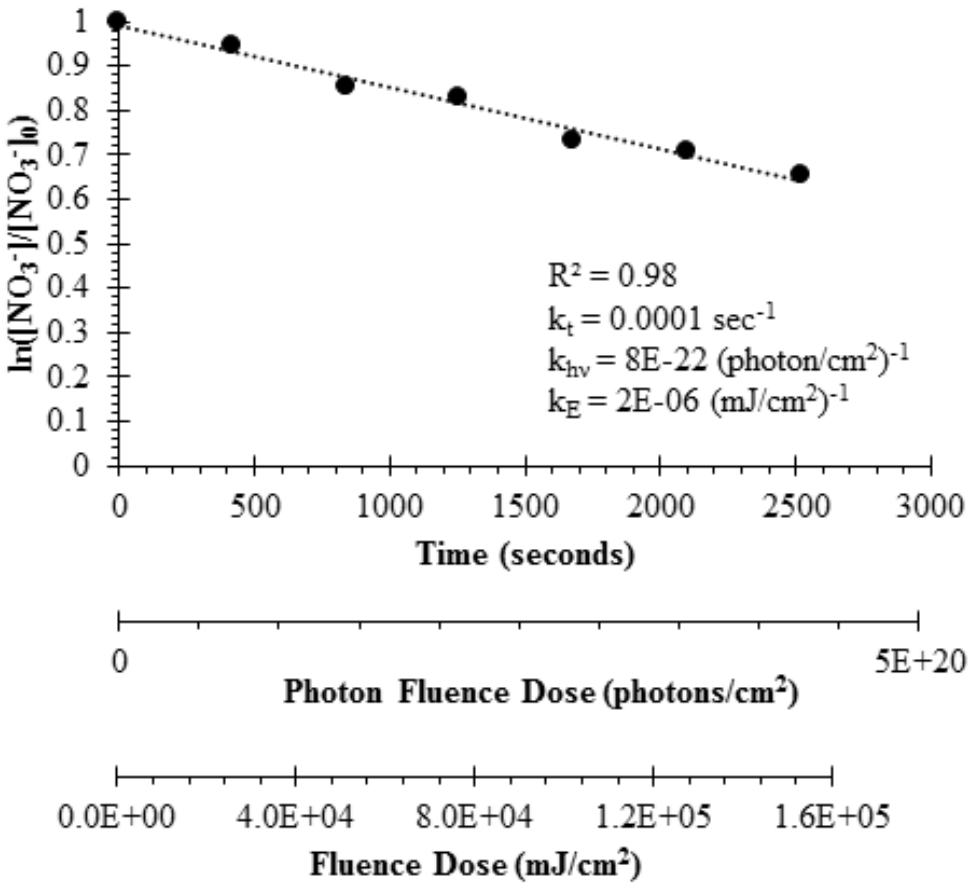

Figure 5-5. Pseudo-first order nitrate removal kinetics using medium pressure lamp with 1 g/L TiO_2 (P90), and 40mM HCOOH (pH = 2.5±0.05) with respect to time, photons, and energy.

Figure 5-6 shows half-lives of nitrate reduction computed from the pseudo-first order rate constants ($t_{1/2} = \frac{\ln 2}{k}$) with respect to experimental time, photon fluence dose, and fluence dose. Shorter $t_{½}$ values occurred for medium pressure Hg irradiation on a time-basis or LED irradiation on a photon- and energy-basis. Accounting for all incident wavelengths (200–1100 nm), the UV-LED combination had the shortest half-life (i.e., best performance) at 1.08×10^{20} photons/cm^2 (0.56×10^5 mJ/cm^2) compared to 1.81×10^{20} photons/cm^2 (0.63×10^5 mJ/cm^2) for the medium pressure Hg lamp. Due to the broad-band

irradiation from the xenon lamp, half-life for reduction of nitrate for both UVC and UVA-UVC irradiation was > 10x higher than that of the medium pressure or LED sources. This is because much of the energy used to produce photons for the medium pressure Hg and xenon lamps is effectively wasted in a TiO_2-based photocatalytic system because UV wavelengths are required for excitation.

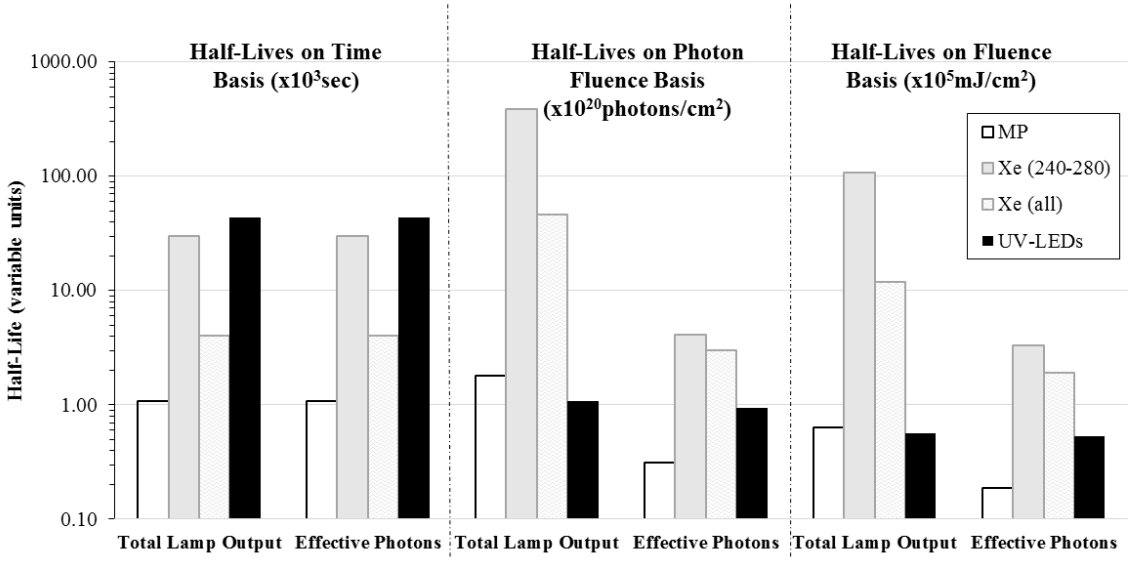

Figure 5-6. Half-life of NO_3^- reduction kinetics with respect to time ($x10^3$ s), photons ($x10^{20}$ photons/cm^2), and energy ($x10^5$mJ/cm^2) for medium pressure lamp, xenon lamp with UV-filter to include 240-280nm only or xenon lamp without UV filter to include all wavelengths, and 285, 300, 365nm UV-LED combination array. Experimental parameters: 100mg-NO_3-N/L, 1 g/L P90, 40mM HCOOH (pH = 2.5±0.05). Total lamp output considers all wavelengths incident to reactor, and effective photons delineates wavelengths (<380nm) absorbable by TiO_2.

Differences in nitrate removal and product selectivity between irradiation sources indicates key wavelengths dominated the process of nitrate reduction to nitrogen gases. In broad-spectrum irradiance conditions, a photonic saturation occurred, where excess light merely lowered efficiency rather than promoting nitrate reduction. A secondary effect was

the known mass-transfer limitation of nitrate in photocatalytic systems. This limitation further induces the photonic saturation while catalyst reactive sites may undergo excitation and recombination prior to contact with aqueous nitrogen species (Shand & Anderson, 2013a).

3.4 Photocatalysis and Direct Photolysis of HONO and NO_2^-

Nitrite photolysis with a xenon lamp led to 9% TNR for the 240–400 nm range and only 4% TNR for the 240–280 nm range (Table 5-1) at a photon fluence dose of $4.83x10^{20}$ photon/cm^2 and $5.49x10^{19}$ photon/cm^2, respectively. In contrast, over the same wavelength ranges, the effect of pH led to HONO photolysis and more removal compared to NO_2^-: 83% TNR (240–400 nm) and 82% TNR (240–280 nm). Photocatalytic xenon lamp experiments with HONO used 1 g/L P90 and achieved 99.9% TNR (240–400 nm) and 84% TNR (240–280 nm). This increased HONO removal (10 times higher performance HONO:NO_2^-) corresponded to only a 1.6x higher molar absorptivity in the ultraviolet wavelength range, further illustrating interplay of quantum yield (Φ) and molar absorptivity (ε). The quantum yield of the photolysis for HONO ($\Phi_{355nm} \approx 0.4$) is significantly higher when compared to nitrite ($\Phi_{355nm} = 0.025$) at 355 nm (Mack & Bolton, 1999b). Acidification of NO_2^- to HONO greatly enhanced total nitrogen removal and increased selectivity away from aqueous ammonium.

On a photon fluence basis, higher aqueous nitrogen removal was observed with LED irradiation compared to the broad-spectrum xenon lamp. HONO (pH= 2.5) reduction using the 365 nm LED achieved >93% TNR for photolysis (Figure 5S1) and >95% TNR with TiO_2 (Figure 5S2). Negligible (<5%) ammonium was produced under individual illumination with 285 nm or 300 nm LED and combined irradiation of 285 nm and 300 nm

LEDs for both photolysis and photocatalysis. Complete reduction of HONO in solution with < 2% ammonium production was observed with 1.71×10^{19} photons/cm^2 at 365 nm. In contrast to the xenon lamp results, the LED light source (365 nm) showed no competitive advantage for nitrite reduction using TiO_2 (compared against direct photolysis) (Figure 5-7) due to the high absorbance and quantum yield of HONO and absorption and scattering of light by TiO_2 at 365 nm. Further, the discrete wavelength irradiation (UV-LED) used only one-third of the photons (200 nm to 1100 nm) compared to the broad-spectrum (xenon) irradiation for complete removal of HONO.

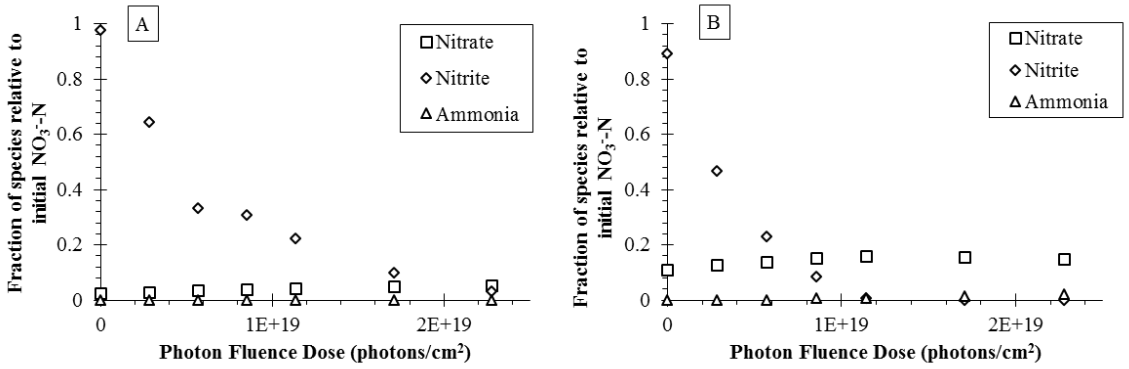

Figure 5-7. Photolytic (A) and photocatalytic (B) nitrite reduction at 365nm with formic acid (pH=2.5) as a sacrificial hole scavenger. Photocatalytic experiments with 1 g/L P90.

Selectivity of HONO reduction under photolytic and photocatalytic conditions with (1) single UV-LEDs (285 nm, 300 nm, or 365 nm) or (2) combinations thereof yielded > 88% and > 94% conversion to N-gases, respectively (Figure 5S1, 5S2). For photocatalytic experiments, selectivity to undesired ammonium was always < 2%. Under illumination of a combination of 285 nm and 300 nm irradiation, up to 100% selectivity to nitrogen gases

was achieved at > 97% photocatalytic reduction of HONO and 92.5% photolytic HONO reduction. HONO oxidation to nitrate was 4.6±0.5% using a single 285 nm or 365 nm LED or a combination of 285, 300, and 365 nm irradiation for photocatalysis and increased to 6.0±0.9% for photolysis across all wavelength combinations. Selectivity of aqueous ammonium in lieu of nitrogen gases in photolytic experiments with UV-LEDs was ordered: $S_{300nm} > S_{285+300+365nm} > S_{365nm} > S_{285nm} > S_{285+300nm}$. These observations led to the understanding of wavelength influences for reaction kinetics, pathways and by-product selectivity as described in Scheme 5-2. Nitrate reduction via direct photolysis is thermodynamically feasible utilizing ultraviolet wavelengths (Goldstein & Rabani, 2007), but it is not kinetically favorable for producing nitrogen gases. This is due to the higher quantum yield of nitrite photolysis (Mack & Bolton, 1999b), which can be both reductive (N_2/NH_4^+) (Treinin & Hayon, 1970) or oxidative (NO_3^-) (Mark et al., 1996). Thermodynamically, conduction band electrons of TiO_2 are not sufficiently energetic to reduce nitrate to nitrite alone (Cook et al., 2001; Sá et al., 2009). Hence, through the use of a hole scavenger such as formic acid, both a reduction in pH and production of radical species $CO_2^{\bullet-}$, which can reduce nitrate (Montesinos, Quici, Destaillats, & Litter, 2015), are achieved. As demonstrated in this work, both photolytic and photocatalytic pathways reduced nitrite to N-gases and aqueous ammonium. Key pathways may be enhanced by combining photocatalytic and photolytic processes with wavelengths targeted toward specific intermediates, e.g., $NO/NO^{\bullet}$ which have been previously demonstrated (Hérissan et al., 2017) to increase N-gas selectivity (Eqns. 11–16). Further, pH is critical because many of the reactions require H^+ (Eqns. 4, 13, 16), and HONO is significantly more

photoactive than NO_2^-. Novel herein is the use of discrete wavelengths to demonstrate enhanced production of N-gases (Figure 5-6, 5S1, 5S2, and Scheme 5-2).

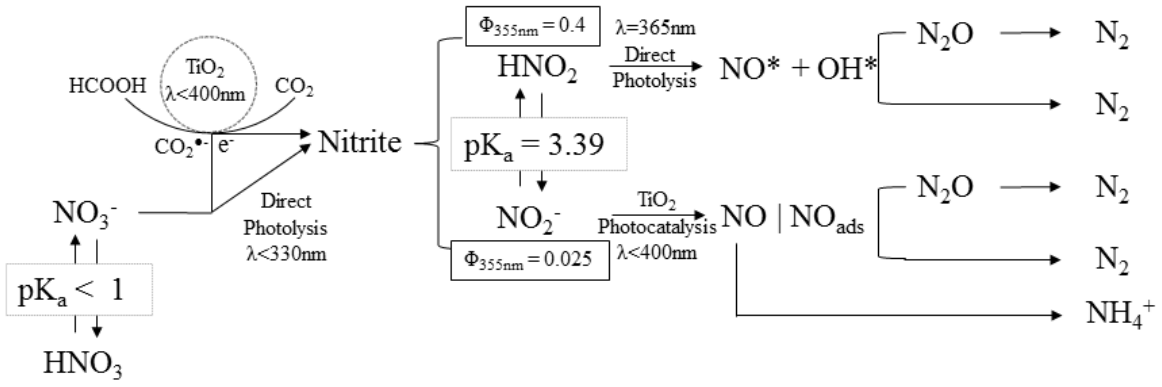

Scheme 5-2. Conceptual model for nitrate reduction to nitrogenous intermediates and by-products in acidic and neutral pH conditions.

Acknowledgements

This work was partially funded through the Nano-Enabled Water Treatment Technologies Nanosystems Engineering Research Center by the National Science Foundation (EEC-1449500). This research was also funded by the United States Environmental Protection Agency (RD 83560301) through the Design of Risk-reducing, Innovative-implementable, Small-system Knowledge (DeRISK) Center. Graduate student support was partially provided by a Dean's Fellowship from the Ira A. Fulton Schools of Engineering at Arizona State University.

Supplementary Information

Table 5-S1. Summary of Kinetic Data for NO_3^- Reduction Experiments under Varied Irradiance Conditions*

Light Source	Final % NO_3^--N Reduction	k_{time} ($10^{-5}s^{-1}$)	k_{light} (10^{-21} cm^2/photon)	k_{energy} ($10^{-6}cm^2$/mJ)	TNR (% N) Removed	Selectivity (%)		
						N_g	NO_2^-	NH_4^+
MP Hg	77.96	64.5	22.2	37.1	69.1	89	0	11
Xe (240-280nm)	13.9	2.31	1.69	3.09	13.9	100	0	0
Xe (240-400nm)	46.2	17.3	2.31	3.66	30.6	100	0	0
UV-LED (285, 300, 365nm)	9.76	1.60	7.41	13.0	9.48	82	2	16

*All experiments in Table S1 were conducted with initial NO_3^--N concentration of 100mg-N/L, 40mM HCOOH, and 1g/L P90 TiO_2 catalyst. Utilizes wavelength data for only UV wavelengths (200-400nm) defined as photocatalytically active wavelengths for TiO_2.

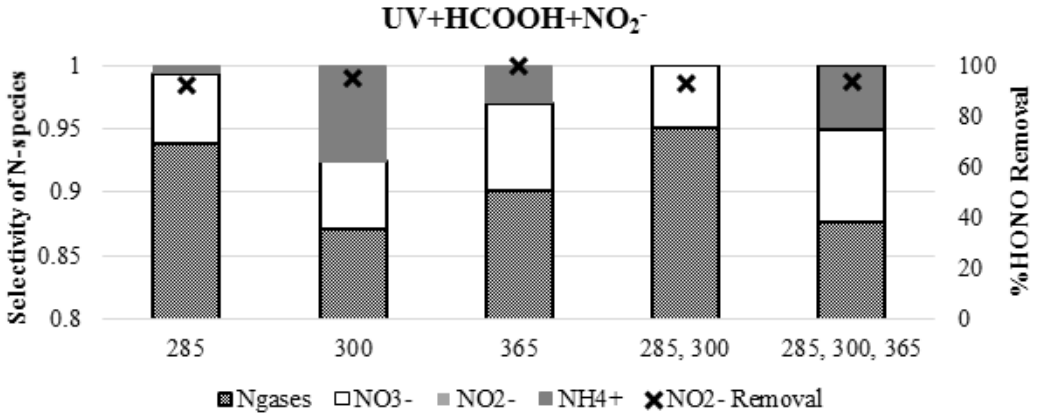

Figure 5-S1. Photolytic reduction of nitrite at varied wavelength with formic acid (pH=2.5) as a sacrificial hole scavenger.

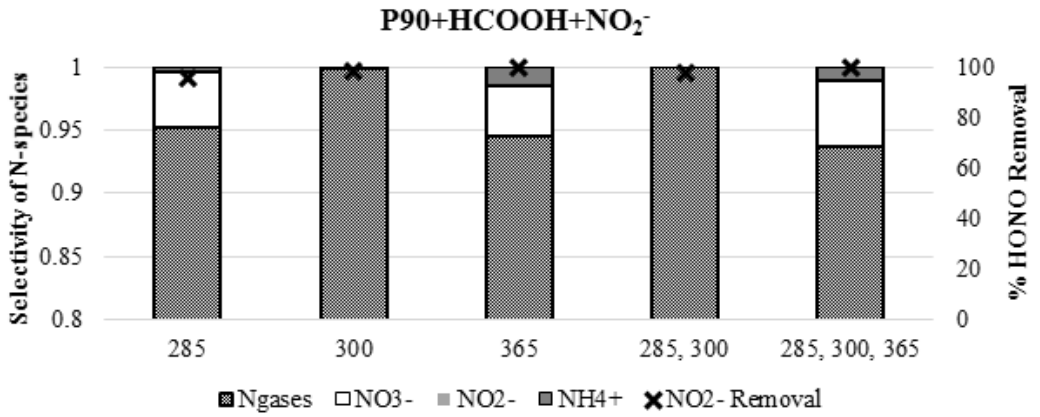

Figure 5-S2. Photocatalytic reduction of nitrite at varied wavelength with formic acid (pH=2.5) as a sacrificial hole scavenger and 1g/L P90 TiO_2.

CHAPTER 6

COUPLING LIGHT EMITTING DIODES WITH PHOTOCATALYST-COATED OPTICAL FIBERS IMPROVES QUANTUM EFFICIENCY OF POLLUTANT OXIDATION

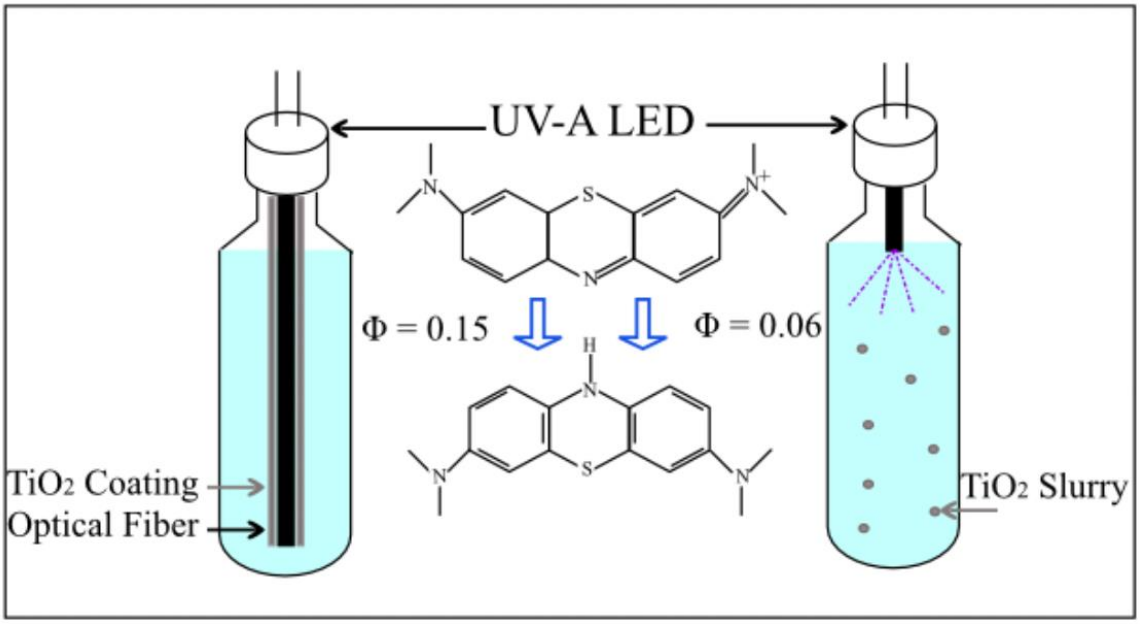

Abstract

A photocatalyst-coated optical fiber was coupled with a 318-nm ultraviolet-A light emitting diode, which activated the photocatalysts by interfacial photon-electron excitation while minimizing photonic energy losses due to conventional photocatalytic barriers. The light delivery mechanism was explored via modeling of evanescent wave energy produced upon total internal reflection and photon refraction into the TiO_2 surface coating. This is the first work to explore aqueous phase LED-irradiated optical fibers for treating organic pollutants and the first to propose a dual-mechanistic approach to light delivery and photocatalytic performance. Degradation of a probe organic pollutant was evaluated as a function of optical fiber coating thickness, fiber length, and photocatalyst attachment method and compared against the performance of an equivalent catalyst mass in a completely mixed slurry reactor. Measured and simulated photon fluence through the optical fibers decreased as a function of fiber length, coating thickness, or TiO_2 mass externally coated on the fiber. Thinner TiO_2 coatings achieved faster pollutant removal rates from solution, and dip coating performed better than sol-gel attachment methods. TiO_2 attached to optical fibers achieved a 5-fold higher quantum yield compared against an equivalent mass of TiO_2 suspended in a slurry solution.

Keywords: oxidation, titanium dioxide, photolysis, reactor, optical fiber

Introduction

Photocatalyst-coated optical fibers have potential to oxidize organic compounds in air or water(Denny, Scott, Peng, et al., 2010; Hou & Ku, 2013; Nicola J Peill & Hoffmann, 1995) while simultaneously overcoming barriers to using photocatalyst suspensions in water treatment, including recovering the suspended particles and reducing the light scattering/occlusion by aqueous constituents and photocatalytic nanoparticles.(Stancl, Hristovski, & Westerhoff, 2015b) However, optical fibers only transmit light axially by coating or cladding fiber surfaces with materials that have higher refractive index than the fiber itself.(Tandon et al., 2013) Challenges for photocatalyst-coated optical fibers include effectively delivering light into the fibers and optimizing photon fluence with fiber length or catalyst thickness.(Nicola J. Peill & Hoffmann, 1998; Nicola J Peill & Hoffmann, 1995) Experimental evidence and modeling suggests an optimal photocatalyst thickness exists to degrade pollutants,(Nicola J Peill & Hoffmann, 1996, 1998; Nicola J Peill et al., 2002; W. Wang & Ku, 2003a) but prior studies exclude contaminant mass transfer to the photocatalyst surface or the electron-hole recombination of the photocatalyst in the coating layer. Concentrated solar light can be delivered into optical fibers,(N J Peill & Hoffmann, 1997b) but without appropriate filters, infrared wavelengths generate heat that causes detachment of coated photocatalysts and composite materials.(Bilodeau, Scheer, & Haugen, 1998; Marinangeli & Ollis, 1980) Additionally, for solar or xenon-arc light sources, heat buildup from the infrared spectrum needs to be reduced using a filtering system to limit light outside the wavelength range suitable for photocatalysis (i.e., 310–375 nm is suitable for TiO_2).(Barton et al., 2016; Denny, Scott, Pareek, et al., 2010; Nicola

J Peill & Hoffmann, 1996) To limit heat buildup, we investigated 318 nm monochromatic light from a light emitting diode (LED) delivered into the optical fiber.

UV-LED technologies reduce the need to filter light from conventional polychromatic UV-radiation sources and deliver narrow bandwidth UV irradiation to the fibers without compromising power output, lifetime, and luminous efficiency. While UV-C LEDs used for pathogen inactivation remain costly,(Beck et al., 2017; Chatterley & Linden, 2010) less expensive visible light, UV-A and UV-B LEDs, are commercially available and more energy efficient(L H Levine et al., 2011) than xenon- or mercury-based light sources. Because of their compact design and technological advancements in the field of optical communications,(Yeh et al., 2014) light from LEDs can be directly coupled to optical fibers for environmental applications. This approach effectively delivers light into the optical fibers and has been investigated for degrading organic pollutants in air.(Denny, Scott, Peng, et al., 2010) In water-based reactors, immobilizing photocatalysts on coated optical fibers eliminates the need to recover (e.g., via ceramic membranes)(Stancl et al., 2015a) suspended nanomaterials from slurry suspensions. Advances in first principles photonic modeling of optical fibers coupled with experimental validation can advance the use of photocatalysis for water purification. We hypothesized that a fixed-film system can be designed to achieve more efficient pollutant degradation than an equivalent slurry system.

There are three key barriers to using optical fibers for water treatment: the longitudinal passage of light; the effects of coating materials, including material thickness and total mass loading; and the radical production pathways on the exterior of optical fibers. We collected data to fill these knowledge gaps by quantifying quantum yield as a

function of TiO_2 coating thickness and optical fiber lengths to optimize catalyst-absorbed light intensity. Electrostatic attachment of commercially-fabricated TiO_2 (P25) was compared against sol-gel precipitation with calcination directly on optical fibers. Experimental evidence using methylene blue (MB) as a probe molecule was also supported by optical modeling to enhance understanding of system parameters and energy interactions at the fiber-catalyst-water interface.

Experimental Methods and Materials

Photocatalytic and photolytic experiments using the UV-LED/TiO_2/optical fiber system were conducted in an 8.5 cm long and 1 cm diameter cylindrical glass batch reactor (V = 10 mL) with magnetic mixing at the bottom. The cylindrical glass batch reactor enabled *in-situ* quantification of methylene blue (MB, Sigma Aldrich) with a spectrophotometer (HACH DR5000) at 664 nm (95000 M^{-1} cm^{-1}, (Cenens & Schoonheydt, 1988)) without the need to extract sample volumes from the reactor for analysis. A 318-nm UV-LED (I = 1.5 mW cm^{-2}, SETi, UV-TOP), which utilized 5 V input at 3 mA, was mounted above the reactor. In most cases, a single fiber was polished as described in SI and attached to the LED. Optical fibers, LED mounts, and polishing/stripping equipment were purchased from Thorlabs (FT1000UMT; numerical aperture of 0.39, Ø1000 µm Core Multimode Optical Fiber, High-OH for 300–1200 nm). Optical fibers were prepared by stripping the polymeric buffer coating and cladding, assembling into a quick-connect SMA (SubMiniature version A) connector, and polishing both ends of each optical fiber (described in SI). Polished fibers were coated by either sequential electrostatic dip coating with preformed TiO_2 (P25 or P90 obtained from Evonik) or sol-gel synthesis

methodologies using titanium (IV) isopropoxide (TTIP) with calcination at 500 ºC to achieve different layer thickness and surface coverage homogeneity. A detailed description of the fiber preparation protocol is provided in SI. Masses of the TiO_2 layers on the optical fibers were measured gravimetrically by the weight of the optical fibers before and after the dip coating/drying cycles (0–20 coating cycles). The TiO_2 coating surface morphology was obtained by scanning electron microscopy with energy dispersive X-ray spectroscopy (SEM/EDX: Philips XL30-EDAX). TiO_2 layer thickness was obtained from SEM images of vertically-oriented fibers.

Optical fibers were suspended into the reactor solution with 4.0 μM MB (pH ≈ 6) in double deionized water at a resistivity above 18.2 MΩ-cm (Millipore Inc.). Direct photolysis experiments were conducted by connecting a 1-cm (longitudinal) uncoated optical fiber to the 318-nm LED to deliver light into the solution. Photocatalytic experiments were conducted with (1) TiO_2-coated optical fibers (7 cm coated length) directly coupled to a 318-nm LED or (2) a mixed slurry system of P25 irradiated with the 1 cm uncoated optical fiber and a 318-nm LED (see SI for details). Experimental parameters are outlined in Table 6-1. Mechanistic understanding of the optical fiber exterior interface was approached via mathematical modeling of the system optics to assess excitation via evanescent wave energy or refraction of photons into the TiO_2 coating layer.

Light intensities emitted from the LED and from the terminal end of the fiber tips were measured by a radiometer (Avaspec 2048L) to compare catalyst coating methods, length, and thickness. The LED had an intensity of 168 μW cm^{-2} between 308 and 330 nm. Light absorbed by the coated photocatalyst was indirectly determined as a difference between radiometric measurements with and without coating. Photon fluence calculations

are shown in SI. Only wavelengths between 308 and 330 nm were considered for the 318-nm LED, which was >99% of emitted light.

Quantum yields (Φ) of the dip-coated fibers, sol-gel-coated fibers, and slurry systems at equivalent catalyst doses were calculated as follows: (J. R. Bolton et al., 2001; Serpone, Salinaro, & N. Serpone, 1999)

$$\Phi = \frac{-k\,V\,[\mathrm{MB}]}{I_{abs}} \qquad \textbf{Equation 1}$$

where k is the pseudo first order reaction rate of MB degradation in different systems (s^{-1}), V is the liquid volume of the reactor (L), [MB] is the initial methylene blue concentration (mol-MB L^{-1}), and I_{abs} is the light intensity absorbed by the TiO_2 coating layer (mol-photons s^{-1}; details for the calculation of I_{abs} are included in SI).

Table 6-1. Experimental Parameters and Resultant Quantum Yields

ID	Catalyst Delivery	Catalyst Mass per Volume (mg/10 mL)	Mass Loading Rate of TiO_2 per Coated Layer	Number of Coating Layers	Quantum Yield, Φ
A	None	0	-	-	0.01
B	P25 Slurry	0.02	-	-	0.02
C	P90 Slurry	0.02	-	-	0.02
D	P25 Slurry	0.1	-	-	0.06
E	P25 Dip-Coat	0.02	0.0029 mg cm^{-1}	1	0.15
F	P90 Dip-Coat	0.02	0.0029 mg cm^{-1}	1	0.12
G	P25 Dip-Coat	0.1	0.0029 mg cm^{-1}	5	0.12
H	Sol-Gel	0.24	0.034 mg cm^{-1}	1	0.14
I	Sol-Gel	1.68	0.034 mg cm^{-1}	5	0.06

Results and Discussion

The dip coating method deposited 0.0029 ± 0.0001 mg cm^{-1} of TiO_2 per coating cycle for each coating cycle up to 20 coating cycles (i.e., 0.4 mg TiO_2 for 20 cycles on a 7 cm fiber). The TiO_2 coating thickness ranged from uncoated to 8175 ± 634 nm with 5 coating cycles (0.1 mg coated mass, Figure 6S1). Additional dip coating, up to 20 total layers, continued to increase TiO_2 mass but did not increase TiO_2 thickness. The higher TiO_2 mass on fibers beyond 5 dip coating cycles was attributed to the filling of cavities on the TiO_2 coating layers (Figure 6S2). The sol-gel-coated fibers contained 0.034 mg cm^{-1} of TiO_2 (per coated layer) and had a denser TiO_2 coating compared to the dip coating method (0.0029 mg cm^{-1}). SEM of sol-gel samples from TTIP and P25 precursors indicated more uniform coating than dip coatings of fewer than 5 coating cycles (Figure S3).

Optimizing catalyst-absorbed light intensity

Figure 6-1a shows the relationship between light intensities absorbed by TiO_2 with increasing coating layers and TiO_2 coating mass for a 28-cm long optical fiber. Higher TiO_2 coating masses resulted in more light flux absorbed by TiO_2, increasing from 1.71 ± 0.52 × 10^{-12} Einstein cm^{-2} s^{-1} to 5.36 ± 0.33 × 10^{-12} Einstein cm^{-2} s^{-1}. These measurements indicate that 16% of photons were absorbed when the fiber was coated with 1 coating layer (0.02 mg TiO_2), whereas 50% were absorbed when the fiber underwent 5 to 20 coating cycles (0.1 mg to 0.4 mg TiO_2), suggesting that the change in light intensity absorbed by TiO_2 followed an attenuating trend. Across all the fiber samples, light transmission exponentially decreased with higher attached catalyst mass or thickness (Figure S4). Light interacting with the TiO_2 coating may generate excitons, heat (i.e., recombination of electrons and holes), or simply become scattered at the fiber-TiO_2 interface.

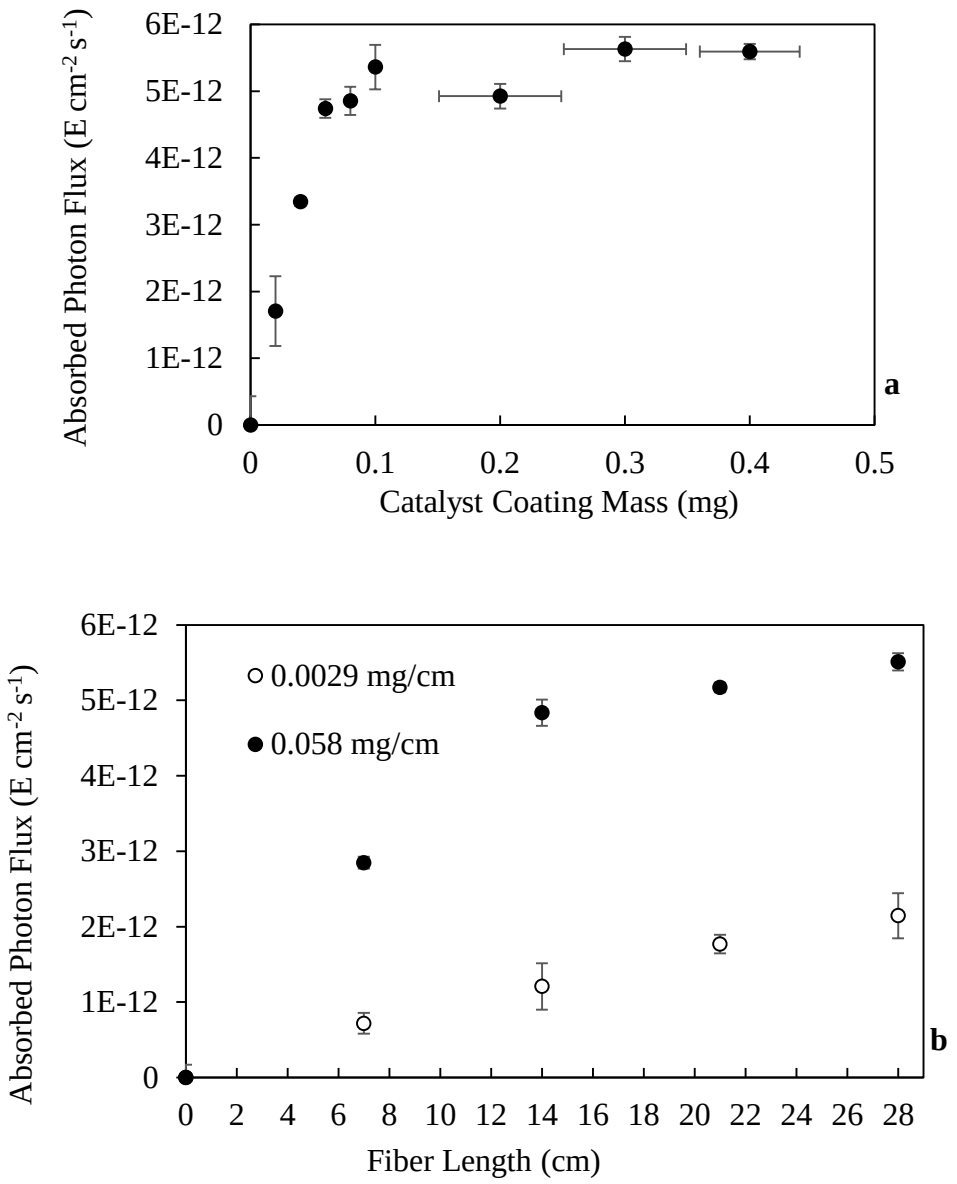

Figure 6-1. Light intensity from 318 nm UV-LED (168 μW cm^{-2}) absorbed in photocatalyst-coated optical fiber as a function of (a) dip-coated mass on 28 cm optical fiber; (b) optical fiber length (0 cm to 28 cm) with two different TiO_2 coating thicknesses (0.0029 mg cm^{-1} and 0.058 mg cm^{-1}, which corresponds to 1 and 20 layers of coating, at 0.02 mg and 0.4 mg total coating, respectively). Error bars represent 1σ of three replicate radiometric or gravimetric measurements.

Experiments conducted with variable optical fiber lengths and similar deposited TiO_2 mass loading are shown in Figure 6-1b. For a dip-coated mass loading rate of 0.0029 mg cm^{-1} (i.e., one coating), the photon flux absorbed by TiO_2 increased 3x from 7.2 ± 1.4 × 10^{-13} to 2.2 ± 0.3 × 10^{-12} Einstein cm^{-2} s^{-1} for a 4x increase in optical fiber length (7 to 28 cm). At a higher dip-coated TiO_2 mass loading (0.058 mg cm^{-1}, 20 coatings), the light intensity absorbed by the TiO_2 has a higher net absorbance, increasing from 2.85 ± 0.08 × 10^{-12} to 5.51 ± 0.14 × 10^{-12} Einstein cm^{-2} s^{-1} at 7 and 28 cm, respectively. In both cases, the light absorption increased to maximum values in longer optical fibers with a decreasing differential photon flux absorbed by TiO_2. The incremental absorption attenuation was more acute in optical fibers with thicker TiO_2 coatings (i.e., higher dip-coated mass loading). This was likely due to the increased homogeneity of TiO_2 in contact with the quartz surface of the optical fibers that occurred with thicker TiO_2 coatings.

For photon flux at an equivalent TiO_2 mass loading, light absorption increased with coated fiber length. Furthermore, a higher TiO_2 coating density (mg cm^{-1}) allowed for higher photon absorbance due to photon refraction into the TiO_2, though the increase was attenuated at higher loadings. Light absorbed by the photocatalyst attenuated asymptotically when increasing the coating mass and the fiber length (Figure 1), leading to complete light attenuation at some point with negligible increased absorbance for added length or thickness. For our UV-LED/TiO_2/optical fiber system, this saturation (i.e., >95% of maximum absorbed photon flux) occurred at 0.1 mg catalyst coating mass and fiber lengths above 14 cm. This observation is consistent with a transition from total internal reflection (TIR) at zero coating layers to complete refraction into the TiO_2 coating layer upon a homogenous surface layer.(Peatross & Ware, 2008) However, note that some light

(~ 47%) transmits through the TiO_2-coated fiber in all cases due to the angle of incidence of those photons and short experimental fiber length (Figure S4). In this case, the photons do not collide with the optical fiber wall and do not result in either TIR or refraction, as seen in other reports.(Nicola J Peill & Hoffmann, 1996) The finding of an exponential attenuation of light density with increasing coating thickness is comparable to Peill et al.'s study.(Nicola J. Peill & Hoffmann, 1998) Wang and Ku reported difficulty in tabulating a value for the photon flux absorbed into the TiO_2 layer with an optical fiber substrate due to the inability to accurately measure the photonic endpoints: scattering, transmission, absorption, and utilization or absorption and recombination/loss(W. Wang & Ku, 2003a). Therefore, in contrast to previous works that solely focused on fixed-length coating thickness, our work significantly advances knowledge and computation methodology for the optimal fiber length based on the attenuating light flux absorbed as illustrated in Figure 6-1b.

Quantum yield of the MB-UV-LED/TiO_2/optical fiber system

Figure 6-2 shows MB transformation kinetics for different TiO_2 coating methods and loadings (defined in Table 6-1). MB degradation follows pseudo-first order kinetics, with rate constants (k) determined as shown in Figure 6S5. Due to MB direct absorption of light at 318 nm,(Dariani et al., 2016) photolysis contributes slightly to the MB bleaching. An uncoated optical fiber (control) degraded less than 5% of the MB over the 4 hour test. Faster MB degradation occurred when TiO_2 was present. For TiO_2 in the mixed slurry reactor, MB degradation rates increased with higher TiO_2 dosages and plateaued for TiO_2 above 5 mg/L. Presumably, MB degradation is limited to a reaction zone where light penetrates the water-TiO_2 slurry.(McCullagh, Robertson, Adams, Pollard, & Mohammed,

2010) MB degradation rates in the TiO_2 slurry reactor were always lower than experiments with equivalent TiO_2 mass attached to optical fibers and the same photon fluence.

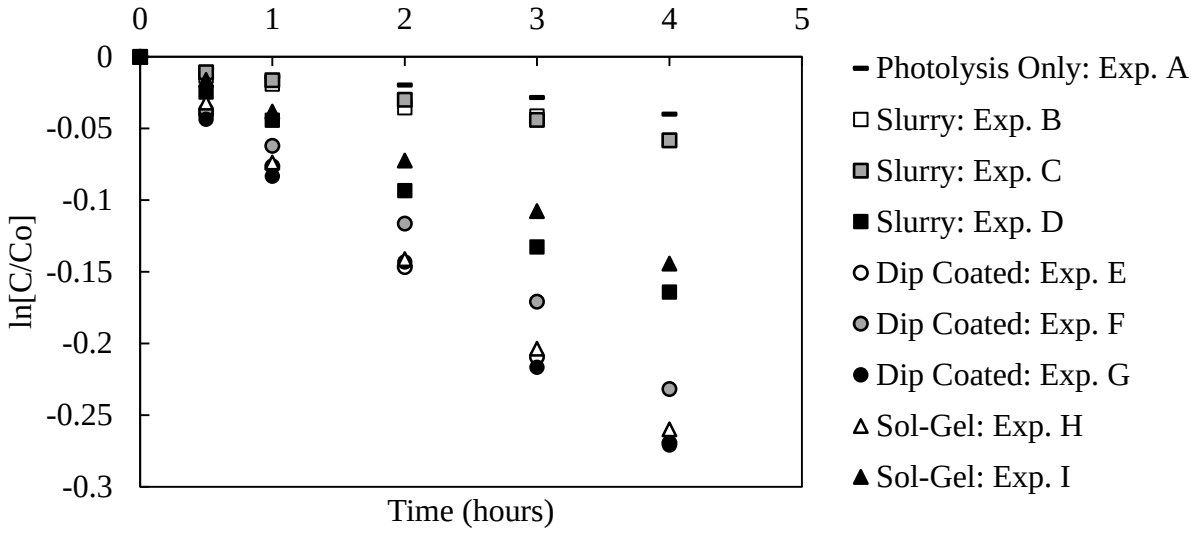

Figure 6-2. Pseudo-first order degradation kinetics for methylene blue at different TiO_2 doses and coating regimes in 10 mL reactor volumes.

Figure 6-2 also shows that similar MB degradation rates were observed for all the dip-coated TiO_2 optical fibers, despite being loaded with 5x different TiO_2 masses. Although more light was absorbed as the coating layer became thicker (Figure 1a), the additional light absorbed by the thicker coating layer did not increase MB degradation. The thicker coating layer potentially created barriers for MB mass transfer to inner reactive sites in the TiO_2 coating layer while also limiting the transfer of excitons through the TiO_2 grain boundaries.(Richter & Schmuttenmaer, 2010; Salafsky, 1999) This resulted in a non-reactive, inert TiO_2 coating zone that only absorbs light and dissipates heat. Therefore, TiO_2 coating layer thickness design should optimize the coating thickness to provide enough reactive sites rather than maximizing absorbed light. Peill et al.(Nicola J Peill &

Hoffmann, 1996) report that 7.0 μm is an optimal thickness for a 20 cm length fiber used in aqueous phase oxidation of 4-chlorophenol, considering 100% light absorbance within the 20 cm fiber length. Thicker coatings have been reported to reduce performance due to exciton trapping prior to transport and utilization at the TiO_2/water interface.(Choi, Ko, Park, & Chung, 2001; Danion, Disdier, et al., 2004; Nicola J Peill & Hoffmann, 1995) Choi et al. conclude 1.75 μm as optimal thickness for a 30 cm length fiber in gas-phase treatment based upon a compromise between light absorption and reactant diffusion to the photocatalytically active sites.(Choi et al., 2001) Our findings align with the desired compromise of higher performance based on the photon utilization and sufficient contaminant mass transport within the reactor to the photocatalytic sites, concluding an optimal coating thickness should be ≤ 2 μm.

To assess the difference in coating methods for MB degradation performance, TiO_2 sol-gel was compared against dip coating. The sol-gel-coated fibers exhibited an inverse relationship between coating thickness and performance (Figure 6-2). This further suggests that thicker and denser mass loadings applied to the optical fibers via sol-gel methods slowed MB degradation. Sol-gel coatings provide more control of TiO_2 coating layer properties (index of refraction, porosity, crystallinity) on quartz substrates.(Hu, Yoko, Kozuka, & Sakka, 1992) However, this work observed inferior MB degradation performance for sol-gel compared against dip coating.

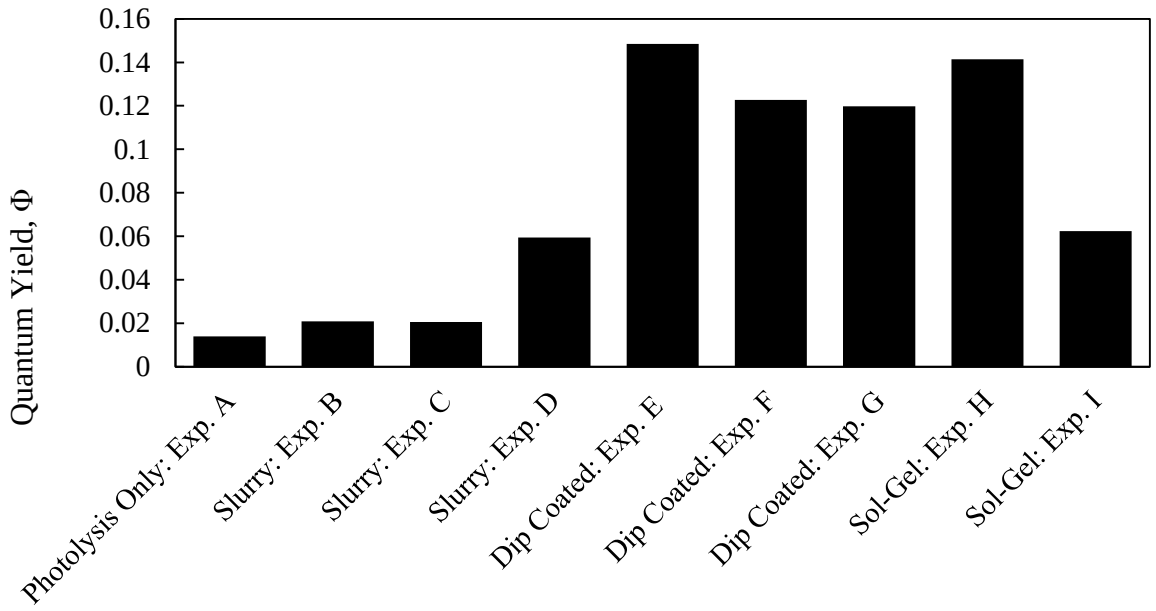

Figure 6-3. Quantum yield (Φ) of MB bleaching using photolytic or photocatalytic conditions (4 μM initial MB concentration and 10 mL reactor volume with a 7 cm fiber and 318-nm LED) based on catalyst delivery and fiber coating techniques reported in Table 6-1.

Figure 6-3, which summarizes quantum yields (Φ) of the dip-coated fibers, sol-gel-coated fibers, and slurry systems at equivalent catalyst doses, shows slurry based systems had marginally higher Φ than photolysis alone. This proves that the UV-LED/TiO_2/optical-fiber system has higher energy utilization efficiency compared to the slurry system. Values for Φ increased between 3x to 10x when the optical fibers were coated compared to photolysis alone. Experiments characterized by highest Φ were single dip-coated or single sol-gel-coated fibers. This outcome is likely a result of light penetration within the TiO_2 layer in conjunction with charge carrier transport limitations.(Könenkamp, 2000) In comparison to previously published work,(Houas et al., 2001; Matthews, 1989) we show a

100x factor improvement in quantum yield of MB bleaching using the UV-LED/TiO_2/optical-fiber system compared to polychromatic lamp-driven slurry systems.

Geometric and theoretical modeling

The fibers used in this study have a numerical aperture of 0.39, which corresponds to an acceptance angle of 23.0° to enter the fiber (relative to the axis of the fiber) and an interior illumination angle (θ) of 15.5° after the light refracts from the air into the quartz fiber. Therefore, all light rays within the fiber are between 0° (perfectly parallel to the fiber axis) and 15.5°. Total internal reflection (TIR) occurs within the fiber when the index of refraction of the fiber (n_f = 1.46 for quartz fibers) is greater than the index of refraction of the surrounding external media (n_e = 1.00 for air, 1.33 for water) and the incident angle (θ_i) of the light, measured relative to the normal of the interface between the fiber and the external media (note that $\theta_i = 90° - \theta$), is greater than the critical angle. The critical angle (θ_c) can be derived from Snell's law as (Peatross & Ware, 2008):

$$\theta_C = \sin^{-1}\left(\frac{n_e}{n_f}\right) \qquad \textbf{Equation 2}$$

Within the fiber, light incident on the quartz interface is refracted out of the fiber when the effective index of refraction of the external material (n_e) is greater than the index of refraction of the quartz fiber (n_f). The n_e depends on the coating characteristics of the fiber. For an infinitely smooth TiO_2 coating ($n_e = 2.6 > n_f$) with a thickness much larger than the illumination wavelength, any light incident on the boundary would refract out of the fiber and into the photocatalyst coating. For the case of no TiO_2 coating, the external material is water ($n_e = 1.3 < n_f$), resulting in TIR within the fiber. Figure 4 illustrates the proposed mechanism of these two activation pathways for TiO_2 coatings on optical fibers.

During TIR, the boundary conditions of Maxwell's equations result in an imaginary wavenumber (**k**), which produces a corresponding electromagnetic energy field E(**r**):(Peatross & Ware, 2008)

$$\mathbf{k} = k_y\hat{\boldsymbol{y}} + k_x\hat{\boldsymbol{x}} = i\alpha\hat{\boldsymbol{y}} + \beta\hat{\boldsymbol{x}} \qquad \textbf{Equation 3}$$

$$E(\hat{\mathbf{r}}) = E_0 e^{-i(i\alpha\hat{y} + \beta\hat{x})} = E_0 e^{\alpha\hat{y} - i\beta\hat{x}} \qquad \textbf{Equation 4}$$

The flow of this energy, (*E(***r̂***)*), called an *evanescent wave,* is parallel to the waveguide surface (x-y plane, along the fiber length), while intensity of the field (*I*) falls off exponentially away from the waveguide surface (z direction). Thus, no energy is transmitted into the second medium, and the intensity of the electric field in the z direction (*I*(z), perpendicular to the waveguide) decreases according to equation (5), described as the evanescent penetration depth: (Lensun, Smith, & Gee, 2002; Atom Sarkar, Robertson, & Fernandez, 2004)

$$I(z) = I(0)e^{-\frac{z}{d}};\ d = \frac{\lambda}{4\pi\sqrt{{n_f}^2 sin^2\theta_i - {n_e}^2}} \qquad \textbf{Equation 5}$$

This rapidly decaying energy field depends on the wavelength of the light inside the fiber (λ), the incident angle of the light to the waveguide (θ_i), and both n_f and n_e. As such, the evanescent field intensity attenuates as distance from the fiber surface (z) increases. For the case of no TiO_2 coating, an evanescent field on the exterior of the fiber was produced with intensity shown in Figure 5. Further, Figure 5 shows z-direction attenuation of the evanescent field with respect to three typical incident angles: 74.5º, 80º, and 90º corresponding to the 0º to 15º acceptance angle of the optical fiber.

The kinetic experimental data (Figure 6-2) is consistent with the theoretical mechanism (Figure 6-4), which demonstrated that increasing the TiO_2 coating thickness

should not increase the photocatalytic degradation rate. This is because neither energy of evanescent waves nor charge carrier transport can reach the TiO_2/water interface to induce reaction in thick coating layers (>2–5 μm).(Choi et al., 2001) However, excitation of the photocatalyst in the fiber-photocatalyst system is possible via either light refracting from the quartz fiber waveguide into the thinly-coated photocatalyst (<2 μm), or through indirect excitation by evanescent energy near the surface of the optical fibers. The production of evanescent waves depends on the collision of photons at the fiber wall and resultant total internal reflection(Y. Xu et al., 2006) and represents a new alternative reactive mechanism. At higher coating thickness, refraction dominates.(Peatross & Ware, 2008) While photons are the well-described energy input through which photocatalytic excitation occurs, excitation by an alternating electromagnetic wave (e.g., evanescent wave) is likewise possible. (He et al., 2011; Motojima, Suzuki, Hishikawa, & Chen, 2003; Ueno & Misawa, 2013; Wada, Yin, & Yanagida, 2002)

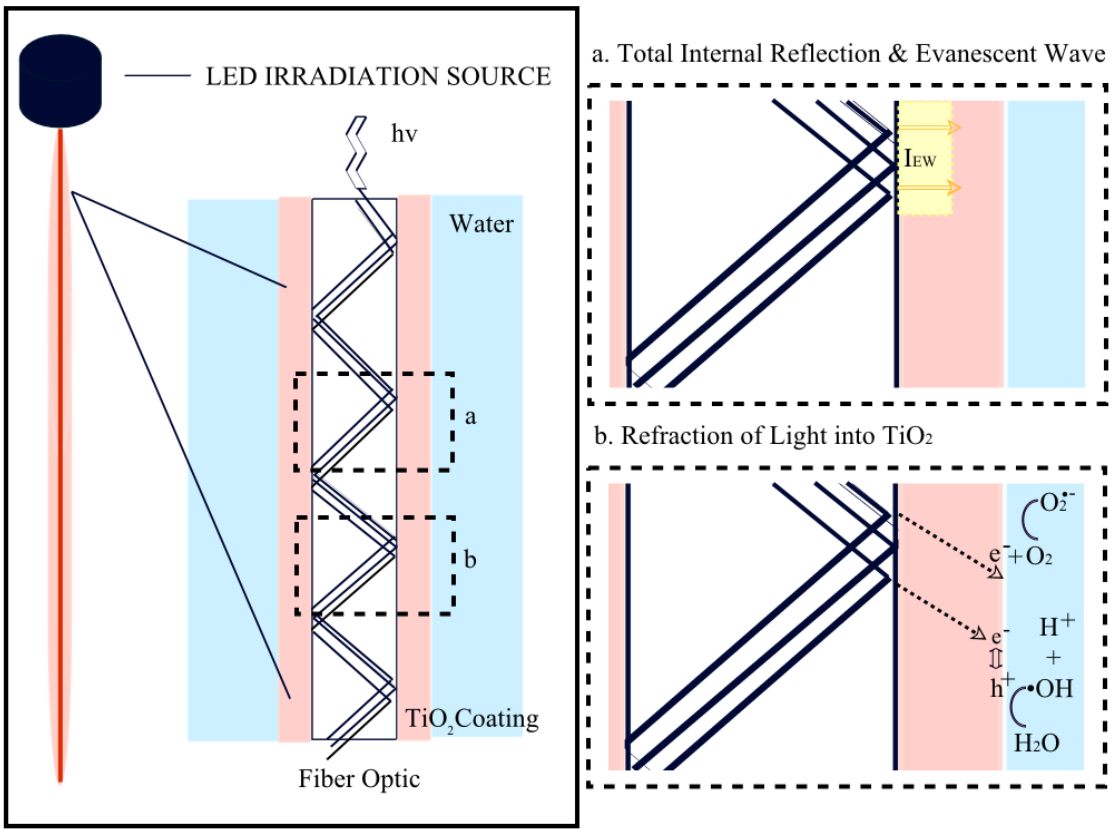

Figure 6-4. Scheme to represent the two potential mechanisms of excitation in the optical fiber/light emitting diode reactor: (a) total internal reflection and production of an evanescent wave at an uncoated interface; (b) refraction of light into TiO_2 and generation of charge carriers to induce aqueous phase oxidation-reduction.

The photocatalyst-coated optical fibers prepared herein were not perfectly uniform when coated with few coating layers (Figure 6S1, 6S2), which likely led to both TiO_2 and water contacting the optical fiber surfaces. A single dip-coat produced a non-homogeneous layer of TiO_2 approximately 2 μm thick, resulting in 16% attenuation of photon flux through the fiber (Figure 6-2). As the coating thickness increased to 8.2 μm (i.e., 5 coatings), the flux of light coming through the fiber decreased to approximately 50% of the photons of an uncoated fiber. Additional dip coatings (up to 20 total coats) did not further decrease the photon flux through the fiber. Similarly, increasing the length of the

fiber up to 28 cm with a coating mass loading rate of 0.058 mg cm^{-1} (i.e., 20 coating cycles) did not reduce the total photon flux through the fiber by more than 50%. This indicates that there was still significant TIR inside the fiber, even with significant TiO_2 loading, and the photocatalyst material near the surface of the fiber (within the first hundred nm, see Figure 6-5) resided within the evanescent wave. Excitation of the photocatalyst in the fiber-photocatalyst system is therefore possible through both light refracting from the quartz fiber waveguide into the photocatalyst coating(W. Wang & Ku, 2003b) and through excitation by evanescent energy near the surface of the optical fibers. Note that while this is supported by the data observed, there was light transmission through the entire fiber even for the thickest coatings. Therefore, a quantifiable fraction of the light is experiencing TIR and reflecting to the end of the fiber due to the short coated length. One report indicates that up to 25% of photon energy can be transferred as evanescent energy(Bao & Van, 2000), indicating a multi-pathway excitation mechanism through evanescent waves and refracted photons may be contributing to photolytic and photocatalytic processes. Further work is needed to elucidate the interplay between these two mechanisms and better understand how they contribute to the significantly improved quantum yield of the system.

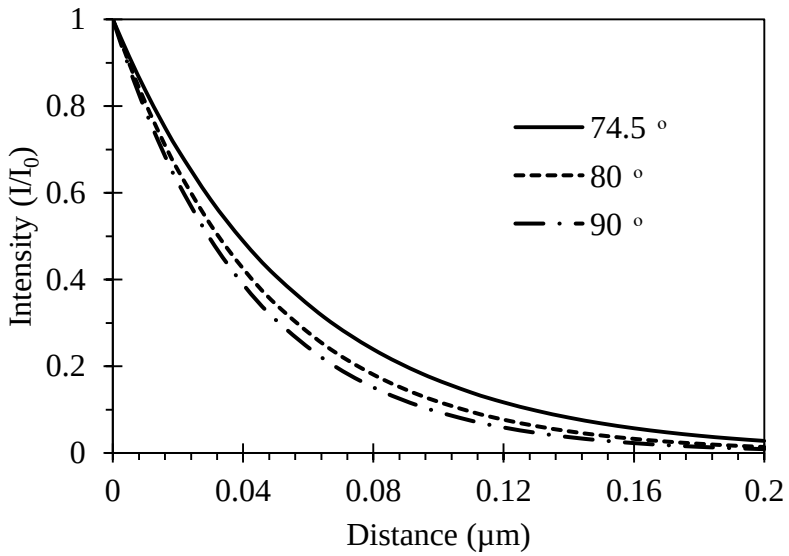

Figure 6-5. Evanescent wave intensity as a function of radial distance (μm) from the optical fiber surface for three photon incident angles (θ_i=74.5°, 80°, 90°) for 318 nm light, n_f = 1.46 (quartz), n_e = 1.33 (water).

Engineering Implications

As shown above, the direct coupling of UV-LEDs to photocatalyst-coated optical fibers demonstrated a viable technology to overcome the major limitations of heterogeneous photocatalysts for water treatment applications. Such barriers include the requirement of slurry catalyst separation from the treated water and light scattering and occlusion by light-absorbing aqueous constituents and nanoparticles. The performance of the UV-LED/TiO_2/optical fiber system suggests that MB oxidation in a controlled-catalyst delivery configuration was enhanced by better light transmittance and significant photon-electron/hole conversion. Inefficient light transmittance to the outer-most TiO_2 coating layer (in contact with aqueous pollutants) resulted from thick coating layers (< 2–5 μm). Further, compared to conventional UV irradiation sources, UV-LEDs provide a narrow-

wavelength output for irradiation, which is capable of removing pollutants via photocatalytic or photolytic mechanisms while decreasing required energy inputs and systemic inefficiency due to heat losses. In our MB degradation experiments, ~47% of incident light was not utilized, suggesting that the pollutant degradation efficiency may be further improved by either altering the incident light angle or elongating the photocatalyst coated optical fibers. Investigation of the excitation mechanism is underway to quantitatively assess the contributions of the excitation provided by evanescent energy, from frustrated total internal reflection, and photon tunneling.

Acknowledgement

This work was partially funded through the Nanotechnology-Enabled Water Treatment Nanosystems Engineering Research Center by the National Science Foundation (EEC-1449500) and USEPA Design of Risk-reducing, Innovative-implementable Small-system Knowledge (DeRISK) Center (RD 83560301).

Supplementary Information for Chapter 6

Fiber stripping and preparation for catalyst deposition

11-cm fiber segments were cut using a ceramic square or ruby blade to achieve a clear fiber cut. To remove the TECS cladding (a clear coating around the fibers that maintains total internal reflection of the light) and external buffer, the fibers were soaked in acetone for 24 hours, and the cladding was manually removed. If necessary, a second 24-hour acetone soak and manual cladding removal step was used. The fibers were then rinsed with water to remove any remaining acetone residual as the catalyst solution was prepared.

Fiber mounting and polishing for enhanced light transmission

Fibers were fixed to the metal connector (SMO5SMA, Thor Labs) using heat shrink wrap (TT100 1/16" and 1/8", 0.5 cm and 1.5 cm, respectively, Tech-Tron) placed (1) between the stripped fiber and the connector and (2) overlaid on the combined fiber-connector. Heated air was used to shrink wrap the components to flush-fit, and the fibers were cooled prior to further treatment or use. Thor Labs ruby blade was used to gently score the fiber and cleave along the mechanical axis of the fiber to achieve smooth ends for polishing. Mounted, cleaved fibers were then polished using a polishing assembly (D50SMA, Thor Labs) with fiber polishing paper (LF30P, LF5P, LF03P). Fiber microscope was used to determine uniformity of clarity at the fiber tip.

LED mounting to optical fiber used a butt-coupling method of direct contact between the LED quartz window and polished optical fiber tip (S05LEDM, SM05M05, SM05SMA, Thor Labs). Male/female SMA (SubMiniature version A) pairing allowed for the LED housing to connect directly to the polished fiber assembly.

Dip coating method for TiO_2 deposition

A dispersion of 1% or 2% (10 g/L, 20 g/L) TiO_2 (P25 or P90, Evonik – formerly Degussa) was created utilizing the CEINT (Center for the Environmental Implications of NanoTechnology) protocol.(Tantra, Sikora, Hartmann, Sintes, & Robinson, 2015) The dispersion solution was nanopure water, and P90 was added to reach 20 g/L, with no additional chemical addition (pH = 4.0-4.5). The solution was sonicated in an immersed sonicator horn, and the sonicated solution maintained stability for up to 48 hours. Two variations of a dip coating protocol were used: (1) extended dip/dry cycling and (2) rapid-enhanced dip/dry cycling. For extended drip/dry cycling, fibers were immersed in the solution for 24 hours to achieve good electrostatic interaction; fibers were then allowed to dry (24 hours) and rinsed with nanopure water to release any excess TiO_2 prior to analysis or use. For rapid-enhanced drip/dry cycling, 30 s dip/dry cycle was conducted with a 2% TiO_2 solution for TiO_2 deposition and hot-air drying to allow for rapid processing of the optical fibers.

Sol-Gel method for TiO_2 deposition

To functionalize the optical fiber surface, the optical fibers were first sonicated for 30 min in acetone, ethanol, and then water. After sonication, fibers were rinsed with distilled water and dried with a stream of nitrogen gas. Then the optical fibers were immersed into piranha solution (H_2O_2:H_2SO_4 = 1:3, volume ratio) to generate hydroxyl-functionalized surfaces (Caution: piranha solution reacts violently with most organic materials and must be handled with extreme care). The functionalized optical fibers were rinsed with water and ethanol, sequentially, then immersed in 6 ml of ethanol (200 proof) containing titanium isopropoxide (TTIP, 0.6 ml). After 5 mins, the fibers were slowly taken

out and exposed to air for another 5 mins to allow TTIP hydrolysis to generate 1 layer of TiO_2 precursor. Repeating the dip coating process can result in multiple TiO_2 precursor layers. Optical fibers were dried at 60 °C for 2 h to allow complete hydrolysis, then heated to 500 °C (2 °C min^{-1}) for 1 h to crystallize the TiO_2 particles. As a control, P25 particles (1wt %) instead of TTIP were dispersed in ethanol and used as precursor solution for dip coating. The samples were characterized by scanning electron microscopy (SEM).

Tabulation of I_{abs}

Geometry of the Optical Fiber

D= 0.1 cm diameter L= 6.5 cm coated length

Area of the optical fiber tip: $A_{FO-tip} = \frac{\pi D^2}{4}$

Surface area of the optical fiber (without tip): $SA_{FO} = \pi DL$

Quantum Yield (general equation)

$$\Phi = \frac{dX/dt}{I_{abs}}$$

$$\frac{dX}{dt} = \frac{moles\ of\ contaminant\ removed}{time}$$

$$\frac{dX}{dt} = \frac{dC}{dt} * \cancel{V}$$

$$\frac{dX}{dt} = \left[\frac{mol - contaminant}{time}\right]$$

$$I_{abs} = \left[\frac{mol - photons}{time}\right]$$

I_{abs}

Photolysis

$$I_{abs(P)} = E_{ZERO} * A_{FO-tip}$$

E_{ZERO} = light from LED/FO tip at zero coatings

Slurry

$$I_{abs(S)} = E_{ZERO} * A_{FO-tip}$$

E_{ZERO} = light from LED/FO tip at zero coatings

Coated Fiber

$$I_{abs(C)} = (E_{ZERO} - E_{XCOAT}) * A_{FO-tip}$$

E_{XCOAT} = light from LED/FO tip at X-coatings

Supplementary Figures

Scanning electron microscopy (SEM) was conducted on fiber optics to visualize titanium dioxide surface coating density and thickness on optical fibers. SEM was conducted using a scanning electron microscope equipped with an energy dispersive X-ray microanalysis system (SEM/EDX; Philips XL30-EDAX). Optical fibers were arranged both horizontally to assess the coating homogeneity along the length of the fiber and vertically to assess the coating thickness via cross-sectional analysis.

Figure S1 shows two optical fibers: blank (no coating, cladding stripped) on the left and five coating layers (TiO_2 dip coating; 0.1 mg added mass) on the right. Zero coating was observed on the stripped fiber surface of the blank sample, and an overall thickness of 8175 ± 634 nm was observed on the optical fiber with five coating layers of P25. Figure S2 portrays images along the longitudinal axis for blank, a single coating layer, and five coating layers. The five P25 coating layers (Figure S2c) shows complete TiO_2 coverage whereas the single coating layer (Figure S2b) showed exposed quartz surfaces and non-homogenous surface coating.

The sol-gel method was also assessed via SEM/EDX to look at coverage completeness and particle size, density, and dispersion (Figure S3). Comparing images from single coating layer to five coating layers of TTIP sol-gel or P25 sol-gel indicated that the TTIP sol-gel method achieved more complete coverage surface coating as well as better surface smoothness and homogeneity.

Presented as the inverse of Fig. 1a (main text), Figure S4 shows the photon flux transmitted through the optical fibers as measured through the tip for various coating

cycles. These were the values measured by the radiometer, and are presented averaged from three collected measurements with error bars.

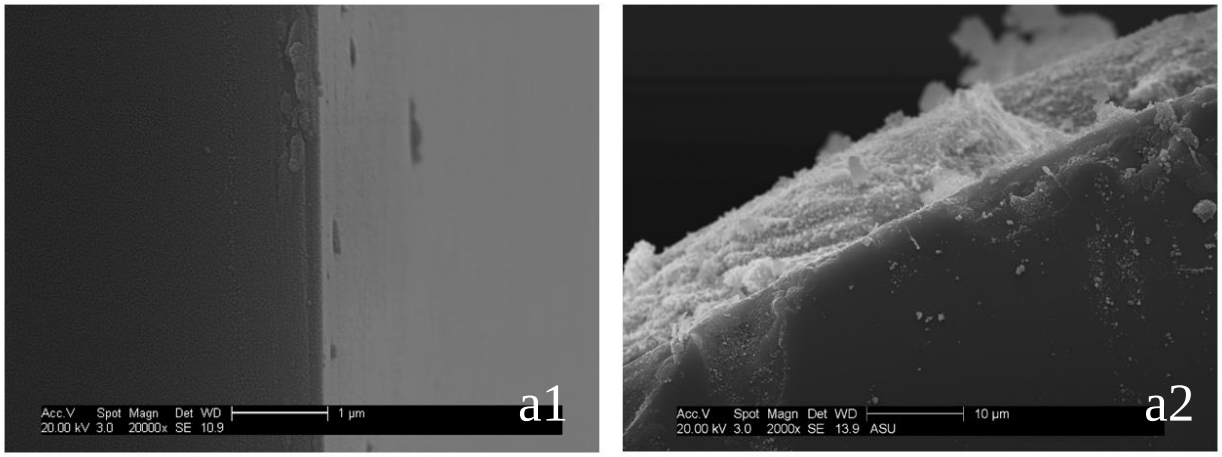

Figure 6S1. (a) Scanning electron microscopy image of: (a1) stripped quartz optical fibers with no catalyst coating, (a2) 5x (0.1 mg) coating on quartz optical fibers (8175 ± 634 nm);

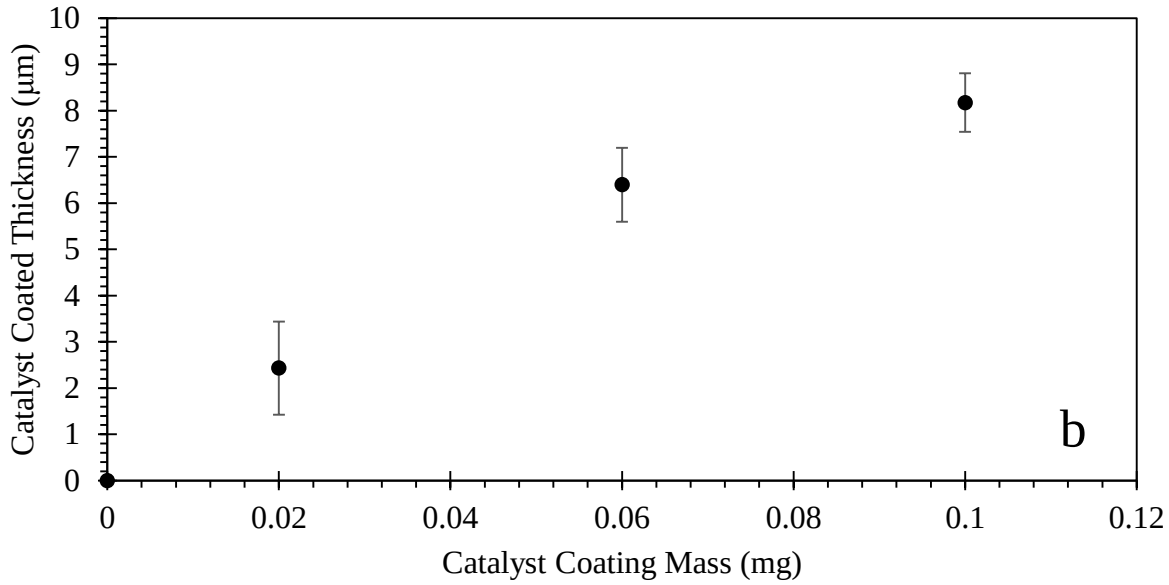

Figure 6S1. (b) catalyst coated thickness (µm) based on catalyst coating mass (mg) for 0, 1, 3, or 5 coating layers. Error bars represent 1σ and are shown for x- and y-axes.

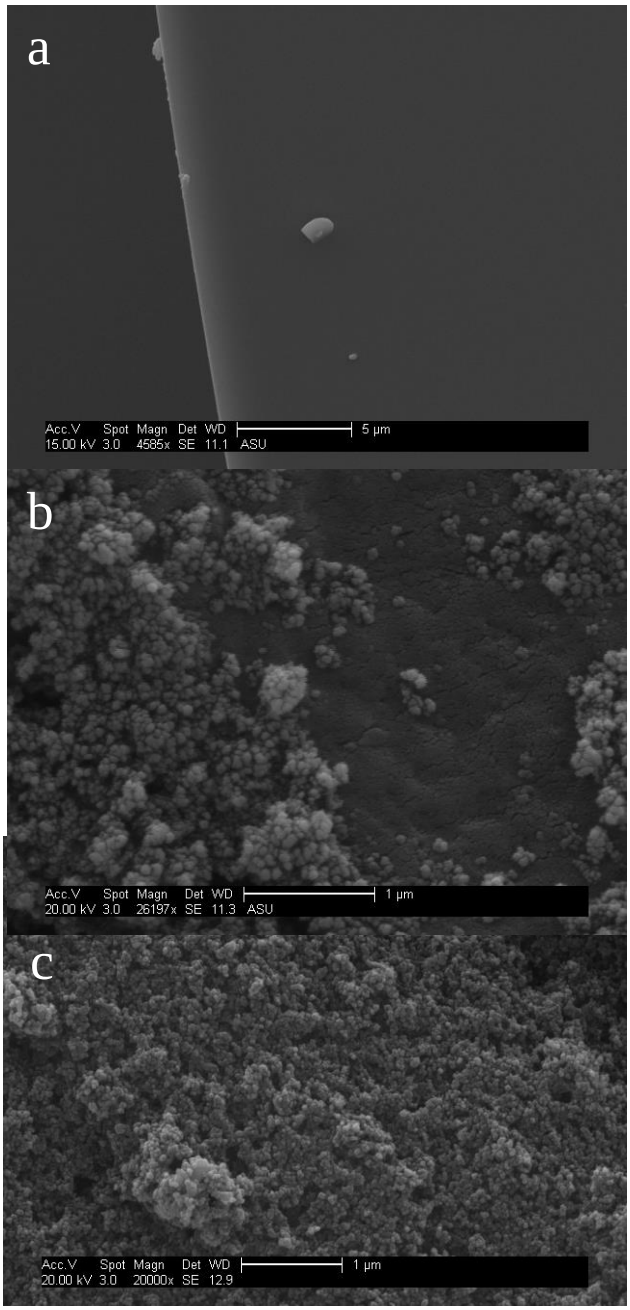

Figure 6S2. Scanning electron microscopy of the side of (a) 0x coated optical fiber (blank); (b) 1x (0.2 mg) coated optical fiber; (c) 5x (0.1 mg) coated optical fibers with catalyst compaction and minimal void space.

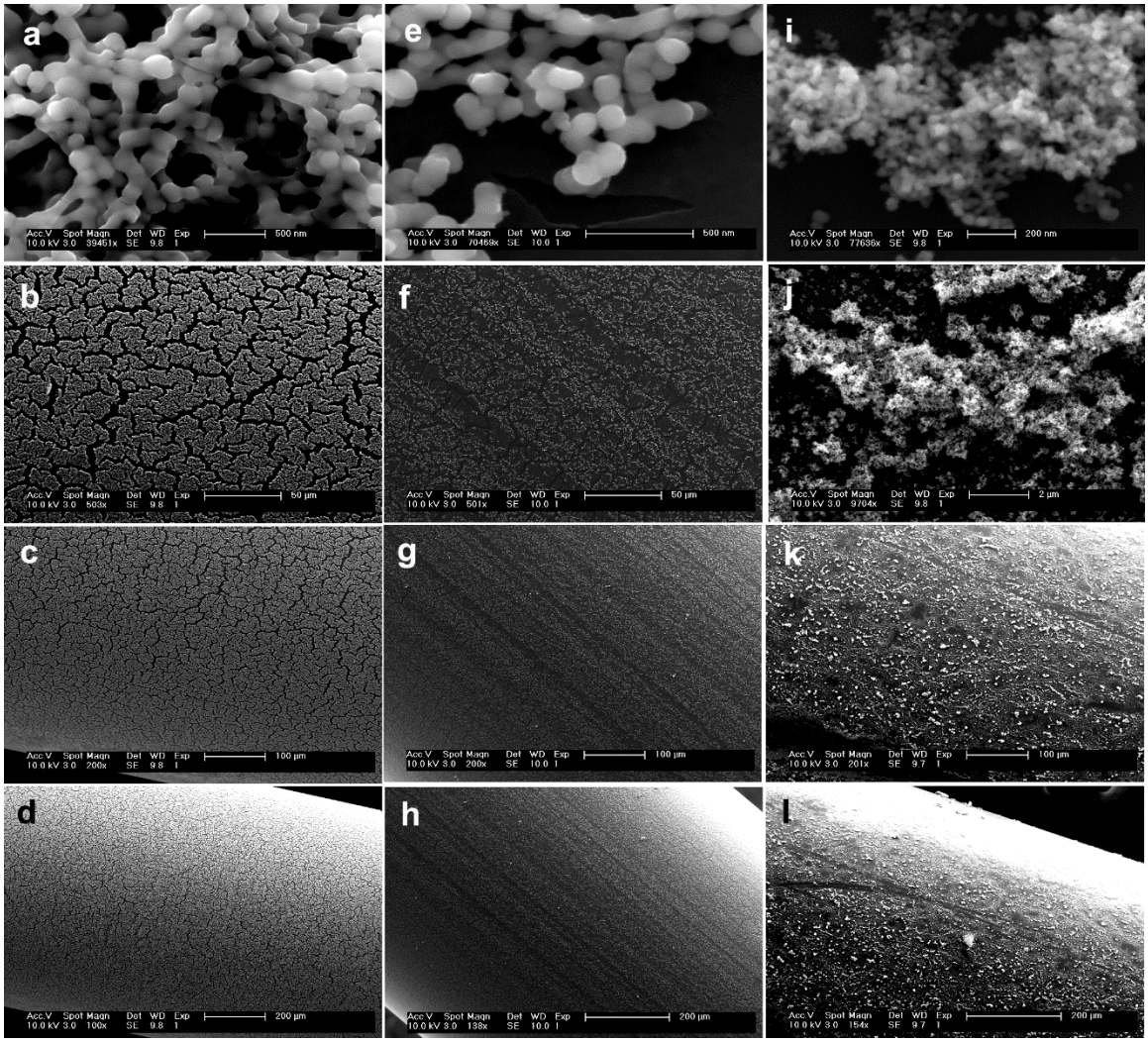

Figure 6S3. Scanning electron microscopy of the side of sol-gel TiO_2 coated optical fibers: (a-d) 5 layers of TiO_2; (e-h) 1 layer of TiO_2, (i-l) 5 layers of TiO_2. TTIP was the precursor in (a-h), and P25 was the precursor in (i-l).

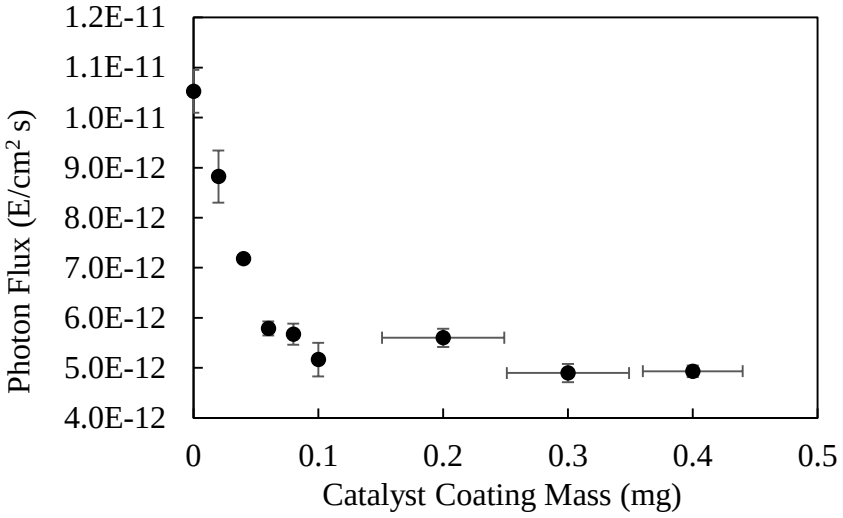

Figure 6S4. Photon flux transmitted through the optical fibers measured at the optical fiber tip as a function of catalyst coating mass. Error bars represent ±1σ of triplicate measurements.

Time-based kinetics were assessed to determine effectiveness of each coating methodology and corresponding mass-equivalent slurry conditions. Apparent rate constants, k_{app} (Figure S5a) were tabulated from first-order (s^{-1}) relationships as shown in Figure S5b. Linear trendlines and coefficients of determination (R^2) were tabulated for each.

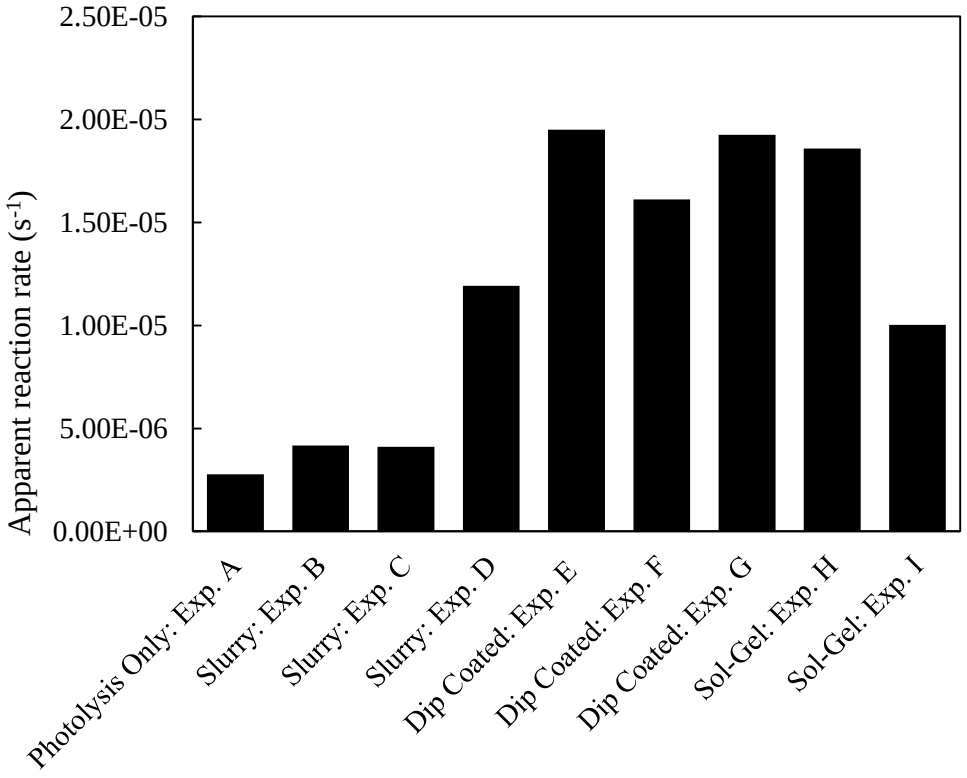

Figure 6S5a. Apparent reaction rate constant, k_{app}, for bleaching of methylene blue under photolytic and photocatalytic conditions.

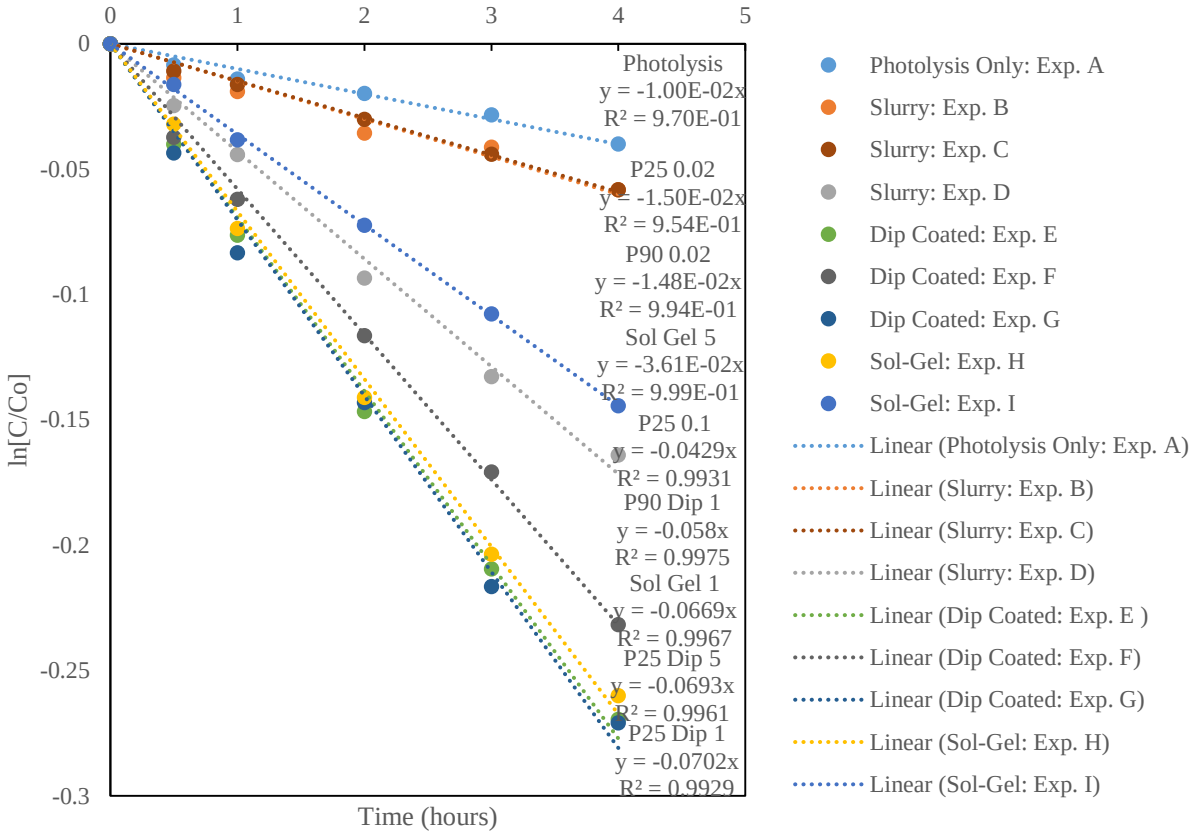

Figure 6S5b. Data fit for apparent reaction rate constant, k_{app}, for bleaching of methylene blue under photolytic and photocatalytic conditions.

CHAPTER 7

COMPACT LIGHT-EMITTING DIODE OPTICAL FIBER IMMOBILIZED TiO_2 REACTOR FOR PHOTOCATALYTIC WATER TREATMENT

Abstract

A key barrier to the implementation of photocatalysis is delivery of light to photocatalysts in contact with aqueous pollutants. Slurry photocatalyst systems suffer from poor light penetration and require catalyst separation, which necessitates the development of photocatalysts fixed films. However, a challenge of photocatalytic films for water treatment is efficient light delivery. TiO_2-coated quartz optical fibers were coupled to light emitting diodes (OF/LED) to improve *in situ* light delivery. Design factors studied for OF/LEDs in a flow-through reactor include: (i) the influence of number of light LED sources coupled to fibers, and (ii) the use of optical fiber bundles. The light delivery mechanism from the optical fibers into the TiO_2 coatings is thoroughly discussed. To demonstrate influence of design variables, experiments were conducted in the reactor using the chlorinated pollutant para-chlorobenzoic acid (pCBA). From the degradation kinetics of pCBA, the quantum efficiencies (Φ) of oxidation and electrical energies per order (E_{EO}) were determined. The use of optical fiber bundles coated with TiO_2 reduces the energy requirements to deliver photons and increases available surface area, which improves Φ and enhances oxidative pollutant removal performance (E_{EO}).

Keywords. Water treatment; Photocatalysis; Nanotechnology; advanced oxidation processes; trace organics, pollutants

Introduction

Photocatalytic principles have been explored since the famous discovery by Fujishima and Honda in 1972 (Fujishima & Honda, 1972), when the photocurrent response of TiO_2 after UV irradiation was first reported. Since then, more than four thousand reports per year on the study of novel nano-materials and their possible applications are published. Photocatalysis as a nano-enabled water treatment technology has been recognized for its promising applications (Nicola J Peill & Hoffmann, 1995). Research for water treatment has focused more on catalyst material design (Schneider et al., 2014b), and less on reactor efficiency in utilizing the catalysts (Lazar et al., 2012; McCullagh, Skillen, Adams, & Robertson, 2011; Van Gerven, Mul, Moulijn, & Stankiewicz, 2007). Reactors designed for photocatalysis are either fluidized slurry (Ibhadon & Fitzpatrick, 2013; Nakata & Fujishima, 2012) or fixed catalyst films (Shan et al., 2010). The photocatalytic reactors designed to date consider the external excitation of the photocatalyst using either lamp sources or natural sunlight by irradiating the catalyst surface (Boyjoo, Ang, & Pareek, 2014; Lan, Lu, & Ren, 2013). The main problem for photocatalyic reactors is light scattering and light propagation (van Grieken, Marugan, Sordo, & Pablos, 2009) within or towards these solutions to efficiently excitate the photocatalysts to photogenerate the charge carriers according to reaction (1):

$$TiO_2 + h\nu \rightarrow e_{cb}^- + h_{vb}^+ \qquad (1)$$

Supporting or fixing the nanoparticles onto substrates as photocatalytic coatings have advantages, namely eliminating the necessity to separate micro- or nano-sized catalyst particles from solution after treatment (Stancl et al., 2015a; Westerhoff, Alvarez, Li, Gardea-torresdey, & Zimmerman, 2016). Fixed film systems involve passage of light from

a source through water to an attached catalyst surface which diminishes light delivery efficiency (van Grieken, Marugan, Sordo, Martinez, et al., 2009). Light transport has been considerably technologically improved for telecomunications applications with the development of low-loss optical fibers. Light is transported through total internal reflection inside these optical fibers without loss due to careful design of external coatings (Peatross & Ware, 2008). Light is internally reflected because the optical fiber (fused SiO_2) has a higher refractive index (n) than the protective polymeric coating represented in Fig. 7-1 as n_1 and n_2, respectively. If the coating n is higher than the characteristic value of the optical fiber (n_1 = 1.5), light can be partially refracted into the coating and subsequently absorbed or scattered. Thereby, an optical fiber coated with TiO_2 (n_3= 2.6) can deliver light to photoexcite TiO_2. Previous work has improved light delivery to the catalyst by using optical fibers (Barton et al., 2016; Marinangeli & Ollis, 1982). The advancement of approach is that the photocatalytic coating is irradiated from inside the photocatalyst support, the optical fibers (Nicola J Peill & Hoffmann, 1996; J. Xu et al., 2008). Thereby, the photonic transport efficiency can be considerably improved (Nicola J. Peill & Hoffmann, 1998; Nicola J Peill & Hoffmann, 1995; W. Wang & Ku, 2003b). Note that refractive events rarely would occur when uncoated fibers are in contact with air (n_{air} = 1.0) or water (n_{water} = 1.3), where total internal reflection would dominate.

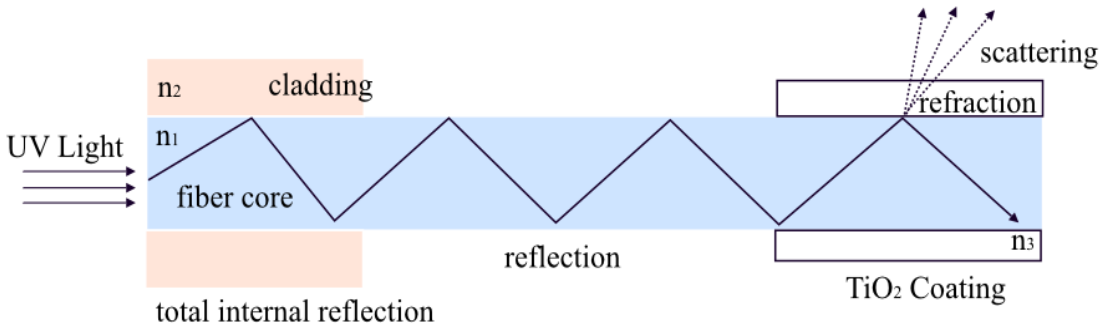

Figure 7-1 – Mechanism of light transport through the optical fiber and light delivery to the photocatalyst. Indices of refraction are denoted: n_1 for the quartz optical fiber, n_2 for the cladding or other outside interface (e.g., water, air), n_3 for the TiO_2 coating.

The coupling of optical fibers and light sources has been conducted previously with emphasis on: collimated lamp sources and solar irradiation (Barton et al., 2016; N J Peill & Hoffmann, 1997a). Due to their high energetic demand, pressurized mercury lamps – though potent in photocatalysis- are not optimized for energy efficient light delivery into optical fiber systems (Denny, Scott, Peng, et al., 2010). Likewise, the solar spectrum, with only 6% ultraviolet irradiation, requires infrared wavelength management and is susceptible to significant losses (N J Peill & Hoffmann, 1997a) due to excess heat generation which can slough off the photocatalyst coating. However with the recent advancement in light emitting diode (LED) technologies (Jo & Kang, 2012; Langanf H. Levine et al., 2011), direct coupling of a discrete wavelength irradiation source to individual optical fibers without added optical lenses could be possible (Hou & Ku, 2013). Further, LEDs are monochromatic and therefore can deliver wavelength-specific light as desired for photocatalytic bandgap excitation (K. Natarajan et al., 2011).

We designed and operated an optical fiber/LED recirculating reactor system to assess performance to remove *para*-chlorobenzoic acid (pCBA), a model compound.

Performance was assessed through both physical measurements of light passage along the optical fibers as a function of TiO_2 coatings, and determination of apparent quantum yields and electrical energy per order for pCBA removal under different reactor configurations. Throughout the course of this study, the main objective was to determine the highest performance light delivery scheme via variance of: (a) number of light emitting diodes; (b) effective surface area through the use of bundled fiber optics or individually coupled fiber optics under identical illumination conditions. In this work we exploit these characteristics to design a photocatalytic compact reactor using fiber optics as a light delivery method.

Experimental

Chemicals and materials

Pure *p*-chlorobenzoic acid (99%) and TiO_2 (P90) were purchased from Sigma-Aldrich and Evonik, respectively. Stock solutions and TiO_2 suspensions were prepared with water from a Millipore Milli-Q system with resistivity >18.2 MΩ cm at 25 ºC. The solution pH was adjusted to 4.0 with analytical grade sulfuric acid and sodium hydroxide supplied by Fisher Chemical. Acetonitrile used for the preparation of the mobile phase was of HPLC grade (>99.9%) from Sigma-Aldrich. Analytical grade acetone purchased from Merck was used to strip the polymeric cladding. LED mounts and optical fibers of numerical aperture 0.39 and 1000 μm diameter were acquired from Thorlabs (FT1000UMT: transmit wavelengths 300-1200 nm). Heat shrink wraps of 0.16 cm and 0.24 cm of diameter were purchased from Tech-Tron while 365 nm ultraviolet (UV) LED emitters were supplied by Digi-Key Electronics (365nm 300mA TO-39).

Fiber optics preparation and TiO_2 coating

Fiber optic segments of 20.0 cm were cut with a ceramic blade obtaining a smoth and flat cut surface. The plastic buffer was manually removed by using a specialized micro-strip fiber optic stripper. Then, the stripped fibers were soaked in acetone to dissolve the polymeric cladding which consists of a thin TECS coating to maintain the total internal reflection of light. Uncoated fibers were subsequently rinsed and cleaned with nanopure water. Prior to polishing, fiber optic segments were individually fixed to metallic LED connectors (SMO5SMA, Thorlabs) by using heat shrink wrap. Fibers were mounted on a fiber support (D50SMA, Thorlabs) to homogeneously polish the cut surface until an specular surface was obtained using optical polishing paper (LF30P, LF5P, LF03P). Both tips of each optical fiber were polished and the uniformity of polished fiber tips was evaluated using a fiber microscope before coating. One of the fiber tips was assembled in direct contact with the LED quartz window through a male/female conection between the LED mount and the LED connector as shown in Fig. 7-2.

The TiO_2 P90 photocatalyst was deposited on the fibers surface using a dip-coating method. A 1.0 % TiO_2 P90 dispersion (10 g/L) was prepared following a published protocol (Tantra et al., 2015). The dispersion solution was prepared in nanopure water and sonicated with a QSonica Misonix immersion sonicator for 15 min. The optical fibers were immersed in the dispersion solution and heat dried to ensure the adherence to the fiber optics surface.

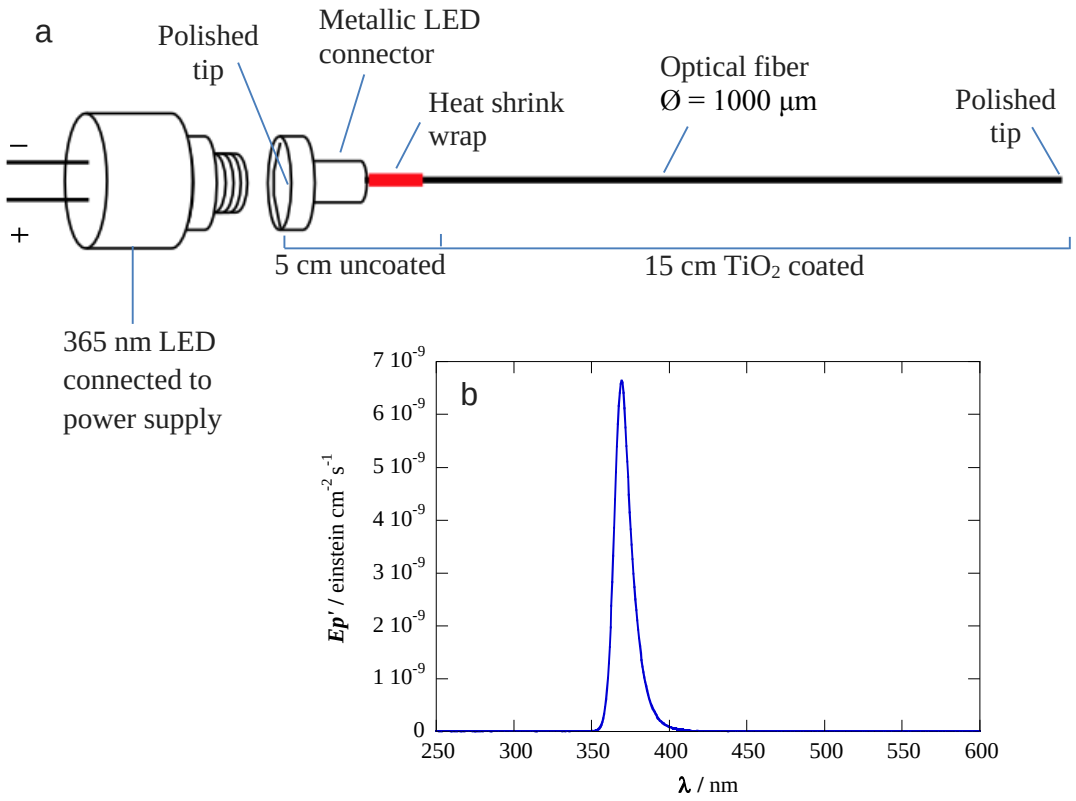

Figure 7-2 (**a**) Scheme of the TiO_2/optical fiber coupling with LED light source. (**b**) Characteristic light emission and photon fluence of the 365nm UV-LED used in the reactor through non-coated fibers.

Reactor design

A sketch of the photocatalytic TiO_2/optical fiber flow reactor is shown in Fig. 7-3. The photoreactor consisted of a Near Clear PVC cylinder (Harrington Plastics) of 2 cm of inner diameter with a total length of 18 cm. The solution reached a total height of 16 cm, which is equivalent to a 50 mL of solution confined inside the reactor under magnetic stirring at 700 rpm and hydraulic retention time of 10 min. The 150 mL solutions containing 0.1 mM of pCBA at pH 4.0 were introduced in the reservoir and recirculated through the system by means of a peristaltic pump at 5 mL min^{-1}. The coated optical fibers

were inserted into the reactor with equal spacing. Note that different set-ups were explored using different fiber-LED couples: (i) individual fibers connected independently to an LED source (OF/LED), (ii) a bundle of three coupled fibers connected to the same LED source, and (iii) a bundle of fifteen fibers coupled to an LED. Furthermore, the influence of increasing number of OF/LED units inside the reactor where considered from 1 to 5.

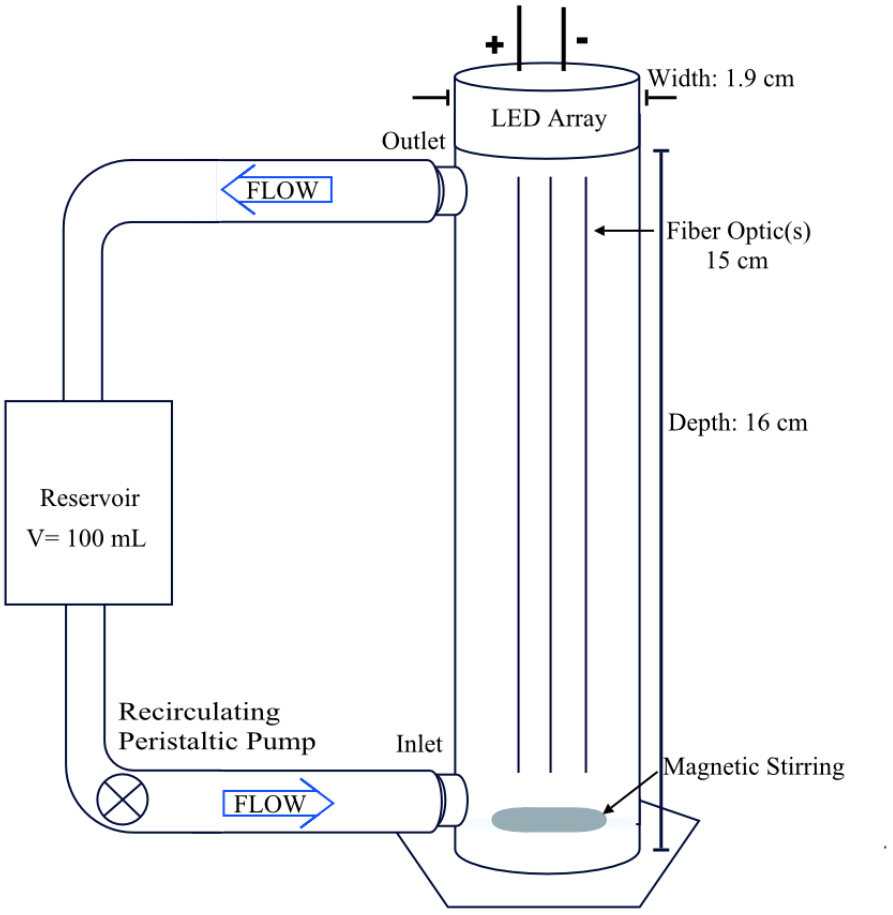

Figure 7-3. Scheme of flow-through reactor design for OF/LED system.

Apparatus and analytical procedures

The light irradiance (*E*) delivered from the light sources and from the output tip of the optical fibers was quantified with a radiometer Avantes AvaSpec 2048 spectrometer with cosine corrector measured as μW cm^{-2}. The photon fluence rate (*Ep*') expressed in einstein cm^{-2} s^{-1} was then calculated as follows (J. R. Bolton et al., 2001):

$$Ep' = \Sigma \frac{5.04 \times 10^9 \, E \, \lambda_i}{n_A} \qquad (2)$$

where λ_i is the *i* wavelength of the light source in nm, n_A is the Avogadro constant (6.022×10^{23} einstein mol of $photons^{-1}$) and 5.04×10^9 is a conversion factor to homogenize units (10^{-6} J s^{-1} μW^{-1} / 1240 eV nm / 1.60×10^{-19} J eV^{-1}). Meanwhile, the photons adsorbed by the TiO_2 coatings (I_{abs}) were estimated from the difference of *Ep'* for the uncoated fibers and the coated fibers (W. Wang & Ku, 2003a). Due to the complexity of accurately measuring light endpoints upon entering the optical fiber, it was assumed that the light loss is associated to the refraction of light into TiO_2 neglecting scattering effects (W. Wang & Ku, 2003a). It is important to remark that light irradiance is always detected at the optical fiber tip, because part of the beam of photons is directly transported through the fiber without undergoing reflection or refraction (Peatross & Ware, 2008; Nicola J Peill & Hoffmann, 1996). Solid analysis of the TiO_2 coatings was conducted using SEM/EDX (Philips XL30-EDAX). Imaging of the vertically oriented optical fibers was used to determine the thickness of the TiO_2 coating. EDX demonstrated the contents of the optical fiber to be quartz (SiO_2) and the coating to be TiO_2.

The pH of the solutions was measured using a Thermo Scientific Orion Star A221 pH-meter. The removal of pCBA was followed by reversed-phase chromatography using a Waters 2695 HPLC with a Waters LiChrosorb® 10 μm RP18 (100 mm x 4.6 mm) column at 25 ºC with a LiChroCART® 4-4 guard column. The photodiode array detector Waters 2996 was set at λ = 233 nm corresponding to the maximum absorbance of pCBA. The analysis were conducted by injecting 20 μL aliquots of samples collected at different photocatalytic treatment times and using a mobile phase 35:65 (v/v) acetonitrile/water mixture at 0.6 ml min^{-1}.

Results and discussion

TiO_2 coatings and light passage characterization

Figure 7-4 shows the SEM images of one fiber optic coated with TiO_2, where the magnification elucidates a smoth coating surface. The cross sectional image of coated fibers evidenced a physical attachment of TiO_2 nanoparticles with an uniform thickness observed through the fiber (see Fig. 7-4c). Optical fibers subjected to several cycles of dip-coating have increasing thickness of 1.1 ± 0.1 μm, 2.2 ± 0.1 μm, 3.2 ± 0.1 μm and 4.7 ± 0.1 μm after 1, 2, 3 and 5 coating cycles, respectively. The steady state intensity of light delivery was monitored at the terminal end of fibers of different coating thickness (individually attached to the 365nm LED). The coating thickness influences not only the photocatalytic response but also the light delivery through the fiber. Fig.7-5 shows the differential Ep' value measured between a coated and uncoated fiber, which corresponds to the number of photons potentially refracted, absorbed and scattered by the TiO_2 coating layer. This value increases with the thickness until reaching a plateau. The increased Ep'

differential can be explained by the higher number of particles in the interface glass/TiO_2 which increase the optical fiber light refraction (Danion, Bordes, et al., 2004; Danion, Disdier, et al., 2004). Whereas, the plateau achieved by thicker coatings can be associated to the saturation of the photocatalytic coating. However, these values are approximate, as the true value of photons absorbed is obscured by those potentially lost via scattering (W. Wang & Ku, 2003a).

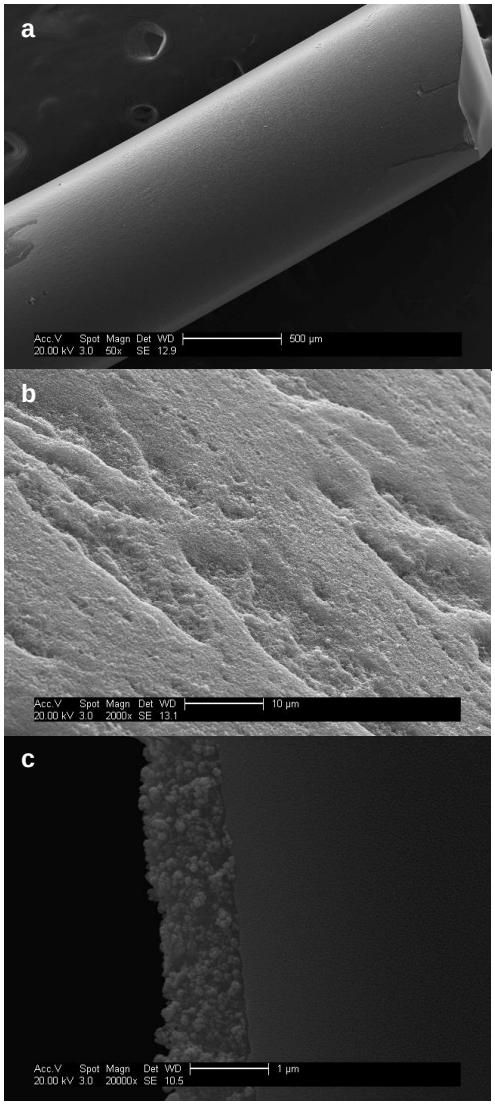

Figure 7-4. Scanning electron microscopy (SEM) images of (a) the optical fiber, (b) the free-surface micrograph of the TiO_2 coating, and (c) the cross section of the TiO_2 coating on fiber optic substrate.

Coating thickness is a highly relevant parameter since photo-generated charge carriers must be transported from the inner TiO_2 coating interface in contact with the optical fiber up to the external TiO_2 interface with the aqueous solution (Choi et al., 2001). The depth penetration of light into the TiO_2 coating is function of $1/\alpha$, where α is the absorption coefficient at the characteristic wavelength of the incident light (Dosta et al., 2016; Hitchman & Tian, 2002). The charge carriers generated in the depletion layer should be transported to the catalyst surface (L. Zhang et al., 2012). The coating thickness should take into account the minority carrier diffusion length of up to 10 μm for TiO_2 electrons (varies by TiO_2 morphology) (Hodes & Kamat, 2015; Könenkamp, 2000), which is the maximum field-free region of photogenerated charge carriers prior to recombination reaction (3).

$$e_{cb}^- + h_{vb}^+ \rightarrow \quad \text{heat} \qquad (3)$$

From Fig. 7-5 we can deduce that longer fiber lengths increase the Ep' differential for a fixed TiO_2 coating thickness. The probability of obtaining refraction from a reflected photon beam increases with length. For long fibers, a plateau is reached because photons are already reflected, refracted and absorbed before reaching the tip of the fiber. For the 365nm LED and optical fibers used in this study, the TiO_2 particles attached over certain length (> 20 cm) will not be effectively photoexcited under any circumstance. Thus, a coated length of 15 cm obtained after 1 coating cycle was determined as optimum for the reactor design. At this length, similar amounts of photons are absorbed regardless of coating thickness.

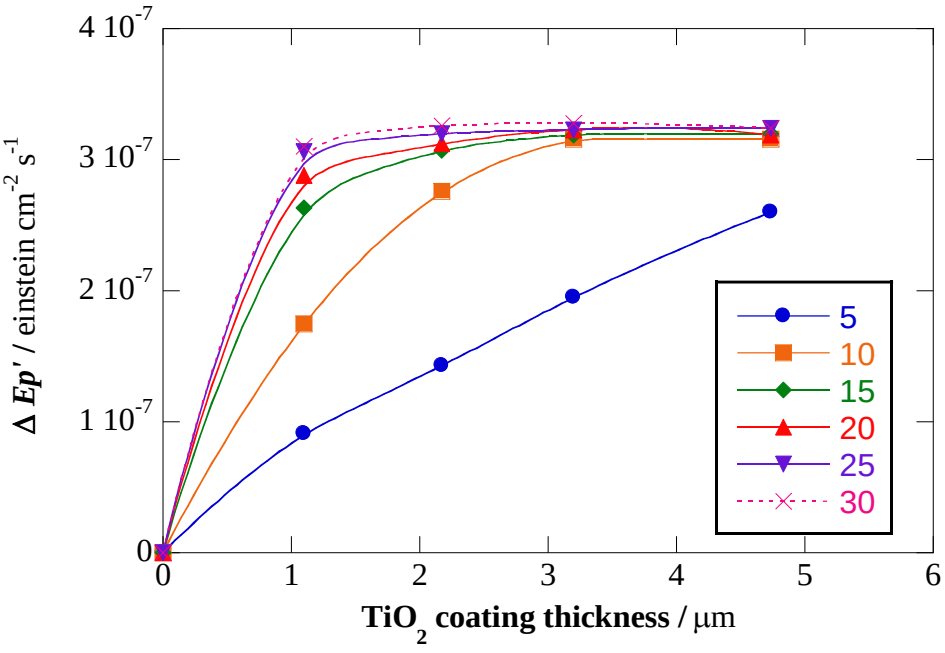

Figure 7-5. Photon fluence differential estimated between uncoated and coated fiber measurements as a function of coating thickness of optical fibers for different coated lengths of: (●) 5 cm, (■) 10 cm, (♦) 15 cm, (▲) 20 cm, (▼) 25 cm, and (x) 30 cm.

Influence of the number of optical fiber/LED couples on pCBA removal

Control experiments on pCBA removal were initially performed to assess the amount of adsorption onto TiO_2 coated optical fibers or losses of pCBA within the reactor. The initial pCBA concentration remained constant after 8 h of recirculation through the reactor without optical fibers. Absorption of the organic pollutant pCBA on the PVC walls of the reactor was not observed. Model pollutant concentration was unaltered after the immersion of uncoated optical fibers, either under dark condition or with illumination when LEDs were attached to the optical fiber. Hence, the influence of photolytic degradation under our experimental conditions was negligible. Moreover, differences lower than 1% were observed during control experiments where pCBA solution was recirculated through

the reactor containing 5 optical fibers TiO_2 coated without delivering light through the OF/LED couples. This behavior indicates that removal of pCBA by its adsorption on TiO_2 does not appreciably contribute to the overall removal. Degradation of pCBA was observed when light was delivered into the TiO_2 coated optical fibers by the LED light sources (Fig. 7-6). This trend suggests that the organic pollutant is oxidized by the photogenerated h_{vb}^+ from reaction (1) or by hydroxyl radical yielded from water oxidation reaction (4) (Zona et al., 2010).

$$h_{vb}^+ + H_2O \rightarrow {}^\bullet OH + H^+ \qquad (4)$$

Combinations of single fiber to single LED couples (1 OF/LED to 5 OF/LED) were configured in parallel as depicted in Fig. 7-2. This configuration was limited to a maximum number of 5 optical fibers due to the diameter of the LED devices in relation to the cylindrical reactor diameter. Fig. 7-6 depicts pCBA transformation for varying number of OF/LED couples in the reactor set-up. The organic pollutant is more rapidly degraded with increasing number of fibers and LEDs because of the higher TiO_2 surface area: volume treated ratio and the increasing number of photons delivered into the system, respectively. The coated surface per fiber is 4.7 cm^2, and increases linearly to 14.1 cm^2 and 23.5 cm^2 when 3 or 5 fibers are contained in the reactor set-up, respectively.

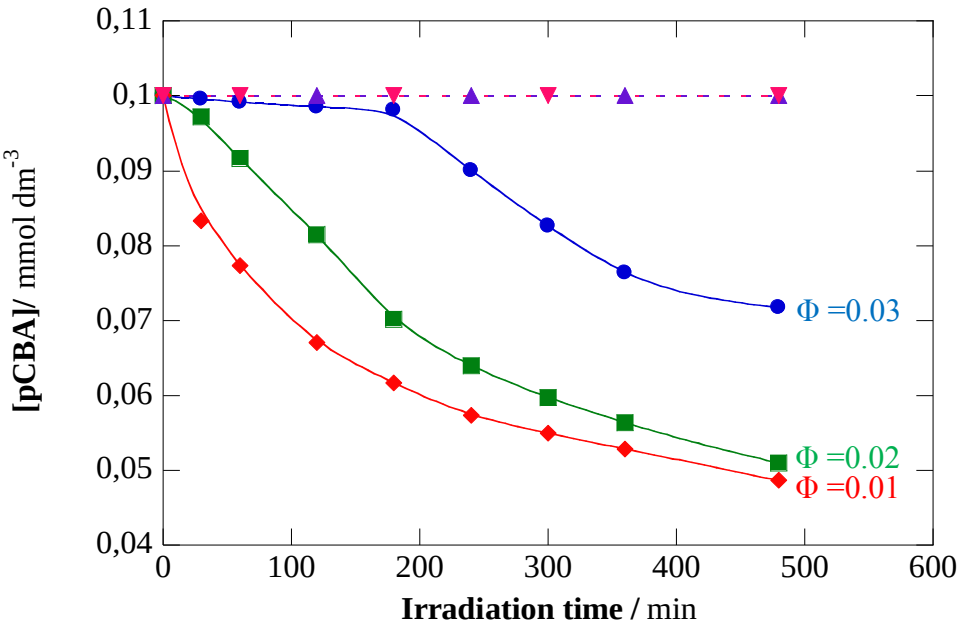

Figure 7-6 – Photocatalytic degradation of 0.1mM pCBA treated in the optical fiber/TiO_2 reactor with increasing number of OF/LED couples utilized in the set up: (▲) 1 uncoated fiber - 1 LED, (▼) 1 fiber – no LED , (●) 1 fiber - 1 LED, (■) 3 fibers – 3 LEDs, (♦) 5 fibers – 5 LEDs. The corresponding estimated quantum yields (Φ) are presented adjacently.

Pseudo first-order kinetics were fit to pCBA removal over time. Pseudo-first order rate constants (k_1) of 2.3 x 10^{-5} s^{-1} (R^2 = 0.99) for 1 OF/ 1 LED, 3.3 x 10^{-5} s^{-1} (R^2 = 0.99) for 3 OF/ 3 LED, and 5.2 x 10^{-5} s^{-1} (R^2 = 0.95) for 5 OF/ 5 LED were obtained. This trend is indicative of a constant photocatalytic production of oxidizing species, such as h_{vb}^+ and $^{\bullet}OH$ ($k_{^{\bullet}OH/pCBA}$= 5.2 x 10^9 $M^{-1}s^{-1}$ (Elovitz & von Gunten, 1999; Pi, Schumacher, & Jekel, 2005)). Previously published reports have also noted decreased kinetic oxidation with increasing irradiation time due to oxidant scavenging by degradation by-products of pCBA (i.e., 4-chlorophenol) (He et al., 2011).

Equation (5) was used to calculate the apparent quantum yield (Φ) assuming the photons measured via the uncoated optical fiber were absorbed by the TiO_2 layer. This

accounts for photon losses inherent to the unique configuration, e.g., optical effects such as scattering, refraction, and reflection which results from the coating layer (W. Wang & Ku, 2003a). The addition of more combinations of optical fibers individually coupled to LEDs influences the apparent Φ since the use of more LED sources linearly increases the number of photons delivered into the reactor. The experimental photon flux delivered by each LED was 4.39 x 10^{-7} einstein cm^{-2} s^{-1}. Light lost in the OF/LED connection was an important parameter. Ca. 46 % of light was directly lost in coupling, with the light delivered through the tip of the fiber measured as 2.37 x 10^{-7} einstein cm^{-2} s^{-1}. This astonishing percentage of direct loss in coupling is compounded to approach 57 % after considering that nearly 20% of the light delivered through the optical fiber is directly transported to the fiber tip without internal reflection as has been noted in other reports (Nicola J Peill & Hoffmann, 1996). One of the major challenges for effective reactor design resides in the coupling of the OF/LED. Thereby, consideration of numerical aperture for the optical fibers can increase the transport of light due to the acceptance of light at a wider range of incident angles.

$$\Phi = \frac{\text{mole of pCBA oxidized}}{\text{mole of photons absorbed}} = \frac{\Delta[\text{pCBA}]\, V_r}{\gamma_{abs}\, \Delta t} \qquad (5)$$

where Δ[pCBA] is the experimental pCBA removed in mol L^{-1}, V_r is the reactor volume in L, γ is the mol of photons delivered through the fiber which can be potentially absorbed by the TiO_2 coating, and Δt is the time of irradiation in s (Brouwer, 2011). There we assume that each mol of photon absorbed potentially generates one mol of oxidant that reacts with one mol of pCBA, where the Φ clarifies the actual efficiency. Then, the apparent quantum efficiency corresponds to

$\Phi_{1OF,1LED,15cm}$= 0.03, $\Phi_{3OF,3LED,15cm}$= 0.02, and $\Phi_{5OF,1LED,15cm}$= for 0.01 for 1 OF/ 1 LED, 3 OF/ 3 LED and 5 OF/ 5 LED couples, respectively. The diminishing Φ at higher *Ep*' indicates that increasing photon flux into the system at fixed photon flux to surface area ratio does not provide added value to the reactor in terms of oxidation efficiency, although higher photon flux does contribute to faster removal kinetics (R.-D. Sun, Nakajima, Watanabe, Watanabe, & Hashimoto, 2000).

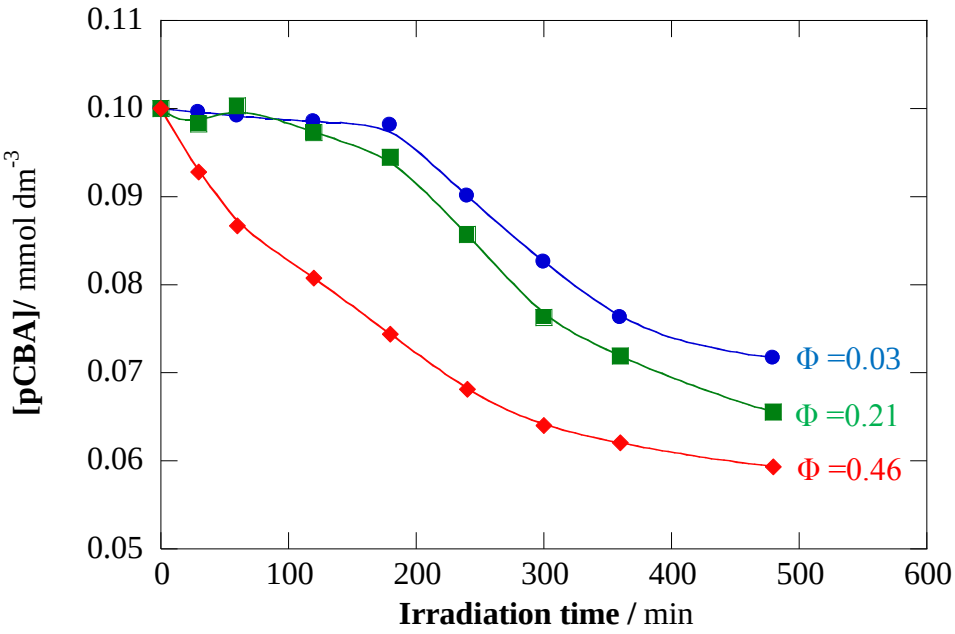

Figure 7-7 – Photocatalytic degradation of 0.1mM pCBA treated in the optical fiber/TiO2 reactor with increasing number of OF/LED couples utilized in the set up: (●) 1 fiber - 1 LED, (■) 3 fibers – 1 LED, (♦) 15 fibers – 1 LED. The corresponding apparent quantum yields (Φ) are presented adjacently.

Influence of fiber-LED configuration: the use of optical fiber bundles

The use of optical fiber bundles connected to the same light source provides an interesting alternative to increase the available TiO_2 surface area while reducing

operational cost resulting from fixed light input. A single LED was coupled to 1, 3, or 15 optical fiber bundles to determine whether additional surface area could increase overall performance of the reactor. As can be seen in Fig. 7-7, the increase of number of fibers by using bundles considerably enhances the degradation of pCBA. This trend can be related to the increase on the number of available catalytic sites by the considerable increase of TiO_2 coating area from 4.7 cm^2 for 1 fiber up to 70.5 cm^2 for the 15 fibers bundle. Furthermore, the presence of a higher number of fibers in solution improves the mass transport of pCBA in the solution to the catalyst surface, promotes turbulence in the flow reactor and consequently diminishes possible short-circuiting (Athanasiou, Romanos, & Falaras, 2016). The kinetic analysis of pCBA abatement denotes pseudo-first order rate constants with values of 2.3 x 10^{-5} s^{-1} (R^2 = 0.99) for 1 optical fiber, 2.6 x 10^{-5} s^{-1} (R^2 = 0.98) for 3 optical fiber bundled, and 2.4 x 10^{-5} s^{-1} (R^2 = 0.99) for 15 optical fiber bundled, respectively.

Even though higher removal is achieved with optical fiber bundles, noteworthy is the fact that efficiency light delivery is dramatically decreased at the OF/LED junction. As discussed above, in the coupling of 1 LED : 1 fiber there is a total loss of 57 % of light emitted by the LED. However, this value increases up to 93 % when the LED is coupled to bundles due to the variation of the incident light angles. The light delivered through the uncoated bundles corresponds to 3.68 x 10^{-8} einstein cm^{-2} s^{-1} and 1.97 x 10^{-8} einstein cm^{-2} s^{-1} for 3 OF / 1 LED and 15 OF/ 1 LED bundles, respectively. Future works could consider the use of optical lenses that could reduce the loss by collimating light directly into the fibers. However, even as the light delivered to the TiO_2 decreased, the effective surface area was able surpass this hindrance to result in higher performance. This trend can be

observed from the estimated Φ which increases with available surface area: $\Phi_{1OF,1LED,15cm}$ = 0.03 for 1 fiber, $\Phi_{3OF,1LED,15cm}$ = 0.21 for one bundle of 3 fibers, and $\Phi_{15OF,1LED,15cm}$ = 0.46 for one bundle of 15 fibers. Due to the tabulation of quantum efficiency based on the light measured through the uncoated optical fiber bundles, there is an order of magnitude difference between the 1:1 couple and 1:15 couple. However, in a comparison with previously published works using irradiation coupled to optical fibers, the lower Φ values correspond well to the optimized coupling reactor from Peill et al. (Nicola J Peill & Hoffmann, 1996) whereas the higher Φ values correlate to more recent work by Wang and Ku (W. Wang & Ku, 2003a). The latter presents higher Φ values, which exponentially decrease by increasing the fluence delivered through the fibers (W. Wang & Ku, 2003a). This trend is coincident with the results observed, where lower fluence is measured through the bundles due to low coupling efficiency compared to single optical fiber – single LED couples. Therefore, higher apparent Φ are determined for bundled optical fibers.

Reactor design influences on the electrical energy per order

Increasing performance by adding additional fiber optics can be achieved with little added capital cost. Electrical energy per order (E_{EO}) from equation (6) is used to assess trade-off between number of fibers and number of LEDs (J. R. Bolton et al., 2001):

$$E_{EO} = \frac{P_{LED}}{v_0 \log(C_0/C)} \qquad (6)$$

where P_{LED} is the electrical input power consumed by the LED light sources in kW, v_0 is the volumetric flow rate in $m^3\ h^{-1}$ and C_0 and C represent the pollutant concentration at

initial and final treatment time. A single LED (V = 3.5 V, I =0.3 A) requires 1.05 W of power.

Table 7-1 reports calculated E_{EO} for each configuration tested. E_{EO} values reported for photocatalytic treatment range from 0.1 kWh m^{-3} $order^{-1}$ up to 100 kWh m^{-3} $order^{-1}$ depending on the targeted pollutant and reactor configuration (M. A. Behnajady, Vahid, Modirshahla, & Shokri, 2009; M. a Behnajady & Modirshahla, 2006; Benotti, Stanford, Wert, & Snyder, 2009; Stancl et al., 2015a). In the case of organochlorinated compounds like pCBA or chlorophenols, E_{EO} is reported with average values ca. 30 to 100 kWh m^{-3} $order^{-1}$ (Z. Zhang, Anderson, & Moo-Young, 2004). In our case, an E_{EO} of 15.8 kWh•m^{-3}•$order^{-1}$ is required for pCBA oxidation in the 1LED:15OF system. A reduction of 3.5 times (70%) in E_{EO} occurs when the 15 fiber bundle is used in comparison to the 5 OF/ 5 LED configuration. From the scenarios investigated the 15 optical fiber bundle results to be the most promising from an engineering perspective. Hence, further work to develop better light delivery for the bundled systems, which are presently non-optimized, could yield opportunity to further enhance the surface area at the same energy requirement.

Table 7-1. Comparison of E_{EO} values for the OF/LED configurations tested.

LEDs / #	Optical Fibers / #	Ep'[a]/ 10^{-7} Einstein•cm^{-2} s^{-1}	Surface Area / cm^2-coated	Quantum Efficiency, Φ	E_{EO} / kWh•m^{-3} •order
1	1	2.37	4.7	0.03	24
1	3	0.37	14.1	0.21	19
1	15	0.20	70.5	0.46	16
3	3	7.11	14.1	0.02	36
5	5	11.7	23.5	0.01	56

[a] Ep' refers to the sum of photon fluence emitted through the uncoated optical fibers for that configuration.

Conclusions

We present a flow-through photocatalytic reactor with TiO_2 photocatalyst immobilized on optical fibers coupled to UV-LEDs (OF/LED). The mechanism of light delivery into this OF/LED system is explored based on the TiO_2 coating thickness on the surface of the optical fibers as well as varied catalyst coating length. Measurement of photon fluence through the optical fibers and into the catalyst coating layer indicated a maximum coating of 15cm at 1.1μm coated thickness was required for optimal light delivery into the TiO_2, which should be used for reactor design. The mechanism of light delivery into the TiO_2 photocatalyst is based on the refractive indices at the TiO_2/quartz interface, at which refraction of photons can be achieved. For locations without TiO_2 coating, total internal reflection dominates, propagating light longitudinally down the optical fiber. Experiments with pCBA were conducted to assess optimal reactor design. Highest kinetics were achieved for 1:1 couples using 5 OF/ 5 LEDs. However, this configuration presents the lowest quantum yield (Φ) and the highest electrical energy per order (E_{EO}) in comparison to the other set-ups. This outcome is explained by the higher numbers of photons emitted that are not consumed in photocatalytic reactions of interest. Hence, to increase overall performance of the system, a single LED was coupled to bundled optical fibers which dramatically increased the available photoactive surface area. For this scenario, oxidation of pCBA increased with increasing number of optical fibers with respect to: kinetics, Φ, and E_{EO}. Challenges inherent to this system are the efficiency of light coupling to both single fibers and bundles, as greater than 40% of light produced by the LED was lost for each scenario.

Acknowledgments

This work was partially funded through the Nano-Enabled Water Treatment Technologies Nanosystems Engineering Research Center by the National Science Foundation (EEC-1449500). This research was funded by the United States Environmental Protection Agency (RD 83560301) through the Design of Risk-reducing, Innovative-implementable, Small-system Knowledge (DeRISK) Center. Graduate student support was partially provided by a Dean's Fellowship from the Ira A. Fulton Schools of Engineering at Arizona State University.

CHAPTER 8

SYNTHESIS

Introduction

Water treatment remains one of the critical challenges of the twenty-first. Quality and quantity of drinking water resources are of concern as global population increases. Oxyanions are among the most ubiquitous contaminants, paralleled by persistent organic pollutants (POPs) (Postigo & Barceló, 2015; Arpan Sarkar & Paul, 2016; Seidel & Corwin, 2013; Spalding & Exner, 1993). Both of these contaminant categories present immense challenges to conventional large scale water treatment processes, as they may by-pass treatment and/or accumulate at various points in the overall process, requiring new treatment strategies. Most commonly, these chemicals are treated through adsorptive processes or ion exchange, in which the constituent is separated from the aqueous phase but remains untreated on the surface of an adsorbent. For example, nitrate and chromate are commonly treated using ion exchange, which transfers the oxo-anion to the ion exchange (IX) resin and ultimately into a brine upon resin regeneration (Owlad, Aroua, Daud, & Baroutian, 2008). These residuals highly concentrate toxic constituents, and their management remains quite difficult. Alternatively, POPs more commonly by-pass IX treatment due to their recalcitrance in biodegradation and required activated carbon adsorption or advanced oxidation processes for removal.

Technologies have emerged to destructively remediate oxyanions and POPs, of which a promising candidate is photocatalysis. Inherent to this processes is the chemical transformation of the initial compound to partially- or terminally- reduced or oxidized

products. Photocatalysis has been explored for its oxidation of organic compounds, potent capacity for disinfection, and potential for reductive decontamination of oxyanions and heavy metals. Few studies have assessed both applications and obstacles for engineered design and implementation of photocatalysis at scale. Process design deficiencies (Abdel-Maksoud, Imam, & Ramadan, 2016; McCullagh et al., 2011; Van Gerven et al., 2007) discussed herein include: (1) catalyst capture and safe design of nanomaterial photocatalytic slurry reactors; (2) potential frameworks for catalyst immobilization with attention to fouling and competing constituents; (3) careful consideration and investigation of optimal light delivery configuration and irradiation source. This work focuses on overcoming barriers to implementation in photocatalytic reactor design and specifically emphasizes the delivery of light and its influence not only on reactor design, but also aqueous reaction efficiency and product selectivity. Herein, the objectives (Chapter 2) presented in this dissertation are critically synthesized.

A Combined Photolytic/Photocatalytic Approach to Drive Selectivity Outcomes

Achieving desired selectivity and efficiency outcomes require tradeoffs of particular design criteria: reactor scale (throughput), time of treatment, methodology of catalyst delivery, and management of irradiation source. A cross-comparison of the resultant E_{EO} for Cr(VI), NO_3^-, NO_2^- reduction in photolytic/photocatalytic slurry reactors ranging from 10 mL to 14 L demonstrates the combined effect of these characteristics (Figure 8-1 and 8-2 (a-b)). For hexavalent chromium, both photocatalytic and photolytic reduction processes occur in solution irradiated by 253.7nm low pressure mercury UV-light (Fig. 8-1). Evidence of photo-induced reduction indicates an indirect mechanism

occurs for Cr(VI) photo-reduction to Cr(III) involving the photolysis of other aqueous constituents which mediate the process (Hsu, Wang, & Tzou, 2007; Kaczynskl & Kleber, 1993; Machado, Lansarin, & Matte, 2014; S. L. Wang et al., 2009). Of subsequent concern is the photo-mediated re-oxidation of surface-adsorbed Cr(III) to aqueous Cr(VI) (Stancl et al., 2015a).

However, it is evident that photocatalytic processes dominate in reduction of Cr(VI) to Cr(III) when a photocatalyst is present (Chapter 3, (Barrera-Díaz, Lugo-Lugo, & Bilyeu, 2012)). Observation of catalyst photo-aggregation in the pilot scale Photo-Cat® TiO_2 slurry reactor demonstrates that both light and aqueous constituents can contribute to diminished photocatalyst surface area and active sites. Further, fouling within photocatalytic slurry reactor systems is a critical obstacle to implementation in real water matrices (e.g., IX brine, groundwater). Significant fouling due to divalent cations and carbonate complexes in conjunction with adsorbed Cr(III) species on the photocatalyst decreased Cr(VI) active sites for reduction (Stancl et al., 2015a).

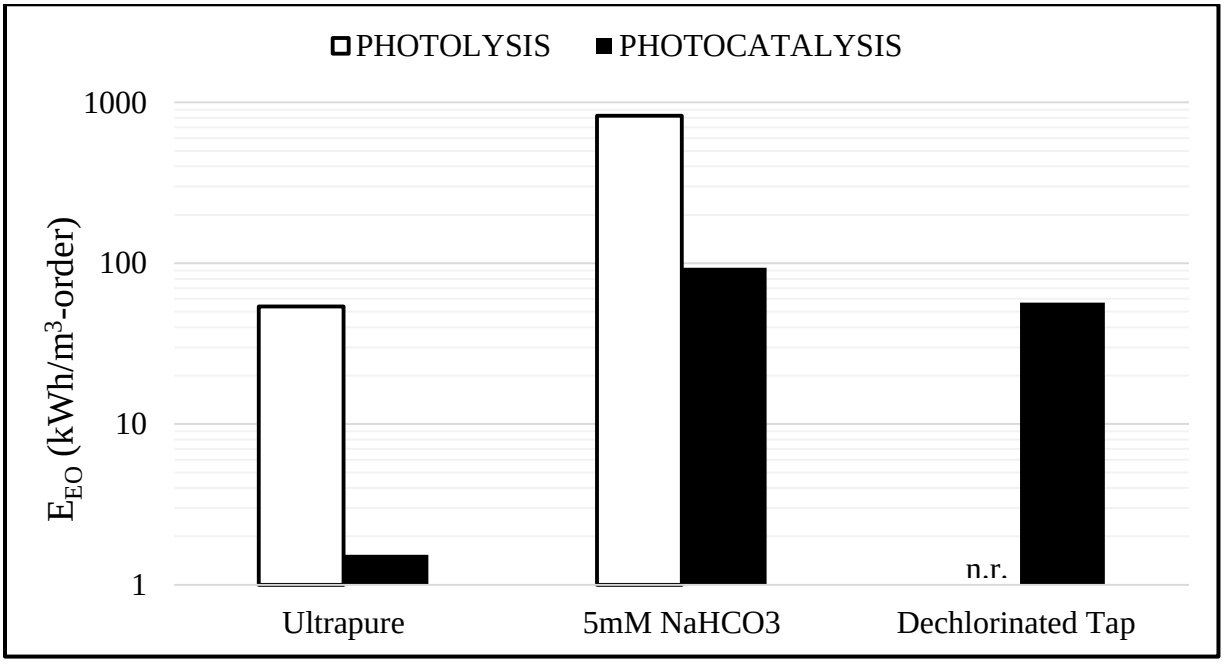

Figure 8-1. Electrical energy per order for photolytic and photocatalytic (1 g/L P90) removal of 500 μg/L Cr(VI) in 14L recirculating PhotoCat® reactor for three water matrices: ultrapure water (pH = 6.5), 5mM $NaHCO_3$ buffered deionized water (pH = 8.5), and dechlorinated tap water (pH = 7.7). Data for photolysis in dechlorinated tap water was not collected.

Figure 8-1 emphasizes the inhibition of photocatalytic reduction of Cr(VI) due to competing species, particularly those which are known to contribute to catalyst surface fouling and aggregation (Y. H. Shih, Liu, & Su, 2012). The efficiency of Cr(VI) removal decreases sixty-fold in real water matrices with carbonate species due to their high scavenging activity and poisoning of the photocatalyst (Kominami, Nakaseko, Shimada, Furusho, Inoue, et al., 2005; F. Zhang et al., 2005). Cr(VI) treatment in dechlorinated tap water requires 37-times more energy input than that of an ultrapure matrix, indicating that competing species and higher pH waters may require pretreatment to achieve complete removal of Cr(VI) at satisfactory E_{EO}. Further, pH influence on the chromium adsorption properties may exacerbate preferential adsorption of inert species (e.g., Ca^{2+}) on the TiO_2 surface (Chenthamarakshan, Rajeshwar, & Wolfrum, 2000). Safe and effective design of photocatalyst slurry systems requires attention to nanomaterial endpoints (leaching) and regenerability and capture of the photocatalyst.

In contrast to Cr(VI), reduction of nitrogen oxo-anions (NO_3^- and NO_2^-) is more influenced by direct photolytic processes (Chapter 4). However, these photolytic processes for NO_3^- rarely progress beyond an NO_3^-/NO_2^- equilibria unless the aqueous conditions are highly acidic. Further, photolytic or photocatalytic production of $CO_2^{\bullet-}$ (G. Liu et al.,

2016b; Mora-Sero et al., 2005; Rengaraj & Li, 2007) or a comparable reducing radical is critical for complete reduction of NO_3^- to nitrogen gases. NO_3^- reduction proceeds via wavelength-dependent pathways toward nitrogen gases, with HONO as a primary bifurcation point (Chapter 5). Hence, the choice of irradiance source influences not only kinetics (number of photons generated at wavelengths with photocatalytic or photolytic excitation potential) but also by-product selectivity (NH_4^+ or N-gases). Figure 8.2 (a) represents the synthesis of data for photocatalytic and photolytic reduction of nitrate in varied water matrices (FNR = HCOOH : NO_3^-) under the following irradiation sources: low pressure mercury lamp (LP), medium pressure mercury lamp (MP), xenon-arc lamp (Xe), light emitting diode into a slurry (LED), optical fiber-coupled to light emitting diode (OF-LED). A main takeaway from the electrical energy per order of these diverse photocatalytic scenarios is the importance of recognizing tradeoffs in efficiency and selectivity. In all cases herein, higher performance (lower EEO) is coupled to higher selectivity of undesirable NH_4^+.

Nitrate reduction is particularly complex due to its multi-step chemistry, for which particular wavelengths and contributing species (TiO_2 e^-_{cb}, $CO_2^{\bullet-}$) can alter both kinetics and selectivity outcomes (to N-gases or NH_4^+ as indicated by secondary y-axis, Fig. 8-2 (a)). The E_{EO} for nitrate reduction increases with decreasing per-photon energy depending on incident wavelengths, which further evidences a coupled photolytic/photocatalytic mechanism. LP lamps (253.7nm monochromatic irradiation) reduced nitrate across equivalent water matrices with significantly less energy per order removed: ~10 lower than MP (broad UV-vis polychromatic spectrum) and ~4 times lower than LED irradiation (285nm, 300nm, 365nm discrete wavelengths). Further, these results suggest energetic

economies of scale may enable efficacy of photocatalysis in effectively designed large-scale reactors. However, a significant tradeoff of selectivity is observed with the LP lamp, which generated 40-64% NH_4^+ as a final product of nitrate reduction. Of the three LP matrices, the highest kinetic performance is achieved without formic acid due to the photolytic/photocatalytic synergism, but yields the highest NH_4^+ because acidic pH and addition of a hole-scavenger are critical for selectivity to N-gases (Sá et al., 2009). Smaller-scale slurry experiments (10mL to 200mL) with MP, Xe, and LED irradiation demonstrated significantly higher E_{EO}, but predominant selectivity to N-gases.

Efficiencies of photolytic and photocatalytic reduction (slurry) of HONO are shown in Fig. 8-2 (b: Xe, LED). Though at the smallest scale, LED irradiation (285nm, 300nm, 365nm) in a slurry presents the lowest electrical energy demand for both photolytic and photocatalytic reduction of HONO, with <98% selectivity to nitrogen gases. For the Xe irradiance source, photocatalysis was more effective, potentially due to the broad wavelength irradiation which can cause oxidation of aqueous nitrogen intermediates (Tugaoen et al., 2017), thereby decreasing kinetics of reduction processes (Chapter 5).

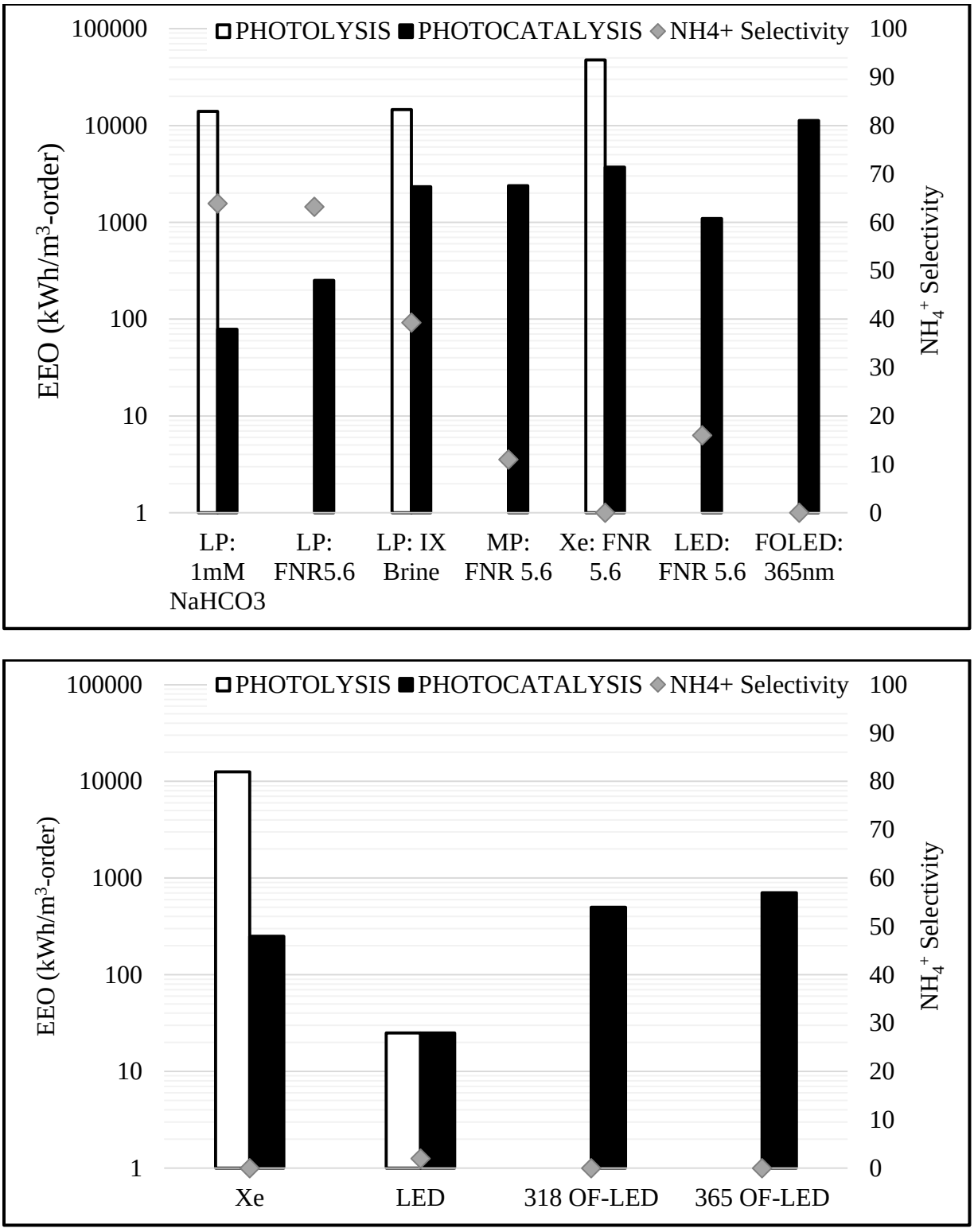

Figure 8-2. Electrical energy per order (E_{EO}, left) and NH_4^+ selectivity (as N, right) for varied irradiance input photolytic and photocatalytic (1 g/L P90) reduction of (**a**) nitrate

with 5.6 HCOOH: NO_3^- (varied concentration NO_3^-; LP:1.4mM, MP, Xe, LED, FOLED: 7.14mM, IX: 107mM) or (**b**) HONO with 5.6 HCOOH: NO_2^- (7.14mM NO_2^--N). Data for bars not shown was not collected.

Implementation Constraints for Photocatalytic Reactors

Though photocatalytic reduction of oxo-anion contaminants proceeded effectively via photolytic/photocatalytic pathways in slurry systems, nanoparticle photocatalyst recovery (for regeneration/reuse) from a large scale slurry system remained a significant obstacle. Due to the liability demonstrated upon implementation (leaching, Chapter 3), immobilization schemes were considered as an alternative for photocatalytic reactor design. Fixed-film systems required investigation into efficiency losses which stem from (1) diminished overall surface area of photocatalyst for contaminant removal, (2) insufficient light delivery mechanism to activate the photocatalyst, and (3) surface fouling and stability of films. Hence, determining an effective catalyst delivery method to enhance performance while managing light delivery was a key focus of this work.

The majority of batch-scale photocatalytic reactors with fixed-film photocatalyst delivery are of the following configurations: flat plate, cylindrical, or fixed bed/mixed-media (McCullagh et al., 2011). Attachment methodologies vary in the literature (Shan et al., 2010), but desired outcomes are strong adherence to the substrate media while maintaining high surface area for reaction and ease of reuse. With these objectives in mind, optical fibers presented the highest potential surface area with *in situ* light transmission directly to the catalyst interface as demonstrated in the literature for methylene blue (MB) oxidation (Nawi & Zain, 2012). Further, the use of quartz media allowed for UV

transmittance to promote photolytic and photocatalytic reactions as most photocatalysts (e.g., TiO_2) require UV irradiation for excitation. Accumulation of foulants on the surface may be readily mitigated by fiber extraction and surface regeneration, after which the quartz optical fibers may be reused.

Managing Light Delivery to Enhance Photocatalytic Performance in a Fixed-Film Reactor

The optimal light delivery source for combined performance in nitrate reduction selectivity and energetic efficiency was irradiation with light emitting diodes (Fig. 8-2). Production of inert wavelengths at high photon fluence dose decreases conventional reactor efficiency (Fig 8-2(a): MP, Xe) but can be managed by LED irradiation sources. These discrete wavelength emitters can be utilized to selectivity photolyze aqueous constituents while concurrently inducing photocatalyst excitation. Implementation of these compact irradiation sources in photocatalytic slurry systems presents similar obstacles to lamp-driven systems with regard to catalyst slurry removal and regeneration. However, UV-LEDs may be efficiently coupled to commercially available quartz optical fibers (Hou & Ku, 2013; Nicola J Peill et al., 2002; W. Wang & Ku, 2003b), which serve as a light delivery medium and substrate for nanomaterial photocatalyst immobilization (Fig. 8-2). In an un-optimized OF-LED system, HONO reduction progressed ~20 times slower than slurry photocatalysis under identical irradiation conditions and NO_3^- reduction was unsatisfactory. Hence, optimization of the OF-LED reactor was required for the remediation of oxo-anion pollutants.

Determination of the photocatalytic oxidation-reduction conditions induced by photocatalyst-coated optical fibers coupled to light emitting diodes was the initial benchmark required to progress towards optimization. Photocatalytic OF-LED treatment of MB and pCBA yielded the optimal reactor conditions for high-efficiency (Φ) removal of contaminants in an aqueous matrix (Chapter 6-7). Data from these investigations is synthesized in Figure 8-3. A fundamental investigation of reactor parameters (including coating length, thickness, light intensity) and resultant reactor performance demonstrated increased efficacy with dip-coating methodology compared to sol-gel, slurry or photolysis alone (Fig 8-3(a)). Thickness of the coating layer plays a key role in the overall efficacy of photocatalysis in the OF-LED configuration due to the necessity of excited charge carrier transport through the TiO_2 film layer to the aqueous interface for photocatalytic reaction (Hodes & Kamat, 2015; Könenkamp, 2000). Further, the when comparing photon fluence dose per unit surface area, the bundled optical fibers (Fig. 8-3 (b)) achieve higher Φ and lower E_{EO} compared to individual 1LED:1Fiber couples, either operating alone or simultaneously.

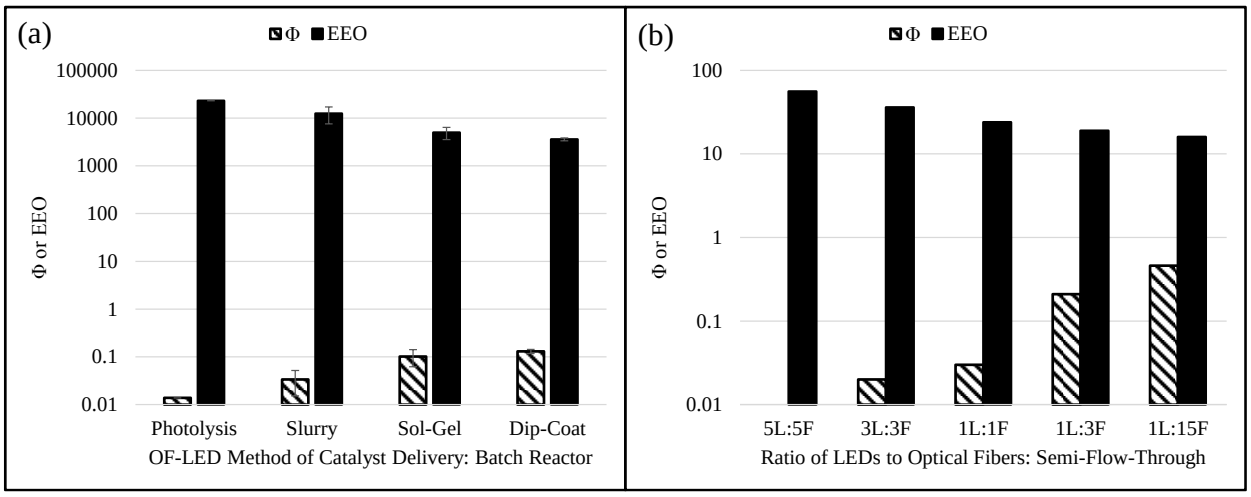

Figure 8-3. Quantum yield (Φ) and E_{EO} for OF-LED system for photocatalysis of: (**a**) methylene blue bleaching in batch reactor (10mL) varying catalyst delivery method under 318nm LED irradiation, and (**b**) pCBA oxidation in recirculating flow-through OF-LED system (150mL) varying photon fluence dose and optical fiber surface area under 365nm LED irradiation.

The OF-LED system capitalizes on the low-energy, discrete wavelength emission of an LED, high surface area per volume of optical fibers which can electrostatically immobilize TiO_2 (or other nanoparticle photocatalysts), and direct light delivery from the LED to the optical fiber/TiO_2 interface via optical refraction processes. Bundled optical fibers reduce the energetic footprint of the OF-LED reactor, while greatly enhancing surface area for photocatalytic reaction. In combination with E_{EO} values, these reactor characteristics meet the aforementioned requirements for a viable photocatalytic system design. Example considerations for successful implementation of the OF-LED photocatalytic configuration include: coupling quantum yield data to wavelengths delivered for varied contaminants (e.g., MB is photolyzed at 318nm but not 365nm, as investigated), and proper selection of photocatalyst to minimize additional chemical inputs (e.g., Ag/TiO_2 to reduce HCOOH demand and residual in NO_3^- reduction (Tugaoen et al., 2017)).

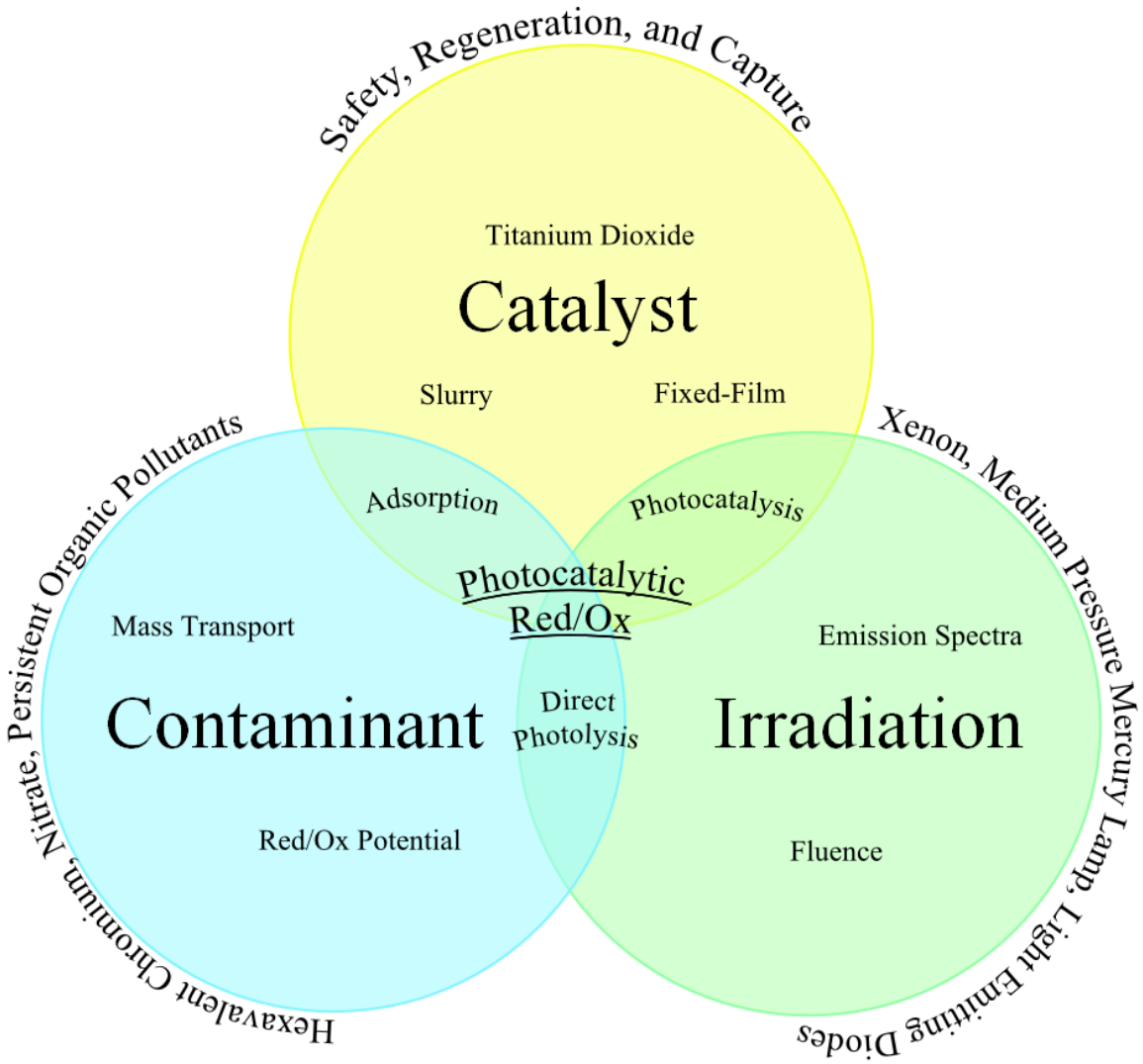

Figure 8-4. Conceptual model of the catalyst-contaminant-irradiation nexus for photocatalysis of aqueous phase contaminants.

A light-based investigative approach with quantifiable metrics such as E_{EO}, photon fluence dose, and quantum yield (Φ) demonstrated key variables for enhancing efficiency and selectivity of photocatalytic processes. Successful implementation of photocatalytic processes requires attention to the characteristic properties of the photocatalyst,

contaminant and irradiation source (Figure 8-4). Combining photocatalytic and photolytic processes for synergistically enhanced performance can ultimately yield viable systems, both for compact small-systems treatment, and application at larger scale to treat recalcitrant pollutants. Oxo-anion treatment requires careful consideration of catalyst fouling management (e.g., Cr(VI)/Cr(III)). Product selectivity (e.g., NO_3^-/NH_4^+) is relevant to both oxo-anions and treatment of organic compounds, where oxidation/reduction endpoints must be lower toxicity than initial compounds. Hence, management of these systems by a combined photolytic/photocatalytic, comprehensive photocatalytic approach can capitalize on known adsorption and photolytic properties to achieve desired outcomes.

CHAPTER 9

SUMMARY, CONCLUSIONS AND FUTURE RECOMMENDATIONS

The overarching research objective of this dissertation was to: **inform and improve light delivery (emission spectra, radiant intensity, reactor configuration) in order to enhance the photocatalytic reduction of hexavalent chromium (Cr(VI)) and nitrate, two common oxo-anions in drinking water, and photocatalytic oxidation of two model organic pollutants (methylene blue, (MB) and para-chlorobenzoic acid (pCBA)).**

Summary

Chapter 2: Review of the Literature

- Light delivery and engineered reactor design for photocatalytic systems are infrequently addressed in the literature but constitute significant contributions to overall system efficiency and opportunity for implementation. More frequent is synthesis, characterization and performance of new catalytic materials
- Hexavalent chromium and nitrate commonly occur in groundwaters used as drinking water supplies and can be reduced to more innocuous products (Cr(III), N_2) which are readily removable from the aqueous phase.
- Where photolysis and photocatalysis transform chemical contaminants, light delivery and light source may be able to target specific product outcomes.
- Model compounds such as methylene blue and para-chlorobenzoic acid are frequently used to determine quantum efficiency and radical production in varied reactor configurations.

Chapter 3: Hexavalent Chromium Removal Using UV-TiO_2/Ceramic Membrane Reactor

1. Under varied water matrix conditions, the removal of Cr(VI) via TiO_2 photocatalytic achieved complete removal of aqueous chromium species via (1) Cr(VI) adsorption, (2) surface reduction of Cr(VI) to Cr(III), followed by (3) precipitation of $Cr(OH)_{3(s)}$ on TiO_2.
2. Higher alkalinity, pH, or presence of divalent salts (e.g., Ca^{2+}) decreased Cr(VI) removal on TiO_2 due to catalyst aggregation and fouling, which increased EE/O.
3. Photo-aggregation of TiO_2 decreased Cr(VI) removal performance over time.
4. ICP-MS demonstrated the benefit of increased particle size: to decrease TiO_2 leaching through the ultrafiltration membrane into the permeate. Leached TiO_2 concentrations of up to 100 μg/L were observed without irradiation and as low as 0.11 μg/L under illumination for dechlorinated tap water.
5. TiO_2 photocatalytic reduction of Cr(VI) is economically feasible based on EE/O, however barriers to implementation at full scale remain: (1) slurry catalyst regeneration to manage foulants and aggregation, (2) optimized light delivery (to steer away from high-energy input UV-C irradiation).

Chapter 4: Challenges in Photocatalytic Reduction of Nitrate as a Water Treatment Technology

1. Photocatalytic reduction of nitrate to nitrogen gases occurs in model water spiked with sacrificial electron donor (e.g., HCOOH) and TiO_2-based photocatalysts.

2. Photogenerated e^- from TiO_2 cannot thermodynamically reduce nitrate to nitrite. $CO_2^{\bullet-}$ radical is noted as the primary reductive mechanism for transformation of nitrate to nitrite in photocatalysis or UV-C photolysis.
3. Photolysis of nitrate or nitrite are highly circular and produce predominant products of nitrate and nitrite, respectively. Photocatalysis can achieve nitrate reduction to NH_4^+/NH_3 or N-gases.
4. Composite catalysts (e.g., Ag/TiO_2) present the highest kinetics of photocatalytic reduction and N-gas selectivity.

Chapter 5: Ultraviolet Wavelengths Influence Kinetics and Selectivity for N-Gases during TiO_2 Photocatalytic Reduction of Nitrate

1. Nitrate reduction to nitrite or nitrogen gases does not proceed with photolysis alone, except under high-dose UV-C irradiation.
2. A bifurcation point occurs in the photocatalytic reduction of nitrate at NO_2^-/HONO ($pK_a = 3.39$), which influences by-product selectivity and reduction kinetics. EEO values for photolytic reduction of NO_2^- was about 30-times higher than HONO.
3. Based upon fluence-based half-lives, discrete wavelength irradiation reduces nitrate to N-gases at higher photonic and energetic efficiency than polychromatic irradiance sources.
4. Reduction of HONO (nitrous acid) in the presence of neat-TiO_2 photocatalysis at a 5.6 formic acid to nitrogen ratio (pH = 2.5) achieved the 100% selectivity to N-gases under a combination of 285 nm and 300 nm irradiation using UV-LEDs.

Chapter 6: Coupling Light Emitting Diodes with Photocatalyst Optical Fibers Improves Quantum Efficiency of Pollutant Oxidation

1. Single-coating layer dip-coated optical fibers were highest performing compared to various catalyst delivery methods (i.e., sol-gel, slurry).
2. Titanium dioxide-coated optical fibers coupled to UV-LEDs achieved higher quantum efficiency (Φ) of photocatalytic bleaching of methylene blue compared to an equivalent mass-dose slurry system. Values of Φ were 0.15 for OF/LED and 0.02 for slurry photocatalysis, respectively.
3. An attenuation of light refracted into the photocatalyst from the optical fibers is noted upon increased coating length and coating thickness for 318nm irradiation.
4. Based on modeling results, a combined effect of: (1) evanescent waves produced via total internal reflection of photons through optical fibers, and (2) refraction of light into the TiO_2 coating layer, are proposed to synergistically enhance photocatalytic reduction of methylene blue.

Chapter 7: Compact Light-Emitting Diode/Optical Fiber/TiO_2 Reactor for Photocatalytic Water Treatment

1. A reactor where light is delivered through TiO_2 coated optical fibers has been designed with modular LED and optical fiber inputs and evaluated using pCBA.
2. Design and optimization of this flow-through photocatalyst-coated optical fiber/light emitting diode reactor was tested for pCBA oxidation to determine •OH production. This yielded key insights regarding light delivery into immobilized catalyst photocatalytic reactors based on coated surface area and photon fluence.

3. Kinetics of pCBA oxidation were assessed in the TiO_2-OF/LED reactor. Highest removal was obtained using an array of LEDs coupled to multiple fibers according to the following ratio: 1LED:3fibers.
4. Quantum efficiency of pCBA oxidation demonstrated the feasibility of the technology for implementation with oxidation and reduction of more complex chemicals. Φ of single OF/LED was 0.01 compared to 0.46 for bundled optical fibers coupled to a single LED.
5. A key barrier for the TiO_2-OF/LED reactor is effectively launching light into the optical fiber bundles.

Conclusions

This work addressed two major barriers for photocatalysis: light delivery and reactor design. First, I concluded that management of light delivery can enable synergistic photocatalytic/photolytic reactions to enable efficient contaminant removal kinetics and desired by-product selectivity. Inherent to the management of light delivery (photon flux, emission spectra) is the physical configuration of the reactor, for which I found that a photocatalyst-coated OF/LED could deliver enhanced removal of organic pollutants compared to an equivalent photocatalyst-mass slurry system. Second, key metrics identified for the effective comparison of different reactors and light delivery configurations were: photon fluence dose, quantum yield (Φ) and electrical energy per order (E_{EO}). Each of these parameters is inherently normalized to quantify results across variables including: contaminant removal, volumetric throughput (or batch volume),

irradiation source intensity and spectrum, and/or energy consumption. Based on photon fluence dose, quantum yield and electrical energy per order, removal of contaminants under UV-LED irradiation exceeded that of polychromatic irradiation sources. This resulted from more efficient utilization of discrete wavelength photons for photocatalytic and photolytic reactions. Finally, an optimized reactor was designed to provide high reactive surface area (bundled optical fibers), direct light delivery to photocatalyst (via LED-generated photons refracting out of the optical fiber), and sufficient photon flux for photocatalyst excitation and photolytic reactions. Implementation of this reactor demonstrated viable E_{EO} and Φ for the oxidation of organic contaminants (methylene blue and pCBA). With attention to photocatalyst selection and photon fluence, this reactor could be modified to photocatalytically treat oxo-anions to innocuous products.

Recommendations for Future Research

From a thorough exploration of nitrate reduction literature, much work on the photocatalytic or photolytic reduction mechanisms has been published. However, a combined photocatalytic/photolytic process for targeted nitrate reduction to nitrogen gases had not been previously investigated. Whereas a synergism between photocatalysis and photolysis had not been considered as a possible mechanism, both processes are inherent to photocatalytic systems. Confirmation that discrete wavelength sources produce different nitrogen reduction endpoints (e.g., N-gases in lieu of NH_4^+) using UV-LEDs (Chapter 5) demonstrates the potential viability of a strategically designed reactor to achieve 100% nitrogen gas selectivity with reasonable kinetics. Further work related to this conclusion could be the implementation of broader-absorption photocatalysts that can readily employ

visible light and/or UV-A irradiation. This would decrease system E_{EO} through use of less energy intensive irradiation (e.g., in contrast to low pressure Hg irradiation) while delivering photons at wavelengths (UV-A, not visible light) that can induce photolytic reduction of nitrate intermediates.

The experimental work (Chapter 5) and the review of nitrate literature (Chapter 4) revealed that the production of $CO_2^{\bullet-}$ from formic acid is critical for photocatalytic reduction of nitrate using wide-band gap materials (e.g., TiO_2) where conduction band electrons do not provide sufficient energy to achieve nitrate-to-nitrite reduction. Therefore, a preliminary assessment of photocatalyst reduction potential to determine thermodynamic feasibility of nitrate reduction via e^-_{cb} is recommended to determine requirements for hole scavenger addition. Reduction of other oxo-anions should be analyzed in a similar manner, to address thermodynamic potentials of their reduction and subsequently select appropriate photocatalysts. Organic contaminants are typically oxidized by either the h^+_{vb} or $\cdot OH$, and hence, appropriately determining the band-edge of the photocatalyst band-gap is essential for effective oxidation.

In tandem to photocatalyst and hole scavenger selection, irradiation sources must be assessed from the perspective of photonic efficiency in the context of photocatalysis and photolysis. Highest efficiency light sources would be those where each emitted photon is capable of producing a meaningful result (e.g., photolysis or band-gap electron excitation). This enhances contaminant removal performance (Φ) and decreases energy consumption (E_{EO}) because electricity is not provided to produce photons outside the photoactive spectrum. Hence, assessment of catalyst-light pairing is important to future research work

to manage energy consumption and increase process viability for coupled photolytic/photocatalytic systems.

Photocatalytic reactor design utilizing immobilized catalyst film on an optical fibers presents a unique opportunity to capitalize on photocatalytic and photolytic reactions at compact reactor scale. With ongoing advancements in both optical fiber technology (and cost) and light emitting diodes, the prospect of implementing *in situ* immobilized photocatalysis with high surface area is becoming realizable. A proof of concept of the technology is provided in Chapters 6-7, as well as discussion a few obstacles that yield opportunity space for new research. Demonstration of higher performance in a fixed-film versus slurry photocatalysis system was achieved using un-optimized conditions (Chapter 6). There is great opportunity for improvement of reactor design and implementation, for which a preliminary attempt was outlined in Chapter 7. A key area of future work would be to improve the percent of light launched into the fiber from ~50% to > 80% using optical lenses. Other improvements include factors related to relative surface area, delivery of appropriate photon flux/dose, and management of coating thickness.

REFERENCES

Abdel-Maksoud, Y., Imam, E., & Ramadan, A. (2016). TiO2 Solar Photocatalytic Reactor Systems: Selection of Reactor Design for Scale-up and Commercialization—Analytical Review. *Catalysts*, *6*(138), 1–26. http://doi.org/10.3390/catal6090138

Afzal, B. M. (2006). Drinking water and women's health. *Journal of Midwifery & Women's Health*, *51*(1), 12–8. http://doi.org/10.1016/j.jmwh.2005.08.014

Akpan, U. G., & Hameed, B. H. (2009). Parameters affecting the photocatalytic degradation of dyes using TiO2-based photocatalysts: A review. *Journal of Hazardous Materials*, *170*, 520–529. http://doi.org/10.1016/j.jhazmat.2009.05.039

Alexiadis, a., Baldi, G., & Mazzarino, I. (2001). Modelling of a photocatalytic reactor with a fixed bed of supported catalyst. *Catalysis Today*, *66*(2–4), 467–474. http://doi.org/10.1016/S0920-5861(01)00255-3

Alexiadis, a., & Mazzarino, I. (2005). Design guidelines for fixed-bed photocatalytic reactors. *Chemical Engineering and Processing: Process Intensification*, *44*(4), 453–459. http://doi.org/10.1016/j.cep.2004.06.009

Altomare, M., Chiarello, G. L., Costa, A., Guarino, M., & Selli, E. (2012). Photocatalytic abatement of ammonia in nitrogen-containing effluents. *Chemical Engineering Journal*, *191*, 394–401. http://doi.org/10.1016/j.cej.2012.03.037

Altomare, M., Vittoria, M., Luca, G., Di, A., Palmisano, L., & Selli, E. (2015). High activity of brookite TiO 2 nanoparticles in the photocatalytic abatement of ammonia in water. *Catalysis Today*, *252*, 184–189. http://doi.org/10.1016/j.cattod.2014.09.031

Anan'ev, V., & Miklin, M. (2005). The peroxynitrite formation under photolysis of alkali nitrates. *Journal of Photochemistry and Photobiology A: Chemistry*, *172*, 289–292. http://doi.org/10.1016/j.jphotochem.2004.12.018

Anderson, J. A. (2011). Photocatalytic nitrate reduction over Au/TiO2. *Catalysis Today*, *175*, 316–321. http://doi.org/10.1016/j.cattod.2011.04.009

Anderson, J. A. (2012). Simultaneous photocatalytic degradation of nitrate and oxalic acid over gold promoted titania. *Catalysis Today*, *181*(1), 171–176. http://doi.org/10.1016/j.cattod.2011.05.027

Ansari, S. A., Khan, M. M., Ansari, M. O., & Cho, M. H. (2016). Nitrogen-doped titanium dioxide (N-doped TiO2) for visible light photocatalysis. *New Journal of Chemistry*, *40*, 3000–3009. http://doi.org/10.1039/C5NJ03478G

Archna, Sharma, S. K., & Sobti, R. C. (2012). Nitrate Removal from Ground Water: A Review. *E-Journal of Chemistry*, *9*(4), 1667–1675.

http://doi.org/10.1155/2012/154616

Aristova, N. A., Leitner, N. K. V., & Piskarev, I. M. (2002). Degradation of Formic Acid in Different Oxidative Processes.pdf, *36*(3), 228–233.

Athanasiou, D. A., Romanos, G. E., & Falaras, P. (2016). Design and optimization of a photocatalytic reactor for water purification combining optical fiber and membrane technologies. *Chemical Engineering Journal*, *305*, 92–103. http://doi.org/10.1016/j.cej.2015.11.080

Autin, O., Romelot, C., Rust, L., Hart, J., Jarvis, P., MacAdam, J., … Jefferson, B. (2013). Evaluation of a UV-light emitting diodes unit for the removal of micropollutants in water for low energy advanced oxidation processes. *Chemosphere*, *92*(6), 745–51. http://doi.org/10.1016/j.chemosphere.2013.04.028

Bao, G., & Van, T. (2000). Modeling of Evanescent Energy in Optical Fibers. *Journal of Computational Physics*, *161*, 700–717. http://doi.org/10.1006/jcph.2000.6528

Barakat, M. A., & Kumar, R. (2016). *Photocatalytic Activity Enhancement of Titanium Dioxide Nanoparticles: Degradation of Pollutants in Wastewater*. Springer. http://doi.org/10.1007/978-3-319-24271-2_1

Barat, F., Gilles, L., Hickel, B., & Sutton. (1970a). Flash Photolysis of the Nitrate Ion in Aqueous Solution: Excitation at 200nm. *Journal of the Chemical Society A: Inorganic, Physical, Theoretical*, 1982–1986. http://doi.org/10.1039/J19700001982

Barat, F., Gilles, L., Hickel, B., & Sutton, J. (1970b). Flash photolysis of the nitrate ion in aqueous solution: excitation at 200 nm. *Journal of the Chemical Society A …*, 1982–1986. Retrieved from http://pubs.rsc.org/en/content/articlehtml/1970/j1/j19700001982

Barrabes, N., & Sa, J. (2011). Catalytic nitrate removal from water, past, present and future perspectives. *Applied Catalysis B: Environmental*, *104*(1–2), 1–5. http://doi.org/10.1016/j.apcatb.2011.03.011

Barrera-Díaz, C. E., Lugo-Lugo, V., & Bilyeu, B. (2012). A review of chemical, electrochemical and biological methods for aqueous Cr(VI) reduction. *Journal of Hazardous Materials*, *223–224*, 1–12. http://doi.org/10.1016/j.jhazmat.2012.04.054

Barton, I., Matejec, V., & Matousek, J. (2016). Photocatalytic activity of nanostructured TiO2 coating on glass slides and optical fibers for methylene blue or methyl orange decomposition under different light excitation. *Journal of Photochemistry and Photobiology A: Chemistry*, *317*, 72–80. http://doi.org/10.1016/j.jphotochem.2015.11.009

Beaumont, J. J., Sedman, R. M., Reynolds, S. D., Sherman, C. D., Li, L.-H., Howd, R. a, … Alexeeff, G. V. (2008). Cancer mortality in a Chinese population exposed to

hexavalent chromium in drinking water. *Epidemiology*, *19*(1), 12–23. http://doi.org/10.1097/EDE.0b013e31815cea4c

Beck, S. E., Ryu, H., Boczek, L. A., Cashdollar, J. L., Jeanis, K. M., Rosenblum, J. S., … Linden, K. G. (2017). Evaluating UV-C LED disinfection performance and investigating potential dual-wavelength synergy. *Water Research*, *109*, 207–216. http://doi.org/10.1016/j.watres.2016.11.024

Bedjanian, Y., & El Zein, A. (2012). Interaction of NO_2 with TiO_2 Surface Under UV Irradiation: Products Study. *The Journal of Physical Chemistry A*, *116*(7), 1758–1764. http://doi.org/10.1021/jp210078b

Behnajady, M. A., Vahid, B., Modirshahla, N., & Shokri, M. (2009). Evaluation of electrical energy per order (EEO) with kinetic modeling on the removal of Malachite Green by US/UV/H2O2 process. *Desalination*, *249*(1), 99–103. http://doi.org/10.1016/j.desal.2008.07.025

Behnajady, M. a, & Modirshahla, N. (2006). Evaluation of electrical energy per order (EEO) with kinetic modeling on the photooxidative degradation of C.I. acid orange 7 in a tubular continuous-flow photoreactor. *Ind. Eng. Chem. Res.*, *45*, 553–557. http://doi.org/10.1016/j.desal.2008.07.025

Bems, B., Jentoft, F. C., & Schlögl, R. (1999). Photoinduced decomposition of nitrate in drinking water in the presence of titania and humic acids. *Applied Catalysis B: Environmental*, *20*(2), 155–163. http://doi.org/10.1016/S0926-3373(98)00105-2

Benotti, M. J., Stanford, B. D., Wert, E. C., & Snyder, S. a. (2009). Evaluation of a photocatalytic reactor membrane pilot system for the removal of pharmaceuticals and endocrine disrupting compounds from water. *Water Research*, *43*(6), 1513–22. http://doi.org/10.1016/j.watres.2008.12.049

Benotti, M. J., Trenholm, R. a, Vanderford, B. J., Holady, J. C., Stanford, B. D., & Snyder, S. a. (2009). Pharmaceuticals and endocrine disrupting compounds in U.S. drinking water. *Environmental Science & Technology*, *43*(3), 597–603. http://doi.org/10.1021/es801845a

Bhatnagar, A., & Sillanpää, M. (2011). A review of emerging adsorbents for nitrate removal from water. *Chemical Engineering Journal*, *168*(2), 493–504. http://doi.org/10.1016/j.cej.2011.01.103

Bianchi, T. S., DiMarco, S. F., Cowan, J. H., Hetland, R. D., Chapman, P., Day, J. W., & Allison, M. A. (2010). The science of hypoxia in the northern Gulf of Mexico: A review. *Science of the Total Environment*, *408*(7), 1471–1484. http://doi.org/10.1016/j.scitotenv.2009.11.047

Bianchini, R., Forte, C., Musumarra, G., Pinzino, C., & Sergi, C. (1997). Spectroscopic evidence of a free-radical mechanism in the reduction of Schiff bases by formic acid.

Tetrahedron, *4020*(20), 6907–6916. Retrieved from http://www.sciencedirect.com/science/article/pii/S0040402097003918

Bilodeau, R. C., Scheer, M., & Haugen, H. K. (1998). Infrared laser photodetachment of transition metal negative ions : studies on Cr − , Mo − , Cu − and Ag −. *J. Phys. B: At. Mol. Opt. Phys.*, *31*, 3885–3891.

Bilski, P., Chignell, C. F., Szychlinski, J., Borkowski, A., Oleksy, E., & Reszka, K. (1992). Photooxidation of Organic and Inorganic Substrates during UV Photolysis of Nitrite Anion in Aqueous Solution. *Journal of the American Chemical Society*, *114*, 549–556. http://doi.org/10.1021/ja00028a023

Blesa, M. A., Weisz, A. D., Morando, P. J., Salfity, J. A., Magaz, G. E., & Regazzoni, A. E. (2000). The interaction of metal oxide surfaces with complexing agents dissolved in water. *Coordination Chemistry Reviews*, *196*(1), 31–63. http://doi.org/http://dx.doi.org/10.1016/S0010-8545(99)00005-3

Blowes, D. W., Ptacek, C. J., & Jambor, J. L. (1997). In-situ remediation of Cr(VI)-contaminated groundwater using permeable reactive walls: Laboratory studies. *Environmental Science and Technology*, *31*(12), 3348–3357. http://doi.org/10.1021/es960844b

Bolton, J. (2000). Calculation of ultraviolet fluence rate distributions in an annular reactor: significance of refraction and reflection. *Water Research*, *34*(13), 3315–3324. http://doi.org/10.1016/S0043-1354(00)00087-7

Bolton, J. R., Bircher, K. G., Tumas, W., & Tolman, C. A. (2001). Figures-of-merit for the technical development and application of advanced oxidation technologies for both electric- and solar-driven systems (IUPAC Technical Report). *Pure and Applied Chemistry*, *73*(4), 627–637. http://doi.org/10.1351/pac200173040627

Bolton, J. R., & Linden, K. G. (2003). Standardization of Methods for Fluence (UV Dose) Determination in Bench-Scale UV Experiments. *Journal of Environmental Engineering*, *129*(March), 209–215. http://doi.org/10.1061/(ASCE)0733-9372(2003)129:3(209)

Bolton, J. R., Mayor-smith, I., & Linden, K. G. (2015). Rethinking the Concepts of Fluence (UV Dose) and Fluence Rate : The Importance of Photon-based Units – A Systemic Review. *Photochemistry and Photobiology*, *91*, 1252–1262. http://doi.org/10.1111/php.12512

Bolton, J. R., & Stefan, M. I. (2002). Fundamental photochemical approach to the concepts of fluence (UV dose) and electrical energy efficiency in photochemical degradation reactions. *Research on Chemical Intermediates*, *28*(7), 857–870. http://doi.org/10.1163/15685670260469474

Bolton, J. R., Stefan, M. I., Shaw, P.-S., & Lykke, K. R. (2011). Determination of the

quantum yields of the potassium ferrioxalate and potassium iodide–iodate actinometers and a method for the calibration of radiometer detectors. *Journal of Photochemistry and Photobiology A: Chemistry*, *222*(1), 166–169. http://doi.org/10.1016/j.jphotochem.2011.05.017

Bolton, J., & Stefan, M. (2002). Fundamental photochemical approach to the concepts of fluence (UV dose) and electrical energy efficiency in photochemical degradation reactions. *Research on Chemical Intermediates*, *28*(7), 857–870. Retrieved from http://link.springer.com/article/10.1163/15685670260469474

Bonner, F. T., & Wang, N.-Y. (1986). Reduction of nitric oxide by hydroxylamine. 1. Kinetics and mechanism. *Inorganic Chemistry*, *25*(4), 1858–1862. http://doi.org/10.1021/ic00231a029

Bonsen, E.-M., Schroeter, S., Jacobs, H., & Broekaert, J. A. C. (1997). Photocatalytic Degradation of Ammonia with TiO2 as Photocatalyst in the Laboratory and under the use of Solar Radiation. *Chemosphere*, *35*(7), 1431–1445. http://doi.org/10.1016/S0045-6535(97)00216-6

Botta, S. G., Navio, J. A., Hidalgo, C., Restrepo, G. M., & Litter, M. I. (1999). Photocatalytic properties of ZrO2 and Fe/ZrO2 semiconductors prepared by a sol – gel technique. *Journal of Photochemistry & Photobiology A: Chemistry*, *129*, 89–99. http://doi.org/10.1016/S1010-6030(99)00150-1

Boule, P., Bahnemann, D., Robertson, P., Vione, D., Maurino, V., Minero, C., & Pelizzetti, E. (2005). Reactions Induced in Natural Waters by Irradiation of Nitrate and Nitrite Ions, *2M*(September), 221–253. http://doi.org/10.1007/b138185

Bowker, C., Sain, A., Shatalov, M., & Ducoste, J. (2011). Microbial UV fluence-response assessment using a novel UV-LED collimated beam system. *Water Research*, *45*(5), 2011–9. http://doi.org/10.1016/j.watres.2010.12.005

Bowker, M. (2007). The surface structure of titania and the effect of reduction. *Current Opinion in Solid State and Materials Science*, *10*, 153–162. http://doi.org/10.1016/j.cossms.2007.03.001

Boyjoo, Y., Ang, M., & Pareek, V. (2014). Lamp emission and quartz sleeve modelling in slurry photocatalytic reactors. *Chemical Engineering Science*, *111*, 34–40. http://doi.org/10.1016/j.ces.2014.02.023

Bravo, A., Garcia, J., Domenech, X., & Peral, J. (1993). Some aspects of the photocatalytic oxidation of ammonium ion by titanium-dioxide. *Journal of Chemical Research*, *9*, 376–377.

Brillas, E., Sires, I., & Oturan, M. A. (2009). Electro-Fenton Process and Related Electrochemical Technologies Based on Fenton's Reaction Chemistry. *Chem. Rev.*, *109*, 6570–6631. http://doi.org/10.1021/cr900136g

Brito, F., Ascanio, J., Mateo, S., Hernfindez, C., Araujo, L., Gili, P., … Mederos, A. (1997). Equilibria of chromate (VI) species in acid medium and ab initio studies of these species. *Polyhedron*, *16*(21), 3835–3846.

Brouwer, A. M. (2011). Standards for photoluminescence quantum yield measurements in solution (IUPAC Technical Report). *Pure and Applied Chemistry*, *83*(12), 2213–2228. http://doi.org/10.1351/PAC-REP-10-09-31

Burkart, M. R., & Kolpin, D. W. (1993). Hydrologic and Land-Use Factors Associated with Herbicides and Nitrate in Near-Surface Aquifers. *Journal of Environment Quality*. http://doi.org/10.2134/jeq1993.00472425002200040002x

Burkart, M. R., & Stoner, J. D. (2007). Nitrate in aquifers beneath agricultural systems. *Water Science and Technology*, *56*(1), 59–69. http://doi.org/10.2166/wst.2007.436

Burow, K. R., Nolan, B. T., Rupert, M. G., & Dubrovsky, N. M. (2010). Nitrate in groundwater of the United States, 1991-2003. *Environmental Science & Technology*, *44*(13), 4988–97. http://doi.org/10.1021/es100546y

Buxton, G. V., Greenstock, C. L., Helman, P. W., & Ross, A. B. (1988). Critical review of rate constants for reactions of hydrated electrons , hydrogen atoms and hydroxyl radicals (·OH /·O-) in aqueous solution. *Journal of Physical and Chemistry Reference Data*, *17*, 513–886. http://doi.org/10.1063/1.555805

Cai, Y., & Feng, Y. P. (2016). Review on charge transfer and chemical activity of TiO2: Mechanism and applications. *Progress in Surface Science*, *91*, 183–202. http://doi.org/10.1016/j.progsurf.2016.11.001

California EPA. (2014). Chromium-6 Drinking Water MCL. Retrieved from http://www.waterboards.ca.gov/drinking_water/certlic/drinkingwater/Chromium6.shtml

Cao, Q., Berski, S., Latajka, Z., Räsänen, M., & Khriachtchev, L. (2014). Reaction of atomic hydrogen with formic acid. *Physical Chemistry Chemical Physics : PCCP*, *16*(13), 5993–6001. http://doi.org/10.1039/c3cp55265a

Carneiro, J. T., Berger, R., Moulijn, J. A., & Mul, G. (2009). An internally illuminated monolith reactor: Pros and cons relative to a slurry reactor. *Catalysis Today*, *147S*, S324–S329. http://doi.org/10.1016/j.cattod.2009.07.041

Cassano, A. E., Martin, C. A., J., B. R., & Alfano, O. M. (1995). Photoreactor Analysis and Design : Fundamentals and Applications. *Ind. Eng. Chem. Res.*, *34*, 2155–2201. http://doi.org/10.1021/ie00046a001

Cenens, J., & Schoonheydt, R. A. (1988). VISIBLE SPECTROSCOPY OF METHYLENE BLUE ON HECTORITE, LAPONITE B, AND BARASYM IN AQUEOUS SUSPENSION. *Clays and Clay Minerals*, *36*(3), 214–224.

http://doi.org/10.1346/CCMN.1988.0360302

Chatterley, C., & Linden, K. (2010, September). Demonstration and evaluation of germicidal UV-LEDs for point-of-use water disinfection. *Journal of Water and Health*. http://doi.org/10.2166/wh.2010.124

Chen, D. H., Ye, X., & Li, K. (2005). Oxidation of PCE with a UV LED photocatalytic reactor. *Chemical Engineering and Technology*, *28*(1), 95–97. http://doi.org/10.1002/ceat.200407012

Chen, D., & K. Ray, A. (2001). Removal of toxic metal ions from wastewater by semiconductor photocatalysis. *Chemical Engineering Science*, *56*(4), 1561–1570. http://doi.org/10.1016/S0009-2509(00)00383-3

Chen, Q., Chang, J., Li, L., & Yuan, J. Y. (2008). A new kinetic model of photocatalytic degradation of formic acid in UV/TiO2 suspension system with in-situ monitoring. *Reaction Kinetics and Catalysis Letters*, *93*(1), 157–164. http://doi.org/10.1007/s11144-008-5201-1

Chen, R. Z., Craik, S. a, & Bolton, J. R. (2009). Comparison of the action spectra and relative DNA absorbance spectra of microorganisms: information important for the determination of germicidal fluence (UV dose) in an ultraviolet disinfection of water. *Water Research*, *43*(20), 5087–96. http://doi.org/10.1016/j.watres.2009.08.032

Chen, Y. X., Zhang, Y., & Chen, G. H. (2003). Appropriate conditions or maximizing catalytic reduction efficiency of nitrate into nitrogen gas in groundwater. *Water Research*, *37*(10), 2489–2495. http://doi.org/10.1016/S0043-1354(03)00028-9

Cheng, X. F., & Leng, W. H. (2007). Enhanced photoelectrocatalytic performance of Zn-doped WO 3 photocatalysts for nitrite ions degradation under visible light, *68*, 1976–1984. http://doi.org/10.1016/j.chemosphere.2007.02.010

Chenthamarakshan, C. R., Rajeshwar, K., & Wolfrum, E. J. (2000). Heterogeneous Photocatalytic Reduction of Cr(VI) in UV-Irradiated Titania Suspensions: Effect of Protons, Ammonium Ions, and Other Interfacial Aspects. *Langmuir*, *16*(6), 2715–2721. http://doi.org/10.1021/la9911483

Choi, W., Ko, J. Y., Park, H., & Chung, J. S. (2001). Investigation on tio2-coated optical fibers for gas-phase photocatalytic oxidation of acetone. *Applied Catalysis B: Environmental*, *31*(3), 209–220. http://doi.org/10.1016/S0926-3373(00)00281-2

Chu, J., & Zhong, L. (2012). Photocatalytic degradation of methylene blue with side-glowing optical fiber deliverying visible light. *Chinese Journal of Chemical Engineering*, *20*(5), 895–899. http://doi.org/10.1016/S1004-9541(12)60415-7

Chu, L., & Anastasio, C. (2003). Quantum Yields of Hydroxyl Radical and Nitrogen Dioxide from the Photolysis of Nitrate on Ice. *Journal of Physical Chemistry A*,

107(45), 9594–9602. http://doi.org/10.1021/jp0349132

Close, J., Ip, J., & Lam, K. H. (2006). Water recycling with PV-powered UV-LED disinfection. *Renewable Energy*, *31*(11), 1657–1664. http://doi.org/10.1016/j.renene.2005.08.034

Coenen, T., Van de Moortel, W., Logist, F., Luyten, J., Van Impe, J. F. M., & Degrève, J. (2013). Modeling and geometry optimization of photochemical reactors: Single- and multi-lamp reactors for UV-H2O2 AOP systems. *Chemical Engineering Science*, *96*, 174–189. http://doi.org/10.1016/j.ces.2013.03.056

Compton, J. E., Harrison, J. A., Dennis, R. L., Greaver, T. L., Hill, B. H., Jordan, S. J., … Campbell, H. V. (2011). Ecosystem services altered by human changes in the nitrogen cycle: A new perspective for US decision making. *Ecology Letters*, *14*(8), 804–815. http://doi.org/10.1111/j.1461-0248.2011.01631.x

Cook, A. R., Dimitrijevic, N., Dreyfus, B. W., Meisel, D., Curtiss, L. A., & Camaioni, D. M. (2001). Reducing Radicals in Nitrate Solutions. The NO32 - System Revisited. *J. Phys. Chem. A*, *105*, 3658–3666. http://doi.org/10.1021/jp0038052

Costa, M. (1997). Toxicity and carcinogenicity of Cr (VI) in animal models and humans. *CRC Critical Reviews in Toxicology*, *27*(5), 431–442. Retrieved from http://informahealthcare.com/doi/abs/10.3109/10408449709078442

Czapski, G., & Peled, E. (1968). On the pH dependence of G-reducing in the radiation chemistry of aqueous solutions. *Israel Journal of Chemistry*, *6*, 421–436. http://doi.org/10.1002/ijch.196800054

Dalrymple, O. K., Stefanakos, E., Trotz, M. A., & Goswami, D. Y. (2010). A review of the mechanisms and modeling of photocatalytic disinfection. *Applied Catalysis B: Environmental*. Elsevier B.V. http://doi.org/10.1016/j.apcatb.2010.05.001

Dalton, J. S., Janes, P. A., Jones, N. G., Nicholson, J. A., Hallam, K. R., & Allen, G. C. (2002). Photocatalytic oxidation of NOx gases using TiO2: A surface spectroscopic approach. *Environmental Pollution*, *120*(2), 415–422. http://doi.org/10.1016/S0269-7491(02)00107-0

Danielopol, D., Griebler, C., Gunatilaka, A., & Notenboom, J. (2003). Present state and future prospects for groundwater ecosystems. *Environmental Conservation*, *30*(2), 104–130. http://doi.org/10.1017/S0376892903000109

Daniels, M. (1968). Photochemistry of the Aqueous Nitrate System. I. Excitation in the 300-mu Band. *Symposium on Inorganic Photochemistry*, *72*(2), 389–399.

Danion, A., Bordes, C., Disdier, J., Gauvrit, J.-Y., Guillard, C., Lantéri, P., & Jaffrezic-Renault, N. (2004). Optimization of a single TiO2-coated optical fiber reactor using experimental design. *Journal of Photochemistry and Photobiology A: Chemistry*,

168(3), 161–167. http://doi.org/10.1016/j.jphotochem.2004.03.002

Danion, A., Disdier, J., Guillard, C., Abdelmalek, F., & Jaffrezic-Renault, N. (2004). Characterization and study of a single-TiO2-coated optical fiber reactor. *Applied Catalysis B: Environmental*, *52*(3), 213–223. http://doi.org/10.1016/j.apcatb.2004.04.005

Danion, A., Disdier, J., Guillard, C., Paisse, O., & Jaffrezic-Renault, N. (2006). Photocatalytic degradation of imidazolinone fungicide in TiO 2-coated optical fiber reactor. *Applied Catalysis B: Environmental*, *62*(3–4), 274–281. http://doi.org/10.1016/j.apcatb.2005.08.008

Dariani, R. S., Esmaeili, A., Mortezaali, A., & Dehghanpour, S. (2016). Photocatalytic reaction and degradation of methylene blue on TiO2 nano-sized particles. *Optik - International Journal for Light and Electron Optics*, *127*(18), 7143–7154. http://doi.org/10.1016/j.ijleo.2016.04.026

Dayan, A. D., & Paine, A. J. (2001). Mechanisms of chromium toxicity, carcinogenicity and allergenicity: review of the literature from 1985 to 2000. *Human & Experimental Toxicology*, *20*(9), 439–451. http://doi.org/10.1191/096032701682693062

de Bem Luiz, D., Andersen, S. L. F., Berger, C., Jose, H. J., & Moreira, R. de F. P. M. (2012). Photocatalytic reduction of nitrate ions in water over metal-modified TiO2. *Journal of Photochemistry & Photobiology, A: Chemistry*, *246*, 36–44. http://doi.org/10.1016/j.jphotochem.2012.07.011

de Bem Luiz, D., José, H. J., & Peralta, R. de F. (2014). Kinetics of photocatalytic reduction of nitrate in synthetic and real effluent using TiO2 doped with Zn as photocatalyst. *J. Chem. Technol. Biotechnol.* http://doi.org/10.1002/jctb.4375

De Laurentiis, E., Minella, M., Berto, S., Maurino, V., Minero, C., & Vione, D. (2015). The fate of nitrogen upon nitrite irradiation: Formation of dissolved vs. gas-phase species. *Journal of Photochemistry and Photobiology A: Chemistry*, *307–308*(3), 30–34. http://doi.org/10.1016/j.jphotochem.2015.04.005

Denny, F., Scott, J., Pareek, V., Peng, G. D., & Amal, R. (2010). Computational fluid dynamics modelling and optimal configuring of a channelled optical fibre photoreactor. *Chemical Engineering Science*, *65*(17), 5029–5040. http://doi.org/10.1016/j.ces.2010.06.003

Denny, F., Scott, J., Peng, G. D., & Amal, R. (2010). Channelled optical fibre photoreactor for improved air quality control. *Chemical Engineering Science*, *65*(2), 882–889. http://doi.org/10.1016/j.ces.2009.09.038

Devahasdin, S., Fan, C., Li, K., & Chen, D. H. (2003). TiO2 photocatalytic oxidation of nitric oxide: Transient behavior and reaction kinetics. *Journal of Photochemistry and Photobiology A: Chemistry*, *156*(1–3), 161–170. http://doi.org/10.1016/S1010-

6030(03)00005-4

Devi, L. G., & Kavitha, R. (2013). A review on non metal ion doped titania for the photocatalytic degradation of organic pollutants under UV/solar light: Role of photogenerated charge carrier dynamics in enhancing the activity. *Applied Catalysis B: Environmental*, *140–141*, 559–587. http://doi.org/10.1016/j.apcatb.2013.04.035

Dey, G. R., Nair, K. N. R., & Pushpa, K. K. (2009). Photolysis studies on HCOOH and HCOO− in presence of TiO2 photocatalyst as suspension in aqueous medium. *Journal of Natural Gas Chemistry*, *18*(1), 50–54. http://doi.org/10.1016/S1003-9953(08)60075-4

Dionysiou, D. D., Suidan, M. T., Bekou, E., Baudin, I., & Laîné, J. M. (2000). Effect of ionic strength and hydrogen peroxide on the photocatalytic degradation of 4-chlorobenzoic acid in water. *Applied Catalysis B: Environmental*, *26*(3), 153–171. http://doi.org/10.1016/S0926-3373(00)00124-7

Dosta, S., Robotti, M., Garcia-Segura, S., Brillas, E., Garcia, I., & Guilemany, J. M. (2016). Influence of atmospheric plasma spraying on the solar photoelectro-catalytic properties of TiO2 coatings. *Applied Catalysis B, Environmental*, *189*, 151–159. http://doi.org/10.1016/j.apcatb.2016.02.048

Doudrick, K., Monzón, O., Mangonon, A., Hristovski, K., & Westerhoff, P. (2012). Nitrate reduction in water using commercial titanium dioxide photocatalysts (P25, P90, and Hombikat UV100). *Journal of Environmental Engineering*, *138*, 852–861. http://doi.org/10.1061/(ASCE)EE.1943-7870.0000529.

Doudrick, K., Yang, T., Hristovski, K., & Westerhoff, P. (2013). Photocatalytic nitrate reduction in water: Managing the hole scavenger and reaction by-product selectivity. *Applied Catalysis B: Environmental*, *136–137*, 40–47. http://doi.org/10.1016/j.apcatb.2013.01.042

Dozzi, M. V., & Selli, E. (2013). Doping TiO2 with p-block elements: Effects on photocatalytic activity. *Journal of Photochemistry and Photobiology C: Photochemistry Reviews*, *14*, 13–28. http://doi.org/10.1016/j.jphotochemrev.2012.09.002

Dung, D., Ramsden, J., & Gratzel, M. (1982). Dynamics of Interfacial Electron-Transfer Processes in Colloidal Semiconductor Systems. *Journal of the American Chemical Society*, *104*, 2977–2985. http://doi.org/10.1021/ja00375a006

El Zein, A., Bedjanian, Y., & Romanias, M. N. (2013). Kinetics and products of HONO interaction with TiO2 surface under UV irradiation. *Atmospheric Environment*, *67*, 203–210. http://doi.org/10.1016/j.atmosenv.2012.11.016

Electronic Code of Federal Regulations. (2017). Appendix A to Subpart O of Part 141 - Regulated Contaminants.

Elliot, A. F., & Gibson, R. J. (1974). *An Introduction to Solid State Physics and its Applications*. New York: Barnes & Noble.

Elovitz, M. S., & von Gunten, U. (1999). Hydroxyl radical ozone ratios during ozonation processes. I. The R-ct concept. *Ozone-Science & Engineering*, *21*(3), 239–260. http://doi.org/10.1080/01919519908547239

Elyasi, S., & Taghipour, F. (2006). Simulation of UV photoreactor for water disinfection in Eulerian framework. *Chemical Engineering Science*, *61*, 4741–4749. http://doi.org/10.1016/j.ces.2006.03.010

Ershov, B. G., Janata, E., Alam, M. S., & Gordeev, A. V. (2008). Studies of the reaction of the hydroxyl radical with the oxalate ion in an acidic aqueous solution by pulse radiolysis. *Russian Chemical Bulletin*, *57*(6), 1187–1189. http://doi.org/10.1007/s11172-008-0148-y

Eskandarloo, H., Badiei, A., Behnajady, M. A., & Ziarani, G. M. (2015). UV-LEDs assisted preparation of silver deposited TiO2 catalyst bed inside microchannels as a high efficiency microphotoreactor for cleaning polluted water. *Chemical Engineering Journal*, *270*, 158–167. http://doi.org/10.1016/j.cej.2015.01.117

Fessenden, R. W., Meisel, D., & Camaioni, D. M. (2000). Addition of Oxide Radical Ions (O-) to Nitrite and Oxide Ions (O2 -) to Nitrogen Dioxide. *Journal of the American Chemical Society*, *122*, 3773–3774. http://doi.org/10.1021/ja994230t

Fischer, M., Wahl, M., & Friedrichs, G. (2012). Design and field application of a UV-LED based optical fiber biofilm sensor. *Biosensors and Bioelectronics*, *33*(1), 172–178. http://doi.org/10.1016/j.bios.2011.12.048

Fischer, M., & Warneck, P. (1996). Photodecomposition of nitrite and undissociated nitrous acid in aqueous solution. *The Journal of Physical Chemistry*, *3654*(96), 18749–18756. http://doi.org/10.1021/jp961692+

Flesch, P. (2006). *Light and Light Sources*. Berlin, Heidelberg: Springer Berlin Heidelberg. http://doi.org/10.1007/978-3-540-32685-4

Foley, J. A., Defries, R., Asner, G. P., Barford, C., Bonan, G., Carpenter, S. R., … Snyder, P. K. (2005). Global Consequences of Land Use. *Science*, *309*, 570–574.

Fowdar, H. S., Hatt, B. E., Breen, P., Cook, P. L. M., & Deletic, A. (2015). Evaluation of sustainable electron donors for nitrate removal in different water media. *Water Research*, *85*, 487–496. http://doi.org/10.1016/j.watres.2015.08.052

Fuerhacker, M. (2009). EU Water Framework Directive and Stockholm Convention: Can we reach the targets for priority substances and persistent organic pollutants? *Environ Sci Pollut Res*, *16*(Suppl 1), S92–S97. http://doi.org/10.1007s/s/11356-009-0126-4

Fujishima, A., & Honda, K. (1972). Electrochemical Photolysis of Water at a Semiconductor Electrode. *Nature*, *238*, 37–38. http://doi.org/10.1038/238037a0

Fujishima, A., Rao, T. N., & Tryk, D. A. (2000). Titanium dioxide photocatalysis. *Journal of Photochemistry & Photobiology, C: Photochemistry Reviews*, *1*, 1–21.

Fujishima, A., & Zhang, X. (2006). Titanium dioxide photocatalysis: present situation and future approaches. *Comptes Rendus Chimie*, *9*(5–6), 750–760. http://doi.org/10.1016/j.crci.2005.02.055

Fujishima, A., Zhang, X., & Tryk, D. A. (2008). TiO2 photocatalysis and related surface phenomena. *Surface Science Reports*, *63*(12), 515–582. http://doi.org/10.1016/j.surfrep.2008.10.001

Galloway, J. N., Dentener, F. J., Capone, D. G., Boyer, E. W., Howarth, R. W., Seitzinger, S. P., … Vorosmarty, C. J. (2004). *Nitrogen cycles: past, present, and future*. *Biogeochemistry* (Vol. 70). http://doi.org/10.1007/s10533-004-0370-0

Galloway, J. N., Townsend, A. R., Erisman, J. W., Bekunda, M., Cai, Z., Freney, J. R., … Sutton, M. a. (2008). Transformation of the Nitrogen Cycle: Recent Trends, Questions, and Potential Solutions. *Science*, *320*, 889–892. http://doi.org/10.1126/science.1136674

Gangolli, S. D., van den Brandt, P. A., Feron, V. J., Janzowsky, C., J.H., K., Speijers, G. J. A., … Wishnok, J. S. (1994). Nitrate, nitrite and N-nitroso compounds. *Environmental Toxicology and Pharmacology*, *292*, 1–38.

Gankanda, A., & Grassian, V. H. (2014a). Nitrate photochemistry on laboratory proxies of mineral dust aerosol: Wavelength dependence and action spectra. *Journal of Physical Chemistry C*, *118*(50), 29117–29125. http://doi.org/10.1021/jp504399a

Gankanda, A., & Grassian, V. H. (2014b). Nitrate Photochemistry on Laboratory Proxies of Mineral Dust Aerosol: Wavelength Dependence and Action Spectra. *Journal of Physical Chemistry C*, *118*(50), 29117–29125. http://doi.org/10.1021/jp504399a

Gao, F., Yang, Y., & Wang, T. (2015). Preparation of porous TiO2/Ag heterostructure films with enhanced photocatalytic activity. *Chemical Engineering Journal*, *270*, 418–427. http://doi.org/10.1016/j.cej.2015.02.048

Gao, W., Jin, R., Chen, J., Guan, X., Zeng, H., Zhang, F., & Guan, N. (2004). Titania-supported bimetallic catalysts for photocatalytic reduction of nitrate. *Catalysis Today*, *90*(3–4), 331–336. http://doi.org/10.1016/j.cattod.2004.04.043

Gao, W., Reis, R., Schelhas, L. T., Pool, V. L., Toney, M. F., Yu, K. M., & Walukiewicz, W. (2016). Formation of Nanoscale Composites of Compound Semiconductors Driven by Charge Transfer. *Nano Letters*, *16*, 5247–5254. http://doi.org/10.1021/acs.nanolett.6b02395

Garcia-segura, S., & Brillas, E. (2011). Mineralization of the recalcitrant oxalic and oxamic acids by electrochemical advanced oxidation processes using a boron-doped diamond anode. *Water Research*, *45*(9), 2975–2984. http://doi.org/10.1016/j.watres.2011.03.017

Garcia-Segura, S., & Brillas, E. (2017). Applied photoelectrocatalysis on the degradation of organic pollutants in wastewaters. *Journal of Photochemistry & Photobiology, C: Photochemistry Reviews*, *31*, 1–35. http://doi.org/10.1016/j.jphotochemrev.2017.01.005

Garcia-Segura, S., Mostafa, E., & Baltruschat, H. (2017). Could NOx be released during mineralization of pollutants containing nitrogen by hydroxyl radical ? Ascertaining the release of N-volatile species. *Applied Catalysis B, Environmental*, *207*, 376–384. http://doi.org/10.1016/j.apcatb.2017.02.046

Gekko, H., Hashimoto, K., & Kominami, H. (2012). Photocatalytic reduction of nitrite to dinitrogen in aqueous suspensions of metal-loaded titanium(IV) oxide in the presence of a hole scavenger: an ensemble effect of silver and palladium co-catalysts. *Physical Chemistry Chemical Physics : PCCP*, *14*(22), 7965–70. http://doi.org/10.1039/c2cp40729a

Gerischer, H., & Mauerer, A. (1970). Untersuchungen Zur anodischen Oxidation von Ammoniak an Platin-Elektroden. *Electroanalytical Chemistry and Interfacial Electrochemistry*, *25*, 421–433. http://doi.org/10.1016/S0022-0728(70)80103-6

Ghorab, M., Djellabi, R., & Messadi, R. (2013). Photo-Reduction of Hexavalent Chromium in Aqueous Solution in the Presence of TiO2 as Semiconductor Catalyst. *E3S Web of Conferences*, *25008*, 1–4. Retrieved from http://www.e3s-conferences.org/articles/e3sconf/abs/2013/01/e3sconf_ichm13_25008/e3sconf_ichm13_25008.html

Ghosh, J. P., Sui, R., Langford, C. H., Achari, G., & Berlinguette, C. P. (2009). A comparison of several nanoscale photocatalysts in the degradation of a common pollutant using LEDs and conventional UV light. *Water Research*, *43*(18), 4499–4506. http://doi.org/10.1016/j.watres.2009.07.027

Giese, N., & Darby, J. (2000). Sensitivity of microorganisms to different wavelengths of UV light: Implications on modeling of medium pressure UV systems. *Water Research*, *34*(16), 4007–4013. http://doi.org/10.1016/S0043-1354(00)00172-X

Giller, H. (2000). A review of UV lamps. *Proceedings of the Water Environment Federation*. Retrieved from http://www.ingentaconnect.com/content/wef/wefproc/2000/00002000/00000002/art00005

Gimenez, J., Aguado, M., & Cervera-March, S. (1996). Photocatalytic reduction of chromium (VI) with titania powders in a flow system. Kinetics and catalyst activity.

Journal of Molecular Catalysis …, *169*(95). Retrieved from http://www.sciencedirect.com/science/article/pii/1381116995001484

Goldstein, S., Behar, D., Rajh, T., & Rabani, J. (2016). Nitrite Reduction to Nitrous Oxide and Ammonia by TiO 2 Electrons in a Colloid Solution via Consecutive One-Electron Transfer Reactions. *The Journal of Physical Chemistry A*, *120*, 2307–2312. http://doi.org/10.1021/acs.jpca.6b01761

Goldstein, S., & Czapski, G. (1996). Formation of Peroxynitrite from the Nitrosation of Hydrogen Peroxide by an Oxygenated Nitric Oxide Solution. *Inorganic Chemistry*, *35*(20), 5935–5940. http://doi.org/10.1021/ic960438t

Goldstein, S., & Rabani, J. (2007). Mechanism of nitrite formation by nitrate photolysis in aqueous solutions: The role of peroxynitrite, nitrogen dioxide, and hydroxyl radical. *Journal of the American Chemical Society*, *129*(34), 10597–10601. http://doi.org/10.1021/ja073609+

Goldstein, S., & Rabani, J. (2008). The ferrioxalate and iodide-iodate actinometers in the UV region. *Journal of Photochemistry and Photobiology A: Chemistry*, *193*(1), 50–55. http://doi.org/10.1016/j.jphotochem.2007.06.006

Goldstein, S., Saha, A., Lymar, S. V., & Czapski, G. (1998). Oxidation of peroxynitrite by inorganic radicals: A pulse radiolysis study. *Journal of the American Chemical Society*, *120*(22), 5549–5554. http://doi.org/10.1021/ja9735362

Gonzalez, M. C., & Braun, A. M. (1995). VUV photolysis of aqueous solutions of nitrate and nitrite. *Research on Chemical Intermediates*, *21*(8–9), 837–859. http://doi.org/10.1163/156856795X00512

Gorges, R., Meyer, S., & Kreisel, G. (2004). Photocatalysis in microreactors. *Journal of Photochemistry and Photobiology A: Chemistry*, *167*(2–3), 95–99. http://doi.org/10.1016/j.jphotochem.2004.04.004

Grabowska, E., Zaleska, A., Sorgues, S., Kunst, M., Etcheberry, A., & Remita, H. (2013). Modification of Titanium (IV) Dioxide with Small Silver Nanoparticles : Application in Photocatalysis. *The Journal of Physical Chemistry C*, *117*(4), 1955–1962.

Gratzel, M., & Frank, A. J. (1982). Interfacial Electron-Transfer Reactions In Colloldal Semiconductor Dispersions . Kinetic Analysis. *Journal of Physical Chemistry*, *86*, 2964–2967. http://doi.org/10.1021/j100212a031

Groth, W., & Rommel, H. J. (1965). Photochemische Untersuchungen im Schumann-Ultraviolett Nr. 12 Die Photolyse des Ammoniaks bei den Wellenlangen 1849A (Hg), 1470A (Xe), 1236 und 1165A (Kr). *Zeitschrift Für Physikalische Chemie*, *45*(1–2), 96–116. http://doi.org/10.1524/zpch.1965.45.1_2.096

Gruber, N., & Galloway, J. N. (2008). An Earth-system perspective of the global nitrogen

cycle. *Nature*, *451*(17), 293–296. http://doi.org/10.1038/nature06592

Gustafsson, R. J., Orlov, A., Griffiths, P. T., Cox, R. a, & Lambert, R. M. (2006). Reduction of NO2 to nitrous acid on illuminated titanium dioxide aerosol surfaces: implications for photocatalysis and atmospheric chemistry. *Chemical Communications*, (37), 3936–8. http://doi.org/10.1039/b609005b

Hamanoi, O., & Kudo, A. (2002). Reduction of nitrate and nitrite ions over Ni-ZnS photocatalyst under visible light irradiation in the presence of a sacrificial reagent. *Chemistry Letters*, *0*(8), 838–839. http://doi.org/10.1246/cl.2002.838

Hamme, R. C., & Emerson, S. R. (2004). The solubility of neon, nitrogen and argon in distilled water and seawater. *Deep-Sea Research I*, *51*, 1517–1528. http://doi.org/10.1016/j.dsr.2004.06.009

Han, C., Yang, W., Wu, Q., Yang, H., & Xue, X. (2016). Heterogeneous Photochemical Conversion of NO_2 to HONO on the Humic Acid Surface under Simulated Sunlight. *Environmental Science & Technology*, (2), acs.est.5b05101. http://doi.org/10.1021/acs.est.5b05101

Harris, G., Adams, V. D., Moore, W. M., & Sorensen, D. L. (1987). Potassium ferrioxalate as chemical actinometer in ultraviolet reactors. *Journal of Environmental Engineering*, *113*, 612–627. Retrieved from http://ascelibrary.org/doi/abs/10.1061/(ASCE)0733-9372(1987)113:3(612)

Hatchard, C. G., & Parker, C. A. (1956). A New Sensitive Chemical Actinometer. II. Potassium Ferrioxalate as a Standard Chemical Actinometer. *Proceedings of the Royal Society of London A: Mathematical, Physical and Engineering Sciences*, *235*(1203), 518–536. http://doi.org/10.1098/rspa.1956.0102

He, Y., Grieser, F., & Ashokkumar, M. (2011). Kinetics and mechanism for the sonophotocatalytic degradation of p-chlorobenzoic acid. *The Journal of Physical Chemistry. A*, *115*(24), 6582–8. http://doi.org/10.1021/jp203518s

Health, W. S. D. of. (2005). *Nitrate Treatment: Alternatives for Small Water Systems*.

Henderson, M. a. (2011). A surface science perspective on TiO2 photocatalysis. *Surface Science Reports*, *66*(6–7), 185–297. http://doi.org/10.1016/j.surfrep.2011.01.001

Henderson, M. A., Szanyi, J., & Peden, C. H. F. (2003). Conversion of N2O to N2 on TiO2(1 1 0). *Catalysis Today*, *85*(2–4), 251–266. http://doi.org/10.1016/S0920-5861(03)00392-4

Heraeus. (2016). Line Sources: High Pressure Mercury Lamps.

Hérissan, A., Meichtry, J. M., Remita, H., Colbeau-justin, C., & Litter, M. I. (2017). Reduction of nitrate by heterogeneous photocatalysis over pure and radiolytically

modified TiO2 samples in the presence of formic acid. *Catalysis Today*, *281*(3), 101–108. http://doi.org/10.1016/j.cattod.2016.05.044

Hickel, B., & Sehested, K. (1992). Reaction of Hydroxyl Radicals with Ammonia in Liquid Water at Elevated Temperatures. *Radiate. Phys. Chem.*, *39*(4), 355–357. http://doi.org/10.1016/1359-0197(92)90244-A

Hirayama, H. (2005). Quaternary InAlGaN-based high-efficiency ultraviolet light-emitting diodes. *Journal of Applied Physics*, *97*(9). http://doi.org/10.1063/1.1899760

Hirayama, J., Abe, R., & Kamiya, Y. (2014). Combinational effect of Pt/SrTiO3:Rh photocatalyst and SnPd/Al2O3 non-photocatalyst for photocatalytic reduction of nitrate to nitrogen in water under visible light irradiation. *Applied Catalysis B: Environmental*, *144*(3), 721–729. http://doi.org/10.1016/j.apcatb.2013.08.005

Hitchman, M. L., & Tian, F. (2002). Studies of TiO2 thin films prepared by chemical vapour deposition for photocatalytic and photoelectrocatalytic degradation of 4-chlorophenol. *Journal of Electroanalytical Chemistry*, *538–539*, 165–172. http://doi.org/10.1016/S0022-0728(02)01252-4

Hodes, G., & Kamat, P. V. (2015). Understanding the Implication of Carrier Diffusion Length in Photovoltaic Cells. *Journal of Physical Chemistry Letters*, *6*(20), 4090–4092. http://doi.org/10.1021/acs.jpclett.5b02052

Hoffmann, M. R., Martin, S. T., Choi, W. Y., & Bahnemann, D. W. (1995). Environmental Applications of Semiconductor Photocatalysis. *Chemical Reviews*, *95*(1), 69–96. http://doi.org/10.1021/cr00033a004

Hofstadler, K., Bauer, R., Novalic, S., & Heisler, G. (1994). New Reactor Design for Photocatalytic Wastewater Treatment with TiO2 Immobilized on Fused-Silica Glass Fibers: Photomineralization of 4-Chlorophenol. *Environmental Science & Technology*, *28*(4), 670–674. http://doi.org/10.1021/es00053a021

Hou, W. M., & Ku, Y. (2013). Photocatalytic decomposition of gaseous isopropanol in a tubular optical fiber reactor under periodic UV-LED illumination. *Journal of Molecular Catalysis A: Chemical*, *374–375*, 7–11. http://doi.org/10.1016/j.molcata.2013.03.016

Houas, A., Laccheb, H., Ksibi, M., Elaloui, E., Guillard, C., & Herrmann, J.-M. (2001). Photocatalytic degradation pathway of methylene blue in water. *Applied Catalysis B: Environmental*, *31*, 145–157. http://doi.org/10.1016/S0926-3373(00)00276-9

Howarth, R., Swaney, D., Billen, G., Garnier, J., Hong, B., Humborg, C., … Marino, R. (2012). Nitrogen fluxes from the landscape are controlled by net anthropogenic nitrogen inputs and by climate. *Frontiers in Ecology and the Environment*, *10*(1), 37–43. http://doi.org/10.1890/100178

Howe, R. F., & Gratzel, M. (1985). EPR Observation of Trapped Electrons in Colloidal TiO2. *Journal of Physical Chemistry*, *89*(7), 4495–4499.

Hsu, C. L., Wang, S. L., & Tzou, Y. M. (2007). Photocatalytic reduction of Cr(VI) in the presence of NO3- and Cl- electrolytes as influenced by Fe(III). *Environmental Science and Technology*, *41*(22), 7907–7914. http://doi.org/10.1021/es0718164

Hu, L., Yoko, T., Kozuka, H., & Sakka, S. (1992). Effects of solvent on properties of sol—gel-derived TiO2 coating films. *Thin Solid Films*, *219*(1–2), 18–23. http://doi.org/10.1016/0040-6090(92)90718-Q

Huang, L., Li, L., Dong, W., Liu, Y., & Hou, H. (2008). Removal of ammonia by OH radical in aqueous phase. *Environmental Science and Technology*, *42*(21), 8070–8075. http://doi.org/10.1021/es8008216

Hughes, M. N. (1999). Relationships between nitric oxide, nitroxyl ion, nitrosonium cation and peroxynitrite. *Biochimica et Biophysica Acta*, *1411*, 263–272. http://doi.org/10.1016/S0005-2728(99)00019-5

Hughes, M. N., & Nicklin, H. G. (1968). The chemistry of pernitrites. Part I. Kinetics of decomposition of pernitrous acid. *Journal of the Chemical Society A: Inorganic, Physical, Theoretical*, *0*(0), 450–452. http://doi.org/papers3://publication/doi/10.1039/J19680000450

Hwang, Y., Kim, D., & Shin, H. (2011). Mechanism study of nitrate reduction by nano zero valent iron. *Journal of Hazardous Materials*, *185*(2–3), 1513–1521. http://doi.org/10.1016/j.jhazmat.2010.10.078

Ibhadon, A., & Fitzpatrick, P. (2013). Heterogeneous Photocatalysis: Recent Advances and Applications. *Catalysts*, *3*, 189–218. http://doi.org/10.3390/catal3010189

Imoberdorf, G. E., Taghipour, F., & Mohseni, M. (2008). Radiation field modeling of multi-lamp, homogeneous photoreactors. *Journal of Photochemistry and Photobiology A: Chemistry*, *198*, 169–178. http://doi.org/10.1016/j.jphotochem.2008.03.006

Inc., C. (2016). *Corning Fibrance Light-Diffusing Fiber |Glowing Fiber Optic Lighting |*.

Jacobi, H. W., Kleffmann, J., Villena, G., Wiesen, P., King, M., France, J., … Staebler, R. (2014). Role of nitrite in the photochemical formation of radicals in the snow. *Environmental Science and Technology*, *48*(1), 165–172. http://doi.org/10.1021/es404002c

Jamali, A., Vanraes, R., Hanselaer, P., & Van Gerven, T. (2013). A batch LED reactor for the photocatalytic degradation of phenol. *Chemical Engineering and Processing: Process Intensification*, *71*, 43–50. http://doi.org/10.1016/j.cep.2013.03.010

Jenny, R. M., Simmons, O. D., Shatalov, M., & Ducoste, J. J. (2014). Modeling a continuous flow ultraviolet Light Emitting Diode reactor using computational fluid dynamics. *Chemical Engineering Science*, *116*, 524–535. http://doi.org/10.1016/j.ces.2014.05.020

Jensen, V. B., Darby, J. L., Seidel, C., & Gorman, C. (2014). Nitrate in Potable Water Supplies: Alternative Management Strategies. *Critical Reviews in Environmental Science and Technology*, *44*, 2203–2286. http://doi.org/10.1080/10643389.2013.828272

Jeong, J., Kim, C., & Yoon, J. (2009). The effect of electrode material on the generation of oxidants and microbial inactivation in the electrochemical disinfection processes. *Water Research*, *43*(4), 895–901. http://doi.org/10.1016/j.watres.2008.11.033

Jin, J., El-Din, M. G., & Bolton, J. R. (2011). Assessment of the UV/Chlorine process as an advanced oxidation process. *Water Research*, *45*(4), 1890–1896. http://doi.org/10.1016/j.watres.2010.12.008

Jin, R., Gao, W., Chen, J., Zeng, H., Zhang, F., Liu, Z., & Guan, N. (2004). Photocatalytic reduction of nitrate ion drinking water by using metal-loaded MgTiO3-TiO2 composite semiconductor catalyst. *Journal of Photochemistry and Photobiology A: Chemistry*, *162*(2–3), 585–590. http://doi.org/10.1016/S1010-6030(03)00420-9

Jinno, M., Kurokawa, H., & Aono, M. (1999). Fundamental Research on Mercuryless Fluorescent Lamps I–Inner Electrode Operation with Pulsed Discharge–. *Japanese Journal of Applied …*, *38*(7), 4608–4612. Retrieved from http://iopscience.iop.org/1347-4065/38/7S/4608

Jinno, M., Okamoto, M., Takeda, M., & Motomura, H. (2007). Luminance and efficacy improvement of low-pressure xenon pulsed fluorescent lamps by using an auxiliary external electrode. *Journal of Physics D: Applied Physics*, *40*(13), 3889–3895. http://doi.org/10.1088/0022-3727/40/13/S08

Jo, W. K., & Kang, H. J. (2012). Photocatalytic performance of cylindrical reactor inserted with UV light-emitting-diodes for purification of low-level toxic volatile organic compounds. *Applied Surface Science*, *259*, 657–663. http://doi.org/10.1016/j.apsusc.2012.07.093

Kaczynskl, S. E., & Kleber, R. J. (1993). Aqueous Trivalent Chromium Photoproduction in Natural Waters. *Environmental Science & Technology*, *27*(8), 1572–1576. http://doi.org/10.1021/es00045a011

Kamble, S. P., Sawant, S. B., & Pangarkar, V. G. (2003). Batch and Continuous Photocatalytic Degradation of Benzenesulfonic Acid Using Concentrated Solar Radiation. *Industrial and Engineering Chemistry Research*, *42*, 6705–6713. http://doi.org/10.1021/ie030493r

Kapinus, E. I., Viktorova, T. I., & Problems, E. (2010). Kinetics of the Photocatalytic Degradation of Methylene Blue on Titanium Dioxide. *Sciences-New York*, *46*(3), 159–163.

Kapoor, B. A., & Viraraghavan, T. (1997). Nitrate Removal from Drinking Water - Review. *Journal of Environmental Engineering*, *123*, 371–380. http://doi.org/10.1061/(ASCE)0733-9372(1997)123:4(371)

Kato, H., & Kudo, A. (2002). Photocatalytic reduction of nitrate ions over tantalate photocatalysts. *Physical Chemistry Chemical Physics*, *4*(12), 2833–2838. http://doi.org/10.1039/b110511f

Katz, A., McDonagh, A., Tijing, L., & Shon, H. K. (2015). Fouling and Inactivation of Titanium Dioxide-Based Photocatalytic Systems. *Critical Reviews in Environmental Science and Technology*, *45*(17), 1880–1915. http://doi.org/10.1080/10643389.2014.1000763

Kebede, M. A., Scharko, N. K., Appelt, L. E., & Raff, J. D. (2013). Formation of nitrous acid during ammonia photooxidation on TiO2 under atmospherically relevant conditions. *Journal of Physical Chemistry Letters*, *4*(16), 2618–2623. http://doi.org/10.1021/jz401250k

Kebede, M. a, Varner, M. E., Scharko, N. K., Gerber, R. B., & Raff, J. D. (2013). Photooxidation of Ammonia on TiO_2 as a Source of NO and NO_2 under Atmospheric Conditions. *Journal of the American Chemical Society*, *135*(23), 8606–8615. http://doi.org/10.1021/ja401846x

Kedziora, a., Strek, W., Kepinski, L., Bugla-Ploskonska, G., & Doroszkiewicz, W. (2012). Synthesis and antibacterial activity of novel titanium dioxide doped with silver. *Journal of Sol-Gel Science and Technology*, *62*(1), 79–86. http://doi.org/10.1007/s10971-012-2688-8

Ketir, W., Bouguelia, A., & Trari, M. (2009). NO3- removal with a new delafossite CuCrO2 photocatalyst. *Desalination*, *244*, 144–152. http://doi.org/10.1016/j.desal.2008.05.020

Khalil, A. M. E., Eljamal, O., Amen, T. W. M., Sugihara, Y., & Matsunaga, N. (2017). Optimized nano-scale zero-valent iron supported on treated activated carbon for enhanced nitrate and phosphate removal from water. *Chemical Engineering Journal*, *309*, 349–365. http://doi.org/10.1016/j.cej.2016.10.080

Kim, D.-H., Lee, J., Ryu, J., Kim, K., & Choi, W. (2014). Arsenite oxidation initiated by the UV photolysis of nitrite and nitrate. *Environmental Science & Technology*, *48*(7), 4030–7. http://doi.org/10.1021/es500001q

Kim, D. H., & Anderson, M. A. (1996). Solution factors affecting the photocatalytic and photoelectrocatalytic degradation of formic acid using supported TiO2 thin films.

Journal of Photochemistry and Photobiology A: Chemistry, *94*(2–3), 221–229. http://doi.org/10.1016/1010-6030(95)04178-8

Kim, J., & Benjamin, M. M. M. M. (2004). Modeling a novel ion exchange process for arsenic and nitrate removal. *Water Research*, *38*(8), 2053–62. http://doi.org/10.1016/j.watres.2004.01.012

Kim, S., Kim, J. B., Jhin, J., Baek, J. H., Lee, I. H., & Jung, G. Y. (2008). Optical and Structural Properties of InGaN–AlGaN Ultraviolet Light-Emitting Diodes. *IEEE Photonics Technology Letters*, *20*(23), 1911–1913. http://doi.org/10.1109/LPT.2008.2004700

Kissner, R., Nauser, T., Bugnon, P., Lye, P. G., & Koppenol, W. H. (1997). Formation and properties of peroxynitrite as studied by laser flash photolysis, high-pressure stopped-flow technique, pulse radiolysis. *Chemical Research in Toxicology*, *10*(11), 1285–1292. http://doi.org/10.1021/tx970160x

Ko, S. (2014). Photochemical Synthesis, Characterization and Enhanced Visible Light Induced Photocatalysis of Ag Modified TiO₂ Nanocatalyst. *Journal of Nanoscience and Nanotechnology*, *14*(9), 6923–6928. http://doi.org/10.1166/jnn.2014.8988

Kobwittaya, K., & Sirivithayapakorn, S. (2014). Photocatalytic reduction of nitrate over TiO2 and Ag-modified TiO2. *Journal of Saudi Chemical Society*, *18*(4), 291–298. http://doi.org/10.1016/j.jscs.2014.02.001

Kochuveedu, S. T., Jang, Y. H., & Kim, D. H. (2013). A study on the mechanism for the interaction of light with noble metal-metal oxide semiconductor nanostructures for various photophysical applications. *Chem. Soc. Rev.*, *42*, 8467–8493. http://doi.org/10.1039/c3cs60043b

Kolkman, A., Martijn, B. J., Vughs, D., Baken, K. A., & Van Wezel, A. P. (2015). Tracing nitrogenous disinfection byproducts after medium pressure UV water treatment by stable isotope labeling and high resolution mass spectrometry. *Environmental Science and Technology*, *49*(7), 4458–4465. http://doi.org/10.1021/es506063h

Kolle, U., Moser, J., & Gratzel, M. (1985). Dynamics of Interfacial Charge-Transfer Reactions in Semiconductor Dispersions. Reduction of Cobaltoceniumdicarboxylate in Colloidal TiO2. *Inorganic Chemistry*, *24*(4), 2253–2258. http://doi.org/10.1021/ic00208a026

Kolpin, D. W., Furlong, E. T., Meyer, M. T., Thurman, M. E., Zaugg, S. D., Barber, L. B., & Buxton, H. T. (2002). Pharmaceuticals, Hormones, and Other Organic Wastewater Contaminants in U.S. Streams, 1999 - 2000: A National Reconnaissance. *Environ. Sci. Technol.*, *36*, 1202–1211.

Kominami, H., Furusho, A., Murakami, S., & Inoue, H. (2001). Effective photocatalytic

reduction of nitrate to ammonia in an aqueous suspension of metal-loaded titanium (IV) oxide particles in the presence of oxalic acid. *Catalysis Letters*, *76*(1), 31–34. http://doi.org/10.1023/A:1016771908609

Kominami, H., Gekko, H., & Hashimoto, K. (2010). Photocatalytic disproportionation of nitrite to dinitrogen and nitrate in an aqueous suspension of metal-loaded titanium (IV) oxide nanoparticles. http://doi.org/10.1039/c0cp00794c

Kominami, H., Nakaseko, T., Shimada, Y., Furusho, A., & Inoue, H. (2005). Selective photocatalytic reduction of nitrate to nitrogen molecules in an aqueous suspension of metal-loaded titanium (IV) oxide particles. *Chem. Commun.*, *3*, 2933–2935. http://doi.org/10.1039/b502909k

Kominami, H., Nakaseko, T., Shimada, Y., Furusho, A., Inoue, H., Murakami, S.-Y., … Ohtani, B. (2005). Selective photocatalytic reduction of nitrate to nitrogen molecules in an aqueous suspension of metal-loaded titanium(IV) oxide particles. *Chemical Communications*, *3*(23), 2933–5. http://doi.org/10.1039/b502909k

Könenkamp, R. (2000). Carrier transport in nanoporous TiO2 films. *Physical Review B*, *61*(16), 11057–11064. http://doi.org/10.1103/PhysRevB.61.11057

Korgel, B. A., & Monbouquette, H. G. (1997). Quantum Confinement Effects Enable Photocatalyzed Nitrate Reduction at Neutral pH Using CdS Nanocrystals. *J. Phys. Chem. B*, *101*, 5010–5017. http://doi.org/10.1021/jp971016n

Kormann, C., Bahnemann, D. W., & Hoffmann, M. R. (1991). Photolysis of Chloroform and other organic molecules in aqueous TiO2 suspensions. *Environ. Sci. Technol.*, *25*(3), 494–500. http://doi.org/10.1021/es00015a018

Kozodoy, R. L., Lundahl, S. L., Bell, D., & Harrington, J. A. (1994). Three-dimensional characterization of the light distribution from diffusing cylindrical optical-fiber tips. *Applied Optics*, *33*(28), 6674–6682. http://doi.org/10.1364/AO.33.006674

Krasae, N., & Wantala, K. (2016). Enhanced nitrogen selectivity for nitrate reduction on Cu – nZVI by TiO 2 photocatalysts under UV irradiation. *Applied Surface Science*, *380*(3), 309–317. http://doi.org/10.1016/j.apsusc.2015.12.023

Ku, Y., & Jung, I. L. (2001). Photocatalytic reduction of Cr(VI) in aqueous solutions by UV irradiation with the presence of titanium dioxide. *Water Research*, *35*(1), 135–42. Retrieved from http://www.ncbi.nlm.nih.gov/pubmed/11257867

Kuipers, J., Bruning, H., Yntema, D., & Rijnaarts, H. (2015). Journal of Photochemistry and Photobiology A : Chemistry Wirelessly powered ultraviolet light emitting diodes for photocatalytic oxidation. *"Journal of Photochemistry & Photobiology, A: Chemistry," 299*, 25–30. http://doi.org/10.1016/j.jphotochem.2014.10.017

Kumar, S. G., & Rao, K. S. R. K. (2015). Tungsten-based nanomaterials (WO3 &

Bi2WO6): Modifications related to charge carrier transfer mechanisms and photocatalytic applications. *Applied Surface Science*, *355*, 939–958. http://doi.org/10.1016/j.apsusc.2015.07.003

Kumar, S. G., & Rao, K. S. R. K. (2017). Comparison of modification strategies towards enhanced charge carrier separation and photocatalytic degradation activity of metal oxide semiconductors (TiO2 , WO3 and ZnO). *Applied Surface Science*, *391*, 124–148. http://doi.org/10.1016/j.apsusc.2016.07.081

Kuo, W. S., & Ho, P. H. (2001). Solar photocatalytic decolorization of methylene blue in water. *Chemosphere*, *45*, 77–83. http://doi.org/10.1016/S0045-6535(01)00008-X

Kwon, C. H., Shin, H., Kim, J. H., Choi, W. S., & Yoon, K. H. (2004). Degradation of methylene blue via photocatalysis of titanium dioxide. *Materials Chemistry and Physics*, *86*, 78–82. http://doi.org/10.1016/j.matchemphys.2004.02.024

Lachheb, H., Puzenat, E., Houas, A., Ksibi, M., Elaloui, E., Guillard, C., & Herrmann, J. M. (2002). Photocatalytic degradation of various types of dyes (Alizarin S, Crocein Orange G, Methyl Red, Congo Red, Methylene Blue) in water by UV-irradiated titania. *Applied Catalysis B: Environmental*, *39*, 75–90. http://doi.org/10.1016/S0926-3373(02)00078-4

Lakshmi, S., Renganathan, R., & Fujita, S. (1995). Study on TiO2-mediated photocatalytic degradation of methylene blue. *Journal of Photochemistry and Photobiology A: Chemistry*, *88*, 163–167. http://doi.org/10.1016/1010-6030(94)04030-6

Lan, Y., Lu, Y., & Ren, Z. (2013). Mini review on photocatalysis of titanium dioxide nanoparticles and their solar applications. *Nano Energy*, *2*(5), 1031–1045. http://doi.org/10.1016/j.nanoen.2013.04.002

Lasek, J., Yu, Y.-H., & Wu, J. C. S. (2013). Removal of NOx by photocatalytic processes. *Journal of Photochemistry and Photobiology C: Photochemistry Reviews*, *14*, 29–52. http://doi.org/10.1016/j.jphotochemrev.2012.08.002

Lazar, M., Varghese, S., & Nair, S. (2012). Photocatalytic Water Treatment by Titanium Dioxide: Recent Updates. *Catalysts*, *2*, 572–601. http://doi.org/10.3390/catal2040572

Leblebici, M. E., Rongé, J., Martens, J. a., Stefanidis, G. D., & Van Gerven, T. (2015). Computational modelling of a photocatalytic UV-LED reactor with internal mass and photon transfer consideration. *Chemical Engineering Journal*, *264*, 962–970. http://doi.org/10.1016/j.cej.2014.12.013

Lecloux, A. J. (1999). Chemical, biological and physical constrains in catalytic reduction processes for purification of drinking water. *Catalysis Today*, *53*(1), 23–34. http://doi.org/10.1016/S0920-5861(99)00100-5

Lee, J., Park, H., & Choi, W. (2002a). Selective photocatalytic oxidation of NH3 to N2 on

platinized TiO2 in Water. *Environmental Science & Technology*, *36*(24), 5462–5468. http://doi.org/10.1021/es025930s

Lee, J., Park, H., & Choi, W. (2002b). Selective Photocatalytic Oxidation of NH 3 to N 2 on Platinized TiO 2 in Water, *36*(24), 5462–5468.

Lee, J., & Seliger, H. H. (1964). Quantum Yield of the Ferrioxalate Actinometer. *The Journal of Chemical Physics*, *40*(2), 519. http://doi.org/10.1063/1.1725147

Lee, K., Ku, H., & Pak, D. (2016). Chemosphere OH radical generation in a photocatalytic reactor using TiO 2 nanotube plates. *Chemosphere*, *149*, 114–120. http://doi.org/10.1016/j.chemosphere.2016.01.103

Lee, S.-K., & Mills, A. (2003). Novel photochemistry of leuco-Methylene Blue. *Chemical Communications (Cambridge, England)*, (July), 2366–2367. http://doi.org/10.1039/b307228b

Lensun, L., Smith, T. A., & Gee, M. L. (2002). Partial denaturation of silica-adsorbed bovine serum albumin determined by time-resolved evanescent wave-induced fluorescence spectroscopy. *Langmuir*, *18*(25), 9924–9931. http://doi.org/10.1021/la020473e

Lesko, D. M. B., Coddens, E. M., Swomley, H. D., Welch, R. M., Borgatta, J., & Navea, J. G. (2015). Photochemistry of nitrate chemisorbed on various metal oxide surfaces. *Phys. Chem. Chem. Phys.*, *17*(32), 20775–20785. http://doi.org/10.1039/C5CP02903A

Levine, L. H., Richards, J. T., Coutts, J. L., Soler, R., Maxik, F., & Wheeler, R. M. (2011). Feasibility of ultraviolet-light-emitting diodes as an alternative light source for photocatalysis. *Journal of the Air & Waste Management Association*, *61*(9), 932–940. http://doi.org/10.1080/10473289.2011.596746

Levine, L. H., Richards, J. T., Soler, R., Maxik, F., Coutts, J., & Wheeler, R. M. (2011). Feasibility of Ultraviolet Light Emitting Diodes as an Alternative Light Source for Photocatalysis, 1–23. http://doi.org/Doi 10.1080/10473289.2011.596746

Li, J., Wang, T., & Du, X. (2012). Preparation of visible light-driven SnS2/TiO2 nanocomposite photocatalyst for the reduction of aqueous Cr(VI). *Separation and Purification Technology*, *101*, 11–17. http://doi.org/10.1016/j.seppur.2012.09.014

Li, L., Xu, Z., Liu, F., Shao, Y., Wang, J., Wan, H., & Zheng, S. (2010). Photocatalytic nitrate reduction over Pt-Cu/TiO2 catalysts with benzene as hole scavenger. *Journal of Photochemistry and Photobiology A: Chemistry*, *212*(2–3), 113–121. http://doi.org/10.1016/j.jphotochem.2010.04.003

Li, Y., & Wasgestian, F. (1998). Photocatalytic reduction of nitrate ions on TiO2 by oxalic acid. *Journal of Photochemistry and Photobiology A: Chemistry*, *112*(2–3), 255–259.

http://doi.org/10.1016/S1010-6030(97)00293-1

Liang, S., Min, J. H., Davis, M. K., Green, J. F., & Remer, D. S. (2003). use of pulsed-UV processes to destroy NDMA, *95*(9), 121–131.

Liga, M. V., Bryant, E. L., Colvin, V. L., & Li, Q. (2011). Virus inactivation by silver doped titanium dioxide nanoparticles for drinking water treatment. *Water Research*, *45*(2), 535–544. http://doi.org/10.1016/j.watres.2010.09.012

Lin, H., & Valsaraj, K. T. (2006). An optical fiber monolith reactor for photocatalytic wastewater treatment. *AIChE Journal*, *52*(6), 2271–2280. http://doi.org/10.1002/aic.10823

Lin, L., Wang, H., Luo, H., & Xu, P. (2015). Enhanced photocatalysis using side-glowing optical fibers coated with Fe-doped TiO<inf>2</inf> nanocomposite thin films. *Journal of Photochemistry and Photobiology A: Chemistry*, *307–308*, 88–98. http://doi.org/10.1016/j.jphotochem.2015.04.010

Linden, K. G., & Darby, J. L. (1997). Estimating Effective Germicidal Dose from Medium Pressure UV Lamps. *Journal of Environmental Engineering*, *123*(11), 1142–1149. http://doi.org/10.1061/(ASCE)0733-9372(1997)123:11(1142)

Linsebigler, A. L., Linsebigler, A. L., Yates Jr, J. T., Lu, G., Lu, G., & Yates, J. T. (1995). Photocatalysis on TiO2 Surfaces: Principles, Mechanisms, and Selected Results. *Chemical Reviews*, *95*(3), 735–758. http://doi.org/10.1021/cr00035a013

Lisachenko, A. A., Mikhailov, R. V, Basov, L. L., Shelimov, B. N., Che, M., Surface, D., & Marie, P. (2007). Photocatalytic Reduction of NO by CO on Titanium Dioxide under Visible Light Irradiation. *Energy*, 14440–14447.

Liu, G., You, S., Huang, H., & Ren, N. (2016a). Removal of Nitrate by Photocatalytic Denitri fi cation Using Nonlinear Optical Material. http://doi.org/10.1021/acs.est.6b03455

Liu, G., You, S., Huang, H., & Ren, N. (2016b). Removal of nitrate by photocatalytic denitrification using nonlinear optical material. *Environmental Science & Technology*, *50*, 11218–11225. http://doi.org/10.1021/acs.est.6b03455

Liu, W., Ni, J., & Yin, X. (2014). Synergy of photocatalysis and adsorption for simultaneous removal of Cr(VI) and Cr(III) with TiO_2 and titanate nanotubes. *Water Research*, *53*(Iii), 12–25. http://doi.org/10.1016/j.watres.2013.12.043

Liu, X., Li, W., & Yu, H. (2014). Chem Soc Rev Cathodic catalysts in bioelectrochemical systems for energy recovery from wastewater. *Chemical Society Reviews*, *43*, 7718–7745. http://doi.org/10.1039/C3CS60130G

Liu, Y., Lee, J., Zhao, Y., Zhang, M., Wang, L., & Duan, Q. (2014). A novel preparation

approach and denitrification performance of TiO2/Fe0 photocatalysts. *Desalination and Water Treatment*, *57*(7), 1–7. http://doi.org/10.1080/19443994.2014.983984

Logager, T., & Sehested, K. (1993). Formation and Decay of Peroxynitrous Acid - a Pulse-Radiolysis Study. *Journal of Physical Chemistry*, *97*(25), 6664–6669. http://doi.org/10.1021/j100127a016

Loganathan, P., Vigneswaran, S., & Kandasamy, J. (2013). Enhanced removal of nitrate from water using surface modification of adsorbents - A review. *Journal of Environmental Management*, *131*, 363–374. http://doi.org/10.1016/j.jenvman.2013.09.034

Loo, K., Moss, G., & Tozer, R. (2004). A dynamic collisional-radiative model of a low-pressure mercury-argon discharge lamp: A physical approach to modeling fluorescent lamps for circuit simulations. *Power Electronics, …*, *19*(4), 1117–1129. Retrieved from http://ieeexplore.ieee.org/xpls/abs_all.jsp?arnumber=1310400

Lozovskii, A. V, Stolyarova, I. V, Prikhod, R. V, & Goncharuk, V. V. (2009). Research of Photocatalytic Activity of the Ag/TiO2 Catalysts in the Reduction Reaction of Nitrate – Ions in Aqueous Media. *Journal of Water Chemistry and Technology*, *31*(6), 360–366. http://doi.org/10.3103/S1063455X09060034

Lu, N., Gao, N. Y., Deng, Y., & Li, Q. S. (2009). Nitrite formation during low pressure ultraviolet lamp irradiation of nitrate. *Water Science and Technology*, *60*(6), 1393–1400. http://doi.org/10.2166/wst.2009.475

Luo, X., Chen, C., Yang, J., Wang, J., Yan, Q., & Shi, H. (2015a). Characterization of La/Fe/TiO2 and its photocatalytic performance in ammonia nitrogen wastewater. *International Journal of Environmental Research and Public Health*, *12*, 14626–14639. http://doi.org/10.3390/ijerph121114626

Luo, X., Chen, C., Yang, J., Wang, J., Yan, Q., & Shi, H. (2015b). Characterization of La / Fe / TiO 2 and Its Photocatalytic Performance in Ammonia Nitrogen Wastewater, (3), 14626–14639. http://doi.org/10.3390/ijerph121114626

MacCraith, B. D. (1993). Enhanced evanescent wave sensors based on sol-gel derived porous glass coatings. *Sensors and Actuators, B: Chemical*, *B11*(1–3), 29–34.

Machado, T. C., Lansarin, M. A., & Matte, N. (2014). Reduction of hexavalent chromium: Photocatalysis and photochemistry and their application in wastewater remediation. *Water Science and Technology*, *70*(1), 55–61. http://doi.org/10.2166/wst.2014.193

Mack, J., & Bolton, J. (1999a). Photochemistry of nitrite and nitrate in aqueous solution: a review. *Journal of Photochemistry and Photobiology A: …*, *128*(June), 26–38. Retrieved from http://www.sciencedirect.com/science/article/pii/S1010603099001550

Mack, J., & Bolton, J. R. (1999b). Photochemistry of nitrite and nitrate in aqueous solution: a review. *Journal of Photochemistry and Photobiology A: Chemistry*, *128*(January 2016), 1–13. http://doi.org/10.1016/S1010-6030(99)00155-0

Malecki, A., & Malecka, B. (2006). Formation of N2O during thermal decomposition of d-metal hydrates nitrates. *Thermochimica Acta*, *446*(1–2), 113–116. http://doi.org/10.1016/j.tca.2006.02.006

Mandal, B. K., & Suzuki, K. T. (2002). Arsenic round the world: A review. *Talanta*, *58*(1), 201–235. http://doi.org/10.1016/S0039-9140(02)00268-0

Marcotte, G., Marchand, P., Pronovost, S., Ayotte, P., Laffon, C., & Parent, P. (2015). Surface-Enhanced Nitrate Photolysis on Ice. *Journal of Physical Chemistry A*, *119*(10), 1996–2005. http://doi.org/10.1021/jp511173w

Mariani, M. L., Brandi, R. J., Cassano, A. E., & Zalazar, C. S. (2013). A kinetic model for the degradation of dichloroacetic acid and formic acid in water employing the H2O2/UV process. *Chemical Engineering Journal*, *225*, 423–432. http://doi.org/10.1016/j.cej.2013.03.098

Marinangeli, R. E., & Ollis, D. F. (1977). Photoassisted heterogeneous catalysis of optical fibers: I. Isolated single fiber. *AlChE Journal*, *23*(4), 415–426.

Marinangeli, R. E., & Ollis, D. F. (1980). Photo-assisted heterogeneous catalysis with optical fibers II. Nonisothermal single fiber and fiber bundle. *AIChE Journal*, *26*(6), 1000–1008. http://doi.org/10.1002/aic.690260615

Marinangeli, R. E., & Ollis, D. F. (1982). Photo-assisted heterogeneous catalysis with optical fibers. Part III: Photoelectrodes. *AlChe Journal*, *28*(6), 945–955.

Mark, G., Korth, H. G., Schuchmann, H. P., & Von Sonntag, C. (1996). The photochemistry of aqueous nitrate ion revisited. *Journal of Photochemistry and Photobiology A: Chemistry*, *101*(2–3), 89–103. http://doi.org/10.1016/S1010-6030(96)04391-2

Marks, R., Yang, T., Westerhoff, P., & Doudrick, K. (2016). Comparative analysis of the photocatalytic reduction of drinking water oxoanions using titanium dioxide. *Water Research*, *104*, 11–19. http://doi.org/10.1016/j.watres.2016.07.052

Matejec, V., Chomat, M., Pospisilova, M., Hayer, M., & Kasik, I. (1995). Optical fiber with novel geometry for evanescent-wave sensing. *Sensors and Actuators: B. Chemical*, *29*(1–3), 416–422. http://doi.org/10.1016/0925-4005(95)01717-8

Matsushita, Y., Ohba, N., Kumada, S., Sakeda, K., Suzuki, T., & Ichimura, T. (2007). Photocatalytic reactions in microreactors. *Chemical Engineering Journal*, *135*(SUPPL. 1), 303–308. http://doi.org/10.1016/j.cej.2007.07.045

Matthews, R. W. (1989). Photocatalytic oxidation and adsorption of methylene blue on thin films of near-ultraviolet-illuminated TiO2. *Journal of the Chemical Society, Faraday Transactions 1*, *85*(6), 1291. http://doi.org/10.1039/f19898501291

McCullagh, C., Robertson, P. K. J., Adams, M., Pollard, P. M., & Mohammed, A. (2010). Development of a slurry continuous flow reactor for photocatalytic treatment of industrial waste water. *Journal of Photochemistry & Photobiology A: Chemistry*, *211*, 42–46. http://doi.org/10.1016/j.jphotochem.2010.01.020

McCullagh, C., Skillen, N., Adams, M., & Robertson, P. K. J. (2011). Photocatalytic reactors for environmental remediation: A review. *Journal of Chemical Technology and Biotechnology*, *86*, 1002–1017. http://doi.org/10.1002/jctb.2650

McMahon, P. B., Böhlke, J. K., Kauffman, L. J., Kipp, K. L., Landon, M. K., Crandall, C. A., … Brown, C. J. (2008). Source and transport controls on the movement of nitrate to public supply wells in selected principal aquifers of the United States. *Water Resources Research*, *44*(4), 1–17. http://doi.org/10.1029/2007WR006252

McMahon, P. B., & Chapelle, F. H. (2008). Redox processes and water quality of selected principal aquifer systems. *Ground Water*, *46*(2), 259–271. http://doi.org/10.1111/j.1745-6584.2007.00385.x

Meng, F., Lu, F., Sun, Z., & Lü, J. (2010). A mechanism for enhanced photocatalytic activity of nano-size silver particle modified titanium dioxide thin films. *Science China Technological Sciences*, *53*(11), 3027–3032. http://doi.org/10.1007/s11431-010-4116-z

Micic, O., & Zhang, Y. (1993). Trapped holes on titania colloids studied by electron paramagnetic resonance. *Journal of Physical Chemistry*, *97*, 7277–7283. Retrieved from http://pubs.acs.org/doi/pdf/10.1021/j100130a026

Milis, A., & Domenech, X. (1993). Photoassisted oxidation of nitrite to nitrate over different semiconducting oxides. *Journal of Photochemistry and Photobiology A: Chemistry*, *72*, 55–59. http://doi.org/10.1016/1010-6030(93)85085-M

Milis, A., Peral, J., & Domenech, X. (1994a). Heterogeneous photocatalytic oxidation of nitrite over iron-doped TiO2 samples. *Journal of Molecular Catalysis*, *67*, 67–74. http://doi.org/10.1016/0304-5102(93)E0213-Z

Milis, A., Peral, J., & Domenech, X. (1994b). Heterogeneous photocatalytic TiOz samples oxidation of nitrite over iron-doped. *Journal of Molecular Catalysis*, *67*, 67–74.

Miller, L., & Anderson, M. A. (1998). Fiber-mediated titanium dioxide photocatalysis. *Journal of Advanced Oxidation Technologies*, *3*(3), 238–242.

Mills, A., & Wang, J. (1999). Photobleaching of methylene blue sensitised by TiO2: an ambiguous system? *Journal of Photochemistry and Photobiology A: Chemistry*,

127(July), 123–134. http://doi.org/10.1016/S1010-6030(99)00143-4

Mishra, T., Mahato, M., Aman, N., Patel, J. N., & Sahu, R. K. (2011). A mesoporous WN co-doped titania nanomaterial with enhanced photocatalytic aqueous nitrate removal activity under visible light. *Catalysis Science & Technology*, *1*, 609–615. http://doi.org/10.1039/c1cy00042j

Mogal, S. I., Gandhi, V. G., Mishra, M., Tripathi, S., Shripathi, T., Joshi, P. A., & Shah, D. O. (2014). Single-step synthesis of silver-doped titanium dioxide: Influence of silver on structural, textural, and photocatalytic properties. *Industrial and Engineering Chemistry Research*, *53*(14), 5749–5758. http://doi.org/10.1021/ie404230q

Mohamed, R. M., & Baeissa, E. S. (2014). Environmental remediation of aqueous nitrate solutions by photocatalytic reduction using Pd/NaTaO3 nanoparticles. *Journal of Industrial and Engineering Chemistry*, *20*(4), 1367–1372. http://doi.org/10.1016/j.jiec.2013.07.020

Mohseni-Bandpi, A., Elliott, D. J., & Zazouli, M. A. (2013). Biological nitrate removal processes from drinking water supply-a review. *Journal of Environmental Health Science & Engineering*, *11*(1), 35. http://doi.org/10.1186/2052-336X-11-35

Montesinos, V. N., Quici, N., Destaillats, H., & Litter, M. I. (2015). Nitric oxide emission during the reductive heterogeneous photocatalysis of aqueous nitrate with TiO2. *RSC Advances*, *5*(3), 85319–85322. http://doi.org/10.1039/C5RA17914A

Montesinos, V. N., Quici, N., Destaillats, H., Litter, M. I., Yang, T., Doudrick, K., … Altshuller, A. P. (2015). Nitric oxide emission during the reductive heterogeneous photocatalysis of aqueous nitrate with TiO 2. *RSC Adv.*, *5*(104), 85319–85322. http://doi.org/10.1039/C5RA17914A

Mook, W. T., Chakrabarti, M. H., Aroua, M. K., Khan, G. M. a, Ali, B. S., Islam, M. S., & Abu Hassan, M. a. (2012). Removal of total ammonia nitrogen (TAN), nitrate and total organic carbon (TOC) from aquaculture wastewater using electrochemical technology: A review. *Desalination*, *285*, 1–13. http://doi.org/10.1016/j.desal.2011.09.029

Mora-Sero, I., Villarreal, T. L., Bisquert, J., Pitarch, Ä., Gomez, R., & Salvador, P. (2005). Photoelectrochemical Behavior of Nanostructured TiO2 Thin-Film Electrodes in Contact with Aqueous Electrolytes Containing Dissolved Pollutants : A Model for Distinguishing between Direct and Indirect Interfacial Hole Transfer from Photocurrent Measurement. *J. Phys. Chem. B*, *109*, 3371–3380. http://doi.org/10.1021/jp045585o

Mori, T., Suzuki, J., Fujimoto, K., Watanabe, M., & Hasegawa, Y. (1999). Reductive decomposition of nitrate ion to nitrogen in water on a unique hollandite photocatalyst. *Applied Catalysis B: Environmental*, *23*(4), 283–289. http://doi.org/10.1016/S0926-3373(99)00086-7

Mori, T., Suzuki, J., Fujimoto, K., Watanabe, M., & Hasegawa, Y. (2000). Photocatalytic reduction of nitrate in water on meso-porous hollandite catalyst: a new pathway on removal of nitrate in water. *Journal of Sol-Gel Science and Technology*, *19*(1–3), 505–510. http://doi.org/10.1023/A:1008724219384

Motojima, S., Suzuki, T., Hishikawa, Y., & Chen, X. (2003). TiO2/C composite microcoils and TiO2 hollow microcoils with high photocatalytic activities and electromagnetic (EM) wave absorption abilities. *Japanese Journal of Applied Physics, Part 2: Letters*, *42*(8 A), L938–L940. http://doi.org/10.1143/JJAP.42.L938

Mozzanega, H., Herrmann, J. M., & Pichat, P. (1979). NH3 oxidation over UV-irradiated TiO2 at room temperature. *J. Phys. Chem.*, *83*(17), 2251–2255. http://doi.org/10.1021/j100480a014

Mukherjee, P. S., & Ray, A. K. (1999). Major challenges in the design of a large-scale photocatalytic reactor for water treatment. *Chemical Engineering & Technology*, *22*(3), 253–260. http://doi.org/Doi 10.1002/(Sici)1521-4125(199903)22:3<253::Aid-Ceat253>3.3.Co;2-O

Murgia, S. M., Poletti, A., & Selvaggi, R. (2005a). DEGRADATION OF AMMONIA CONCENTRATION WATER SOLUTIONS BY TiO 2, (2).

Murgia, S. M., Poletti, A., & Selvaggi, R. (2005b). Photocatalytic degradation of high ammonia concentration water solutions by TiO2. *Annali Di Chimica*, *95*(2), 1–9. http://doi.org/10.1002/adic.200590038

NAE, G. C. (2017). Manage the Nitrogen Cycle.

Nakamura, K., Yoshida, Y., Mikami, I., & Okuhara, T. (2006). Selective hydrogenation of nitrate in water over Cu–Pd/mordenite. *Applied Catalysis B: Environmental*, *65*(3), 31–36. http://doi.org/10.1016/j.apcatb.2005.12.012

Nakata, K., & Fujishima, A. (2012). TiO2 photocatalysis: Design and applications. *Journal of Photochemistry and Photobiology C: Photochemistry Reviews*, *13*(3), 169–189. http://doi.org/10.1016/j.jphotochemrev.2012.06.001

Nan, M., Jin, B., Chow, C. W. K., & Saint, C. (2010). Recent developments in photocatalytic water treatment technology : A review. *Water Research*, *44*(10), 2997–3027. http://doi.org/10.1016/j.watres.2010.02.039

Natarajan, K., Natarajan, T. S., Bajaj, H. C., & Tayade, R. J. (2011). Photocatalytic reactor based on UV-LED/TiO 2 coated quartz tube for degradation of dyes. *Chemical Engineering Journal*, *178*, 40–49. http://doi.org/10.1016/j.cej.2011.10.007

Natarajan, T. S., Thomas, M., Natarajan, K., Bajaj, H. C., & Tayade, R. J. (2011). Study on UV-LED/TiO2 process for degradation of Rhodamine B dye. *Chemical Engineering Journal*, *169*(1–3), 126–134. http://doi.org/10.1016/j.cej.2011.02.066

National Academy of Engineering. (2017). NAE Grand Challenges for Engineering.

Navio, J. A., Colon, G., Trillas, M., Peral, J., Domenech, X., Testa, J. J., … Litter, M. (1998). Heterogeneous photocatalytic reactions of nitrite oxidation and Cr (VI) reduction on iron-doped titania prepared by the wet impregnation method. *Applied Catalysis B: Environmental*, *16*, 187–196. http://doi.org/10.1016/S0926-3373(97)00073-8

Nawi, M. a., & Zain, S. M. (2012). Enhancing the surface properties of the immobilized Degussa P-25 Ti-O2 for the efficient photocatalytic removal of methylene blue from aqueous solution. *Applied Surface Science*, *258*(16), 6148–6157. http://doi.org/10.1016/j.apsusc.2012.03.024

Neta, P., Maruthamuthu, P., Carton, P. M., & Fessenden, R. W. (1978). Formation and Reactivity of the Amino Radical. *Journal of Physical Chemistry*, *82*(17), 1875–1878. http://doi.org/10.1021/j100506a004

Nguyen, N. H., & Bai, H. (2014). Photocatalytic removal of NO and NO2 using titania nanotubes synthesized by hydrothermal method. *Journal of Environmental Sciences*, *26*(5), 1180–1187. http://doi.org/10.1016/S1001-0742(13)60544-6

Nilsson, G., Christensen, H., Pagsberg, P., & Nielsen, S. O. (1971). Transient Electrons in Pulse-Irradiated Crystalline Water and Deuterium Oxide Ice. *Journal of Physical Chemistry*, *76*(7), 1000–1008. http://doi.org/10.1021/j100651a009

Nolan, B. T., Hitt, K. J., & Ruddy, B. C. (2002). Probability of nitrate contamination of recently recharged groundwaters in the conterminous United States. *Environmental Science and Technology*, *36*(10), 2138–2145. http://doi.org/10.1021/es0113854

Oguma, K., Kita, R., Sakai, H., Murakami, M., & Takizawa, S. (2013). Application of UV light emitting diodes to batch and flow-through water disinfection systems. *Desalination*, *328*, 24–30. http://doi.org/10.1016/j.desal.2013.08.014

Oka, M., Miseki, Y., Saito, K., & Kudo, A. (2015). Photocatalytic reduction of nitrate ions to dinitrogen over layered perovskite BaLa4Ti4O15 using water as an electron donor. *Applied Catalysis B, Environmental*, *179*, 407–411. http://doi.org/10.1016/j.apcatb.2015.05.037

Ou, H.-H., Liao, C.-H., Liou, Y.-H., Hong, J.-H., & Lo, S.-L. (2008). Photocatalytic Oxidation of Aqueous Ammonia over Microwave-Induced Titanate Nanotubes. *Environmental Science & Technology*, *42*(12), 4507–4512. http://doi.org/10.1021/es703211u

Ou, H., & Liao, C. (2008). Photocatalytic Oxidation of Aqueous Ammonia over Microwave-Induced Titanate Nanotubes, *42*(12), 4507–4512.

Owlad, M., Aroua, M. K., Daud, W. A. W., & Baroutian, S. (2008). Removal of Hexavalent

Chromium-Contaminated Water and Wastewater: A Review. *Water, Air, and Soil Pollution*, *200*(1–4), 59–77. http://doi.org/10.1007/s11270-008-9893-7

Palanivelu, K., Im, J. S., & Lee, Y. (2007). Carbon Doping of TiO2 for Visible Light Photo Catalysis - A review. *Carbon Science*, *8*(3), 214–224. http://doi.org/10.5714/CL.2007.8.3.214

Pan, J. R., Huang, C., Hsieh, W., & Wu, B. (2012). Reductive catalysis of novel TiO2/Fe0 composite under UV irradiation for nitrate removal from aqueous solution. *Separation and Purification Technology*, *84*, 52–55. http://doi.org/10.1016/j.seppur.2011.06.024

Parastar, S., Nasseri, S., Borji, S. H., Fazlzadeh, M., Mahvi, A. H., Javadi, A. H., & Gholami, M. (2013). Application of Ag-doped TiO2 nanoparticle prepared by photodeposition method for nitrate photocatalytic removal from aqueous solutions. *Desalination and Water Treatment*, *51*, 7137–7144. http://doi.org/10.1080/19443994.2013.771288

Park, D., Shahbaz, H. M., Kim, S. H., Lee, M., Lee, W., Oh, J. W., … Park, J. (2016). Inactivation efficiency and mechanism of UV-TiO2 photocatalysis against murine norovirus using a solidified agar matrix. *International Journal of Food Microbiology*, *238*, 256–264. http://doi.org/10.1016/j.ijfoodmicro.2016.09.025

Park, H., Park, Y., Kim, W., & Choi, W. (2013). Surface modification of TiO2 photocatalyst for environmental applications. *Journal of Photochemistry and Photobiology C: Photochemistry Reviews*, *15*, 1–20. http://doi.org/10.1016/j.jphotochemrev.2012.10.001

Park, J. S., Choi, H., & Cho, J. (2004). Kinetic decomposition of ozone and para-chlorobenzoic acid (pCBA) during catalytic ozonation. *Water Research*, *38*(9), 2284–2291. http://doi.org/10.1016/j.watres.2004.01.040

Park, S., Kim, H., Kim, J. S., Yoo, K., Lee, J. C., Anderson, W. A., & Lee, J. (2007). Photocatalytic Reduction of Nitrate in Wastewater Using ZnO Nanopowder Synthesized by Solution Combustion Method. *Journal of Nanoscience and Nanotechnology*, *7*(11), 4069–4072. http://doi.org/10.1166/jnn.2007.065

Paschoal, F. M. M., Nuñez, L., Lanza, M. R. D. V., & Zanoni, M. V. B. (2013). Nitrate Removal on a Cu/Cu2O Photocathode under UV Irradiation and Bias Potential. *J. Adv. Oxid. Technol.*, *16*(1), 63–70. http://doi.org/10.1515/jaots-2013-0106

Paschotta, R. (2016). The Encyclopedia of Laser Physics and Technology. Retrieved from https://www.rp-photonics.com/encyclopedia.html

Peatross, J., & Ware, M. (2008). *Physics of Light and Optics* (2011c ed.). Brigham Young University. Retrieved from http://optics.byu.edu/BYUOpticsBook_2011c.pdf

Peill, N. J., Bourne, L., & Hoffmann, M. R. (1997). Iron(III)-doped Q-sized TiO2 coatings

in a fiber-optic cable photochemical reactor. *Journal of Photochemistry and Photobiology A: Chemistry*, *108*(2–3), 221–228. http://doi.org/10.1016/S1010-6030(97)00018-X

Peill, N. J., & Hoffmann, M. R. (1995). Development and Optimization of a TiO2-Coated Fiber-Optic Cable Reactor : Photocatalytic Degradation of 4-Chlorophenol. *Environmental Science and Technology*, *29*(12), 2974–2981. http://doi.org/10.1021/es00012a013

Peill, N. J., & Hoffmann, M. R. (1996). Chemical and physical characterization of a TiO2-coated fiber optic cable reactor. *Environmental Science and Technology*, *30*(9), 2806–2812. http://doi.org/10.1021/es960047d

Peill, N. J., & Hoffmann, M. R. (1997a). Development of Solar-Powered Photocatalytic Fiber-Optic Cable Reactor for Waste Stream Remediation. *Journal of Solar Energy Engineering*, *119*, 229–236.

Peill, N. J., & Hoffmann, M. R. (1997b). Solar-Powered Photocatalytic Fiber-Optic Cable Reactor for Waste Stream Remediation. *Journal of Solar Energy Engineering*, *119*(3), 229. http://doi.org/10.1115/1.2888024

Peill, N. J., & Hoffmann, M. R. (1998). Mathematical Model of a Photocatalytic Fiber-Optic Cable Reactor for Heterogeneous Photocatalysis. *Environmental Science & Technology*, *32*(3), 398–404. http://doi.org/10.1021/es960874e

Peill, N. J., & Hoffmann, M. R. (1998). Mathematical Model of a Photocatalytic Fiber-Optic Cable Reactor for Heterogeneous Photocatalysis Mathematical Model of a Photocatalytic Fiber-Optic Cable Reactor for Heterogeneous Photocatalysis, *32*(3), 398–404. http://doi.org/10.1021/es960874e

Peill, N. J., Hoffmann, M. R., & Laboratories, M. M. K. (2002). Development and Optimization of a TiO2-Coated Fiber-Optic Cable Reactor : Photocatalytic Degradation of 4-Chlorophenol Development and Optimization of a Ti02-Coated FiberiOptic Cable Photocatalytic Degradation of 4-Chlorophenol. *EnvironSciTechnol*, *29*(May), 2974–2981. http://doi.org/10.1021/es00012a013

Pelaez, M., Nolan, N. T., Pillai, S. C., Seery, M. K., Falaras, P., Kontos, A. G., … Dionysiou, D. D. (2012). A review on the visible light active titanium dioxide photocatalysts for environmental applications. *Applied Catalysis B: Environmental*, *125*, 331–349. http://doi.org/10.1016/j.apcatb.2012.05.036

Penpolcharoen, M., Amal, R., & Brungs, M. (2001). Degradation of sucrose and nitrate over titania coated nano-hematite photocatalysts. *Journal of Nanoparticle Research*, *3*(4), 289–302. http://doi.org/10.1023/A:1017929204380

Perlman, H. (2014). Groundwater Use in the United States. Retrieved from http://water.usgs.gov/edu/wugw.html

Petriconi, G., & Papee, H. (1968). Decomposition of sodium nitrate solutions under ultra-violet irradiation at 25° C. *Journal of Inorganic and Nuclear Chemistry*, *30*(1963), 1525–1535. Retrieved from http://www.sciencedirect.com/science/article/pii/0022190268802921

Pi, Y., Schumacher, J., & Jekel, M. (2005). The Use of para-Chlorobenzoic Acid (pCBA) as an Ozone/Hydroxyl Radical Probe Compound. *Ozone: Science & Engineering*, *27*(6), 431–436. http://doi.org/10.1080/01919510500349309

Pintar, A. (2003). Catalytic processes for the purification of drinking water and industrial effluents. *Catalysis Today*, *77*(4), 451–465. http://doi.org/10.1016/S0920-5861(02)00385-1

Pipelzadeh, E., Babaluo, a. a., Haghighi, M., Tavakoli, a., Derakhshan, M. V., & Behnami, a. K. (2009). Silver doping on TiO2 nanoparticles using a sacrificial acid and its photocatalytic performance under medium pressure mercury UV lamp. *Chemical Engineering Journal*, *155*(3), 660–665. http://doi.org/10.1016/j.cej.2009.08.023

Pirkanniemi, K., & Sillanpää, M. (2002). Heterogeneous water phase catalysis as an environmental application: a review. *Chemosphere*, *48*(10), 1047–60. Retrieved from http://www.ncbi.nlm.nih.gov/pubmed/12227510

Ploch, N. L., Rodriguez, H., Stölmacker, C., Hoppe, M., Lapeyrade, M., Stellmach, J., … Kneissl, M. (2013). Effective Thermal Management in Ultraviolet Light-Emitting Diodes With Micro-LED Arrays. *IEEE Transactions on Electron Devices*, *60*(2), 782–786. Retrieved from http://cat.inist.fr/?aModele=afficheN&cpsidt=26854151

Plumb, R., & Edwards, J. (1992). Color centers in UV-irradiated nitrates. *The Journal of Physical Chemistry*, (15), 3245–3247. Retrieved from http://pubs.acs.org/doi/abs/10.1021/j100187a014

Polatides, C., Dortsiou, M., & Kyriacou, G. (2005). Electrochemical removal of nitrate ion from aqueous solution by pulsing potential electrolysis. *Electrochimica Acta*, *50*(25–26 SPEC. ISS.), 5237–5241. http://doi.org/10.1016/j.electacta.2005.01.057

Pollema, C. H., Milosavljevi, E. B., Hendrix, J. L., Soluji, L., & Nelson, J. H. (1992a). Photocatalytic Oxidation of Aqueous Ammonia (Ammonium Ion) to Nitrite or Nitrate at TiO2 Particles, *339*, 333–339.

Pollema, C. H., Milosavljevi, E. B., Hendrix, J. L., Soluji, L., & Nelson, J. H. (1992b). Photocatalytic Oxidation of Aqueous Ammonia (Ammonium Ion) to Nitrite or Nitrate at TiO2 Particles. *Chemical Monthly*, *339*, 333–339. http://doi.org/10.1007/BF00810945

Postel, S. L. (2000). Entering an Era of Water Scarcity : The Challenges Ahead. *Ecological Applications*, *10*(4), 941–948.

Postigo, C., & Barceló, D. (2015). Synthetic organic compounds and their transformation products in groundwater: Occurrence, fate and mitigation. *Science of the Total Environment*, *503–504*, 32–47. http://doi.org/10.1016/j.scitotenv.2014.06.019

Prüsse, U., Hähnlein, M., Daum, J., & Vorlop, K.-D. (2000). Improving the catalytic nitrate reduction. *Catalysis Today*, *55*(1–2), 79–90. http://doi.org/10.1016/S0920-5861(99)00228-X

Prusse, U., & Vorlop, K. D. (2001). Supported bimetallic palladium catalysts for water-phase nitrate reduction. *Journal of Molecular Catalysis A: Chemical*, *173*(1–2), 313–328. http://doi.org/10.1016/S1381-1169(01)00156-X

Puckett, L. J., Tesoriero, A. J., & Dubrovsky, N. M. (2011). Nitrogen contamination of surficial aquifers-A growing legacy. *Environmental Science and Technology*, *45*(3), 839–844. http://doi.org/10.1021/es1038358

Pulz, O., Gerbsch, N., & Buchholz, R. (1995). Light energy supply in plate type and ligh diffusing optical fiber bioreactors. *Journal of Applied Phycology*, *7*(2), 145–149.

Qu, X., Alvarez, P. J. J., & Li, Q. (2013). Applications of nanotechnology in water and wastewater treatment. *Water Research*, *47*(12), 3931–3946. http://doi.org/10.1016/j.watres.2012.09.058

Radeka, M., Markov, S., Lončar, E., Rudić, O., Vučetić, S., & Ranogajec, J. (2014). Photocatalytic effects of TiO2 mesoporous coating immobilized on clay roofing tiles. *Journal of the European Ceramic Society*, *34*(1), 127–136. http://doi.org/10.1016/j.jeurceramsoc.2013.07.010

Radjenovic, J., Petrovic, M., & Barceló, D. (2007). Analysis of pharmaceuticals in wastewater and removal using a membrane bioreactor. *Analytical and Bioanalytical Chemistry*, *387*(4), 1365–1377. http://doi.org/10.1007/s00216-006-0883-6

Ranjit, K. T., Krishnamoorthy, R., Varadarajan, T. K., & Viswanathan, B. (1995). Photocatalytic reduction of nitrite on CdS. *Journal of Photochemistry and Photobiology, A: Chemistry*, *86*(1–3), 185–189. http://doi.org/10.1016/1010-6030(94)03930-S

Ranjit, K. T., Krishnamoorthy, R., & Viswanathan, B. (1994). Photocatalytic reduction of nitrite and nitrate on ZnS. *Journal of Photochemistry & Photobiology A: Chemistry*, *81*, 55–58. http://doi.org/10.1016/1010-6030(93)03772-9

Ranjit, K. T., Varadarajan, T. K., & Viswanathan, B. (1995). Photocatalytic reduction of nitrite and nitrate ions to ammonia on Ru/TiO2 catalysts. *Journal of Photochemistry and Photobiology, A: Chemistry*, *89*(1), 67–68. http://doi.org/10.1016/1010-6030(94)04029-2

Ranjit, K. T., & Viswanathan, B. (1997a). Photocatalytic reduction of nitrite and nitrate

ions over doped TiO2 catalysts. *Journal of Photochemistry and Photobiology A: Chemistry*, *107*(1–3), 215–220. http://doi.org/10.1016/S1010-6030(97)00025-7

Ranjit, K. T., & Viswanathan, B. (1997b). Photocatalytic reduction of nitrite and nitrate ions to ammonia on M/TiO2 catalysts. *Journal of Photochemistry and Photobiology A: Chemistry*, *108*(1), 73–78. http://doi.org/10.1016/S1010-6030(96)04505-4

Rasoulifard, M., Fazli, M., & Eskandarian, M. (2014). Kinetic study for photocatalytic degradation of Direct Red 23 in UV-LED/nano-TiO2/S2O82- process: Dependence of degradation kinetic on operational parameters. *Journal of Industrial and Engineering Chemistry*, *20*(5), 3695–3702. http://doi.org/10.1016/j.jiec.2013.12.068

Raupp, G. B., Alexiadis, A., Hossain, M. M., & Changrani, R. (2001). First-principles modeling, scaling laws and design of structured photocatalytic oxidation reactors for air purification. *Catalysis Today*, *69*, 41–49. http://doi.org/10.1016/S0920-5861(01)00353-4

Reeves, P., Ohlhausen, R., Sloan, D., Pamplin, K., Scoggins, T., Clark, C., … Green, D. (1992). Photocatalytic destruction of organic dyes in aqueous TiO2 suspensions using concentrated simulated and natural solar energy. *Solar Energy*, *48*(6), 413–420. http://doi.org/10.1016/0038-092X(92)90050-K

Removal of indoor alpha-pinene with a fiber optic illuminated honeycomb monolith photocatalytic reactor.pdf. (n.d.).

Ren, H. T., Jia, S. Y., Zou, J. J., Wu, S. H., & Han, X. (2015). A facile preparation of Ag2O/P25 photocatalyst for selective reduction of nitrate. *Applied Catalysis B: Environmental*, *176–177*, 53–61. http://doi.org/10.1016/j.apcatb.2015.03.038

Rengaraj, S., & Li, X. Z. (2007). Enhanced photocatalytic reduction reaction over Bi3+–TiO2 nanoparticles in presence of formic acid as a hole scavenger. *Chemosphere*, *66*, 930–938. http://doi.org/10.1016/j.chemosphere.2006.06.007

Richter, C., & Schmuttenmaer, C. A. (2010). Exciton-like trap states limit electron mobility in TiO2 nanotubes. *Nature Nanotechnology*, *5*, 769–772. http://doi.org/10.1038/nnano.2010.196

Rosseler, O., Sleiman, M., Montesinos, V. N., Shavorskiy, A., Keller, V., Keller, N., … Destaillats, H. (2013). Chemistry of NO, (2), 1–6. http://doi.org/10.1021/jz302119g

Rossetti, R., & Brus, L. (1982). Electron-Hole Recombination Emission as a Probe of Surface Chemistry in Aqueous CdS Colloids. *Journal of Physical Chemistry*, *96*, 4470–4472. http://doi.org/10.1021/j100220a003

Rupert, M. G. (2008). Decadal-scale changes of nitrate in ground water of the united states, 1988-2004. *Journal of Environment Quality*, *37*, S240–S248. http://doi.org/10.2134/jeq2007.0055

Rusu, C. N., & Yates, J. T. (2000). Photochemistry of NO Chemisorbed on TiO 2 (110) and TiO 2 Powders. *The Journal of Physical Chemistry. B*, *104*(8), 1729–1737.

Rusu, C. N., & Yates Jr., J. T. (2001). N2O Adsorption and Photochemistry on High Area TiO2 Powder. *J. Phys. Chem. B*, *105*(13), 2596–2603. http://doi.org/10.1021/jp0040345

Sá, J. (2015). *Fuel production with heterogeneous catalysis*. (J. Sá, Ed.) (CRC Press). Boca Raton.

Sá, J., Agüera, C. A., Gross, S., & Anderson, J. a. (2009). Photocatalytic nitrate reduction over metal modified TiO2. *Applied Catalysis B: Environmental*, *85*(3–4), 192–200. http://doi.org/10.1016/j.apcatb.2008.07.014

Sá, J., Barrabe, N., Kleymenov, E., Lin, C., Fottinger, K., Safonova, O. V, … Rupprechter, G. (2012). The oxidation state of copper in bimetallic (Pt-Cu, Pd–Cu) catalysts during water denitration. *Catal. Sci. Technol.*, *2*, 794–799. http://doi.org/10.1039/c2cy00461e

Safari, M., Rezaee, A., Ayati, B., & Jonidi-Jafari, A. (2015). Simultaneous removal of nitrate and its intermediates by use of bipolar electrochemistry. *Research on Chemical Intermediates*, *41*(3), 1365–1372. http://doi.org/10.1007/s11164-013-1279-9

Salafsky, J. S. (1999). Exciton dissociation, charge transport, and recombination in ultrathin, conjugated polymer-TiO2 nanocrystal intermixed composites. *Physical Review B*, *59*(16), 885–894.

Sarkar, A., & Paul, B. (2016). The global menace of arsenic and its conventional remediation - A critical review. *Chemosphere*, *158*, 37–49. http://doi.org/10.1016/j.chemosphere.2016.05.043

Sarkar, A., Robertson, R. B., & Fernandez, J. M. (2004). Simultaneous atomic force microscope and fluorescence measurements of protein unfolding using a calibrated evanescent wave. *Proceedings of the National Academy of Sciences*, *101*(35), 12882–12886. http://doi.org/10.1073/pnas.0403534101

Scanlon, D. O., Dunnill, C. W., Buckeridge, J., Shevlin, S. a, Logsdail, A. J., Woodley, S. M., … Sokol, A. a. (2013). Band alignment of rutile and anatase TiO_2. *Nature Materials*, *12*(9), 798–801. http://doi.org/10.1038/nmat3697

Schaefer, R., Grapperhaus, M., Shaefer, I., & Linden, K. (2007). Pulsed UV lamp performance and comparison with UV mercury lamps. *Journal of Environmental Engineering and Science*, *310*, 303–310. http://doi.org/10.1139/S06-068

Scharko, N. K., Berke, A. E., & Ra, J. D. (2014). Release of Nitrous Acid and Nitrogen Dioxide from Nitrate Photolysis in Acidic Aqueous Solutions.

Schiavello, M. (1997). *Heterogeneous Photocatalysis*. Chichester: Wiley.

Schlesinger, W. H. (2009). On the fate of anthropogenic nitrogen. *Proceedings of the National Academy of Sciences*, *106*(1), 203–208. http://doi.org/10.1073/pnas.0810193105

Schneider, J., Matsuoka, M., Takeuchi, M., Zhang, J., Horiuchi, Y., Anpo, M., & Bahnemann, D. W. (2014a). Understanding TiO2 Photocatalysis : Mechanisms and Materials. *Chem. Rev.*, *114*, 9919–9986. http://doi.org/10.1021/cr5001892

Schneider, J., Matsuoka, M., Takeuchi, M., Zhang, J., Horiuchi, Y., Anpo, M., & Bahnemann, D. W. (2014b). Understanding TiO 2 Photocatalysis : Mechanisms and Materials. *Chemical Reviews*, *114*, 9919–9986. http://doi.org/10.1021/cr5001892

Schuttlefield, J., Rubasinghege, G., El-Maazawi, M., Bone, J., & Grassian, V. H. (2008). Photochemistry of adsorbed nitrate. *Journal of the American Chemical Society*, *130*(37), 12210–12211. http://doi.org/10.1021/ja802342m

Sedman, R. M., Beaumont, J., McDonald, T. a, Reynolds, S., Krowech, G., & Howd, R. (2006, April). Review of the evidence regarding the carcinogenicity of hexavalent chromium in drinking water. *Journal of Environmental Science and Health. Part C, Environmental Carcinogenesis & Ecotoxicology Reviews*. http://doi.org/10.1080/10590500600614337

Seeger, K. (2002). *Semiconductor Physics: An Introduction.* Berlin: Springer. http://doi.org/10.1007/978-3-662-09855-4

Seery, M. K., George, R., Floris, P., & Pillai, S. C. (2007). Silver doped titanium dioxide nanomaterials for enhanced visible light photocatalysis. *Journal of Photochemistry and Photobiology A: Chemistry*, *189*(2–3), 258–263. http://doi.org/10.1016/j.jphotochem.2007.02.010

Sehested, K., & Christensen, H. (1990). The Rate Constant of the Bimolecular Reaction of Hydrogen Atoms at Elevated Temperatures. *Radiat. Phys. Chem*, *36*(3), 499–500. http://doi.org/10.1016/1359-0197(90)90040-O

Seidel, C., & Corwin, C. (2013). Total chromium and hexavalent chromium occurrence analysis. *Journal of the American Water Works Association*, *105*(6), 37–40. Retrieved from http://scholar.google.com/scholar?hl=en&btnG=Search&q=intitle:total+chromium+and+hexavalent+chromium+occurrence+analysis#0

Selase, M., Low, J., Qin, Z., Wageh, S., & Al, A. A. (2015). Nitrogen-doped TiO2 microsheets with enhanced visible light photocatalytic activity for CO2 reduction. *Chinese Journal of Catalysis*, *36*(12), 2127–2134. http://doi.org/10.1016/S1872-2067(15)60989-5

Serpone, N., Salinaro, A., & N. Serpone, A. S. (1999). Terminology, Relative Photonic Efficiencies and Quantum Yields in Heterogeneous Photocatalysis. Part I: Suggested Protocol. *Pure & Appl. Chem.*, *71*(2), 303–320. http://doi.org/10.1351/pac199971020303

Shaban, Y. A., El, A. A., Kh, R., & Farawati, A. (2016a). Journal of Photochemistry and Photobiology A : Chemistry Photocatalytic reduction of nitrate in seawater using C / TiO 2 nanoparticles. *"Journal of Photochemistry & Photobiology, A: Chemistry," 328*, 114–121. http://doi.org/10.1016/j.jphotochem.2016.05.018

Shaban, Y. A., El, A. A., Kh, R., & Farawati, A. (2016b). Journal of Photochemistry and Photocatalytic reduction of nitrate in seawater using C/TiO2 nanoparticles. *Journal of Photochemistry & Photobiology, A: Chemistry*, *328*, 114–121. http://doi.org/10.1016/j.jphotochem.2016.05.018

Shah, M. S. A. ., Park, A. R., Zhang, K., Park, J. H., & Yoo, P. J. (2012). Green Synthesis of Biphasic TiO2 − Reduced Graphene Oxide Nanocomposites with Highly Enhanced Photocatalytic Activity. *Applied Materials and Interfaces*, *4*, 3893–3901. http://doi.org/10.1021/am301287m

Shan, A. Y., Ghazi, T. I. M., & Rashid, S. A. (2010). Immobilisation of titanium dioxide onto supporting materials in heterogeneous photocatalysis: A review. *Applied Catalysis A: General*, *389*(1–2), 1–8. http://doi.org/10.1016/j.apcata.2010.08.053

Shand, M., & Anderson, J. a. (2013a). Aqueous phase photocatalytic nitrate destruction using titania based materials: routes to enhanced performance and prospects for visible light activation. *Catalysis Science & Technology*, *3*(4), 879. http://doi.org/10.1039/c3cy20851f

Shand, M., & Anderson, J. a. (2013b). Aqueous phase photocatalytic nitrate destruction using titania based materials: routes to enhanced performance and prospects for visible light activation. *Catalysis Science & Technology*, *3*(4), 879. http://doi.org/10.1039/c3cy20851f

Sharma, S. K., Petrusevski, B., & Amy, G. (2008). Chromium removal from water: a review. *Journal of Water Supply: Research and Technology—AQUA*, *57*(8), 541. http://doi.org/10.2166/aqua.2008.080

Sharpless, C., & Linden, K. (2005). Interpreting collimated beam ultraviolet photolysis rate data in terms of electrical efficiency of treatment. *Journal of Environmental …*, *4*, S19–S26. http://doi.org/10.1139/S04-045

Shavisi, Y., Sharifnia, S., Hosseini, S. N., & Khadivi, M. A. (2014). Application of TiO2/perlite photocatalysis for degradation of ammonia in wastewater. *Journal of Industrial and Engineering Chemistry*, *20*, 278–283. http://doi.org/10.1016/j.jiec.2013.03.037

Shen, Y. S., & Wang, D. K. (2002). Development of photoreactor design equation for the treatment of dye wastewater by UV/H2O2 process. *Journal of Hazardous Materials*, *89*, 267–277. http://doi.org/10.1016/S0304-3894(01)00317-X

Shi, B. J. Y., Leng, W. H., Zhu, W. C., Zhang, J. Q., & Cao, C. N. (2006). Electrochemically Assisted Photocatalytic Oxidation of Nitrite over Cr-Doped TiO 2 under Visible Light, (1). http://doi.org/10.1002/ceat.200500236

Shifu, C., & Gengyu, C. (2002). Photocatalytic oxidation of nitrite by sunlight using TiO2 supported on hollow glass microbeads. *Solar Energy*, *73*(1), 15–21. http://doi.org/10.1016/S0038-092X(02)00033-6

Shih, Y. H., Liu, W. S., & Su, Y. F. (2012). Aggregation of stabilized TiO2 nanoparticle suspensions in the presence of inorganic ions. *Environmental Toxicology and Chemistry*, *31*(8), 1693–1698. http://doi.org/10.1002/etc.1898

Shih, Y., Zhuang, C., Peng, Y., Lin, C., & Tseng, Y. (2012). The effect of inorganic ions on the aggregation kinetics of lab-made TiO2 nanoparticles in water. *Science of the Total Environment*, *435–436*, 446–452. http://doi.org/10.1016/j.scitotenv.2012.06.076

Shin, H., Jung, S., Bae, S., Lee, W., & Kim, H. (2014). Nitrite Reduction Mechanism on a Pd Surface. *Environmental Science & Technology*, *48*, 12768–12774.

Shinde, S. S., Bhosale, C. H., & Rajpure, K. Y. (2011). Photocatalytic activity of sea water using TiO2 catalyst under solar light. *Journal of Photochemistry & Photobiology, B: Biology*, *103*(2), 111–117. http://doi.org/10.1016/j.jphotobiol.2011.02.002

Simic, M., & Hayon, E. (1971). Intermediates Produced from from the One-Electron Oxidaiton and Reduction of Hydroxylamines. Acid-Base Properties of the Amino, Hydroxylamino, and Methoxyamino Radicals. *Journal of the American Chemical Society*, *93*(23), 5982–5986. http://doi.org/10.1021/ja00752a005

Soares, O. S. G. P., Pereira, M. F. R., Orfao, J. J. M., Faria, J. L., & Silva, C. G. (2014). Photocatalytic nitrate reduction over Pd-Cu/TiO2. *Chemical Engineering Journal*, *251*, 123–130. http://doi.org/10.1016/j.cej.2014.04.030

Soares, O. S. G. P., Pereira, M. F. R., Órfão, J. J. M., Faria, J. L., & Silva, C. G. (2014). Photocatalytic nitrate reduction over Pd–Cu/TiO2. *Chemical Engineering Journal*, *251*, 123–130. http://doi.org/10.1016/j.cej.2014.04.030

Sobana, N., Muruganadham, M., & Swaminathan, M. (2006). Nano-Ag particles doped TiO2 for efficient photodegradation of Direct azo dyes. *Journal of Molecular Catalysis A: Chemical*, *258*(1–2), 124–132. http://doi.org/10.1016/j.molcata.2006.05.013

Sobti, R. C., Sharma, S. K., & Archina. (2011). Nitrate removal from ground water. *Water*

Research, *9*(4), 1667–1675. http://doi.org/10.1016/S0043-1354(87)80018-0

Sommer, R., Cabaj, A., Pribil, W., & Haider, T. (1997). Influence of lamp intensity and water transmittance on the UV disinfection of water. *Water Science and Technology*, *35*(11), 113–118. http://doi.org/10.1016/S0273-1223(97)00244-8

Sowmya, A., & Meenakshi, S. (2015). Photocatalytic reduction of nitrate over Ag-TiO2 in the presence of oxalic acid. *Journal of Water Process Engineering*, *8*, e23–e30. http://doi.org/10.1016/j.jwpe.2014.11.004

Spalding, R. F., & Exner, M. E. (1993). Occurrence of nitrate in groundwater - a review. *Journal of Environmental Quality*. http://doi.org/10.2134/jeq1993.00472425002200030002x

Stackelberg, P. E., Furlong, E. T., Meyer, M. T., Zaugg, S. D., Henderson, A. K., & Reissman, D. B. (2004). Persistence of pharmaceutical compounds and other organic wastewater contaminants in a conventional drinking-water- treatment plant. *Science of the Total Environment*, *329*, 99–113. http://doi.org/10.1016/j.scitotenv.2004.03.015

Stancl, H. O. N., Hristovski, K., & Westerhoff, P. (2015a). Hexavalent Chromium Removal Using UV-TiO2/Ceramic Membrane Reactor. *Environmental Engineering Science*, *32*(8), 676–683. http://doi.org/10.1089/ees.2014.0507

Stancl, H. O. N., Hristovski, K., & Westerhoff, P. (2015b). Hexavalent Chromium Removal Using UV-TiO 2 /Ceramic Membrane Reactor 1, *, 1–9. http://doi.org/10.1089/ees.2014.0507

Stefan, M., & Bolton, J. (2005). Fundamental approach to the fluence-based kinetic and electrical energy efficiency parameters in photochemical degradation reactions: polychromatic light. *Journal of Environmental Engineering …*, *18*, 13–18. http://doi.org/10.1139/S04-026

Stefan, M. I., & Bolton, J. R. (2005). Fundamental approach to the fluence-based kinetic and electrical energy efficiency parameters in photochemical degradation reactions: Polychromatic light. *J. Environ. Eng. Sci.*, *4*, S13–S18. http://doi.org/10.1139/S04-026

Subagio, D. P., Srinivasan, M., Lim, M., & Lim, T. T. (2010). Photocatalytic degradation of bisphenol-A by nitrogen-doped TiO2 hollow sphere in a vis-LED photoreactor. *Applied Catalysis B: Environmental*, *95*(3–4), 414–422. http://doi.org/10.1016/j.apcatb.2010.01.021

Sun, D., Yang, W., Zhou, L., Sun, W., Li, Q., & Shang, J. K. (2016). The selective deposition of silver nanoparticles onto {101} facets of TiO2 nanocrystals with co-exposed {001}/{101} facets, and their enhanced photocatalytic reduction of aqueous nitrate under simulated solar illumination. *Applied Catalysis B: Environmental*, *182*,

85–93. http://doi.org/10.1016/j.apcatb.2015.09.005

Sun, J., Guo, L., Zhang, H., & Zhao, L. (2014). UV Irradiation Induced Transformation of TiO2 Nanoparticles in Water: Aggregation and Photoreactivity. *Environmental Science & Technology*, *48*, 11962–11968. Retrieved from http://pubs.acs.org/doi/abs/10.1021/es502360c

Sun, R.-D., Nakajima, A., Watanabe, I., Watanabe, T., & Hashimoto, K. (2000). TiO2-coated optical fiber bundles used as a photocatalytic filter for decomposition of gaseous organic compounds. *Journal of Photochemistry and Photobiology A: Chemistry*, *136*, 111–116. http://doi.org/10.1016/S1010-6030(00)00330-0

Suriyaraj, S. P., Benasir Begam, M., Deepika, S. G., Biji, P., & Selvakumar, R. (2014). Photocatalytic removal of nitrate using TiO 2 /polyacrylonitrile nanofiber membrane synthesized by co-electrospinning process. *Water Science & Technology: Water Supply*, *14*(4), 554. http://doi.org/10.2166/ws.2014.007

Sutton, R. (2010). *Chromium-6 in U.S. Tap Water*. *Environmental Working Group*. Retrieved from http://static.ewg.org/reports/2010/chrome6/chrome6_report_2.pdf

Suwanchawalit, C., Wongnawa, S., Sriprang, P., & Meanha, P. (2012). Enhancement of the photocatalytic performance of Ag-modified TiO2 photocatalyst under visible light. *Ceramics International*, *38*(6), 5201–5207. http://doi.org/10.1016/j.ceramint.2012.03.027

Suzuki, T., Moribe, M., Oyama, Y., & Niinae, M. (2012). Mechanism of nitrate reduction by zero-valent iron: Equilibrium and kinetics studies. *Chemical Engineering Journal*, *183*(3), 271–277. http://doi.org/10.1016/j.cej.2011.12.074

Svoboda, O., Kubelová, L., & Slavíček, P. (2013). Enabling forbidden processes: Quantum and solvation enhancement of nitrate anion UV absorption. *Journal of Physical Chemistry A*, *117*(48), 12868–12877. http://doi.org/10.1021/jp4098777

Svoboda, O., & Slavíček, P. (2014). Is nitrate anion photodissociation mediated by singlet-triplet absorption? *Journal of Physical Chemistry Letters*, *5*(11), 1958–1962. http://doi.org/10.1021/jz500713a

Tan, S., Egawa, T., Luo, X. D., Sun, L., Zhu, Y. H., & Zhang, J. C. (2016). Influence of barrier height and p-cladding layer on electroluminescent performance of AlGaN deep ultraviolet light-emitting diodes. *Journal of Physics D: Applied Physics*, *49*(12), 125102. http://doi.org/10.1088/0022-3727/49/12/125102

Tandon, P., Li, M. J., Bookbinder, D. C., Logunov, S. L., & Fewkes, E. J. (2013). Nano-engineered optical fibers and applications. *Nanophotonics*, *2*(5–6), 383–392. http://doi.org/10.1515/nanoph-2013-0032

Tantra, R., Sikora, A., Hartmann, N. B., Sintes, J. R., & Robinson, K. N. (2015).

Comparison of the effects of different protocols on the particle size distribution of TiO2 dispersions. *Particuology*, *19*, 35–44. http://doi.org/10.1016/j.partic.2014.03.017

Tawkaew, S., Fujishiro, Y., Yin, S., & Sato, T. (2001). Synthesis of cadmium sulfide pillared layered compounds and photocatalytic reduction of nitrate under visible light irradiation. *Colloids and Surfaces A: Physicochemical and Engineering Aspects*, *179*, 139–144. http://doi.org/10.1016/S0927-7757(00)00649-X

Tawkaew, S., Uchida, S., Fujishiro, Y., & Sato, T. (2006). Photoreduction of NO3 and NO2 under visible light irradiation with layered H4Nb6O17/CdS and H2Ti4O9/CdS nanocomposites. *Molecular Crystals and Liquid Crystals*, *341*, 237–242. http://doi.org/10.1080/10587250008026146

Tawkaew, S., Yin, S., & Sato, T. (2001). Photoreduction of nitrate ion and photoevolution of hydrogen on unsupported TiO2 and TiO2 pillared H4Nb6O17 nanocomposites. *International Journal of Inorganic Materials*, *3*, 855–859. http://doi.org/10.1016/S1466-6049(01)00096-4

Taylor, C. D., & Neurock, M. (2005). Theoretical insights into the structure and reactivity of the aqueous/metal interface. *Current Opinion in Solid State and Materials Science*, *9*(1–2), 49–65. http://doi.org/10.1016/j.cossms.2006.03.007

Teh, C. M., & Mohamed, A. R. (2011). Roles of titanium dioxide and ion-doped titanium dioxide on photocatalytic degradation of organic pollutants (phenolic compounds and dyes) in aqueous solutions: A review. *Journal of Alloys and Compounds*, *509*(5), 1648–1660. http://doi.org/10.1016/j.jallcom.2010.10.181

Tesoriero, A. J., Liebscher, H., & Cox, S. E. (2000). Mechanism and rate of denirification in an agricultural watershed: Electron and mass balance along groundwater flow paths. *Water Resources Research*, *36*(6), 1545–1559.

Tesoriero, A. J., Terziotti, S., & Abrams, D. B. (2015). Predicting Redox Conditions in Groundwater at a Regional Scale. *Environmental Science and Technology*, *49*(16), 9657–9664. http://doi.org/10.1021/acs.est.5b01869

Thøgersen, J., Kissner, R., Nauser, T., Koppenol, W. H., Richter, B., Jensen, F., … Jensen, S. J. K. (2015). Primary photochemistry of peroxynitrite in aqueous solution. *Chemical Physics Letters*, *641*, 187–192. http://doi.org/10.1016/j.cplett.2015.10.056

Tokode, O., Prabhu, R., Lawton, L. a., & Robertson, P. K. J. (2014). The effect of pH on the photonic efficiency of the destruction of methyl orange under controlled periodic illumination with UV-LED sources. *Chemical Engineering Journal*, *246*, 337–342. http://doi.org/10.1016/j.cej.2014.03.002

Trasatti, S. (1972). Electronegativity, Work Function, Heat of Adsorption of Hydrogen on Metals. *Journal of the Chemical Society, Faraday Transactions 1: Physical Chemistry*

in Condensed Phases, *68*, 229–236. http://doi.org/10.1039/f19726800229

Treinin, A., & Hayon, E. (1970). Absorption spectra and reaction kinetics of NO2, N2O3, and N2O4 in aqueous solution. *Journal of the American Chemical Society*, *92*(20), 5821–5828. Retrieved from http://pubs.acs.org/doi/abs/10.1021/ie50494a016

Trogler, W. C. (1999). Physical properties and mechanisms of formation of nitrous oxide. *Coordination Chemistry Reviews*, *187*, 303–327. http://doi.org/Doi 10.1016/S0010-8545(98)00254-9

Tugaoen, H. O. N., Garcia-Segura, S., Hristovski, K., & Westerhoff, P. (2017). Challenges in the photocatalytic reduction of nitrate as a water treatment technology. *Science of the Total Environment*, *599–600*, 1524–1551. http://doi.org/http://dx.doi.org/10.1016/j.scitotenv.2017.04.238

Tung, R. T. (2014). The physics and chemistry of the Schottky barrier height. *Applied Physics Reviews*, *1*(11304), 1–54. http://doi.org/10.1063/1.4858400

Turki, A., Guillard, C., Dappozze, F., Berhault, G., Ksibi, Z., & Kochkar, H. (2014). Design of TiO2 nanomaterials for the photodegradation of formic acid – Adsorption isotherms and kinetics study. *Journal of Photochemistry and Photobiology A: Chemistry*, *279*, 8–16. http://doi.org/10.1016/j.jphotochem.2014.01.008

Ueno, K., & Misawa, H. (2013). Surface plasmon-enhanced photochemical reactions. *Journal of Photochemistry and Photobiology C: Photochemistry Reviews*, *15*, 31–52. http://doi.org/10.1016/j.jphotochemrev.2013.04.001

Uhrlandt, D., Bussiahn, R., Gorchakov, S., Lange, H., Loffhagen, D., & Nötzold, D. (2005). Low-pressure mercury-free plasma light sources: experimental and theoretical perspectives. *Journal of Physics D: Applied Physics*, *38*(17), 3318–3325. http://doi.org/10.1088/0022-3727/38/17/S37

Underwood, G. M., Miller, T. M., & Grassian, V. H. (1999). Transmission FT-IR and Knudsen Cell Study of the Heterogeneous Reactivity of Gaseous Nitrogen Dioxide on Mineral Oxide Particles. *Journal of Physical Chemistry A*, *103*(2), 6184–6190. http://doi.org/10.1021/jp991586i

United States Environmental Protection Agency. (1996). National Primary Drinking Water Regulations: Nitrates and Nitrites. http://doi.org/EPA 816-F-09-004

United States Environmental Protection Agency. (2014). *The Third Unregulated Contaminant Monitoring Rule (UCMR 3): Data Summary*.

USEPA. (2017). Ground Water and Drinking Water Table of Regulated Drinking Water Contaminants.

Vamathevan, V., Amal, R., Beydoun, D., Low, G., & McEvoy, S. (2002). Photocatalytic

oxidation of organics in water using pure and silver-modified titanium dioxide particles. *Journal of Photochemistry and Photobiology A: Chemistry*, *148*(1–3), 233–245. http://doi.org/10.1016/S1010-6030(02)00049-7

Van Cleemput, O., & Baert, L. (1984). Nitrite: a key compound in N loss processes under acid conditions? *Plant and Soil*. http://doi.org/10.1007/BF02205583

Van Gerven, T., Mul, G., Moulijn, J., & Stankiewicz, A. (2007). A review of intensification of photocatalytic processes. *Chemical Engineering and Processing: Process Intensification*, *46*, 781–789. http://doi.org/10.1016/j.cep.2007.05.012

van Grieken, R., Marugan, J., Sordo, C., Martinez, P., & Pablos, C. (2009). Photocatalytic inactivation of bacteria in water using suspended and immobilized silver-TiO2. *Applied Catalysis B: Environmental*, *93*(1–2), 112–118. http://doi.org/10.1016/j.apcatb.2009.09.019

van Grieken, R., Marugan, J., Sordo, C., & Pablos, C. (2009). Comparison of the photocatalytic disinfection of E. coli suspensions in slurry, wall and fixed-bed reactors. *Catalysis Today*, *144*(1–2), 48–54. http://doi.org/10.1016/j.cattod.2008.11.017

Vanderford, B. J., Rosario-Ortiz, F. L., & Snyder, S. A. (2007). Analysis of p-chlorobenzoic acid in water by liquid chromatography-tandem mass spectrometry. *Journal of Chromatography A*, *1164*(1–2), 219–223. http://doi.org/10.1016/j.chroma.2007.07.035

Vereb, G., Ambrus, Z., Pap, Z., Kmetyk??, ??, Dombi, A., Danciu, V., … Mogyor??si, K. (2012). Comparative study on UV and visible light sensitive bare and doped titanium dioxide photocatalysts for the decomposition of environmental pollutants in water. *Applied Catalysis A: General*, *417–418*, 26–36. http://doi.org/10.1016/j.apcata.2011.12.018

Vignesh, K., Priyanka, R., Rajarajan, M., & Suganthi, A. (2013). Photoreduction of Cr(VI) in water using Bi2O3–ZrO2 nanocomposite under visible light irradiation. *Materials Science and Engineering: B*, *178*(2), 149–157. http://doi.org/10.1016/j.mseb.2012.10.035

Villars, D. (1927). The photolysis of potassium nitrate. *Journal of the American Chemical Society*, *49*(1907), 326–337. Retrieved from http://pubs.acs.org/doi/abs/10.1021/ja01401a003

Vione, D., Maurino, V., Minero, C., & Pelizzetti, E. (2001). Phenol photonitration upon UV irradiation of nitrite in aqueous solution I: Effects of oxygen and 2-propanol. *Chemosphere*, *45*, 893–902. http://doi.org/10.1016/S0045-6535(01)00035-2

Vohra, M. S., Selimuzzaman, S. M., & Al-Suwaiyan, M. S. (2010). NH4+-NH3 removal from simulated wastewater using UV-TiO2 photocatalysis: effect of co-pollutants and

pH. *Environmental Technology*, *31*, 641–654. http://doi.org/10.1080/09593331003596536

Voronov, a. (2008). New Generation of Low Pressure Mercury Lamps for Producing Ozone. *Ozone: Science & Engineering*, *30*(6), 395–397. http://doi.org/10.1080/01919510802341012

Wada, Y., Yin, H., & Yanagida, S. (2002). Environmental remediation using catalysis driven under electromagnetic irradiation. *Catalysis Surveys from Japan (United States)*, *5*(2), 127–138. http://doi.org/10.1023/A:1015171801455

Wagner, I., Strehlow, H., & Busse, G. (1980). Flash photolysis of nitrate ions in aqueous solution. *Zeitschrift Für Physikalische Chemie*, *123*(1), 1–33. Retrieved from http://www.degruyter.com/view/j/zpch.1980.123.issue-1/zpch.1980.123.1.001/zpch.1980.123.1.001.xml

Waldner, G., & Kr, J. (2005). Photocurrents and degradation rates on particulate TiO 2 layers Effect of layer thickness , concentration of oxidizable substance and illumination direction. *Electrochimica Acta*, *50*, 4498–4504. http://doi.org/10.1016/j.electacta.2005.02.028

Wang, A., Edwards, J. G., & Davies, J. A. (1994a). PHOTOOXIDATION OF AQUEOUS AMMONIA WITH TITANIA-BASED HETEROGENEOUS CATALYSTS, *52*(6), 459–466.

Wang, A., Edwards, J. G., & Davies, J. A. (1994b). Photooxidation of aqueous ammonia with titanium-based heterogeneous catalysts. *Solar Energy*, *52*(6), 459–466. http://doi.org/10.1016/0038-092X(94)90653-X

Wang, H., Su, Y., Zhao, H., Yu, H., Chen, S., Zhang, Y., & Quan, X. (2014). Photocatalytic oxidation of aqueous ammonia using atomic single layer Graphitic-C3N4. *Environmental Science & Technology*, *48*, 11984–11990. http://doi.org/10.1021/es503073z

Wang, H., & Turner, J. A. (2013). Photoelectrochemical reduction of nitrates at the illuminated p-GaInP2 photoelectrode. *Energy & Environmental Science*, *6*, 1802–1805. http://doi.org/10.1039/c3ee40745d

Wang, R., Yue, M., Cong, R., Gao, W., & Yang, T. (2015). Photocatalytic reduction of nitrate over chalcopyrite CuFe0.7Cr0.3S2 with high N2 selectivity. *Journal of Alloys and Compounds*, *651*(3), 731–736. http://doi.org/10.1016/j.jallcom.2015.08.182

Wang, S. L., Chen, C. C., Tzou, Y. M., Hsu, C. L., Chen, J. H., & Lin, C. F. (2009). A mechanism study of light-induced Cr(VI) reduction in an acidic solution. *Journal of Hazardous Materials*, *164*(1), 223–228. http://doi.org/10.1016/j.jhazmat.2008.07.145

Wang, W., & Ku, Y. (2003a). Photocatalytic degradation of gaseous benzene in air streams

by using an optical fiber photoreactor. *Journal of Photochemistry and Photobiology A: Chemistry*, *159*(43), 47–59. http://doi.org/10.1016/S1010-6030(03)00111-4

Wang, W., & Ku, Y. (2003b). The light transmission and distribution in an optical fiber coated with TiO2 particles. *Chemosphere*, *50*(8), 999–1006. http://doi.org/10.1016/S0045-6535(02)00641-0

Wang, W. Y., & Ku, Y. (2006). Photocatalytic degradation of Reactive Red 22 in aqueous solution by UV-LED radiation. *Water Research*, *40*, 2249–2258. http://doi.org/10.1016/j.watres.2006.04.041

Wang, X., & Lim, T. T. (2010). Solvothermal synthesis of C-N codoped TiO2 and photocatalytic evaluation for bisphenol A degradation using a visible-light irradiated LED photoreactor. *Applied Catalysis B: Environmental*, *100*(1–2), 355–364. http://doi.org/10.1016/j.apcatb.2010.08.012

Wang, X., Pehkonen, S. O., & Ray, A. K. (2004). Removal of Aqueous Cr(VI) by a Combination of Photocatalytic Reduction and Coprecipitation. *Industrial & Engineering Chemistry Research*, *43*(7), 1665–1672. http://doi.org/10.1021/ie030580j

Wang, Y., Yang, J., Gao, W., Cong, R., & Yang, T. (2014). Organic-free hydrothermal synthesis of chalcopyrite CuInS2 and its photocatalytic activity for nitrate ions reduction. *Materials Letters*, *137*, 99–101. http://doi.org/10.1016/j.matlet.2014.08.144

Wani, K. (1994). Ladderlike ionization of the mercury atom in Hg-Ar low-pressure discharge and its modeling. *Journal of Applied Physics*, *75*(10), 4917. http://doi.org/10.1063/1.355780

Ward, M. D., White, J. R., & Bard, A. J. (1983). Electrochemical investigation of the energetics of particulate titanium dioxide photocatalysts. The Methyl Viologen-Acetate system. *Journal of the American Chemical Society*, *105*, 27–31. http://doi.org/10.1021/ja00339a007

Warneck, P., & Wurzinger, C. (1988). Product quantum yields for the 305-nm photodecomposition of nitrate in aqueous solution. *The Journal of Physical Chemistry*, (3), 6278–6283. Retrieved from http://pubs.acs.org/doi/abs/10.1021/j100333a022

Washida, N., Inoue, G., & Suzuki, M. (1985). Vacuum UV photolysis of NH3: Rotational distribution of NH(c1P) and the heat of formation of NH. *Chemical Physics Letters*, *114*(3), 274–278. http://doi.org/10.1016/0009-2614(85)80912-X

Wayne, R. P., Barnes, I., Biggs, P., Burrows, J. P., Canosa-Mas, C. E., Hjorth, J., … Sidebottom, H. (1991). The nitrate radical: Physics, chemistry, and the atmosphere. *Atmospheric Environment Part A, General Topics*, *25*(1), 1–203.

http://doi.org/10.1016/0960-1686(91)90192-A

Wehbe, N., Jaafar, M., Guillard, C., Herrmann, J.-M., Miachon, S., Puzenat, E., & Guilhaume, N. (2009). Comparative study of photocatalytic and non-photocatalytic reduction of nitrates in water. *Applied Catalysis A: General*, *368*(1–2), 1–8. http://doi.org/10.1016/j.apcata.2009.07.038

Weiss, R., & Price, B. (1980). Nitrous Oxide Solubility in Water and Seawater. *Marine Chemistry*, *8*, 347–359. http://doi.org/10.1016/0304-4203(80)90024-9

Wenderich, K., & Mul, G. (2016). Methods, Mechanism, and Applications of Photodeposition in Photocatalysis: A Review. *Chemical Reviews*, *116*, 14587–14619. http://doi.org/10.1021/acs.chemrev.6b00327

Westerhoff, P., Alvarez, P., Li, Q., Gardea-torresdey, J., & Zimmerman, J. (2016). Overcoming implementation barriers for nanotechnology in drinking water treatment. *Environmental Science: Nano*, *3*, 1241–1253. http://doi.org/10.1039/C6EN00183A

WHO. (2016). Nitrate and nitrite in drinking-water.

Wols, B. A., & Hofman-Caris, C. H. M. (2012). Review of photochemical reaction constants of organic micropollutants required for UV advanced oxidation processes in water. *Water Research*, *46*(9), 2815–2827. http://doi.org/10.1016/j.watres.2012.03.036

Wols, B. a., Shao, L., Uijttewaal, W. S. J., Hofman, J. a M. H., Rietveld, L. C., & van Dijk, J. C. (2010). Evaluation of experimental techniques to validate numerical computations of the hydraulics inside a UV bench-scale reactor. *Chemical Engineering Science*, *65*(15), 4491–4502. http://doi.org/10.1016/j.ces.2010.04.013

Wu, J. C. S., Wu, T. H., Chu, T., Huang, H., & Tsai, D. (2008). Application of optical-fiber photoreactor for CO2 photocatalytic reduction. *Topics in Catalysis*, *47*(3–4), 131–136. http://doi.org/10.1007/s11244-007-9022-7

Würtele, M. a, Kolbe, T., Lipsz, M., Külberg, a, Weyers, M., Kneissl, M., & Jekel, M. (2011). Application of GaN-based ultraviolet-C light emitting diodes--UV LEDs--for water disinfection. *Water Research*, *45*(3), 1481–9. http://doi.org/10.1016/j.watres.2010.11.015

Xu, J., Ao, Y., Fu, D., Lin, J., Lin, Y., Shen, X., … Yin, Z. (2008). Photocatalytic activity on TiO2-coated side-glowing optical fiber reactor under solar light. *Journal of Photochemistry and Photobiology A: Chemistry*, *199*(2–3), 165–169. http://doi.org/10.1016/j.jphotochem.2008.05.019

Xu, Y., Cottenden, A., & Jones, N. B. (2006). A theoretical evaluation of fibre-optic evanescent wave absorption in spectroscopy and sensors. *Optics and Lasers in Engineering*, *44*(2), 93–101. http://doi.org/10.1016/j.optlaseng.2005.05.003

Y, Q., SO, P., & MB, R. (2004). Evaluation of three different lamp emission models using novel application of potassium ferrioxalate actinometry. *Industrial & Engineering Chemistry Research*, *43*(4), 948–955.

Yamazoe, S., Okumura, T., Hitomi, Y., Shishido, T., & Tanaka, T. (2007). Mechanism of photo-oxidation of NH3 over TiO2: Fourier Transform Infrared study of the intermediate species, (x), 11077–11085. http://doi.org/10.1021/jp0726790

Yang, J., Dai, J., & Li, J. (2013). Visible light induced photocatalytic removal of nitrate with Nd, n-codoped titania particles. *Science of Advanced Materials*, *5*, 1013–1023.

Yang, J., Lee, S., & Farrokhi, M. (2012). Photocatalytic removal of Cr (VI) with illuminated TiO2. *Desalination and Water Treatment*, *46*, 375–380. Retrieved from http://www.tandfonline.com/doi/abs/10.1080/19443994.2012.677564

Yang, Q., Ling Ang, P., Ray, M. B., & Pehkonen, S. O. (2005). Light distribution field in catalyst suspensions within an annular photoreactor. *Chemical Engineering Science*, *60*, 5255–5268. http://doi.org/10.1016/j.ces.2005.02.067

Yang, T., Doudrick, K., & Westerhoff, P. (2013). Photocatalytic reduction of nitrate using titanium dioxide for regeneration of ion exchange brine. *Water Research*, *47*(3), 1299–307. http://doi.org/10.1016/j.watres.2012.11.047

Ye, C., Gao, H., Zhang, N., & Zhou, X. (2016). Photolysis of Nitric Acid and Nitrate on Natural and Artificial Surfaces. *Environmental Science & Technology*. http://doi.org/10.1021/acs.est.5b05032

Yeh, N., Yeh, P., Shih, N., Byadgi, O., & Cheng, T. C. (2014). Applications of light-emitting diodes in researches conducted in aquatic environment. *Renewable and Sustainable Energy Reviews*, *32*, 611–618. http://doi.org/10.1016/j.rser.2014.01.047

Yeom, Y. H., Henao, J., Li, M. J., Sachtler, W. M. H., & Weitz, E. (2005). The role of NO in the mechanism of NOx reduction with ammonia over a BaNa-Y catalyst. *Journal of Catalysis*, *231*(1), 181–193. http://doi.org/10.1016/j.jcat.2005.01.014

Zaboub, M., Guessoum, A., Demagh, N. E., & Guermat, A. (2016). Fabrication of polymer microlenses on single mode optical fibers for light coupling. *Optics Communications*, *366*, 122–126. http://doi.org/10.1016/j.optcom.2015.12.010

Zacharia, I. G., & Deen, W. M. (2005). Diffusivity and Solubility of Nitric Oxide in Water and Saline. *Annals of Biomedical Engineering*, *33*(2), 214–222. http://doi.org/10.1007/s10439-005-8980-9

Zafiriou, O. C., & Bonneau, R. (1987). Wavelength-dependent quantum yield of hydroxyl radical formation from photolysis of nitrite ion in water. *Photochemistry and Photobiology*, *45*, 723–727. http://doi.org/10.1111/j.1751-1097.1987.tb07873.x

Zafiriou, O. C., & True, M. B. (1979). Nitrite Photolysis in Seawater by Sunlight. *Marine Chemistry*, *8*, 9–32.

Zellner, R., Exner, M., & Herrmann, H. (1990). Absolute OH Quantum Yields in the Laser Photolysis of Nitrate , Nitrite and Dissolved H202 at 308 and 351 nm in the Temperature Range 278-353 K. *Journal of Atmospheric Chemistry*, *10*(3), 411–425.

Zhang, F., Jin, R., Chen, J., Shao, C., Gao, W., Li, L., & Guan, N. (2005). High photocatalytic activity and selectivity for nitrogen in nitrate reduction on Ag/TiO2 catalyst with fine silver clusters. *Journal of Catalysis*, *232*(2), 424–431. http://doi.org/10.1016/j.jcat.2005.04.014

Zhang, F., Pi, Y., Cui, J., Yang, Y., Zhang, X., & Guan, N. (2007). Unexpected Selective Photocatalytic Reduction of Nitrite to Nitrogen on Silver-Doped Titanium Dioxide. *The Journal of Physical Chemistry C*, *111*(9), 3756–3761. http://doi.org/10.1021/jp067807j

Zhang, L., Mohamed, H. H., Dillert, R., & Bahnemann, D. (2012). Kinetics and mechanisms of charge transfer processes in photocatalytic systems: A review. *Journal of Photochemistry and Photobiology C: Photochemistry Reviews*, *13*(4), 263–276. http://doi.org/10.1016/j.jphotochemrev.2012.07.002

Zhang, R., Shuai, D., Guy, K. a., Shapley, J. R., Strathmann, T. J., & Werth, C. J. (2013). Elucidation of Nitrate Reduction Mechanisms on a Pd-In Bimetallic Catalyst using Isotope Labeled Nitrogen Species. *ChemCatChem*, *5*(1), 313–321. http://doi.org/10.1002/cctc.201200457

Zhang, Z., Anderson, W. A., & Moo-Young, M. (2004). Radiation modeling of air phase corrugated plate photocatalytic reactor. *Dynamics of Continuous, Discrete and Impulsive Systems Series B: Applications and Algorithms*, *11*(1–2), 59–68. http://doi.org/10.1016/j.cej.2004.01.001

Zhao, Q., Shang, C., Zhang, X., Ding, G., & Yang, X. (2011). Formation of halogenated organic byproducts during medium-pressure UV and chlorine coexposure of model compounds, NOM and bromide. *Water Research*, *45*(19), 6545–54. http://doi.org/10.1016/j.watres.2011.09.053

Zhu, X., Castleberry, S. R., Nanny, M. A., & Butler, E. C. (2005). Effects of pH and catalyst concentration on photocatalytic oxidation of aqueous ammonia and nitrite in titanium dioxide suspensions. *Environmental Science and Technology*, *39*(10), 3784–3791. http://doi.org/10.1021/es0485715

Zhu, X., Nanny, M. A., & Butler, E. C. (2008). Photocatalytic oxidation of aqueous ammonia in model gray waters. *Water Research*, *42*, 2736–2744. http://doi.org/10.1016/j.watres.2008.02.003

Zona, R., Solar, S., Getoff, N., Sehested, K., & Holcman, J. (2010). Reactivity of OH

radicals with chlorobenzoic acids-A pulse radiolysis and steady-state radiolysis study. *Radiation Physics and Chemistry*, *79*(5), 626–636. http://doi.org/10.1016/j.radphyschem.2009.12.005

Zukauskas, A., Shur, M., & Gaska, R. (2002). *Introduction to Solid-State Lighting*. New York: J. Wiley.

Zuo, Y., & Deng, Y. (1998). The near-UV absorption constants for nitrite ion in aqueous solution. *Chemosphere*, *36*(1), 181–188. http://doi.org/10.1016/S0045-6535(97)10028-5

APPENDIX A

SUPPLEMENTARY BACKGROUND INFORMATION

Lamp Mechanics

Conventional lamps consist of four crucial elements to functionality: gaseous metal ions, electron current induced by a potential difference across an electrode, a noble and inert gas, and a light permeable/impermeable sleeve depending on the desired photonic output. Thus, from the AC current output from the wall, an electric current is induced across a +/- electrode pair within the lamp housing. This induces a flow of electrons throughout this sleeve. Gaseous metal ions, most commonly mercury, exist in a mobile state within the sleeve, coexisting with the inert gas. The inert gas, most commonly argon, is added to serve as the means for pressure modification and additionally to reduce electron collisions with the sleeve wall.

Thus, upon lamp turn-on, a flow of electrons driven by the potential difference between the two electrodes propagates through the argon-mercury media and undergoes collisions. Electron-wall collisions induce a release thermal heat upon electron energy exchange, creating no meaningful photonic output. Electron-argon collisions do not significantly degrade the energy of the electrons, while leaving the argon unchanged and thus represent a quasi-neutral energy transaction. The important collisions for photon emission are the electron-mercury ion collisions, in which mobile electrons transfer energy to mobile mercury electrons. This energy transfer leads to a promotion of an electron within the mercury valence to an excited state. Upon relaxation of this electron to the pre-existing state, or another quantized level of lesser energy, a photon is emitted. Based on the resonance energy of the electron excitation and return, the photon will emit at a particular wavelength. Higher energy discharge corresponds to a shorter wavelength emission.

The inert gas is essential to the process of buffering the electrons from the tube walls to prevent heat transfer upon collision. Additionally, this gas increases the frequency of elastic collisions between gaseous constituents, thereby reducing the mean free path of electrons (and their energy upon collision). This property can be manipulated to increase the number of spectral output wavelengths or to increase high quality low wavelength output by pressure modification. Additionally, energy loss in collisions with the inert gas does not diminish the electron energy level to the extent that the excitation of metal atoms is negated by additional collisions (Flesch, 2006).

Photon Generation in Xe and Hg Low and Medium Pressure Lamps

Photocatalytic processes most commonly employ mercury and 'mercury-free' xenon lamps to provide light irradiation to activate the catalyst. Depending on the chemical constituent of interest, either low pressure or medium pressure lamps are utilized, the former with sharper peaks and singular wavelength ultraviolet (UV) outputs and the latter with a broader spectrum of available wavelength in the UV and low wavelength visible range. The lamp properties that induce these output differences relate to the material utilized (Hg/Xe), the abundance of that material, as well as pressure of the system.

Mercury Lamps

Low pressure mercury lamps are pervasive as efficient fluorescent lamps (Wani, 1994), but are also widely implemented in photocatalytic and germicidal processes due to their wavelength of emission. The emission spectrum of mercury has two high efficiency resonance lines of wavelength 253.7nm and 184.9nm at low pressure (Voronov, 2008). The exclusive emission of these two wavelengths is related to the mean free path the

electron is able to travel within the lamp. Within a low pressure system, the mean free path of electrons is sufficiently large that it can gain enough velocity, and thereby kinetic energy ($KE=1/2mv^2$), that collision with mercury ions produces significant electron excitation – velocities too high result in electron annihilation. The baseline velocity of the electrons may be altered by changing the potential difference between the electrodes. As discussed, the introduction of the inert gas helps to mitigate energy lost in electron-wall collisions and maintain a desired balance of electron velocity and collision frequency. If the pressure is too low, then the probability of electron-mercury collisions diminishes and the likelihood of annihilation increases. At a reasonably low pressure, however, sufficiently high energy collisions may occur resultant in the desired 6^3P_1 to 6^1S_0 transition between resonance states in the mercury that provide a photonic output at 253.7nm (Loo, Moss, & Tozer, 2004).

At pressures between 1-10 bar, what constitutes the medium pressure range, the mean free path length of electrons is shortened due to heightened collision frequency resultant from higher mercury vapor pressure. Thus, an increased applied voltage is necessary to induce electron-ion collisions of sufficient energy to produce photons. The wavelength outputs of medium pressure lamps are longer than those of low pressure lamps due to the diminished energy transfer from electrons to the mercury valence. Due to the higher non-radiative losses and wall losses, the ultraviolet efficiency of medium pressure lamps is lower than that of low pressure lamps (Giller, 2000).

Xenon Lamps

Due to emerging environmental and health concerns from mercury residual from lamp disposal and failure in addition to point of use concerns with warm up time, xenon lamps are being pursued as alternatives (Schaefer, Grapperhaus, Shaefer, & Linden, 2007). Xenon is currently the most promising mercury replacement due to strong resonance and excimer emissions in the VUV region, from 100-200nm (Masafumi Jinno, Okamoto, Takeda, & Motomura, 2007). Xenon lamps similarly utilize a quartz envelope and electric potential between to electrodes; however, they only employ xenon – a noble gas – to provide excitation from electron collisions against a neon gas background. Pulsed xenon-neon lamp emissions have two peaks, one during the discharge current and a second during the afterglow period. Depending on the partial pressure of xenon in the envelope, the afterglow intensity varies – it increases with increasing Xe content (M Jinno, Kurokawa, & Aono, 1999). Discharge wavelengths of pulsed xenon-neon lamps are 147nm and 172nm. Additional output wavelengths between 200-300nm have been reported (Liang, Min, Davis, Green, & Remer, 2003). Xenon efficiencies and luminosities are generally lower than mercury lamps, although for the 147nm output 75% efficiencies have been obtained (Uhrlandt et al., 2005).

Photon Generation in Light-Emitting Diodes

In contrast to xenon or mercury lamp sources which rely on gas discharge, light-emitting diodes (LEDs) are solid state emitters capitalizing on excitation and radiative recombination of electrons and holes in semiconductors to generate photons. Radiative recombination of the injected carriers (electrically-supplemented electrons) has been

demonstrated to have incredibly high efficiency, with some reports of quantum yields close to unity with respect to photon generation (Zukauskas, Shur, & Gaska, 2002).The process of excitation in light emitting diodes is injection luminescence, also called electroluminescence, in which ionization of within a solid state semiconductor or at a p-n junction results in radiant output. Electrons and holes separated within the semiconductor via input energy can recombine in two ways: non-radiatively, which generates vibration, phonons (heat), due to native defects, or a radiative recombination, in which a band-to-band (CB→VB) transition occurs resulting in an emitted photon (Zukauskas et al., 2002). Due to conservation of energy and momentum, the emitted photon will have equivalent energy to the distance between the two bands, the band-gap, unless doped materials or impurities allow for inter-band states (Zukauskas et al., 2002).

Direct gap semiconductors, such as InAlGaN-based LEDs, have been engineered to produce ultraviolet light in the wavelength range of 290-375nm depending on the composition of the material (H. Hirayama, 2005). Longstanding use of gallium arsenide or gallium nitride direct-gap semiconductors to produce visible or white light emitting diodes has yielded innovation to produce wavelengths in the near-UV and UVA/UVB/UVC regions with high efficiency and continuously diminishing cost (H. Hirayama, 2005; S. Kim et al., 2008; Tan et al., 2016).

Mechanistic Assessment of Aqueous Electron/Hole Lifetimes

Ideally, the electrons and holes generated may be utilized to induce chemical reactions at the surface of the metal oxide semiconductor. Fundamental to semiconductor function is the behavior of the p-n junction, where a contact potential exists between the p-type and n-type portions of a semiconductor lattice at equilibrium; this potential

contributes to separation of electrons and holes at the n-type and p-type sides, respectively (Moll, 1964). If this potential is decreased by increasing the positivity of the p-side, charge carriers may more readily diffuse from regions of majority to minority along a charge gradient. However, if the p-type becomes more negative than the n-type side, the barrier is increased and diffusion is greatly diminished. Thus, to understand and catalyze reactions, the process of production and transport of e^-/h^+ pairs in semiconductors as well as the potential for recombination must first be assessed and accounted for.

Production

Conduction electrons and holes are produced in pairs within a semiconductor and at the surface upon proper irradiation. The rate of production (number per unit volume per unit time) depends on the semiconductor material (energy and momentum needed to produce a pair) in addition to the thermal activity of the surroundings (Adler, Smith, and Longini, 1964). Temperature changes in the solution may produce sufficient thermal vibrations within the lattice to produce an electron-hole pair via the breaking of a valence bond. More commonly in photocatalytic endeavors, this production is prompted by a light source (photon emission/absorption) that provides sufficient energy to the semiconductor to break a covalent lattice bond.

Transport

Transit time for holes and electrons to reach photocatalyst surface are related to the radius of the particle, R, and a diffusion coefficient of the excited charge carriers $\tau = R^2/\pi D$ (Gratzel and Frank 1982). Thus, for particles between 10-20nm, a common TiO2 nanoparticle size range, transit time from the point of origin within the structure to the

surface is in the range of picoseconds. Additionally, the morphology of the space-charge region, the near surface region of charge density that differs from the bulk solution, strongly influences charge carrier transport. Distinct band bending patterns result from either an ohmic contact or Schottky barrier which represent electrical properties of semiconductor-metal interfaces (Kolansinski, 2009). The Schottky barrier may be defined as a carrier depletion region at the surface that is resultant from the electrical dipole layer rejection of majority charge carriers from the surface toward the bulk (Seeger, 2002). Additionally, variation in surface states (from a nonhomogeneous semiconductor surfaces) provide a potential for disparity between the electron density at the surface relative to the bulk. This difference allows for diffusive transport of electrons to lower density regions.

The valence band wavefunction of TiO_2 particles has a larger curvature than that of the conduction band, indicating that the 'effective' mass of the hole is smaller than that of the electron; therefore, at the surface, there would likely be more photogenerated holes, whereas electrons would be more readily trapped in the interior (Rajh, Poluektov and Thurnauer 2003). Photoactivation may occur via the surface localization of photogenerated charge carriers traveling from the bulk of the semiconducting material (Cunningham 1988). These charge carriers persist longer at the interface (Cunningham, Goold, and Fierro 1982).

Recombination, Trapping, and Surface Reactions

Upon band gap irradiation, three primary photochemical processes occur in a colloidal TiO_2 nanoparticle system: 1) recombination, 2) trapping, and 3) reactions with surface adsorbed constituents. Recombination occurs as a thermodynamic mechanism of

restoring thermal equilibrium, and it constitutes the largest energy inefficiency of TiO_2. Charge carriers (e^-/h^+) are formed due to the absorption of light into the titanium dioxide nanostructure. Recombination can occur as radiative or non-radiative according to the following equation: $e^-_{cb\ OR\ tr} + h^+_{vb\ OR\ tr} \rightarrow TiO_2 + energy$, where *cb* represents the conduction band, *vb* represents the valence band and *tr* represents a trapped charge carrier (either electron or hole as indicated) (Bahnemann, Dillert, and Robertson 2003). With insufficient transportation rates and/or pathways and external reaction source, i.e., hole scavenger, electron-pair holes will recombine, releasing heat.

Trapping of electrons and holes occurs within the metal oxide lattice and on the surface, slowing recombination rates. There is consensus that electrons prefer trapping at the surfaces of the TiO_2, though there is some evidence and theoretical modeling efforts that suggest bulk trapping supersedes surface trapping (M. a. Henderson, 2011). Upon low temperature irradiation, a small number of electrons are trapped in the interior to produce Ti^{3+} interstitial ions. Electron paramagnetic resonance indicates two types of electron traps in TiO_2 nanoparticles: 1) internal traps with a narrow and axially symmetric EPR signal, and 2) surface traps with broad EPR lines (Rajh, Poluektov and Thurnauer 2003). Hole trapping, however, occurs on oxygen species within and on the titanium dioxide lattice: $Ti^{4+}O^{-}{\blacksquare}Ti^{4+}OH^-$ or $Ti^{4+}O^{2-}Ti^{4+}O^{-}{\blacksquare}$ (Howe & Gratzel, 1985) dependent on surface modifications to the TiO_2 and temperature treatment.

Recombination may be successfully deferred in through consumption of electrons and holes at the surface of the semiconductor. Reactive electrons available for interface transfer from TiO_2 colloids to surface constituents occur at the surface Ti atoms that are coordinated with solvent molecules (Kolle, Moser, & Gratzel, 1985). Reactive holes

transfer at surface oxygen molecules that are covalently linked to titanium atoms (Micic & Zhang, 1993). Radical species generation are postulated as a significant acceptor of surface holes and electrons throughout interfacial transfer, in this case at the solid-liquid interface. This provides both direct and indirect oxidation-reduction pathways. In photocatalytic redox reactions over TiO_2, surface trapped photogenerated holes are the essential to the process, most commonly oxidizing aqueous organic species. In order to maintain neutrality, a balance of oxidation-reduction reactions must exist as photogenerated electrons (-) and holes (+) are consumed. In order to have successful oxidation-reduction reactions of constituents at the surface of the photocatalyst the following two properties must exist: 1) for reduction, the conduction band have a more negative potential than the reducing species; 2) for oxidation, the valence band must have a more positive potential than that of the oxidizing species. Therefore, the bandgap and contaminant must be band-paired to undergo successful redox reaction.

Metal Oxide Surface Charge and Zeta Potential

Chemistry at the water-metal interface, i.e., of semiconductors, is determined by the reactivity of water on the metal, chemical reactivity changes due to the electrochemical potential and steric and electrostatic effects of the solvent (Taylor and Neurock, 2005). Surface layers can be classified in four categories based the carrier densities of the n-type semiconducting surface (in comparison to the bulk): 1) accumulation layers ($n_s>n_b$), 2) flat band ($n_s=n_b$), 3) depletion layers ($n_s<n_b$ and $p_s\leq n_b$), 4) inversion layers ($p_s>n_b$) with n and p representing the carrier densities at the surface (Berz 1975). The accumulation layer is charge dense, while the depletion layer has a lower charge density than the bulk.

The water layer structure is influenced by the metal, but also by the presence of co-adsorbates, dissociation capacity, and the presence of an electric field created by the ionic species (which would induce a dipole alignment). Subsequently, under varied pH conditions, water molecule alignment changes due to changing surface charge of the metal surface (Kolansinski 2009). The point of zero charge (pH_{pzc}), also called the isoelectric point, is defined as the pH at which the overall surface charge is neutral. As the pH or potential changes, the net surface charge will change, most often moving more negative with increasing pH and vice versa. For colloidal species, this pH_{pzc} is the point of zero zeta potential. Zeta potential is defined as the potential differential between a surface and the surrounding bulk liquid. The pH_{pzc} is significant because changes in the surface charge (dipole) cause changes in both the adjoining aqueous layer, but also the accessibility for adsorption of other species in solution (cations to negative surfaces and anions to positive surfaces). The zeta potential represents a net surface charge, and thus represents an aggregate sum of charges on the surface – even at very high pH or electric potential a mix of charges will exist on the surface, allowing for diversity of reactivity and surface adsorption capacity though most often the majority of charge is either positive or negative.

Surface charge of metal oxides is additionally highly dependent on pH due to the variation of (de)protonation of surface sites with increasing or decreasing pH. At high pH, the surface sites would be highly deprotonated, and thus surfaces would likely be more negative. A hydroxylated surface can serve as a proton donor (Bronsted acid) or a proton acceptor (Bronsted base). Electrochemical measurements determine the isoelectric point of the surface – the pH value of a solution in contact with the surface that yields an

equal concentration of XOH2+ and XO- sites. At this point, the surface has a net charge of zero. A high isoelectric point indicates a strong surface basicity, whereas a low isoelectric point indicates a strong surface acidity. These relationships pertain to the ability to donate or accept electrons and influence adsorbate-substrate charge transfers but do not directly address adsorption energy. Adsorption energy pertains mainly to the electrostatic and covalent energy. TiO2 for example, would be protonated at low pH, with surfaces covered by –OH groups:

$$\equiv \mathrm{TiOH_2^+} \leftrightarrow \equiv \mathrm{TiOH} + \mathrm{H^+} \quad \log k_{a1} = -2.5$$

$$\equiv \mathrm{TiOH} \leftrightarrow \equiv \mathrm{TiO^-} + \mathrm{H^+} \quad \log k_{a2} = -8.0$$

which show deprotonation on the surface with increasing pH (Duro, Bruno and Honeyman 2001). In acidic environment, the surface would reflect the first equation with a mix of $TiOH_2^+$ (a very protonated species) and TiOH with excess hydrogen in solution, whereas in an alkaline environment, the surface would reflect the equilibrium of the second equation. Additionally, though the species are the majority in solution, there will be a mix of charges both at low pH and high pH but these equations represent the majority case of the surface charge: (+) at low pH due to the extra hydrogen on the surface and (-) at high pH due to deprotonation with increasing pH.

Electrostatic Surface Complexation Models: Accounting for Ion-Metal Oxide Interactions

Overview of Metal Oxide Surfaces

Metal oxide surfaces experience a surface energy due to an imbalance of forces between atoms, ions and molecules at the surface. Thereby, a finely dispersed solid metal oxide will attempt to reduce its surface area by complexing with adjacent phase

molecules and ions, thus decreasing its overall surface energy. In an aqueous matrix, these molecules may coordinate water molecules by dissociative chemisorption, most often leaving hydroxyl groups at the surface. Because of the metal Ti ions in TiO_2 act as Lewis acids (electron pair acceptor), these surface hydroxyl groups may be replaced by adsorbing oxyanions (Schindler 1981). The charging of a solid surface in a liquid occurs as a result of three mechanisms: 1) ionization or dissociation of surface groups; 2) adsorption or binding of ions from solution onto a charge neutral surface (ion exchangeable surface); 3) charge exchange where charges (protons or electrons) shift to another surface and induce an electrostatic attraction in an acid-base and opposite charge manner (Israelachvili 2011).

Solid-Liquid Interface

The solid-liquid interface can be divided into four regions: the bulk liquid, the bulk solid, the surface of the solid along with its adsorbates, and a region just above the adsorbed layer that is different from the bulk liquid. In aqueous solution, water will complex on the semiconductor surface based on the pH. As such, pH is the master variable that determines the extent of adsorption of aqueous species onto the surface. Basic oxides exhibit a weak covalent energy with respect to the surface OH^{-}bond, but as oxide acidity increases, the covalent energy increases. This is attributable to increasing electronegativity and decreasing ionic radius. Electrostatic energy is more complex due to Coulombic interactions and adsorbate-substrate charge transfers. The overall adsorbate-substrate interaction is influenced by attractive and repulsive interaction with all substrate ions; the charge transfer at this interface is responsible for a charge decrease

of both species as hydroxyl groups and surface oxygen lose electrons and protons and surface cations capture electrons (Noguera 1996).

Ion Adsorption

Adsorption of anion species onto metal oxide surfaces occurs through ligand exchange, a common type of specific adsorption, and correlates to the pH of solution (Hingston 1981). An anion and its conjugate acid will experience an increase in adsorption as the pH increases until dissociation is complete (Bowden, et al. 1973), i.e.:

$$HCrO_4^- \leftrightarrow CrO_4^{2-} + H^+ \quad pK_a = 5.9 \text{ (Brito et al., 1997)}$$

$$HCr_2O_7^- \leftrightarrow Cr_2O_7^{2-} + H^+ \quad pK_a = 1.8 \text{ (Brito et al., 1997)}$$

Thereafter, a decrease in adsorption will occur past the pk_a of the anion/conjugate acid pair. For chromium, it would be expected that above pH 5.9, the majority of the species would be deprotonated and thus experience diminished but existent adsorption rates to the TiO_2 surface.

At the pH_{pzc} of TiO_2 is at pH=6.2, cationic species would more readily adsorb than anionic species due to the reversal in net surface charge. Minimal cation sorption occurs at or below the pH_{pzc}, but above the pH_{pzc}, cations are adsorbed to counterbalance the overall negative surface charge. Part of the net surface charge is also counterbalanced by the exclusion of anion adsorption at higher pH. Therefore, for metal oxides, cation adsorption increases with increasing pH. Cation selectivity is also influenced by changes in oxidation state, which would be represented in this case as Cr(VI) to Cr(III) and their aqueous complexes. With multivalent cations, small changes in pH can lead to relatively large changes in sorption capacity (Kinniburgh & Jackson, 1981).

Surface Complexation Models

Whether ions are specifically or nonspecifically adsorbed within the innermost layer (closest to the metal oxide) depends on the electric field strength and the chemical properties of the ions, while the outer Helmholtz layer includes fully solvated ions. The combination of both of these layers forms the electric double layer. The overall surface charge is determined by the compensation of the excess charge of the first layer at the surface (Kolansinski 2009). With preliminary definitions for the electric double layer and a conceptual framework of charge at the surface, surface complexation models will be explored. The diffusive layer model (two layer model), the constant capacitance model, and the triple layer model are utilized to describe chemical reactions at the surfaces of metal oxides.

The constant capacitance model addresses scenarios when surface potentials are small or high ionic strength in the bulk solution compresses the solution side of the electric double layer. In such a case, the surface potential is proportional to the surface charge:

$$\Psi = \frac{\sigma}{C}$$

where Ψ is the potential in volts, σ is the surface charge in Coulombs/m^2, and C is the integral capacitance in Farad/m^2 (Stumm 1992). Assumptions of the constant capacitance model include: 1) all surface complexes are inner-surface complexes; 2) constant ionic medium reference state determines the activity of aqueous species meaning that no surface complexes are formed with background ions; 3) the surface is represented by one plane of charge (Goldberg 1995). This model most closely resembles the Helmholtz double layer because adsorbing ions are directly adjacent to the surface. The diffuse layer

model, also called the two-layer model, makes another set of assumptions: 1) surface complexes are inner-sphere complexes; 2) complexes do not form with the background ions; 3) the surface is represented by two planes of charge. The triple layer model was created with the assumptions that: 1) H+ and OH- ions form the inner-sphere complexes; 2) outer sphere and inner sphere surface complexes are formed by ion adsorption reactions; 3) outer sphere surface complexes are formed by background ions; 4) three planes of charge represent the surface. The surface-solution interface may also be displayed graphically (potential versus distance from particle surface), with the constant capacitance model as sloped line, the two layer model a horizontal and subsequently curved line (the diffuse layer is the boundary), and the triple layer model a sloped line followed by a line of steeper slope and finally a curve representing the three layers and their potential v. distance relationship.

Surface complexation models describe the interaction of anions and metal oxide surfaces as undergoing a chemisorption substitution process where the anion substitutes for water hydrated or hydroxylated surface species (Blesa et al., 2000). In the constant capacitance or diffusive layer model this would occur in the first coordination sphere, whereas in the triple layer model in the outer layer. It has been shown that the electronic state of the metal in addition to the surrounding solution greatly influence reactivity at the interface, but dynamics within the double layer have not been well documented in literature (Taylor & Neurock, 2005).

Validation of Photon Flux and Potential for Photocatalytic Activity

Quantum yields are well characterized for wavelengths between 205-365nm (Goldstein & Rabani, 2008) for the following reactions (Harris, Adams, Moore, & Sorensen, 1987):

$$[Fe(C_2O_4)_n]^{(3-2n)+} \xrightarrow{hv} Fe^{2+} + (n-1)C_2O_4^{2-} + C_2O_4^-$$

A synergistic thermal reaction causes the quantum efficiencies to exceed unity at wavelengths shorter than 436nm according to the following reaction (Harris et al., 1987):

$$[Fe(C_2O_4)_n]^{(3-2n)+} + C_2O_4^- \rightarrow Fe^{2+} + (n)C_2O_4^{2-} + CO_2$$

These reactions yield a calculation of the dose of light into the system

$$\text{Dose } (\frac{\text{mWs}}{\text{cm}^3}) = \frac{[Fe^{++}]_{\text{after}} - [Fe^{++}]_{\text{before}}}{\Phi} \times \frac{4.719\text{x}10^8 \text{mWs}}{\text{einstein}} \times \frac{\text{L}}{10^3 \text{cm}^3}$$

The value for Φ represents the quantum yield of production of Fe^{++} per Einstein of light:

$$\Phi = \text{quantum yield } (\frac{\text{moles } Fe^{++}}{\text{einstein}})$$

Φ is valued at 1.26 moles Fe^{++}/Einstein for wavelengths less than 365.6nm (assumed to be constant (John Lee & Seliger, 1964)).

Radiant intensity is equivalent to irradiance and fluence rate, and can be ultimately converted to a fluence dose. The energy of each wavelength of light may be articulated on a per-photon basis via the Planck-Einstein relationship:

$$E = \frac{hc}{\lambda}; \qquad hc = 1240eV * nm$$

Fluence rate may be transformed to a photon fluence (or fluence dose) through the use of the following transformation at each measured wavelength:

$$\text{At Xnm: } \frac{10^{-3}\text{mW}}{\text{cm}^2} * \frac{\text{J}/_\text{S}}{1\text{ W}} * \frac{1\text{eV}}{1.6021\text{ x }10^{-19}\text{ J}} * \frac{1\text{ photon}}{\text{E}_\lambda\text{ (eV)}} = \frac{\text{photon}}{\text{cm}^2 - \text{s}}$$

Commonly utilized units are Einsteins/cm^2-s to provide the number of moles of photons delivered at each wavelength.

Accordingly, these values must be multiplied by the time of irradiation to provide a fluence dose instead of a fluence rate. Outputs from each wavelength can be summed to

form the total fluence dose, with differentiation of effective photon dose versus total photon dose. Effective photon dose is similar to the germicidal dose in disinfection (R. Z. Chen, Craik, & Bolton, 2009; Giese & Darby, 2000; Linden & Darby, 1997): accounting for the number of photons delivered to the system that are expected to have a contribution to the desired reaction. In the case of germicidal dose, photons are normalized to the output at 254nm, whereas for photocatalysis, the effective photon dose wavelength range would typically be between ~200-400nm for titanium dioxide-based catalysts due to the large bandgap. Final fluence dose values will most often be of the form photon/cm^2 or einstein/cm^2 where either increment allows for a holistic, normalized view of the energetic and photonic input into the system and is comparable across irradiation sources. Simply reporting irradiation times is inadequate for accurate representation of aqueous photochemistry, and particularly unhelpful for complex reactions such as nitrate reduction to nitrogen gases, where photonic efficiencies vary widely (Mack & Bolton, 1999b) and wavelength-dependent outcomes are hypothesized.

BIOGRAPHICAL SKETCH

Mrs. Tugaoen (formerly Ms. Stancl) is a proud undergraduate physics alumnae from Pepperdine University in Malibu, California. She spent three years doing astrophysics research in her undergraduate course of study which prepared her for the research process. As she transitioned to environmental engineering, she was able to pursue her aspirations of providing clean water and helping those around her. She completed her Master of Science in Environmental Engineering from Arizona State University in December of 2013. She is currently finishing a doctoral program at Arizona State University, working under Dr. Paul Westerhoff and Dr. Kiril Hristovski.

Throughout her doctoral studies, she has developed a hands-on understanding of photochemistry, photocatalysis, optical optimization, and engineered reactor design. Overcoming obstacles in the field of engineering, critical thinking and creative problem solving are skills she is grateful to have gained in the last five years while working on her Ph.D. Married in the spring of 2017, Heather O'Neal Tugaoen is grateful to be a new wife, and soon be officially H.O.T., Ph.D. Beyond the lab, Mrs. Tugaoen is enthusiastic about education and has enjoyed teaching Fluid Mechanics (CEE 341) at Arizona State University. She plans to continue pursuing her passion for vocational teaching in the fall working full time as a university instructor.